A FLEXIBLE MODELING FRAMEWORK FOR GAS TRANSPORT AND REACTION:

APPLIED TO OXIDE REMOVAL FROM NON-OXIDE POROUS MEDIA

By JOSEPH ALBERT PANTINA

A dissertation submitted to the

Graduate School-New Brunswick

Rutgers, The State University of New Jersey

In partial fulfillment of the requirements

For the degree of

Doctor of Philosophy

Graduate Program in Materials Science and Engineering

Written under the direction of

M. John Matthewson and Richard A. Haber

and approved by

_____

_____

_____

_____

New Brunswick, New Jersey

October 2015

ABSTRACT OF THE DISSERTATION

A Flexible Modeling Framework for Gas Transport and Reaction:

Applied to Oxide Removal from Non-Oxide Porous Media

By Joseph Albert Pantina

Dissertation Director: M. John Matthewson

Co-Dissertation Director: Richard A. Haber

Many non-oxide ceramics are produced through the densification of a non-oxide powder compact by sintering. A pervasive problem when processing non-oxide powders is the growth of a native oxide layer on the powder surface due to oxidation. Non-oxide powders sinter poorly without the addition of sintering additives to aid in the removal of surface oxide and lower grain boundary energies. Reducing agents, such as C, remove the oxide layer at hold temperatures much below the sintering temperature, forming a significant amount of gas (mainly $CO_{(g)}$) to be removed. However, sintering additives to enhance densification at the sintering temperature can also form gas at the lower temperature, depleting the additive before reaching the sintering temperature.

In this work, we have developed an analytical modeling framework to simulate gas transport and reaction in a porous medium comprised of an arbitrary collection of chemical species. This modeling framework automatically generates the necessary conditions to calculate the thermodynamic equilibrium composition at a given temperature and uses the Dusty Gas Model (DGM) to predict the gas transport. This model accounts for processing parameters including the initial powder composition, sample thickness, porosity, pore radius, and tortuosity of the powder compact, plus the furnace pressure and heating cycle.

This model was used to predict the time for complete oxide removal (t_c) and residual composition for three material systems. The C/SiC/SiO_2 and B_4C/B_2O_3/C systems were studied to identify the functional dependence of t_c with respect to each processing parameter. Additionally, the C/SiC/SiO_2 system was studied to determine optimal heating cycles to control the rate of $CO_{(g)}$ effusion into the furnace while reduce heating times. The C/SiC/SiO_2/B_4C system was studied to quantify the amount B_4C depleted and redistributed during SiO_2 removal for samples of varying thicknesses, initial SiO_2 content, and holding temperature. B_4C was depleted from the center of the samples and re-deposited at the edges; the most drastic compositional variations occurred at higher temperatures and greater SiO_2 content.

This modeling framework can be applied to other material systems to optimize heating cycles, control gas removal rates and residual sintering additive distributions, and predict t_c due to process variations.

AKNOWLEDGEMENTS

I would like to thank my advisor, Dr. M. J. Matthewson, for all of his support, advice, and patience over the many years I have been at Rutgers University. I would also like to thank my co-advisor, Dr. R. A. Haber, for all of his support and always including me as a part of the Haber group. I am also very grateful of Dr. W. Rafaniello for being so accommodating through this process, lending his experience and knowledge to help improve my thesis, and your underlying work on the study of density gradients in sintered SiC samples that was a major motivation for this work. I would like to thank Dr. V. Domnich for, on short notice, being a part of my committee. Lastly, I would like to express my gratitude to the Ceramic, Composite, and Optical Materials Center (CCOMC) for funding this research project.

Throughout my long tenure at Rutgers University, there have been many people which have provided me opportunities and experiences that have helped me develop as a material scientist. Though at any given time the group has been small, I would like to thank the rest of the members of the Matthewson group, including Anil, Mark, Matt, and Joe. I would like to again thank Dr. R. A. Haber and also Chris Ziccardi for providing me a job to work in the lab as an undergraduate. It was then, Steve Mercurio, which first taught me how to transcend from being just a laboratory technician, into a researcher, through discussions of how the underlying mechanisms influence experiments and how to understand the outcomes. Additionally, I greatly appreciate Michelle Sole, Claudia Kuchinow, and graduate director Dr. L. Klein for all their help and allowing the department to run as smoothly as it does.

I would be amiss to not acknowledge all of the friends that I have acquired over the years. In particular, I thank my friends Ben, Jesse, and Steve B. for the many lunches that we spent together over the early years of grad school, using that time to take more interest in your

projects rather than discussing mine. I must also thank Nick, Tyler, and Vince for your friendship during my extended stay here at Rutgers. Vince deserves extra praise for putting up with me as an officemate. He was subject to the constant questions of “How do you spell that?”, “Is this even a word?”, or “Can you come over here and read this?” (Including, as I write this, “Does anyone know when to actually use ‘Who’ or ‘Whom’?”.). There are many other fellow graduate students, post-docs, undergraduates and faculty at Rutgers University who have assisted me in this process on both a professional and social level, for which I am greatly appreciative.

Finally, I would like to express my deep gratitude towards my family. My parents, Joe and Debbie, who have been nothing but supportive and proud of me during this process. It is to them that I owe so much. My sisters, Toni and Christina, both of which are older and wiser; I seem never to be able to catch up with them on either front. My amazing grandparents, Michael and Filomena, whom I love so much. Lastly, I would like to thank my fiancé, Marina Rombom. She has brought joy to the many years I have spent at Rutgers, ever since we fatefully meet as we lived across the hall as undergraduates. I have been extremely lucky to have had her in my life and by my side throughout this whole endeavor. As this chapter in my life closes, I look confidently at the next because she is with me.

TABLE OF CONTENTS

Page

LIST OF TABLES

LIST OF ILLUSTRATIONS

1 Introduction

The development and use of advanced ceramic materials has improved the technological capabilities of many industries because such materials possess enhanced properties compared to previous generations. Highly controlled processing of advanced ceramics is vital to realizing all of the property benefits that they have to offer. Many applications require completely dense ceramic parts to fully realize the benefits of using that type of material. The class of materials known as non-oxide ceramics are known for their exceptional thermal, structural, mechanical, and chemical properties.[1-10] Non-oxide ceramics include borides, carbides, and nitrides, with some important technical materials being silicon carbide (SiC), boron carbide (B_4C), titanium diboride (TiB_2), silicon nitride (Si_3N_4), etc.

There are a number of ways to synthesis non-oxide ceramics and powders. For industrial applications, large quantities of non-oxide ceramics need be produced. This led to the process of making porous ceramic green bodies using powder processing and subsequent densification through sintering. Different powder synthesis methods tend to be limited by production constraints including compositional purity, particle morphology, particle size distribution, cost, production capacity, etc.[2, 4, 8, 11] Common undesirable characteristic of almost all non-oxide powders are the oxidation reactions that occur at the surface of the powder and that they tend to be difficult to sinter due to their high degree of covalent bonding.[2, 5, 10] Often, oxidation reactions result in an oxide passivation layer on the powder surface. The difficulty in sintering non-oxide ceramics has led to inclusion of various sintering additives in the powder mixture to assist with densification by reducing the oxide content and lowering grain boundary energies during sintering.[5, 11, 12]

The inclusion of sintering additives to non-oxide powder compacts promotes reactions and different mass transport mechanisms to occur during sintering, with the goal of enhancing densification.[12, 13] Reactions that occur inside the porous body can produce gas species, which are mobile and travel through the porous body, often being evacuated due to an external vacuum. The evacuation of gas is known to occur during the various heating stages associated with sintering ceramic materials. This reaction and transport behavior of gas in non-oxide porous media has acted as the motivation for this thesis. Because this is a general problem, applicable to many different material systems, a general modeling framework for simulating the gas transport and reaction problem was sought. The modeling framework ultimately developed is capable of simulating, for an arbitrary chemical system and heating cycle, the transport of a multispecies gas mixture through a porous medium where reactions are assumed to occur to keep the material composition in local thermodynamic equilibrium.

The remaining sections of this chapter begin with further discussion of the pervasiveness of oxide contamination in non-oxide powders. Then, the importance of carbon and boron sintering additives specifically for the SiC material system are considered. Next, the selection and formulation of the physical models necessary to characterize the gas transport and reaction problem are described. Finally, an outline is given of the method of attack for creating the gas transport and reaction model and introducing the SiC, B_4C, and SiC with B_4C material systems analyzed with the framework developed.

1.1 Oxide Contamination of Non-Oxide Powders

The steps performed in order to form a non-oxide powder compact will dictate the final oxide content of the compact. These steps can be loosely classified as powder synthesis, powder processing, powder storage, and green body formation.[11] During each step, the amount of oxide

contamination and/or surface oxidation of the powder will vary with the particle size distribution and morphology, due to their influence on the particle surface area. Washing techniques can be used to eliminate some oxide contamination before green body formation, but may not fully remove all of the oxide plus there is still the ability to re-introduce more oxide at later stages. Ultimately, to ensure the elimination of oxide from green body before reaching the sintering temperature, sintering additives must be used to reduce the oxide during the initial stages of sintering. A brief overview of some aspects of oxide contamination for a variety of non-oxide powders is presented to highlight the generality of this problem.

There are many different methods to synthesize raw non-oxide ceramic powders. Two popular production methods use either gas phase reactors or carbothermic reduction.[2, 11] Gas phase reactors can utilize any number of different source gases and are capable of producing most non-oxide powders and in very high purity.[1, 2, 11] They tend to have tightly controlled vacuum or inert atmosphere environments, limiting powder oxidation during synthesis. They mostly produce very fine particles (< 500 nm), and as a result have large surface areas.[11] Though oxidation of the particle surface may not occur during synthesis due to the controlled environment, the powder must still be transferred from the synthesis environment to be further processed, which may permit oxide formation.

Carbothermic reduction methods produce non-oxide powders through the reduction of a metal oxide by carbon. This is a popular way to make large volumes of SiC and B_4C, typically resulting in large particle sizes.[2] These powders require comminution for size reduction, which increases the surface area available for oxidation.[14] Unreacted oxide precursor may be present as discrete particles or have coated the non-oxide powders due to melting of the oxide phase at elevated temperatures.[2, 15] Again, even if the powders can be produced without oxide contamination, they may become contaminated during further processing.

Once the powder has been synthesized, it can either be stored until needed or milled. These powders are normally further processed by milling to incorporate additives or comminuted to reduce the particle size produced during synthesis. There are wide variety of milling and comminution techniques that can be used, with different levels of control of the processing environment.[11, 16] Comminution reduces the particle size by fracturing the particles which, creates new surfaces that may oxidize and further increase the oxide content of the powder. A study on turbomilling SiC showed that a powder with 0.31 weight percent oxygen (wt% O) prior to milling, had 1.61 wt% O after milling in air.[17] Some attempts to reduce oxidation of the newly formed surface are to mill in non-polar solvents and/or dry the powder in an inert gas atmosphere, but there are not fully effective at halting further oxidation.[17-19] For example, an as-received HfB_2 powder containing 0.44 weight percent oxygen (wt% O) prior to milling, had 0.89 wt% O after controlled milling in cyclohexane and drying in an inert gas atmosphere; a doubling of the oxide content occurred even when carefully trying to avoid oxidation.[19] Thus, milling will tend to unavoidably increase the oxide content of most non-oxide powders.

It is emphasized that oxide contamination may occur during powder synthesis and will almost always occur during milling. There are a number of different washing techniques that can be used to remove surface oxide from non-oxide powders. These methods and their effectiveness, differ based upon the form of the oxide present (SiO_2, B_2O_3, ZrO_2, HfO_2, WO_3, etc.). It is common for as-received SiC and B_4C powders to contain a few wt% O in the form of SiO_2 and B_2O_3, respectively. To remove SiO_2 from SiC, it is found that washing the powder in an acidic solution of HF or basic solution of NaOH or KOH is effective at reducing the oxygen content, but >0.5 wt% O may remain after washing.[2] HF washing Si_3N_4 powder is also effective at removing SiO_2.[20] Repeated washing of B_4C in methanol can remove B_2O_3 to levels undetectable by XRD measurement.[21] The removal of ZrO_2 and HfO_2 can be achieved with HF, but ZrB_2 and

HfB_2 often have residual B_2O_3 on the surface which can also be reduced by repeated washing in methanol.[22-24] The surface oxide of WC can actually be removed by storing it in water, ENREF_25 the surface of the WC does oxidize, but forms tungstic oxide hydrate, which spalls off the surface and precipitates out of solution.[25] This process continuously occurs, acting to reduce the amount of WC present. Washing techniques can reduce or eliminate surface oxide that is introduced by prior processing steps and can be done either by the powder manufacturer and/or the end user.

After a powder is produced, milled, and possibly washed, it still undergoes some period of storage before being formed into a green body. The relevant timeframe for powder storage is set by the time it takes a manufacturer to sell and ship the powder after production, the time between powder processing and fabrication by an end user, or a combined influence of both. The amount of oxidation during storage is strongly influenced by the particle surface area and the storage environment. Higher surface area powders will have higher oxide content compared to low surface area powders because the surface oxidation is occurring over a larger area. High temperature studies show that surface oxidation is diffusion controlled and follows a parabolic rate law.[26-29] SiC will oxidize to SiO_2 at room temperature even with low oxygen exposure.[29] The surface of Si_3N_4 has also been shown to oxidize in air at room temperature.[20] WC oxidizes in pure oxygen at room temperature after only an hour and it will grow to a thickness of a few nanometers in high humidity air over the course of a week.[25] Thus, even if the powder is produced with low oxide content or washed to remove oxide, the oxide contamination may be reintroduced during storage.

Finally, the powder must be formed into a green body. The oxide contaminants introduced during the initial processing steps and storage will still be present unless an end user decides it necessary to wash the powder before forming. However, this may not be possible if,

for example, the powder has already been spray dried. There are many wet and dry processing techniques to form the requisite green body to be sintered.[10-12, 16] If the processing environment is not controlled during green body formation or drying of the green body is required, then the oxide content of the final powder compact may increase again. The presence of oxides in the green body can inhibit densification during sintering.

Since it is known that some amount of oxide will be present in the powder green body, sintering additives are typically added to aid the oxide removal during the initial stages of sintering. The sintering additives can be added as powders to the bulk powder formulation or incorporated as binders that leave a residue during "binder burnout".[11, 12, 30] Carbon is a common sintering additive for a number of systems including SiC, B_4C, ZrB_2, HfB_2, *etc*., because it reacts with their respective oxides to form $CO_{(g)}$ that can be removed under vacuum during initial stages of sintering.[5, 13, 18, 31-33] There are other sintering additive combinations used for some materials. For example, it is found that for ZrB_2 and $Zr(Hf)B_2$,WC or B_4C and C are both effective at removing the residual oxide by forming gas.[5]

In summary, the processing steps prior to and including the formation of a non-oxide green body influence the oxide content of the resulting powder compact. Oxide removal from the powder compact, prior to sintering, relies on the formation of oxygen containing gas species throughout the interior of the powder compact which must be removed under vacuum.

1.2 Modeling Motivation – SiC with C and B Sintering Additives

The foundations of this thesis were built upon studying the initial stages of solid state sintering in SiC green bodies. The pressureless sintering of SiC has been studied since pioneering work by Prochazka (1975), using boron and carbon as sintering additives.[34, 35] In this early work it was observed that the presence of C alone was not responsible for enhanced densification, but

was necessary, along with B, to achieve above 95% theoretical density.[34] It has since been widely accepted that the addition of C aids the removal of the native surface oxide layer of SiO_2 from the surface of SiC particles by the formation of $CO_{(g)}$ through the overall reaction[8, 13, 33, 36-39]

$$SiO_2 + 3C \rightarrow SiC + 2CO_{(g)} \quad (1)$$

The removal of oxide, prior to reaching the sintering temperature, helps achieve a higher sintered density.[13, 31, 33, 40]

The interdependence of B and C as sintering additives spawned a number of studies to identify the individual effects of B and C additives.[31, 38-44] Stobierski *et al.* (2003) examined the hot-pressing and pressureless sintering of SiC by independently varying the B and C content in SiC green bodies.[33, 45] Both samples comprised of pure SiC and SiC with 3.0 wt% C show a decrease in oxygen content with increasing temperature. The onset of oxygen removal begins below 1000°C with the maximum removal rate occurring between 1200°-1600°C, as shown in Figure 1-1.

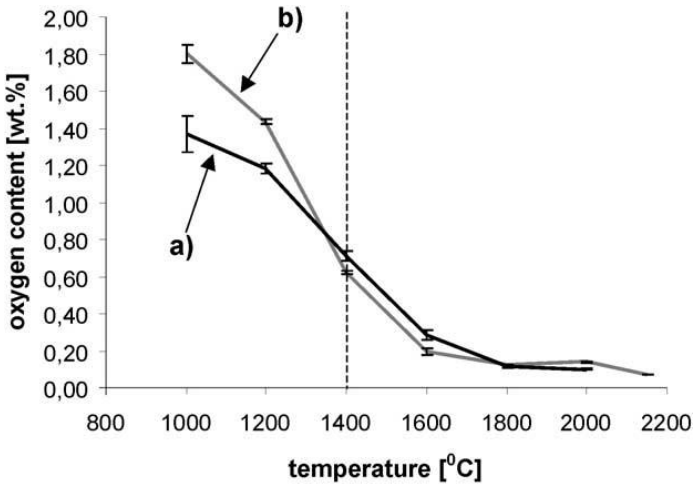

Figure 1-1: Change in oxygen content for the following systems: (a) SiC containing 3 wt% C (b) pure SiC.[33]

Since both systems show a decrease in oxygen content, oxide reduction by free carbon cannot be the oxide removal mechanism. In the absence of C it is suggested that the SiO_2 is reduced by SiC through the reaction

$$2SiO_2 + SiC \rightarrow 3SiO_{(g)} + CO_{(g)} \quad (2)$$

resulting in a significant amount of $SiO_{(g)}$.[31, 33]

Further work by Stobierski *et al.* (2001) examined the optimal boron additive concentration and showed that a relatively small additive concentration is needed to achieve near full density.[31, 45] SiC with 3.0 wt% C and varying amounts of B were sintered by various techniques to observe the effect on densification. Figure 1-2 shows that between 0.2 and 0.5 wt% B achieved the highest densities, with a decrease in density for higher B concentrations when pressure-less sintering.

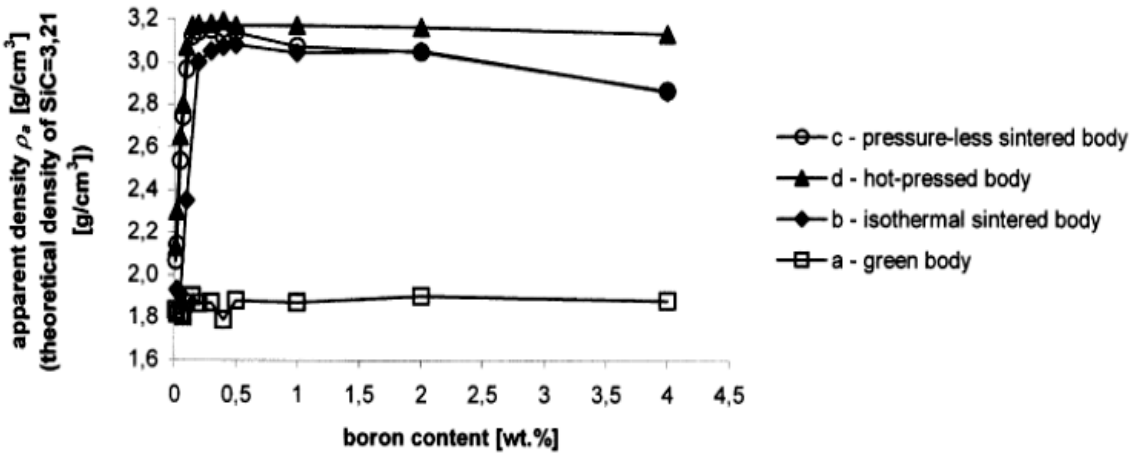

Figure 1-2: Apparent density for the following materials: (a) green body, (b) isothermal sintered body, (c) pressureless (polythermal) sintered body, (d) hot pressed body.[45]

Additionally, they reported that the grain growth mechanism for samples above 0.5 wt% B shows a clear change to discontinuous grain growth and elongated grains in the sintered microstructure. Figure 1-3 shows the occurrence of exaggerated grain growth and increased porosity of the SiC microstructure as the B additive concentration is increased.[45]

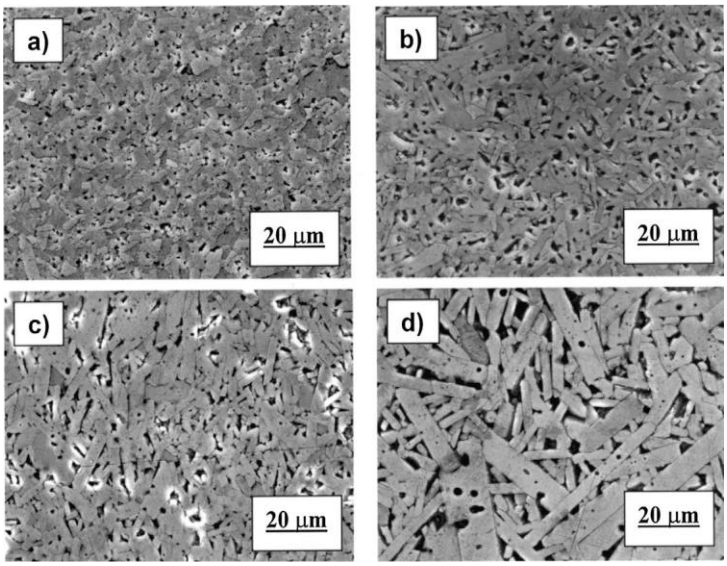

Figure 1-3: Tendency to discontinuous and directional grain growth. Sintered bodies containing (a) 0.5%, (b) 1%, (c) 2%, and (d) 4 wt% of boron. (All samples contain 3 wt% of carbon).[45]

For a given choice of sintering method, the addition of boron in different concentrations impacts the densification of SiC, the type of grain growth, and the microstructure. Instead of

adding B, B_4C can be used as a sintering additive with a similar effect on the density and microstructure of sintered SiC compacts.[36, 44, 46]

Ness and Rafaniello (1994) showed that a SiC compact held under vacuum at an intermediate holding temperature of 1400°-1700°C before reaching the sintering temperature will result in a higher density than without the intermediate hold.[36] It was found that thicker samples and lower temperature holds were less effective at increasing the overall final density, as shown in Figure 1-4.

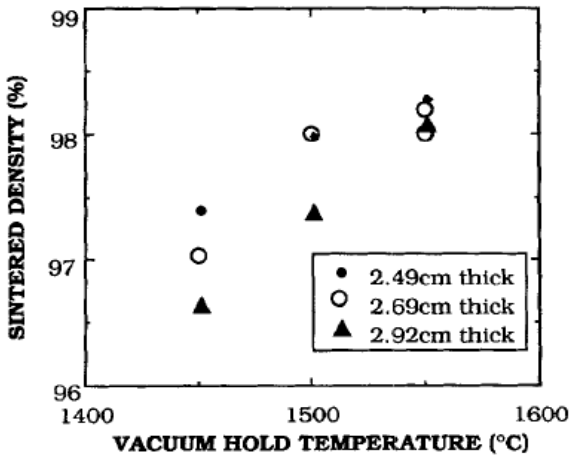

Figure 1-4: Effect of 2-hour vacuum hold on final density (sintered at 2120°C) of 12-cm square tile with thicknesses indicated.[36]

There is a density gradient across the sintered SiC compacts, with the highest densities at the edges. This trend is seen in Figure 1-5 when comparing the density of cubes taken across the thickness of sintered tiles using different intermediate hold temperatures.

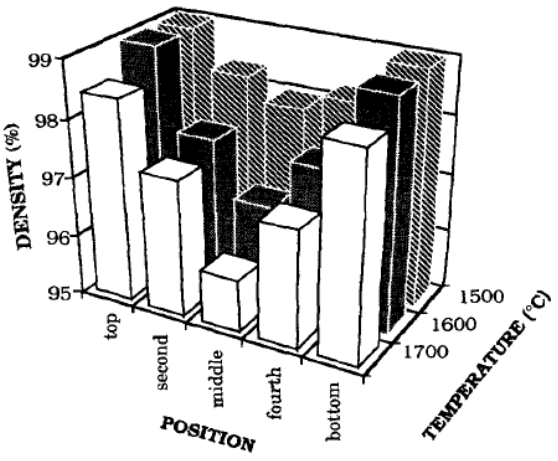

Figure 1-5: Densities of individual cubes following 2-h vacuum holds at indicated temperatures.[36]

It was proposed that the higher densities were most likely due to the faster removal rate of $CO_{(g)}$ at the edges, which allows the reaction between C and SiO_2 to proceed faster. The lower densities in the center of the samples held at higher temperatures were attributed to microstructural coarsening by $SiO_{(g)}$.[13, 31, 36] Observed compositional and density gradients across the sintered thickness suggests that the SiO_2 removal process is transport limited and not reaction rate limited.[36]

The improved densification of SiC due to the removal of SiO_2 through the formation of $CO_{(g)}$, starting at temperatures as low as 1000°C, has been observed by many researchers.[31, 33, 38, 39, 41] Tanaka (1991) reports that the formation of $CO_{(g)}$ will react with B to form $B_2O_{3(g)}$ and $BO_{(g)}$ according to the reactions[13]

$$2B + 3CO_g \rightarrow B_2O_{3(g)} + 3C \quad (3)$$

$$B + CO \rightarrow BO + C \quad (4)$$

These reactions will diminish the amount of B in the sample, before reaching sintering temperatures.[13, 41] It is recommended to heat slowly in the range from 1000°C-1500°C or to use an extended hold at an intermediate temperature. The suggested heating profile and holding

temperature range is consistent with the work of Ness and Rafaniello (1994). However, this suggestion is made to also account for the effect B depletion will have on the residual B concentration present at the sintering temperature.

The proposal that the transport rate of $CO_{(g)}$ out of the powder compact is responsible for controlling the removal rate of surface oxide acts as a quantifiable phenomenon that impacts the densification of SiC and other non-oxide ceramics. Additionally, the presence and transport of $CO_{(g)}$ may cause secondary effects such as depletion of B sintering additives, which are seen to affect the sintered microstructure. These factors motivated the selection of a gas transport and reaction scheme that can be used to model multispecies gas flow through a porous medium over a broad range of conditions (*e.g.* a porous SiC green body with varying Knudsen numbers).

The selected reaction scheme assumes and maintains local thermodynamic equilibrium between the solid and gas species, throughout the porous medium, as transport occurs. The choice of local thermodynamic equilibrium is consistent with the observation that the process is not reaction rate limited since that would not lead to the observed property gradients. Ultimately, a general modeling framework allowing for arbitrary material systems, compositions, and pore structures has been developed to replicate the different scenarios possible in which one has a non-oxide powder compact, its native surface oxide layer, and a variety of sintering additives.

1.3 Transport in Porous Media

The problem of fluid transport in porous media is a mature subject that has been studied extensively in many different fields including chemical, mechanical, hydrological engineering, etc.[47-60] The computational modeling of fluid transport generally termed

computational fluid dynamics (CFD), has gas transport modeling as a subset of CFD. One of the most widely used and best known models is based upon the Navier-Stokes equation (NSE).[52, 59, 60] The NSE is a continuum model derived from the conservation of mass, momentum, and energy. These equations are generally used for single phase fluid transport and require modification to incorporate multi-species fluid mixtures.[59] To complete the description of the NSE, a representation of all the fluid boundaries is required. For a porous medium, this would be an actual structural representation of the porous body, such as that given in Figure 1-6.

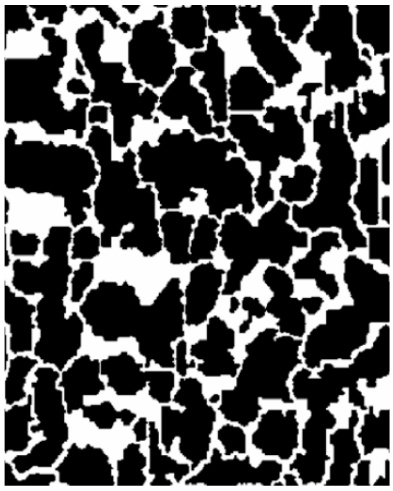

Figure 1-6: Digitized porous microstructure of sandstone computed from X-ray Micro Tomography (XMT). Solid particles are black and pore area is white. Sample dimensions 1418 µm by 1774 µm with a resolution of 24.54 µm.[61]

The incorporation of the pore structure, which is generally too complex to measure accurately, and the computational cost and complexity of solving a system with such complex boundary conditions, makes the NSE unacceptable for most fluid transport problems in porous media.

The Lattice Boltzmann Model (LBM) is a discretized model originating from the Boltzmann equation in kinetic theory.[61-63] The LBM also requires a representation of the actual pore structure of the porous medium. This method assumes that the fluid and porous medium can be discretized as points on a grid, where the fluid is imagined as fictitious particles on the

grid points that have a prescribed velocity. The movement of the particles and their new velocity after each time step is based upon evaluating an appropriate collision operator to describing the dynamics of the particles. The porous medium is included by prohibiting movement onto any boundary grid points. While this model has a straightforward interpretation, the number of grid points and consequently the computational cost required to model large porous systems becomes prohibitive without the use of large computing clusters.

Both the NSE and the LBM applied to porous media can be considered as high fidelity models that give a description of the flow behavior across the whole porous medium, as well as the flow field within individual pores. For many applications, the detailed nature of the flow field within the pore structure is not needed and the pore structure is not known to a high enough degree of accuracy to justify the use of these complex models. Relaxing the condition to model the detailed flow field within the pores, opens up a number of approximate or phenomenological models for describing the fluid flow across a porous medium.

The simplest model for fluid flow across a porous medium is based upon Darcy's law:[57, 58]

$$q = -\frac{\kappa}{\mu}\nabla p \tag{5}$$

which is used to predict the flux, q, of a single fluid phase with viscosity, μ, through a porous medium with a specified permeability, κ, and pressure gradient, ∇p. This is a simple example of a phenomenological model for describing fluid transport in a porous medium because it incorporates the whole description of the resistance to fluid flow caused by the porous structure into one parameter for the permeability.

There are a vast number of fluid transport models for porous media, each applicable to different physical systems. An identification of a few classes of models are: single phase gas transport, single phase liquid transport, gas and liquid phase transport, single phase multispecies gas transport, multiple immiscible liquid phase transport, multispecies gas and liquid phase transport, *etc*.[52, 53, 57-60, 64] Within each class of model, there are multiple forms of the governing equations depending on assumptions made about the nature of the porous medium (homogenous, fractured, *etc*.) and the fluid properties (Newtonian, non-Newtonian, compressible, etc.).[49, 53, 57, 58, 64] Despite there being a wide variety of models to fit the needs of different fields of study, these models all attempt to characterize the structure of the porous medium using only a few parameters.

Webb (1996) conducted a comparison of an advection-dispersion flux model implemented using the widely used software package TOUGH2 and the Dusty Gas Model for binary gas diffusion.[65, 66] The simulated results were compared to a number of binary gas diffusion experiments in porous media and showed that only the DGM was able to accurately predict the correct behavior in the Knudsen flow regime.[65] For the purpose of this thesis, single phase multispecies gas transport in a porous medium was analyzed using the Dusty Gas Model (DGM).[49, 53, 55] The DGM is described in detail in Chapter 3.

Characterizing the structure of a porous medium can be performed by two different methods. The first is to formulate an experiment to measure the relevant parameters empirically. For instance, the Darcy's law permeability can be measured with a fluid of known viscosity and measurements of flow rates for different pressure gradients. The slope of the linear regression obtained from a plot of the flow rate *versus* the pressure gradient should give a good approximation of $-\frac{\kappa}{\mu}$, from which κ can easily be extracted. This approach provides an

accurate description of the porous medium that can be used along with the Darcy's law model to make predictions for flow rates not measured. The downside of this approach is that using a different porous medium would require a new set of experiments to determine the permeability. However, it has the significant advantage that it is a functional measurement of the flow mode

The second method of characterizing the structure is to estimate the relevant parameters, such as permeability, by using knowledge of the pore structure and an appropriate structure model. These models tend to be based on idealized microstructures of porous media, such as those shown in Figure 1-7.

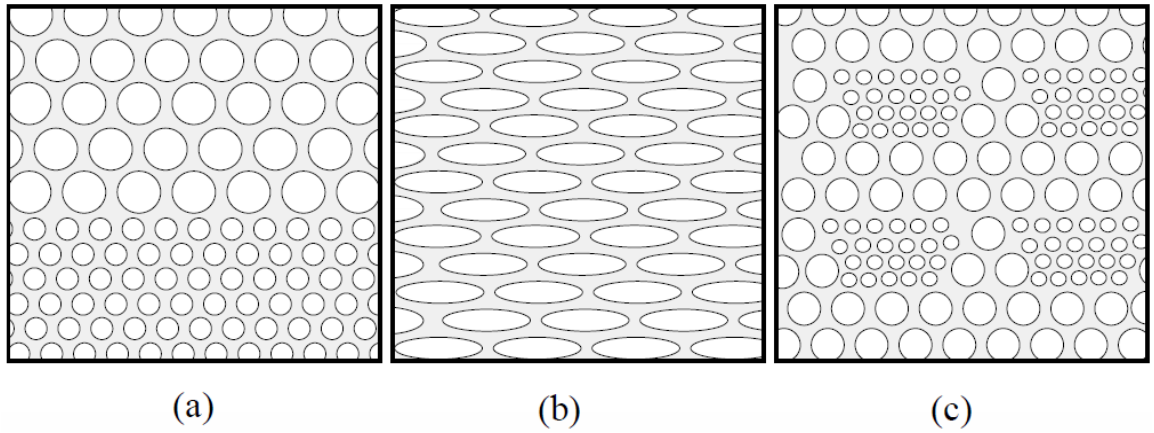

Figure 1-7: Idealized microstructures of porous media which illustrate heterogeneity and anisotropy.[64]

A simple gas permeability model for a packed bed of homogenous spherical particles was developed by Kozeny and Carman:[12]

$$\kappa = \frac{\varepsilon^{3}}{5(1-\varepsilon)^{2}S^{2}\rho_{s}^{2}} \tag{6}$$

where, ε is the porosity, S is the specific surface area of the solid particles ($m^2 \cdot kg^{-1}$), and ρ_s ($kg \cdot m^{-3}$) is the density of the solid phase.

Structure based models have the advantages of being more flexible and the parameters of the structure models are often more easily measured than direct measurement of the flow parameters (*i.e.* permeability). The disadvantage of structure models is that they are often less accurate than direct measurement because of limiting assumptions made during their derivation. To provide flexibility in analyzing different porous media, structure models were used to approximate the flow parameters for the DGM and are described in Chapter 4. The structure parameters used in this work to describe porous media are the porosity, tortuosity, and pore radius given by ε, q, and r, respectively. The tortuosity is defined by the square of the ratio between the effective gas pathway and the sample thickness. A schematic representing the tortuosity is given in Figure 1-8.

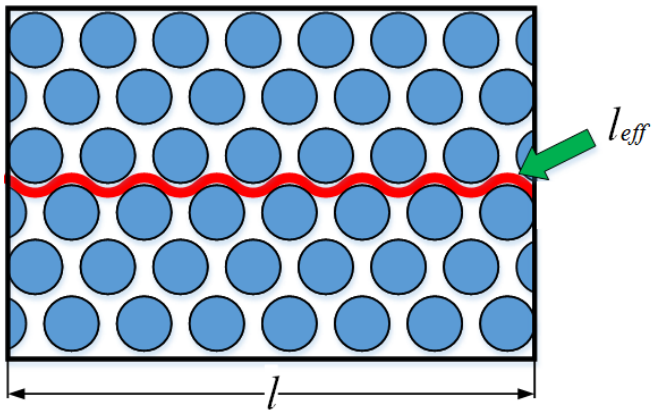

Figure 1-8: Tortuosity, q, of an idealized homogeneous powder compact.

Even with the use of structure models it is not a trivial task to characterize a real porous medium in terms of a reduced set of parameters. For a powder compact, the parameters will be highly coupled and dependent on the particle morphology, particle size distribution, powder agglomeration, and forming method. The amount of powder agglomeration tends to increase as the particle size distribution is reduced. Powder agglomeration and non-uniform particle morphology cause the porosity to increase. [11] As the particle size distribution is reduced the

pore radius will decrease. For a given level of porosity, the tortuosity increases as the particle aspect ratio increases and as the particle size distribution decreases. [67] However, decreasing the porosity increases the tortuosity. Increasing the compaction pressure will decrease the porosity up to some lower limit.[11]

Due to the amount of detail needed to describe powders and forming methods, it is generally not possible to predict the porosity, tortuosity, and pore radius of the resulting powder compact. However, some trends in how these parameters vary with changing powder characteristics and forming methods were described. Additionally, given the values of the porosity, tortuosity, and pore radius is not possible to give an accurate physical description of the powder compact, even if these parameters were determined for a particular powder compact.

1.4 Chemical Equilibrium of a Closed System

The equilibrium state of a chemical system is a useful way to approximate the true chemical composition of a fast reacting system or of a system with slowly varying initial composition.[68-70] The assumption that a system has fast reaction kinetics means that the system will instantaneously adjust itself to the equilibrium composition in response to any perturbation in the initial composition. The assumption of a slowly varying initial composition indicates that the system will have enough time to reach the equilibrium state, even if the reaction kinetics are slow, which can be seen in some geological processes. The equilibrium state assumption may appear like a drastic approximation but is a common assumption to reduce the complexity of a problem when the reaction kinetics occur on a much faster time scale than other physical processes. Thus, if the transport of material is on a slower scale than the reaction rate, the equilibrium state assumption is a good approximation. Pragmatically, for a system at high

temperature and with unknown, hard to measure, or complicated reaction kinetics, the equilibrium state assumption allows one to drastically reduce the problem complexity.

The calculation of the equilibrium state of a closed system is a mature problem that has been investigated by numerous authors.[51, 68, 71, 72] Only the basics of chemical equilibrium will be introduced in this section. A specific treatment of the methods used to calculate chemical equilibrium are presented in Chapter 5. A detailed description of different formulations of the chemical equilibrium problem and a comparison of solution algorithms is given by Smith and Missen (1982).[68]

The concept of a chemical system must be introduced before one can formalize the problem of calculating the chemical equilibrium of a closed system. A chemical system consists of a number of chemical species and chemical elements, where each chemical species can be assembled from the appropriate chemical elements. A chemical species is discerned by its phase, chemical formula, and structure. A chemical element is regarded as a basic building block of a chemical species and does not necessarily have to be an atomic element. The chemical equilibrium of a closed system is constrained by the conservation of mass and the chemical thermodynamic conditions dictated by the Second Law of Thermodynamics.

The problem of calculating the chemical equilibrium of a closed system may be formulated in two equivalent ways, namely the stoichiometric and non-stoichiometric formulations.[68] The conservation of mass of a closed system can be represented in two separate ways; the first method is by a set of element abundance equations that constrains the possible chemical species compositions to linear combinations of chemical species such that the total element number of each chemical element is conserved. The initial composition of a closed system uniquely determines the amount of each chemical element present. The chemical

elements that comprise the chemical species can be used to create a set of element abundance equations which must always be satisfied. A simple example of these conditions can be seen by looking at the chemical system

$$\{(C, CO, CO_2, O_2), (C, O)\} \tag{7}$$

The two element abundance equations for this system are

$$b_C = n_C + n_{CO} + n_{CO_2} \tag{8}$$

$$b_O = n_{CO} + 2n_{CO_2} + 2n_{O_2} \tag{9}$$

where, the chemical element concentrations are, b_i, and the chemical species concentrations are, n_i. The general form of these equations can be written as

$$\sum_{i=1}^{N} a_{ki} n_i = b_k \text{ for } k = 1..M \tag{10}$$

where, *N* is the number of chemical species and *M* is the number of chemical elements. The initial species compositions, given by $\{n_C, n_{CO}, n_{CO_2}, n_{O_2}\}$, sets the quantity of the chemical elements $\{b_C, b_O\}$. Any reaction that takes place, causing a change in the chemical species compositions, must still satisfy the element abundance equations.

An alternate formulation of the conservation of mass of a closed system can be done through the use of an appropriate set of stoichiometric equations. A valid set of stoichiometric equations for the chemical system {(C, CO, CO_2, O_2), (C, O)} are given by

$$C + O_2 = CO_2 \tag{11}$$

$$2CO + O_2 = 2CO_2 \tag{12}$$

The stoichiometric equations represent reactions that transform one collection of chemical species into another, in a fixed ratio, such that mass is conserved. The stoichiometric equations are not unique, therefore any formulation constructed from different but valid stoichiometric equations will be equivalent to any other, but not unique!

The amount of transformation between one collection of chemical species to another is typically regarded as the extent of reaction, ξ.[68, 70] The general form of the mass balance implied by the stoichiometric equations is given by the extent of reaction equations

$$n_i = n_i^{\circ} + \sum_{j=1}^{R} v_{ij}\xi_j \text{ for } i = 1..N \tag{13}$$

where, *R* is the number of equations, n_i° is the initial concentration of the i^{th} chemical species, and v_{ij} is the stoichiometric coefficient of the i^{th} chemical species in the j^{th} reaction.

The element abundance and stoichiometric equations are two ways to set constraints on the conservation of mass. The element abundance equations represent a direct way of accounting for the conservation of mass. The stoichiometric equations are an indirect way of accounting for the conservation of mass, because they ensure that any reaction between chemical species maintains a mass balance. For both methods there is the implicit physical assumption that the composition of each chemical species is non-negative. The non-negative constraints are represented as an inequality for each chemical species, e.g. $n_C \geq 0, n_{CO} \geq 0, n_{CO_2} \geq 0, n_{O_2} \geq 0$.

The thermodynamic conditions and potential function used for chemical equilibrium are derived from the second law of thermodynamics for a particular choice of state variables. A common representation of the thermodynamic conditions for chemical equilibrium are through the minimization of the Gibbs free energy function (G), at constant temperature (*T*) and

pressure (*P*), subject to the element abundance constraints. This particular set of conditions for equilibrium can be written as[68]

$$\begin{gathered} \min G(\mathbf{n}) = \sum_{i=1}^{N} n_i \mu_i \\ \text{subject to } \sum_{i=1}^{N} a_{ki} n_i = b_k \text{ for } k = 1..M \text{ and } n_i \geq 0 \text{ for } i = 1..N \end{gathered} \tag{14}$$

where, μ_i is the chemical potential of the i^{th} species and $\mathbf{n}$ is a vector of species concentrations. The representation of the problem given by Equation 14 is known as the non-stoichiometric formulation. The chemical potentials associated with the Gibbs function are represented by

$$\mu_i = \left(\frac{\partial G}{\partial n_i}\right)_{T,P,n_{i\neq j}} \tag{15}$$

i.e. they are the partial molar free energy of each species. The explicit form for μ_i depends on the phase mixture model used to describe the chemical species.

It can be shown an alternate formulation, *i.e.* the stoichiometric formulation, of the conditions for chemical equilibrium utilizing the stoichiometric coefficients is given by[68]

$$\sum_{i=1}^{N} v_{ij} \mu_i = 0 \text{ for } j = 1..R \tag{16}$$

It is common to introduce auxiliary variables to represent the chemical activity (a_i) of the i^{th} chemical species, the Gibbs free energy ($\Delta G_{rx,j}$) of the j^{th} reaction, and the reaction equilibrium constant ($K_{eq,j}$) of the j^{th} reaction. The chemical potential of a species can now be expressed in terms of a standard chemical potential (μ°), the chemical activity, and temperature given by[68]

$$\mu_i = \mu_i^\circ + RT\ln(a_i) \tag{17}$$

Using the form of μ_i from Equation 17 transforms the stoichiometric equilibrium conditions from Equation 16 into

$$\sum_{i=1}^{N} v_{ij}\mu^\circ{}_i + RT\sum_{i=1}^{N} v_{ij}\ln(a_i) = 0 \tag{18}$$

Equation 18 is commonly written in the more familiar form given by[68]

$$\Delta G_{rx,j} = -RT\ln(K_{eq,j}) \tag{19}$$

where, $\Delta G_{rx,j}$ is given by

$$\Delta G_{rx,j} = \sum_{i=1}^{N} v_{ij}\mu^\circ{}_i \tag{20}$$

and $K_{eq,j}$ is given by

$$K_{eq,j} = \prod_{i=1}^{N} a_i^{v_{ij}} \tag{21}$$

For various species, $\mu^\circ{}_i$ (or alternatively $\Delta G^\circ{}_i$) can be found in thermodynamic databases.[73, 74] The form of a_i depends on assumptions made for the species or mixture type. For ideal gases, a_i is assumed to be equal to the gas partial pressure, p_i, measured in atmospheres. For ideal pure solids and liquids, a_i is assumed to be equal to unity, but only if the species is present at equilibrium! Equation 16 (and its alternative formulation Equation 18) is a set of nonlinear algebraic equations to be solved simultaneously with an appropriate set of constraints for the conservation of mass (either the element abundance equations or the reaction extent equations).

The two formulations, *i.e.* the stoichiometric and non-stoichiometric, of the chemical equilibrium problem are equivalent.[68] The non-stoichiometric formulation is generally considered as a constrained minimization problem and the stoichiometric formulation is a non-linear algebraic equation problem. The formulation of the problem into a precise mathematical model has allowed researchers to apply mathematical solution algorithms to solve for the equilibrium species concentrations. Despite the problem having a clear description and many mathematical tools existing to, in theory, solve the problem, there tend to be convergence issues with general solution methods.[56, 68, 75, 76]

The convergence problem happens for a number of reasons including the large differences (many orders of magnitude) in species concentrations, flat minimums of the free energy function, and the non-negative constraint on species compositions. The non-negative constraint is rather troublesome because one's solution algorithm must decide between very small amounts of a species being stable in equilibrium compared to the species being identically equal to zero; such problems are difficult when using floating-point operations on a computer. Additionally, methods based upon a stoichiometric formulation must be recast for the absence of each chemical species because a species may no longer participate in the reaction if it is absent from the system (*e.g.* becomes exhausted). A number of specially designed solution algorithms (Brinkley, NASA, RAND, VCS, etc.) have been created to take advantage of the structure of the chemical equilibrium problem and address convergence issues.[56, 68, 75, 77]

1.5 Transport and Reaction in Porous Media

The problem of fluid transport and equilibrium reactions in porous media has been widely studied for applications in the fields of chemical and hydrogeochemical engineering.[51, 55, 56, 64, 78, 79] It has been observed that there are essentially three different classifications of how the

partial differential equations of fluid transport and the algebraic equations of chemical reaction equilibrium may be coupled together.[78] These methods are classified as a mixed differential and algebraic set of equations (DAE), direct substitution to explicitly eliminate the algebraic conditions (DSA), and the sequential iteration approach (SIA) which successively solves the transport problem followed by the equilibrium problem. There are specific difficulties with each of the three methods.

The DAE method requires significant levels of computation because the fluid flow and reaction are treated simultaneously. Additionally, the variation of the variables may occur on much different time scales causing difficulties in convergence due to numerical stiffness.[78, 80] The DSA approach suffers from a number of problems. Using the DSA, a suitable set of variables from the algebraic equations must be identified for elimination. The elimination variables must be substituted into the partial differential equations from the transport problem, often requiring significant algebraic manipulations to achieve the final form which is a set of highly non-linear partial differential equations.[78] The DSA approach also suffers from the need to properly identify suitable elimination variables, because the formulated equations become invalid if any of the primary variables precipitate or dissolve due to reaction. However, recent work describes systematic methods for eliminating these constraints and applying efficient algorithms to solve the coupled transport and reaction problem for equilibrium and kinetic reactions.[56, 79]

The SIA approach decouples the problem of transport and reaction into separate sub-problems.[51, 78] This approach solves the transport problem over a small time-scale, allowing for a redistribution of material. It is followed by solving the chemical equilibrium problem to re-equilibrate the chemical composition. The sequential iteration between the two methods can cause some numerical oscillations and mandate small time steps be taken.[78] However, the SIA approach is often used because it allows efficient methods developed for fluid transport and

chemical equilibrium reactions to be applied directly to each sub-problem. SIA is widely cited as the method of choice in the field of hydrogeochemistry, with commercial packages such as TOUGH2 and PORFLOW designed to specifically handle hydrogeological fluid flow.[51, 55, 66, 78, 81] The decoupling and discretization of a general transport and reaction equation used in this thesis is shown in Chapter 2.

1.6 Method of Attack

The goal of this thesis is to analyze the removal of oxide contaminants from porous media consisting of a mixture of non-oxide powder and sintering additives. To achieve this task, a suitable model to describe the relevant physical phenomena was developed and applied to three material systems of interest. The remainder of the thesis can be sectioned into the development of the model, the application of the model to the three material systems, and a few additional simulations to highlight additional capabilities of the modelling framework.

The development of the model is outlined as:

1. Formulation of a discretized gas transport and reaction equation that can be used to simulate the problem by the sequential iteration approach. (Chapter 2)
    a. Effectively splitting the problem into a sub-problem for calculating gas transport and a sub-problem for calculating chemical reaction.
2. Provide a detailed background on the Dusty Gas Model (DGM) used to model multispecies gas transport. (Chapter 3)
    a. Recast the DGM into a discretized form which can be used to predict the flux of the relevant gas species.
3. Provide a detailed description and algorithm for a novel method to calculating the equilibrium composition of a closed chemical system. (Chapter 4)

   a. Use the {SiC, SiO_2, C, $CO_{(g)}$, $CO_{2(g)}$, $SiO_{(g)}$} chemical system as an example to identify the difficulty in calculating the equilibrium composition if it is unknown whether all of the SiO_2 depleted.

The application of the model to the three material systems is outlined as:

1. Systematic study of SiO_2 removal from SiC porous media consisting of species from the {SiC, SiO_2, C, $CO_{(g)}$, $CO_{2(g)}$, $SiO_{(g)}$} chemical system. (Chapter 5)
   a. Analyze the time for complete oxide removal due to changing the porous media parameters and isothermal holding temperature.
   b. Analyze the effect of different heating cycles on the time for complete oxide removal and attempts to control the $CO_{(g)}$ effusion rate by varying the heating rate.
2. Systematic study of B_2O_3 removal from B_4C porous media consisting of species from the {B_4C, B_2O_3, C, $CO_{(g)}$, $B_2O_{3(g)}$, $B_2O_{2(g)}$} chemical system. (Chapter 6)
   a. Analyze the time for complete oxide removal due to changing the porous media parameters and isothermal holding temperature.
3. Systematic study of SiO_2 removal from SiC porous media consisting of species from the {C, SiC, SiO_2, B_4C, $CO_{(g)}$, $SiO_{(g)}$, $B_2O_{3(g)}$, $B_2O_{2(g)}$} chemical system. (Chapter 7)
   a. Analyze the time for complete oxide removal due to changing initial oxide content, sample thickness, and isothermal holding temperature.
   b. Analyze the residual B_4C concentration profile due to changing initial oxide content, sample thickness, and isothermal holding temperature.
4. Demonstrate additional model capabilities. (Chapter 8)
   a. Simulate the removal of ZrO_2 from ZrC porous media consisting of species from the {C, ZrC, ZrO_2, $CO_{(g)}$, $CO_{2(g)}$, $ZrO_{(g)}$} chemical system.

b. Study the effect B_2O_3 removal from B_4C porous media subject to a temperature gradient across thickness of the sample.

2 General Transport and Reaction Equation

A general formulation of multi-species transport and reaction is represented by the system of partial differential equations (PDEs)

$$\frac{\partial \boldsymbol{n}}{\partial t} = \nabla \cdot \boldsymbol{J} + \boldsymbol{R} \tag{22}$$

where, the species concentrations, $\boldsymbol{n}$ (mol·cm^{-3}), the species flux vector, $\boldsymbol{J}$ (mol·cm^{-2}·s^{-1}), and the reaction rate, $\boldsymbol{R}$ (mol·cm^{-3}·s^{-1}), are multivariable vector functions.[50, 59, 60] For each vector function, there are s component functions, where s is the number of chemical species. The functional form and dependencies of $\boldsymbol{n}$, $\boldsymbol{J}$, and $\boldsymbol{R}$ are determined by the choice of chemical species, spatial domain, constituent flux and reaction models.

In this thesis, the physical problem being modeled is one-dimensional gas transport in a reactive porous medium, with the reaction constrained by thermodynamic chemical equilibrium. The corresponding spatial domain, flux rates, and reaction rates are modeled using a one dimensional (1-D) spatial domain, x, the Dusty Gas Model (DGM), and a chemical equilibrium model, respectively. Additionally, the temperature profile, T, is allowed to vary across the spatial domain during the time evolution of the problem to simulate heating and cooling. Because energy transfer is neglected in this model, any change in the temperature profile across space and time is solely due predetermined simulation conditions set by the user. The physical implication of this choice is that there is an external force, not explicitly simulated, that is assumed to be able to produce the desired temperature profile.

The functional dependencies of $\boldsymbol{n}$, T, $\boldsymbol{J}$, and $\boldsymbol{R}$, are given by Equations 23-26, respectively.

$$\boldsymbol{n} = \boldsymbol{n}(x, t) \tag{23}$$

$$T = T(x, t) \tag{24}$$

$$\boldsymbol{J} = \boldsymbol{J}(\boldsymbol{n}, x, t, T) \tag{25}$$

$$\boldsymbol{R} = \boldsymbol{R}(\boldsymbol{n}, x, T) \tag{26}$$

Each component function associated with Equations 23, 25, and 26 corresponds to one of the s chemical species in the model. For example, the components of the flux vector are

$$\boldsymbol{J} = (J_1, J_2, \dots, J_i, \dots, J_s) \tag{27}$$

It is also useful to split the components into two disjoint groups for condensed (solid or liquid) and gas species, where c and g are the number of condensed and gas species, respectively. Because the groupings are disjoint, the components satisfy $s = c + g$. Using this grouping, the flux vector is expressed as

$$\boldsymbol{J} = (\boldsymbol{J}_c, \boldsymbol{J}_g) \tag{28}$$

Where, $\boldsymbol{J}_c$ and $\boldsymbol{J}_g$ are the condensed and gas species flux vectors given by

$$\boldsymbol{J}_c = (J_1, J_2, \dots, J_c) \tag{29}$$

$$\boldsymbol{J}_g = (J_1, J_2, \dots, J_g) \tag{30}$$

This grouping easily extends to Equations 23 and 26. However, this grouping has a particular advantage when describing the flux of chemical species using the DGM. A key feature of the DGM is that the condensed chemical species are represented as large, stationary *dusty gas molecules; i.e.* $\boldsymbol{J}_c = 0$.

2.1 Numerical Discretization Scheme

The set of PDEs represented by Equation 22, with its constitutive equations, needs to be solved in order to simulate the multi-species transport in a reactive porous medium. This is an intractable problem to be solved in closed form, thus a numerical approximation to the solution is sought. There exist a large number of different numerical approximation techniques that have their own strengths and weaknesses.[50, 52, 59, 60] However, one must identify the physical features to be preserved by the numerical solution (*e.g.* conservation of mass) and chose a numerical discretization scheme that satisfies those constraints.

The most important physical property to preserve during the simulation is the conservation of matter during both chemical reaction and the flux of matter. The numerical discretization schema chosen to preserve these properties uses the Finite Control Volume Method (FCVM) for the spatial discretization and the forward Euler method for the time discretization. The FCVM must be applied to the integral form of a differential equation. Integrating Equation 22 over space and time gives the integral representation[52]

$$\iint_{V\,t} \frac{\partial \boldsymbol{n}}{\partial t}\, dt\, dV = \iint_{t\,V} \nabla \cdot \boldsymbol{J}\, dV\, dt + \iint_{t\,V} \boldsymbol{R}\, dV\, dt \tag{31}$$

Restricting Equation 31 to 1-D yields

$$\iint_{x\,t} \frac{\partial \boldsymbol{n}}{\partial t}\, dt\, dx = \iint_{t\,x} \frac{\partial}{\partial x}\boldsymbol{J}\, dx dt + \iint_{t\,x} \boldsymbol{R}\, dx\, dt \tag{32}$$

2.1.1 Finite Control Volume Method: Spatial Discretization

The restriction of the problem to 1-D provides a major simplification. This restriction is valid for flat plates having a finite thickness with infinite length and width, such that transport

and reaction only takes place across the thickness of the plate. However, this is a reasonable assumption whenever the ratio of the length and width to the thickness is large, indicating that edge effects are negligible. A sample computational domain and FCVM discretization is shown in Figure 2-1, where each discretized cell is a *control volume*. The volume of each control volume, using the 1-D FCVM, is completely characterized by its length; the height and depth of each control volume are assumed to be of unit length.

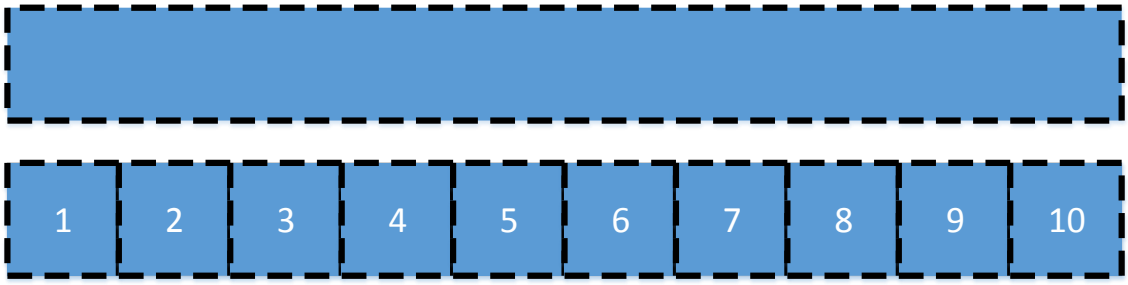

Figure 2-1: (Top) Non-discretized computational domain. (Bottom) Finite control volume discretization. The height and depth (not shown) of each control volume are assumed to have unit length.

Each control volume has a nodal point to represent the value of the species composition and other parameters for each discretized point in space and time. A schematic for the relation between nodal points in adjacent control volumes for an arbitrary discretization is shown in Figure 2-2.

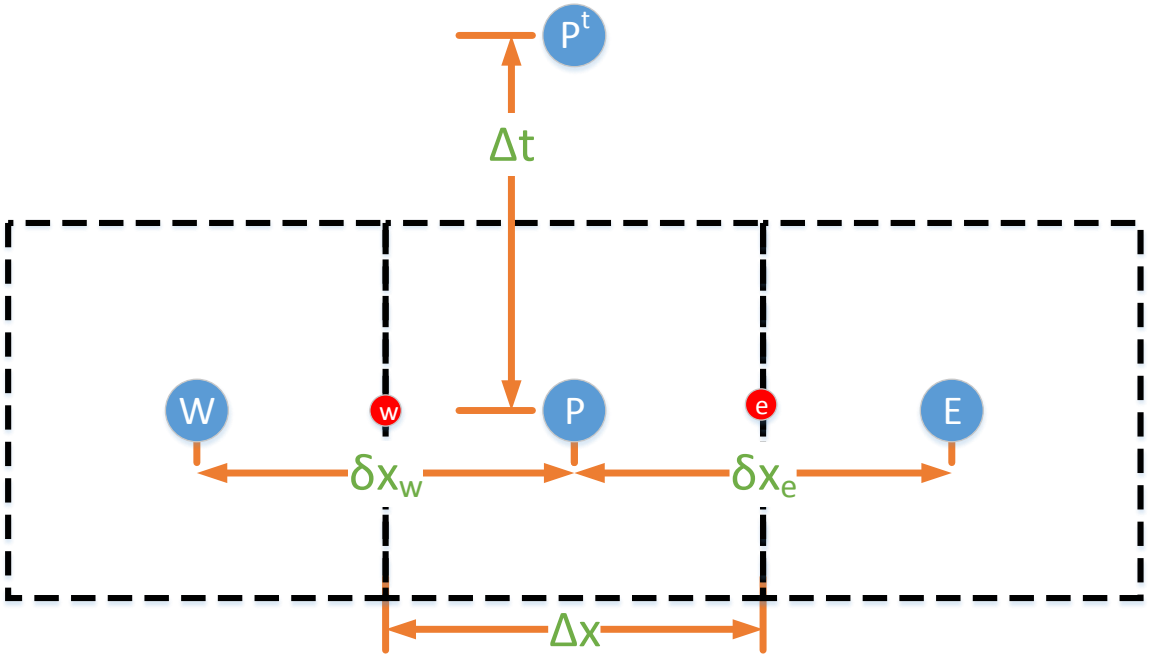

Figure 2-2: Schematic diagram of relations between finite control volumes. W, P, E are the nodal points in adjacent control volumes at the current time. P^t is the nodal point at the next time step for the node P. The position and values at the interfaces between control volumes are w and e.

The nodal discretization shown in Figure 2-2 can be applied to Equation 28, yielding the integral form for each control volume[52]

$$\int_{w}^{e}\int_{t}^{t+\Delta t} \frac{\partial \boldsymbol{n}}{\partial t}\, dt\, dx = \int_{t}^{t+\Delta t}\int_{w}^{e} \frac{\partial}{\partial x}\boldsymbol{J}\, dx dt + \int_{t}^{t+\Delta t}\int_{w}^{e} \boldsymbol{R}\, dx\, dt \tag{33}$$

The divergence theorem is applied to the first term on the RHS of Equation 33, which replaces the integral over the control volume with a surface integral over the boundary of the control volume.[50, 52, 59] The result of this transformation is.

$$\int_{w}^{e}\int_{t}^{t+\Delta t} \frac{\partial \boldsymbol{n}}{\partial t}\, dt\, dx = \int_{t}^{t+\Delta t} (\boldsymbol{J}_e - \boldsymbol{J}_w)\, dt + \int_{t}^{t+\Delta t}\int_{w}^{e} \boldsymbol{R}\, dx\, dt \tag{34}$$

The next step in the FCVM is to choose a profile assumption for each integral in Equation 34 using the control volume nodal points.[52] The profile assumption for each integral

term need not be the same. The profile assumption, for the first term on the RHS of Equation 34, must be continuous across the control volume boundaries. This is necessary so the flux on the control volume boundaries is equal but opposite in direction, as depicted in Figure 2-3.

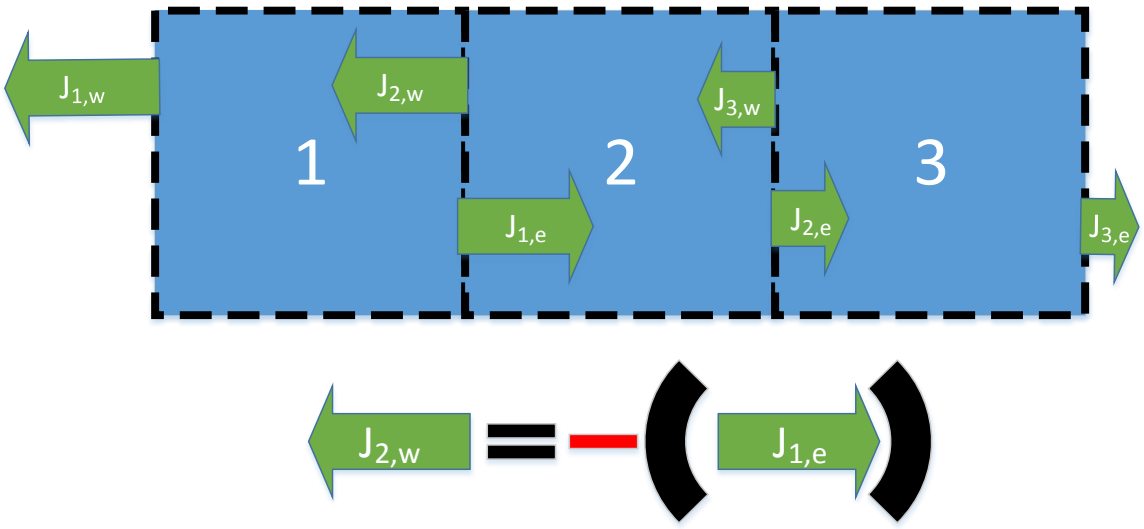

Figure 2-3: Flux across each control volume boundary is equal but opposite in direction, a consequence of the profile assumption being continuous across the boundaries.

This condition automatically ensures that matter is conserved for any flux between control volumes. There is no connection between control volumes in the second term on the RHS of Equation 34, thus no continuity constraints are required by the profile assumption. The simplest valid profile assumptions for the discretization of the integral terms on the RHS of Equation 34 is shown in Figure 2-4.

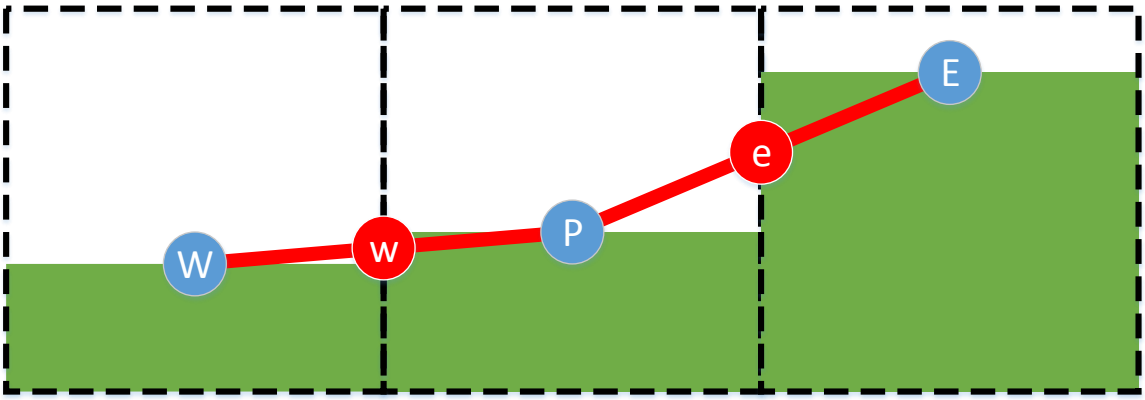

Figure 2-4: Profile assumptions for FCVM integrals. RHS Term 1, piecewise linear interpolation between control volumes (Red). RHS Term 2, piecewise constant across a control volume (Green)

The first term on the RHS of Equation 34 is assumed to have a piecewise linear interpolation between control volumes. This implies that interpolated species composition at the left and right boundaries are

$$\boldsymbol{n}_w = \frac{\boldsymbol{n}_W - \boldsymbol{n}_P}{\delta x_w}\left(\frac{\Delta x}{2}\right) + \boldsymbol{n}_P \tag{35}$$

$$\boldsymbol{n}_e = \frac{\boldsymbol{n}_P - \boldsymbol{n}_E}{\delta x_e}\left(\frac{\Delta x}{2}\right) + \boldsymbol{n}_P \tag{36}$$

The species composition gradient at the left and right boundaries are

$$\left.\frac{\partial \boldsymbol{n}}{\partial x}\right|_w = \frac{\boldsymbol{n}_P - \boldsymbol{n}_W}{\delta x_w} \tag{37}$$

$$\left.\frac{\partial \boldsymbol{n}}{\partial x}\right|_e = \frac{\boldsymbol{n}_E - \boldsymbol{n}_P}{\delta x_e} \tag{38}$$

Similarly, Equations 35-38 can be used to produce the interpolants and gradients for the temperature and pressure profiles by substituting T and $\boldsymbol{p}$ in for $\boldsymbol{n}$, respectively. The interpolants and gradients are not explicit in Equation 34. However, they are needed to discretize the DGM, which is solved to get the left and right boundary fluxes $\boldsymbol{J}_w$ and $\boldsymbol{J}_e$,

respectively. An explanation of the DGM and a procedure to compute the discretized gas flux is discussed in Chapter 3.

2.2 Reaction Rates from Chemical Equilibrium

The reaction rate $\boldsymbol{R}$ included in Equation 34 represents the rate of chemical reaction necessary to achieve chemical equilibrium composition. The use of the reaction rate in this context is different from the usual notion of a reaction rate from reaction kinetics. Here, the reaction rate is limited by the flux of material from adjacent control volumes or due to temperature change. For example, if the system is already in a state of chemical equilibrium (at constant T) and there is no change in composition due to a material flux, then the reaction rate is zero.

A justification for introducing an *equilibrium composition function* $\boldsymbol{F}$ is provided for an instantaneously closed, constant temperature system that has changing composition with time. The auxiliary function $\boldsymbol{F}$ is introduced to represent the function that calculates the thermodynamic chemical equilibrium composition of a closed system. To show the relation between $\boldsymbol{R}$ and $\boldsymbol{F}$**,** it is necessary to introduce a few variables and properties of the function $\boldsymbol{F}$. The variables $\boldsymbol{n}$, $\boldsymbol{n}_o$, and $\boldsymbol{n}^t$ represent the equilibrium, the non-equilibrium, and the equilibrium chemical composition at the next time step, t, respectively. The change in the chemical composition, during a time interval Δt, is given by Δn^t. The incremental change in the composition results in the non-equilibrium composition $\boldsymbol{n}_o^t$ given by Equation 39.

$$\boldsymbol{n}_o^t = \boldsymbol{n} + \Delta \boldsymbol{n}^t \tag{39}$$

The function $\boldsymbol{F}$ satisfies the properties represented by Equations 40-42.

$$\boldsymbol{F}(\boldsymbol{n}_o) = \boldsymbol{n} \tag{40}$$

$$\boldsymbol{F}(\boldsymbol{n}) = \boldsymbol{n} \tag{41}$$

$$\boldsymbol{F}(\boldsymbol{n}_o^t) = \boldsymbol{n}^t \tag{42}$$

Applying the function $\boldsymbol{F}$ to the non-equilibrium composition returns the equilibrium composition. And, applying $\boldsymbol{F}$ to the equilibrium composition also returns the equilibrium composition.

The reaction rate $\boldsymbol{R}$ can be defined by Equation 43 as a type of derivative of $\boldsymbol{F}$ with respect to time.

$$\boldsymbol{R} = \lim_{\Delta t \to 0} \frac{F(\boldsymbol{n} + \Delta \boldsymbol{n}^t) - F(\boldsymbol{n})}{\Delta t} \tag{43}$$

Equation 43 can be written as Equation 44 by using Equation 39.

$$\boldsymbol{R} = \lim_{\Delta t \to 0} \frac{\boldsymbol{F}(\boldsymbol{n}_o^t) - F(\boldsymbol{n})}{\Delta t} \tag{44}$$

Since the function $\boldsymbol{F}$ satisfies Equation 41, Equation 44 can be rewritten as Equation 45.

$$\boldsymbol{R} = \lim_{\Delta t \to 0} \frac{\boldsymbol{F}(\boldsymbol{n}_o^t) - \boldsymbol{n}}{\Delta t} \tag{45}$$

Alternatively, the equilibrium composition at the next time step can be expressed as Equation 46.

$$\boldsymbol{F}(\boldsymbol{n}_o^t) = \lim_{\Delta t \to 0} \boldsymbol{R}\Delta t + \boldsymbol{n} = \boldsymbol{n}^t \tag{46}$$

This representation gives a more intuitive connection between the flux limited reaction rate $\boldsymbol{R}$ and the equilibrium composition function $\boldsymbol{F}$. The form of Equation 46 fits well with the forward Euler method approximation, where Δt is taken to be a finite step size. A change in the temperature of the closed system with each time step will also cause a shift in the equilibrium

chemical composition. A slight generalization (not shown) of the concepts used to generate Equation 46 are used to account for the reaction rate that occurs from a change in temperature with each time step. The concept of the equilibrium composition function is an abstract function and a systematic way of evaluating this function for specific chemical systems is developed further in the subsequent chapters.

2.3 Numerical Approximation Sequence

The FCVM integral representation of transport and reaction equation given by Equation 34 is transformed into a discretized equation using the profile assumptions and the equilibrium composition function. Substituting these assumptions into Equation 34 yields the discretized form

$$\lim_{\Delta t \to 0} [(\boldsymbol{n}_P^t - \boldsymbol{n}_P)\, \Delta x = (\boldsymbol{J}_e - \boldsymbol{J}_w)\, \Delta t + (\boldsymbol{F}(\boldsymbol{n}_P^t) - \boldsymbol{n}_P)\, \Delta x] \tag{47}$$

where, the subscripts *P*,*e*, and *w* refer the value of each variable at the locations corresponding to the discretization schematic shown in Figure 2-4. Rearranging the terms in Equation 47 yields

$$\lim_{\Delta t \to 0} [\boldsymbol{n}_P^t = (\boldsymbol{J}_e - \boldsymbol{J}_w)\, \frac{\Delta t}{\Delta x} + \boldsymbol{F}(\boldsymbol{n}_P^t)] \tag{48}$$

Equation 48 is valid strictly in the limit $\Delta t \to 0$. To address this problem, it is assumed that the flux of material happens over time of Δt and yielding the non-equilibrium composition at the next time step, $\boldsymbol{n}_{P,o}^t$, given by

$$\boldsymbol{n}_{P,o}^t = (\boldsymbol{J}_e - \boldsymbol{J}_w)\, \frac{\Delta t}{\Delta x} \tag{49}$$

After the material flux, applying the equilibrium composition function to the non-equilibrium composition simulates the reaction yielding the equilibrium composition at the next time step, $\boldsymbol{n}_P^t$, which is simply described by

$$\boldsymbol{n}_P^t = \boldsymbol{F}\left(\boldsymbol{n}_{P,o}^t\right) \tag{50}$$

The preceding discussion was provided to outline the general governing equations of the model, the underlying assumptions, and the numerical discretization strategy. This strategy results in a two-step process where material is allowed to flow from one discrete region to another for a fixed time, followed by reaction that yielding the equilibrium composition at the new time. The collection of condensed and gas species will greatly impact the final form of the PDEs to be solved. The construction of the functional form for each of the constituent models and the necessary parameters are discussed in later chapters.

3 Gas Transport Model

The Dusty Gas Model (DGM) was chosen to model the transport of a multi-species gas mixture in porous media. Mason and Malinauskas (1983) derived the DGM by applying restrictions to the multi-species gas transport equations generated from a rigorous treatment of the kinetic theory of gases, to account for the structure of a porous medium.[53] A brief introduction to kinetic theory and the DGM is provided to shed light on the relevant transport phenomena, the constituent equations needed for the transport coefficients, and further simplifications made to the DGM. Finally, a procedure is presented for generating a function to calculate the gas flux in a porous medium.

3.1 Kinetic Gas Theory Overview

A simplified view of kinetic gas theory can be understood as the scattering and transport of mass, momentum, and energy of interacting molecules based upon the laws of motion. The dynamics of gas molecules can be determined using the interaction potential between them. Computing the molecular dynamics of a collection of gas molecules of the size of interest for most transport phenomenon is an intractable problem. However, using a suitable description of the intermolecular potentials in a gas mixture, many physically observable phenomena can be described to varying orders of approximation by the theory.

A starting point for deriving transport phenomena in gases is using the Boltzmann Transport Equations (BTE). The BTE set the integro-differential conditions which are to be satisfied by the molecular distribution functions of the gas mixture, along with an assumption that molecular collisions are uncorrelated, *i.e. molecular chaos*. *Molecular chaos* is a fundamental assumption that precludes the same theory to be applicable for multi-species liquid transport due to the highly correlated molecular motion that arises in dense systems. The

perturbative expansion method of Chapman and Enskog is used to approximate solutions of the BTE for small deviations from equilibrium (*i.e.* non-equilbrium systems) for conserved quantities such as mass, momentum, and energy. The perturbations to the BTE yields a system of first order differential equations for the flux of each conserved quantity. These equations and the coefficients of these equations, *i.e.* transport coefficients, correspond to linear physical phenomena, such as Fick's law and diffusion coefficients, respectively. The perturbative expansion method also provides a theoretical justification for the transport coefficients, as compared to experimentally measured or empirical forms for these parameters.[82]

Applying the perturbative expansion for a physical system consisting of *v'* gas species, yields a system of *v'* transport equations for each conserved quantity. Of the *v'* equations, only *v'*-1 are linearly independent due to the continuity equation for the conserved quantity. It is from these approximations that the functional form of the flux vectors (mass, momentum, and energy density) and transport coefficients are recovered for effects such as ordinary diffusion, viscosity, thermal conductivity, and thermal diffusion (among other higher order effects). The transport coefficients are all expressible in terms of a set of collision integrals $\Omega_{ij}(l,s)$ determined from the intermolecular potential functions for the mixture components, where l and s are the series expansion parameters. A rigorous derivation of the transport equations and approximate forms for the transport coefficients are given by Hirschfelder *et al.* (1954).[83]

3.2 Dusty Gas Model

The Dusty Gas Model was proposed as a way to apply the results of rigorous kinetic theory to gas transport in a porous medium. This is a very complicated problem if trying to solve the multi-component gas transport equations for anything other than a very simple pore geometry (i.e. transport down a long capillary) due to the incorporation of complex geometric

boundary conditions. The DGM provides an alternative description of the problem, incorporating the pore structure (*i.e.* boundary conditions) into the transport equations directly by treating the porous medium as a collection of large, uniformly dispersed, stationary '*dust*' molecules as one of the *ν'* gas species in the mixture.

3.2.1 Gas Flow Regimes (Simplified Arguments)

The transport of a gas mixture in a porous medium has many different heuristic derivations. A simple heuristic presentation of the flow regimes is shown to generate physical intuition, before passing to the *dusty gas limit*. The modes of transport in porous media are often identified by Knudsen, diffusive, and viscous flow regimes.

3.2.1.1 *Knudsen Flow*

Knudsen flow describes the flow a rarified gas through small openings. The defining characteristic in this flow regime is that gas density is low-enough that molecule-wall interactions dominate and molecule-molecule interactions are negligible. The flux of gas molecules across an opening can be described as the probability per unit time per unit area that a gas molecule impinging upon the opening will not be reflected back by collision with the opening's boundaries. The assumption for Knudsen flow is that the motion of each molecule of the gas acts independently of each other.

The flux of the ith gas, J_{iK} (molecules·cm^{-2}·s^{-1}), in the Knudsen flow regime is

$$J_{iK} = w n_i \bar{v}_i \tag{51}$$

where, w is a dimensionless probability factor for the opening geometry, $\bar{v}_i$ is the mean molecular velocity (cm·s^{-1}), and n_i is the molecular density (molecules·cm^{-3}) of the ith gas species. The mean molecular speed of a gas species is

$$\bar{v}_i = \left(\frac{8k_B T}{\pi m_i}\right)^{1/2} \tag{52}$$

where, k_B (erg·K^{-1}) is the Boltzmann constant, T (K) is the absolute temperature and m_i (g·molecule^{-1}) is the molecular mass of the i^{th} gas species.

The net flux that occurs due to Knudsen flow occurring on both sides of an opening is proportional to the gradient in molecular density across the opening. Writing the Knudsen flux from Equation 51 in the differential form gives

$$J_{iK} = -\overline{D}_{iK} \nabla n_i \tag{53}$$

where, $\overline{D}_{iK}$ (cm^2·s^{-1}) is the Knudsen diffusion coefficient that characterizes the motion of a gas species across a small opening. The Knudsen diffusion coefficient can be shown to have the form

$$\overline{D}_{iK} = \frac{4}{3} K_0 \bar{v}_i \tag{54}$$

where, K_0 (cm) is the Knudsen coefficient that depends only on the geometry of the opening and the gas-surface scattering law. This parameter can be measured directly from experiment or calculated for a specific pore structure. For simple capillary geometries the value of K_0 is

$$K_0 = \frac{r}{2} \tag{55}$$

where, r is the radius of the capillary.

3.2.1.2 *Continuum diffusion*

Continuum diffusion represents the physical interaction and transport of different species of gas molecules relative to each other. The continuum diffusion coefficient is defined for a binary mixture when the net flux is zero and there is no bulk pressure gradient, *i.e.* there is no viscous flow. The resultant pure diffusive fluxes, J_{1D} and J_{2D}, are

$$J_{1D} = -\overline{D}_{12}\nabla n_1 \tag{56}$$

$$J_{2D} = -\overline{D}_{21}\nabla n_2 \tag{57}$$

where, $\overline{D}_{12}$ and $\overline{D}_{21}$ ($cm^2 \cdot s^{-1}$) are the continuum diffusion coefficients. There is a symmetric relationship between the diffusion of each species, *i.e.* $\overline{D}_{12} = \overline{D}_{21}$, as evident from the definitional conditions of no net flux and no pressure gradient given by

$$J_{1D} + J_{2D} = J_D = 0 \tag{58}$$

$$\nabla(n_1 + n_2) = 0 \tag{59}$$

This relationship can be extended to the case of multiple gases, provided that only binary molecular collisions occur. A detailed derivation of the binary continuum diffusions coefficients using Chapman-Enskog theory shows that a first-order approximation is given by Equation 60.

$$\left[\overline{D}_{ij}\right]_1 = \frac{3}{8}\left(\frac{\pi k_B T}{2\mu_{ij}}\right)^{1/2} \frac{1}{n\pi {\sigma_{ij}}^2 {\Omega_{ij}}^{(1,1)^\star}(T^*)} \tag{60}$$

Where, μ_{ij} (g) is the reduced mass of the molecular pair, σ_{ij} (cm) is a distance parameter for the mutual collision diameter of the molecular pair, and ${\Omega_{ij}}^{(1,1)^\star}$ is a dimensionless transport collision integral, and T^* is the reduced temperature. ${\Omega_{ij}}^{(1,1)^\star}$ is normalized to unity for collisions between rigid elastic spheres of mutual collision diameter σ_{ij}, otherwise depends on the choice of intermolecular potential. σ_{ij} and μ_{ij} are given by Equations 61 and 62, respectively

$$\sigma_{ij} = \frac{\sigma_i + \sigma_j}{2} \tag{61}$$

$$\frac{1}{\mu_{ij}} = \frac{1}{m_i} + \frac{1}{m_j} \tag{62}$$

where, σ_i, σ_j and m_i, m_j are the collision diameter and molecular mass of the i^{th} and j^{th} particles, respectively.

The first order approximation of the diffusion coefficients only account for the interaction of a particular ij-pairs. However, the full expansion of the binary diffusion coefficient requires the weighted contribution of all distinct ij-pairs, but this only amounts to a small correction. The binary diffusion coefficient, $\overline{D}_{ij}$, for a multi-species gas mixture, is obtained by applying the correction factor, Δ_{ij}, in Equation 63. Where, Δ_{ij} is much less than unity.

$$\overline{D}_{ij} = \frac{\left[\overline{D}_{ij}\right]_1}{1 - \Delta_{ij}} \approx \left[\overline{D}_{ij}\right]_1 \tag{63}$$

3.2.1.3 *Viscous flow*

The bulk flow of gas, due to a bulk pressure gradient in a gas mixture, is known as viscous flow. For a non-accelerating fluid, the viscous-drag force must balance the force due to the pressure gradient across that region. The resulting expression for the viscous flux is

$$J_{visc} = \frac{Flow}{Area} = -(\frac{nB_0}{\eta})\nabla p \tag{64}$$

where, J_{visc} (molecules·cm^{-2}·s^{-1}) is the total viscous flux, n (molecules·cm^{-3}) is the total molecular density, $B_0$is the viscous flow coefficient, η (g·cm^{-1}·s^{-1}) is the total viscosity of the gas , and p (dyne·cm^{-2}) is the total pressure of the gas. B_0 is a characteristic constant of the pore geometry having units of cm^2. For simple capillary geometries the value of B_0 is

$$B_0 = \frac{r^2}{8} \tag{65}$$

where, r is the radius of the capillary.

Because viscous flow moves the gas as a bulk fluid parcel and the gas species do not separate, the viscous flux of the i^{th} species, $J_{i,visc}$, is proportional to its mole fraction, x_i, in the mixture and is given by

$$J_{i,visc} = x_i \cdot J_{visc} \tag{66}$$

3.2.1.3.1 Viscosity of a gas mixture

Although not formally part of the DGM, a constitutive model is needed for the viscosity of a multi-species gas mixture. As derived from kinetic gas theory, the first approximation to viscosity of a pure gas species, $[\eta]_1$, is[83].

$$\eta = \frac{5}{16} \frac{\sqrt{\pi\, m\, k_b\, T}}{\pi\, \sigma\, {\Omega_{ij}}^{(2,2)^*}(T^*)} \tag{67}$$

Where, σ (cm) is the Lennard-Jones (LJ) collision diameter for the gas molecule, m (g·molecule^{-1}) is the gas molecular weight, ${\Omega_{ij}}^{(2,2)^*}$ is a transport collision integral, T^* is the reduced temperature, and T (K) is the temperature. The viscosity of a gas mixture can be approximated by using an empirical formula that scales the pure gas viscosities using a simple rule of mixing

$$\eta_{mix} = \frac{\sum x_i \eta_i {m_i}^{1/2}}{\sum x_i {m_i}^{1/2}} \tag{68}$$

where, x_i is the mole fraction, η_i is the viscosity, and m_i is the molecular weight of the i^{th} gas species. There are many higher order approximations for multi-species gas viscosities in the literature; however, they will not be used in this work.

3.2.1.3.2 Collision Integrals $\Omega(l,s)$ (Omega-integrals)

The transport coefficients are all determined by binary and/or collections of binary interactions. The binary interactions involve the *collision* of two gas molecules, causing a change in their trajectory. These collisions obey the laws of motion and conserve certain quantities, such as energy in an elastic collision. The collision integrals, series expansions from Chapman-Enskog theory, are represented by the integral

$$\Omega_{ij}^{(l,s)}(T) = \sqrt{\frac{2\pi k_B T}{\mu_{ij}}} \int_{0,0}^{\infty,\infty} e^{-{\gamma_{ij}}^2} \gamma_{ij}^{2s+3} (1 - \cos^l \chi) b \, db \, d\gamma_{ij} \tag{69}$$

where, l and s are the series expansion parameters.

The collision integrals are defined in terms of the impact parameter, b, the angle of deflection, χ, and the reduced initial relative speed, γ_{ij}, of molecules i and j. The impact parameter is distance of nearest approach between two molecules in the absence of a force field. These integrals are integrated over all impact parameters and reduced initial relative molecular speeds. The parameter χ is related to b and γ_{ij} by Equations 70 and 71, respectively

$$\chi(g_{ij}, b) = \pi - 2b \int_{r_m}^{\infty} \frac{dr/r^2}{\sqrt{1 - \frac{b^2}{r^2} - \frac{\varphi(r)}{\frac{1}{2}\mu_{ij} g_{ij}^2}}} \tag{70}$$

$$\gamma_{ij}^2 = \frac{\frac{1}{2}\mu_{ij} g_{ij}^2}{k_B T} \tag{71}$$

where, r_m is the distance of nearest approach and g_{ij} is the initial relative speed of molecules i and j.

For a given g_{ij} and b, the angle of deflection remains arbitrary up to a choice of the intermolecular potential $\varphi(r)$ and temperature during the collision. Substituting the angle of deflection into the collision integral keeps the collision integral arbitrary up to the choice of intermolecular potential and temperature during the collision. Throughout this thesis, the LJ 12-6 potential was used to represent the molecular potentials of the gas species. The functional form of the LJ 12-6 potential is

$$\varphi_{ij}(r) = 4\epsilon_{ij}[\left(\frac{\sigma_{ij}}{r}\right)^{12} - \left(\frac{\sigma_{ij}}{r}\right)^{6}] \tag{72}$$

where, σ_{ij} is the reduced hard sphere diameter and ϵ_{ij} is the reduced potential energy parameter given by

$$\sigma_{ij} = \frac{\sigma_i + \sigma_j}{2} \tag{73}$$

$$\epsilon_{ij} = \left(\epsilon_i \epsilon_j\right)^{1/2} \tag{74}$$

The collision integrals, as a function of temperature with use of the LJ 12-6 potential, have been extensively studied, tabulated, and have approximate empirical functions to avoid the direct calculation of the integrals. Pragmatically, it is common for other researchers to represent the molecular potential functions of gases by LJ 12-6 parameters; which facilitated the search for the material properties necessary to model gas transport.

It is standard procedure to treat *rigid sphere* molecular potentials as zeroth order approximations when evaluating the collision integrals. When using a more realistic (complicated) functional form for the intermolecular potential, it is common to represent those collision integrals as a ratio normalized by the *rigid sphere* collision integral 75.

$$\Omega_{ij}^{(l,s)\star}(T^*) = \frac{\Omega_{ij}^{(l,s)}(T^*)}{\left[\Omega_{ij}^{(l,s)}\right]_{rigid\ sphere}} \tag{75}$$

The reduced temperature, T^*, is the dimensionless scaling parameter

$$T^* = \frac{k_B T}{\epsilon} \tag{76}$$

where, ϵ (ergs) is the LJ potential well depth and k_B (erg·K^{-1}) is the Boltzmann constant.

The LJ parameters, σ and ϵ, are normally fit to a LJ potential from viscosity experiments.[83-86] A LJ collision integral must be calculated directly, looked up in standard tables, or evaluated using an empirical formula.[84] At this level of approximation, the two required collision integrals are ${\Omega_{ij}}^{(1,1)^\star}$ and ${\Omega_{ij}}^{(2,2)^\star}$; the empirical formula for each is

$${\Omega_{ij}}^{(1,1)^\star}(T^*) = \frac{1.0636}{{T^*}^{0.1561}} + \frac{0.193}{\exp(0.47635\,T^*)} + \frac{1.03587}{\exp(1.52996\,T^*)} + \frac{1.76474}{\exp(3.89411\,T^*)} \tag{77}$$

$${\Omega_{ij}}^{(2,2)^\star}(T^*) = \exp\begin{bmatrix} 0.45667 - 0.53955\cdot\ln(T^*) + 0.187265\cdot\ln(T^*)^2 \\ -0.03629\cdot\ln(T^*)^3 + 0.00241\cdot\ln(T^*)^4 \end{bmatrix} \tag{78}$$

, respectively.[87, 88] The formula for ${\Omega_{ij}}^{(2,2)^\star}$ used in the modeling simulations was given by Kaza (2006) with a reference to Hirschfelder *et al.* (1954), but it was not found in that reference.[83, 88] Despite there being no reference, the values calculated using ${\Omega_{ij}}^{(2,2)^\star}$ from Kaza (2006) match closely to the values calculated using ${\Omega_{ij}}^{(2,2)^\star}$ from Neufeld (1972).[87, 88] In this thesis, the $\Omega_{ij}^{(l,s)\star}$ and $\Omega_{ij}^{(l,s)}$ refer to the reduced and non-reduced LJ 12-6 functional form for the intermolecular potential, respectively.

3.2.2 Dusty Gas Limit

The transport mechanisms used in the DGM were introduced by giving heuristic arguments for Knudsen, diffusive, and viscous flow. The full theory is developed using the

Chapman Enskog treatment of kinetic theory to yield the multi-component gas transport equations in free space. These equations do not explicitly include Knudsen flow but they include a number of secondary effects, such as thermal transpiration (giving rise to a thermomolecular pressure difference) and thermal diffusion, which are not part of the heuristic derivation.[53] It also gives a rigorous approximation for the transport coefficients used within the gas transport equations. The DGM is reached by taking the gas transport equations to the *dusty gas limit*.[53] The dusty gas limit is a set of restrictions placed on the gas transport equations that incorporates the structure of the porous medium by effectively treating it as a collection of large stationary *dusty gas molecules*, *i.e.* $J_{Dust} \equiv 0$. Additionally, Knudsen flow is incorporated into the model by considering the binary interaction between actual gas molecules and dust molecules as representative of Knudsen type interactions.

3.2.2.1 *Pore structure modified gas transport parameters*

In the DGM framework, incorporating the pore structure amounts to modifying the transport coefficients of the previously described continuum diffusion, viscous, and Knudsen flow regimes. The modifications to these regimes are incorporated by an appropriate scaling by the porosity and tortuosity, ε and q, of the porous medium, respectively. Based upon the pore structure arguments presented by Mason and Malinauskas, the Knudsen, viscous flow, and continuum diffusion coefficients should be scaled by ε/q.[53]

$$B_0 \rightarrow \frac{\varepsilon}{q} B_0 \tag{79}$$

$$K_0 \rightarrow \frac{\varepsilon}{q} K_0 \tag{80}$$

$$D_{ij} = \frac{\varepsilon}{q} \overline{D}_{ij} \tag{81}$$

This approach has the benefit of considerably simplifying the resulting transport equations rather than incorporating them from first principles along with a detailed kinetic gas theory treatment. An additional, but rather pragmatic, benefit is that detailed treatment of a pore structure from first principles often describes idealized geometries that often do not reflect the real pore structure. All of these parameters can be measured experimentally for specific pore structures to further refine the DGM without needing to re-derive the appropriate gas transport equations.

3.2.2.2 *Modified Dusty Gas Model Equations*

The combined gas transport equations, neglecting thermal-diffusion, thermal transpiration and body forces, are

$$\sum_{j=1}^{v} \frac{n_j}{nD_{ij}}\left(\frac{J_i}{n_i}-\frac{J_j}{n_j}\right)+\frac{1}{D_{iK}}\left[\frac{J_i}{n_i}+\frac{B_0}{\eta}(\nabla p - nF)\right] = -\nabla \ln\left(\frac{n_i}{n}\right) - \nabla ln(p) \quad \text{for } i = 1,2,\dots,v \tag{82}$$

There are *v* equations, where *v* is the number of gas species. Equation 82 is reduced to Equation 83 by using the equation of state, $n = p/k_B T$, and assuming the external force, F, on each gas molecule is zero.

$$\sum_{j=1}^{v} \frac{n_j}{nD_{ij}}\left(\frac{J_i}{n_i}-\frac{J_j}{n_j}\right)+\frac{1}{D_{iK}}\left[\frac{J_i}{n_i}+\frac{B_0}{\eta}\nabla p\right] = -\left(\frac{\nabla p_i}{p_i}\right) \tag{83}$$

3.2.2.3 *Algebraic Manipulation of the Modified Dusty Gas Model Equations*

The modified dusty gas model equations represent a set of v coupled linearly independent equations. The form of the equations is most easily presented when in Stefan-Maxwell form, where the relative flux of each species is proportional to the driving force for

concentration and pressure diffusion plus the Knudsen and viscous flow. However, this same form leaves the flux vectors highly coupled, leaving the solution process non-obvious. The goal of the algebraic manipulation is to identify a matrix form of the modified dusty gas equations that will facilitate computation of the flux vectors. Equation 84 is produced by expanding the summation, distributing the Knudsen diffusion coefficient, and collecting like terms containing J_i/n_i.

$$\sum_{j=1}^{v}\left(\frac{n_j}{nD_{ij}}+\frac{1}{D_{iK}}\right)\left(\frac{J_i}{n_i}\right)-\sum_{j=1\ \&\ j\neq 1}^{v}\left(\frac{n_j}{nD_{ij}}\right)\left(\frac{J_j}{n_j}\right)=-\frac{B_o}{D_{iK}\eta}-\left(\frac{\nabla p_i}{p_i}\right) \tag{84}$$

This set of equations is further reduced to Equation 85 by multiplying both sides of Equation 84 by n and cancelling terms.

$$\frac{1}{n_i}\left(\frac{n}{D_{iK}}+\sum_{j=1,j\neq i}^{v}\frac{n_j}{D_{ij}}\right)J_i-\sum_{j=1\ \&\ j\neq i}^{v}\frac{1}{D_{ij}}J_j=-n\left(\frac{B_o}{D_{iK}\eta}\nabla p+\frac{\nabla p_i}{p_i}\right) \tag{85}$$

$$\text{for } i=1,2,\ldots,v$$

The advantage of this form is that all of the unknown flux vectors are on the LHS and the differential terms are on the RHS. The matrix form of the equations is given by Equations 86-89.

$$\mathbf{Ax}=\mathbf{b} \tag{86}$$

$$\mathbf{A} = \begin{pmatrix} \frac{1}{n_1}\left(\frac{n}{D_{1K}} + \sum_{j=1,j\neq 1}^{v} \frac{n_j}{D_{1j}}\right) & \cdots & -\frac{1}{D_{ij}} & \cdots & -\frac{1}{D_{1v}} \\ \vdots & \ddots & & & \vdots \\ -\frac{1}{D_{ij}} & & \frac{1}{n_i}\left(\frac{n}{D_{iK}} + \sum_{j=1,j\neq i}^{v} \frac{n_j}{D_{ij}}\right) & & -\frac{1}{D_{ij}} \\ \vdots & & & \ddots & \vdots \\ -\frac{1}{D_{1v}} & \cdots & -\frac{1}{D_{ij}} & \cdots & \frac{1}{n_v}\left(\frac{n}{D_{vK}} + \sum_{j=1,j\neq v}^{v} \frac{n_j}{D_{vj}}\right) \end{pmatrix} \tag{87}$$

$$\mathbf{b} = -n \begin{pmatrix} \frac{B_o}{D_{1K}\eta}\nabla p + \frac{\nabla p_1}{p_1} \\ \vdots \\ \frac{B_o}{D_{iK}\eta}\nabla p + \frac{\nabla p_i}{p_i} \\ \vdots \\ \frac{B_o}{D_{vK}\eta}\nabla p + \frac{\nabla p_v}{p_v} \end{pmatrix} \tag{88}$$

$$\mathbf{x} = \begin{pmatrix} J_1 \\ \vdots \\ J_i \\ \vdots \\ J_v \end{pmatrix} \tag{89}$$

This approach isolates the multi-species flux vector, $\mathbf{x}$, in a form that resembles a system of linear algebraic equations. Substituting the appropriate equations for the transport coefficients, gas species properties, and porous medium properties into Equations 86-89 leaves them arbitrary up to a choice of numerical discretization. Using the FCVM numerical discretization, from the previous chapter, for the gas concentrations and gradients produces a set of linear algebraic equations for the gas flux at each control volume interface. Ultimately, once the numerical values for $\mathbf{A}$ and $\mathbf{b}$ are known, then any method for solving linear algebraic equations can be used to solve for $\mathbf{x}$. The necessary algebraic construction is only performed once using symbolic programming techniques to produce expressions for the direct calculation of $\mathbf{x}$ by forming $\mathbf{A^{-1}b}$. These expressions are used to generate the function, *DGFlux*, which is

used to calculate the gas flux using the current species concentrations and the FCVM discretization.

```
function Jexp = DGFlux(speciesE,speciesW,TE,TW,VtotalE,VtotalW,qE,qW,rE,rW,hE,hW)%#codegen
%DGFLUX
%    JEXP = DGFLUX(SPECIESE,SPECIESW,TE,TW,VTOTALE,VTOTALW,QE,QW,RE,RW,HE,HW)
%    This function was generated by the Symbolic Math Toolbox version 6.0.
%    12-Feb-2015 13:04:59

C = speciesE(:,1);
CO2g = speciesE(:,5);
COg = speciesE(:,4);
...(177 Lines Omitted)
t171 = t31.*t38.*t42.*t43.*t45.*t59.*t61.*t67.*t71.*t72.*5.812771385628337e-50;
t172 = t26.*t31.*t39.*t52.*t55.*t56.*t57.*t59.*t61.*t65.*8.54354801964593e-23;
t173 = t157+t158+t159+t160+t161+t162+t163+t164+t165+t166+t167+t168+t169+t170+t171+t172;
...(2 Lines Omitted)
Jexp = [t143.*t154.*t155.*t156.*t174.*(t26.*t39.*t42.*t51.*t52.*t56.*t57.*t59.*t63.*t73.*...
    t88.*t90.*t100.*9.962122725920379e-22+t26.*t39.*t42.*t52.*t56.*t57.*t59.*t61.*t65.*t73.*...
    t88.*t90.*t100.*8.76327312350219e-22+t31.*t39.*t42.*t52.*t56.*t57.*t59.*t61.*t63.*t73.*...
    ...(72 Lines Omitted)
    t44.*t51.*t55.*t61.*t67.*t90.*t100.*t105.*t106.*t107.*3.537159943789424e-76+t26.*t28.*t31.*
    ...(22 Lines Omitted)
    t67.*t71.*t72.*t87.*t90.*t98.*t139.*t150.*3.875180923752225e-50).*1.218658242650942e-2];
```

Figure 3-1: DGFlux is a MATLAB function generated from symbolic expressions to calculate the gas flux. The input parameters correspond to the values need for the FCVM discretization and the output is the gas flux, Jexp.

4 Chemical Equilibrium Model

The goal of this chapter is to explain the process for generating the necessary functions to calculate the thermodynamic chemical equilibrium composition of a closed chemical system and identify the needed physical parameters. The overall approach can be viewed as a type of *Model Reduction*. Model reduction is a generic technique of decomposing a large complex problem into a set of small simple problems, ensuring under suitable conditions the solution to the small problems will solve the larger problem. The formalism to represent an individual chemical system is based upon an overview of chemical equilibrium analysis by Smith and Missen and is used to facilitate the description of the chemical equilibrium model presented in this work.[68] The *chemical system* {{C, SiC, SiO_2, $CO_{(g)}$, $CO_{2(g)}$, $SiO_{(g)}$},{C, O, Si}} will be used to demonstrate the algorithmic process needed to generate the required functions. For the remainder of this discussion, all chemical systems will be denoted by only the chemical species, with their constituent indestructible elements implicitly identified by the atomic elements comprising them. Thus, the previous chemical system is identified as {C, SiC, SiO_2, $CO_{(g)}$, $CO_{2(g)}$, $SiO_{(g)}$}.

4.1 Chemical Equilibrium by Model Reduction

A *chemical set* is used to describe the most general *chemical system* being considered for modeling chemical equilibrium, *i.e.* the large complex problem. A *chemical set* can be broken down into a number of *chemical regimes, i.e.* smaller, simpler problems. A *chemical regime* refers to a particular decomposition of a *chemical set* into a smaller, simpler *chemical system* containing all the gas species of the *chemical set* and possibly excluding some or all of the condensed species *, e.g.* {C, SiC, $CO_{(g)}$, $CO_{2(g)}$, $SiO_{(g)}$}. Both a chemical set and a chemical regime are chemical systems, but a chemical regime carries the distinction of being one element of a

collection (or subset) of chemical systems belonging to a specific chemical set. If *N* is the number of condensed chemical species in a chemical set, then there are 2^N unique chemical regimes needed to represent the full decomposition of the chemical set. For the example chemical set, there are 8 chemical regimes:

1. {C, SiC, SiO_2, $CO_{(g)}$, $CO_{2(g)}$, $SiO_{(g)}$}
2. {C, SiC, $CO_{(g)}$, $CO_{2(g)}$, $SiO_{(g)}$}.
3. {C, SiO_2, $CO_{(g)}$, $CO_{2(g)}$, $SiO_{(g)}$}.
4. {C, $CO_{(g)}$, $CO_{2(g)}$, $SiO_{(g)}$}.
5. { SiC, SiO_2, $CO_{(g)}$, $CO_{2(g)}$, $SiO_{(g)}$}.
6. { SiC, $CO_{(g)}$, $CO_{2(g)}$, $SiO_{(g)}$}.
7. { SiO_2, $CO_{(g)}$, $CO_{2(g)}$, $SiO_{(g)}$}.
8. { $CO_{(g)}$, $CO_{2(g)}$, $SiO_{(g)}$}.

One chemical regime represents the same chemical system as the chemical set, *i.e.*,{C, SiC, SiO_2, $CO_{(g)}$, $CO_{2(g)}$, $SiO_{(g)}$}. While, another includes only the gas species, *i.e.*, {$CO_{(g)}$, $CO_{2(g)}$, $SiO_{(g)}$}. The set concept is used to denote membership, so reordering the elements within each set does not change the physical nature of the problem.

The decomposition of the chemical set into simpler sub-problems requires identifying whether the solution to the sub-problem also satisfies the solution to the larger problem. A critical assumption is that there will always be some non-zero amount of each elemental species from the chemical system present in the closed system; otherwise it would not be a well-posed problem. Additionally, all condensed species are considered to be ideal condensed species to simplify the equilibrium analysis.

Three validity checks are used to confirm if an equilibrium solution for a chemical regime is valid for the chemical set:

1. The quantity of each elemental species determined from the initial, non-equilibrium species composition must be equal to the final, equilibrium species composition.
2. Positivity of all species quantities in a chemical regime at equilibrium.
3. The activity of all condensed species in the regime are equal to 1 and the activity of all condensed species not in the regime are less than 1.

The first validity check asserts that there is no gain or loss of matter during the equilibration process, a criteria imposed by the closed system constraint. The second validity check requiring the positivity of all species in the regime is needed for a physically reasonable solution; a zero quantity would indicate a different chemical regime would be a better representative sub-problem. The third validity check requires finding the activity of each condensed species in the chemical set using the calculated equilibrium composition for the proposed chemical regime.

4.2 Generating Activity Checks

The equations for checking the activity of each condensed species in a chemical set can be generated systematically. This process assumes that the condensed phases are pure, the gases are ideal, and the Gibbs free energy for each species is known. Additionally, the molar mass, M_i, and density, ρ_i, of each condensed species is needed to determine the pore volume, V_{pore}, for a closed system of total volume, V_{total}. Figure 4-1 shows the process to be demonstrated for the chemical set {C, SiC, SiO_2, $CO_{(g)}$, $CO_{2(g)}$, $SiO_{(g)}$}.

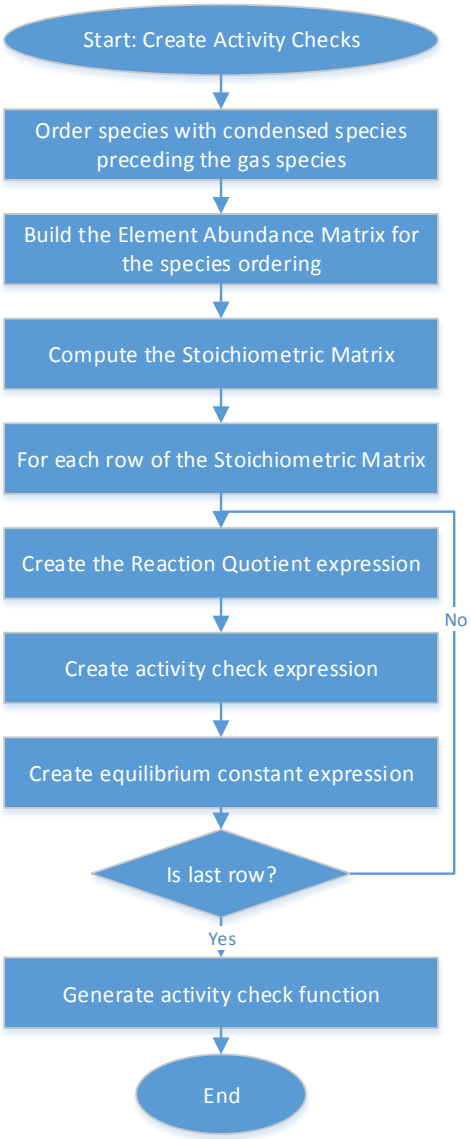

Figure 4-1: Flowchart for generating activity check expressions

The initial and most critical step of the process to generate activity checks is to order the chemical species with the condensed species preceding the gas species. A suitable ordering of the chemical set, {C, SiC, SiO_2, $CO_{(g)}$, $CO_{2(g)}$, $SiO_{(g)}$}, is in fact the list, (C, SiC, SiO_2, $CO_{(g)}$, $CO_{2(g)}$, $SiO_{(g)}$). The systematic process used to generate a complete set of independent stoichiometric reactions will tend to isolate the species in the beginning of the list into separate reactions. The

isolation of a chemical species to only one stoichiometric reaction also provides a unique way of labeling each reaction in the set.

4.2.1 Element Abundance: Matrix, Equations, and Expressions

The ordered list of species and alphabetic ordered list of elements are used to create an *element abundance matrix* which provides a mapping between each species and its constituent elements. [68] It can also be used to identify the total amount of each element for a given species composition. An element abundance matrix for the chemical set {C, SiC, SiO_2, $CO_{(g)}$, $CO_{2(g)}$, $SiO_{(g)}$} is

	C	SiC	SiO_2	$CO_{(g)}$	$CO_{2(g)}$	$SiO_{(g)}$
C	1	1	0	1	1	0
O	0	0	2	1	2	1
Si	0	1	1	0	0	1

(90)

This matrix is one possible mapping used to represent the *element abundance equations* given by

$$n_C + n_{SiC} + n_{CO_{(g)}} + n_{CO_{2(g)}} = b_C \tag{91}$$

$$2n_{SiO_2} + n_{CO_{(g)}} + 2n_{CO_{2(g)}} + n_{SiO_{(g)}} = b_O \tag{92}$$

$$n_{SiC} + n_{SiO_2} + n_{SiO_{(g)}} = b_{Si} \tag{93}$$

where, n_i is a species quantity and b_i is an elemental quantity.

The element abundance equations can be represented symbolically by multiplying Equation 90 by the vector of symbolic values for the chemical species, (C, SiC, SiO_2, $CO_{(g)}$, $CO_{2(g)}$, $SiO_{(g)}$)^T, and setting it equal to the symbolic vector for the chemical elements, {b_C, b_O, b_{si}}. An almost identical construct is used for the *element abundance*

expressions which are symbolic expressions implicitly assumed to be equal to zero. The element abundance expressions are given by Equations 94, 95, and 96; the negative of the whole expression is an alternate form of the same expression when equality to zero is implied.

$$n_C + n_{SiC} + n_{CO_{(g)}} + n_{CO_{2(g)}} - b_C \tag{94}$$

$$2n_{SiO_2} + n_{CO_{(g)}} + 2n_{CO_{2(g)}} + n_{SiO_{(g)}} - b_O \tag{95}$$

$$n_{SiC} + n_{SiO_2} + n_{SiO_{(g)}} - b_{Si} \tag{96}$$

Throughout this work, equations will be presented to explicitly show the equality between symbolic variables. With each equation there is often an associated expression that is implicitly equal to zero or some other intuitively connected variable. The strategy of using expressions closely resembles the process used for the symbolic programming because expressions can be substituted in place of variables in other expression. Substitution of an equation into another equation or expression is generally not a well-defined concept. Additionally, when generating code from symbolic expressions, the inputs would be values for the variables and the output would be the value of the expression when evaluating the generated function. Generating code for symbolic equations would imply generating a function that takes values for the inputs of the symbolic variables and outputs a Boolean value that indicates if the inputs satisfy the given equality.

4.2.2 Stoichiometry: Stoichiometric Matrix, Equations, and Expressions

The next step in the process is to generate the canonical *stoichiometric matrix* associated with the element abundance matrix. [68] The null space matrix, $\mathbf{x}$, is a maximal set of linearly independent vectors that satisfy

$$\mathbf{Ax} = \mathbf{0} \tag{97}$$

for a given matrix, $\mathbf{A}$. A null space matrix can be computed using standard techniques from linear algebra. [89] The null space matrix is not unique because any matrix consisting of arbitrary linear combinations of the columns of $\mathbf{x}$ will also satisfies Equation 97.

A stoichiometric matrix is given simply by transposing the null space matrix associated with an elemental abundance matrix. The stoichiometric matrix can be put in canonical form by computing the reduced row echelon form. The canonical stoichiometric matrix for Equation 90 is

	C	SiC	SiO_2	$CO_{(g)}$	$CO_{2(g)}$	$SiO_{(g)}$
Rx 1	1	0	0	−2	1	0
Rx 2	0	1	0	−3	2	−1
Rx 3	0	0	1	1	−1	−1

(98)

A stoichiometric matrix represents a mapping satisfied by stoichiometric equations. Each row of the stoichiometric matrix represents an individual reaction where the positive and negative numbers are the coefficients of the product and reactant species, respectively. The reaction and product labeling is just used as naming convention and does not imply a reaction path mechanism because only equilibrium reactions are considered. The stoichiometric equations represented by the stoichiometric matrix are

$$2CO_{(g)} = C + CO_{2(g)} \tag{99}$$

$$3CO_{(g)} + SiO_{(g)} = SiC + 2CO_{2(g)} \tag{100}$$

$$CO_{2(g)} + SiO_{(g)} = SiO_2 + CO_{(g)} \tag{101}$$

Strategically ordering the condensed species helps ensure that each stoichiometric equation has only one condensed species involved per reaction and that its stoichiometric coefficient is unity.

This makes it particularly simple to generate a function to check the activity of each condensed species in terms of other known quantities. In each row of the stoichiometric matrix, the species corresponding to the first non-zero entry can be used as a labeling for the reaction corresponding to the respective row because it will not be present in other reactions; *i.e.* Equations 99, 100, and 101 can be labeled by C, SiC, and SiO_2, respectively.

4.2.3 Reaction Quotients and Equilibrium Constants

The reaction quotient is then built for each row of the stoichiometric matrix. The reaction quotient is normally given by the product of the reaction product activities raised to their stoichiometric coefficient power divided by the product of the reaction reactants activities raised to the power of their stoichiometric coefficient. Alternatively, using the positive and negative coefficients it can be written as the product of the reaction species activities raised to the power of their stoichiometric coefficient. At chemical equilibrium, the reaction quotient is equal to the equilibrium constant, K_{eq}. A compact formula for K_{eq} is

$$K_{eq} = \prod_i a_i^{\nu_i} \tag{102}$$

where, the activity and stoichiometric coefficient of the i^{th} species is given by a_i and ν_i, respectively.

Using the ideal gas assumption allows the activity of the gas species to be replaced with the gas partial pressure. Using the leading species labeling for each reaction, the reaction quotient equations are

$$K_{eq,C} = \frac{a_C p_{co_2}}{p_{CO}^2} \tag{103}$$

$$K_{eq,SiC} = \frac{a_{SiC} p_{CO_2}^2}{p_{CO}^3 p_{SiO}} \tag{104}$$

$$K_{eq,SiO_2} = \frac{a_{SiO_2} p_{CO}}{p_{CO_2} p_{SiO}} \tag{105}$$

4.2.4 Activity Checks

Each reaction quotient equation is transformed to isolate the condensed species activity in terms of gas pressures and the associated equilibrium constant. The transformation equation for each reaction can be given by

$$K_{eq} \cdot \prod_{\substack{i \neq condensed \\ label\ index}} p_i^{-v_i} = a_{\substack{condensed \\ label\ index}} \tag{106}$$

since there is only one condensed species per reaction, its stoichiometric coefficient is one, and all other species are gases.

The transformed equations, for the example chemical set, are

$$\frac{K_{eq,C} p_{CO}^2}{p_{co_2}} = a_C \tag{107}$$

$$\frac{K_{eq,SiC} p_{CO}^3 p_{SiO}}{p_{co_2}^2} = a_{SiC} \tag{108}$$

$$\frac{K_{eq,SiO_2} p_{CO_2} p_{SiO}}{p_{CO}} = a_{SiO_2} \tag{109}$$

The closed system constraint are used to express the pore volume in terms of the total volume and the condensed species compositions as

$$V_{pore} = V_{total} - \frac{(n_C M_C)}{\rho_C} - \frac{(n_{SiC} M_{SiC})}{\rho_{SiC}} - \frac{\left(n_{SiO_2} M_{SiO_2}\right)}{\rho_{SiO_2}} \tag{110}$$

Using the ideal gas law and the closed system constraint, Equations 107, 108, and 109 are rewritten as

$$\frac{K_{eq,C}\, n_{CO_{(g)}}^2}{n_{CO_{2(g)}}}\left(\frac{RT}{V_{pore}}\right) = a_C \tag{111}$$

$$\frac{K_{eq,SiC} n_{CO_{(g)}}^3 n_{SiO_{(g)}}}{n_{CO_{2(g)}}^2}\left(\frac{RT}{V_{pore}}\right)^2 = a_{SiC} \tag{112}$$

$$\frac{K_{eq,SiO_2} n_{CO_{2(g)}} n_{SiO_{(g)}}}{n_{CO_{(g)}}}\left(\frac{RT}{V_{pore}}\right) = a_{SiO_2} \tag{113}$$

where, the pore volume is given by Equation 110.

Equations 111, 112, and 113 are written in terms of quantities that are known after calculating the equilibrium composition of the closed system at a given temperature, thus providing a way of calculating the activity of the condensed species. All of these manipulations and substitutions are done using symbolic expressions. The final symbolic expressions are then used to generate the *activity_check* function. The *activity_check* function for the {C, SiC, SiO_2, $CO_{(g)}$, $CO_{2(g)}$, $SiO_{(g)}$} chemical set is shown in Figure 4-2.

```
function activities = activity_check(speciesIn,Keq,T,Vtotal)%#codegen
%ACTIVITY_CHECK
%    ACTIVITIES = ACTIVITY_CHECK(SPECIESIN,KEQ,T,VTOTAL)

%    This function was generated by the Symbolic Math Toolbox version 6.0.
%    19-Sep-2014 14:49:07

C = speciesIn(:,1);
CO2g = speciesIn(:,5);
COg = speciesIn(:,4);
Keq1 = Keq(:,1);
Keq2 = Keq(:,2);
Keq3 = Keq(:,3);
SiC = speciesIn(:,2);
SiO2 = speciesIn(:,3);
SiOg = speciesIn(:,6);
t2 = COg.^2;
t3 = C.*5.719380952380952;
t4 = SiC.*1.249102803738318e1;
t5 = SiO2.*2.731104545454545e1;
t6 = -Vtotal+t3+t4+t5;
t7 = 1.0./t6;
activities = [(Keq1.*T.*t2.*t7.*(-8.205746000000001e1))./CO2g,...
    1.0./CO2g.^2.*COg.*Keq2.*SiOg.*T.^2.*t2.*1.0./t6.^2.*6.733426741651601e3,...
    (CO2g.*Keq3.*SiOg.*T.*t7.*(-8.205746000000001e1))./COg];
```

Figure 4-2: The activity_check MATLAB function generated from symbolic expressions used for checking the activities of C, SiC, and SiO_2. Input: in1 = species compositions, in2: equilibrium constants, T: temperature, Vtotal: total volume. Output: activities = [a_C, a_{SiC}, a_{SiO2}].

The needed equilibrium constants $K_{eq,C}$, $K_{eq,SiC}$, and K_{eq,SiO_2} are generated in a systematic way using thermodynamic data, the stoichiometric matrix, and the relation $\Delta G_{rx} = -RT\ln(K_{eq})$. The Gibbs free energy functions for individual species and the stoichiometric matrix can be used to compute the necessary ΔG_{rx} for each reaction. The necessary ΔG_{rx} for each reaction can be computed using the individual free energy functions for each species and the canonical stoichiometric matrix, Equation 98:

$$\Delta G_{rx,C} = G_C + G_{CO_{2(g)}} - 2G_{CO_{(g)}} \tag{114}$$

$$\Delta G_{rx,SiC} = G_{SiC} + 2G_{CO_{2(g)}} - 3G_{CO_{(g)}} - G_{SiO_{(g)}} \tag{115}$$

$$\Delta G_{rx,SiO_2} = G_{SiO_2} + G_{CO_{(g)}} - G_{CO_{2(g)}} - G_{SiO_{(g)}} \quad (116)$$

A detailed example is given in Appendix IV.ii outlining how to generate a function to calculate the equilibrium constant for each stoichiometric reaction automatically, using a thermodynamic database and symbolic programming techniques.

4.3 Generating Chemical Regime Equilibrium Functions: Method 1

In order to calculate the equilibrium composition for a chemical regime, a set of constraint equations must be generated to represent the equilibrium conditions. A well-determined set of constraint equations, *i.e.* the same number of equations as unknown quantities, can be generated by combining the mass balance constraints for a closed system with the thermodynamic equilibrium constraints $\Delta G_{rx} = -RT\ln(K_{eq})$. The constraint equations can then be solved using numerical techniques such as the Newton-Raphson method for a system of nonlinear equations. Figure 4-3 outlines the process for generating the chemical regime equilibrium functions needed for calculating the equilibrium composition. Chemical regime 2, {C, SiC, $CO_{(g)}$, $CO_{2(g)}$, $SiO_{(g)}$}, is used as an example to illustrate the process and any assumptions used.

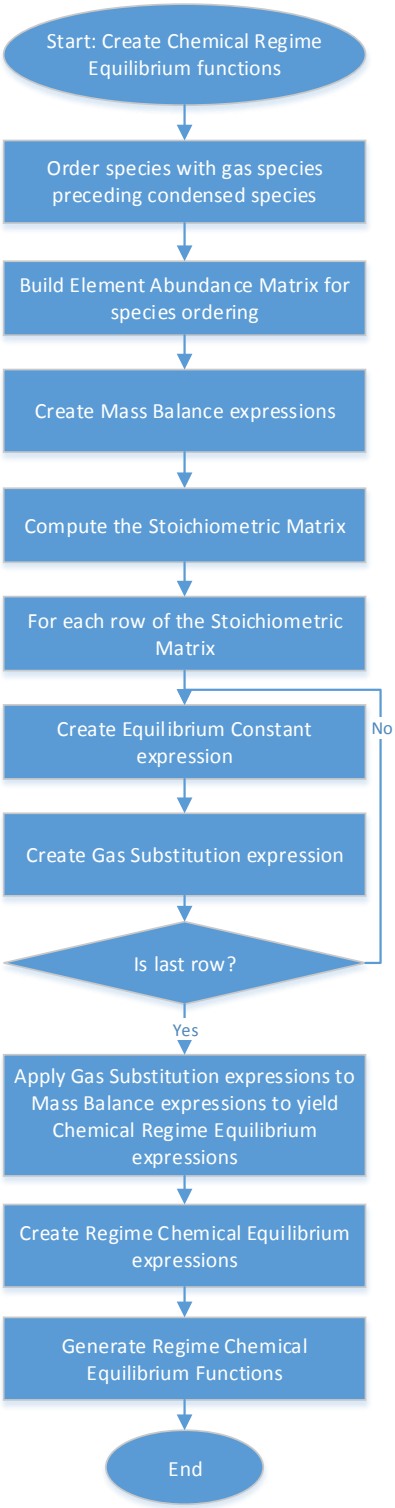

Figure 4-3: Flowchart for generating Chemical Regime Equilibrium Functions (Method 1).

4.3.1 Element Abundance and Mass Balance Expressions

The most critical step to facilitate combining the thermodynamic and mass balance constraints is to properly order the chemical species, the chemical species should be ordered with the gas species preceding the condensed species. A suitable ordering of the chemical regime, {C, SiC, $CO_{(g)}$, $CO_{2(g)}$, $SiO_{(g)}$}, is the list, ($SiO_{(g)}$, $CO_{2(g)}$, $CO_{(g)}$, C, SiC). Similar to generating the activity checks, the systematic process used to generate a complete set of independent stoichiometric reactions will tend to isolate the species in the beginning of the list to separate reactions and provides a unique way of labeling the reactions in the set. A choice was made to list the most minor gas species first, because they will be explicitly eliminated from the equilibrium constraints and can help with the numerical stability during the solution process.

The chosen species ordering is used to create an associated element abundance matrix. For example, the element abundance matrix for the ($SiO_{(g)}$, $CO_{2(g)}$, $CO_{(g)}$, C, SiC) species ordering is

	$SiO_{(g)}$	$CO_{2(g)}$	$CO_{(g)}$	C	SiC
C	1	1	1	1	1
O	0	2	1	0	0
Si	1	0	0	0	1

(117)

The element abundance matrix can be used to calculate the initial elemental composition from the non-equilibrium species composition before equilibration. The elemental composition must be held constant during the equilibration process due to the closed system constraints. The element abundance matrix is also used to generate the set of expressions representing the mass balance constraints given by

$$b_C = n_{CO_{2(g)}} + n_{CO_{(g)}} + n_C + n_{SiC} \tag{118}$$

$$b_O = n_{SiO_{(g)}} + 2n_{CO_{2(g)}} + n_{CO_{(g)}} \tag{119}$$

$$b_{Si} = n_{SiO_{(g)}} + n_{SiC} \tag{120}$$

The mass balance constraint consists of only 3 equations and contains 5 unknown variables representing the equilibrium species composition. The elemental composition variables are set by the non-equilibrium species composition. Additional constraints must be introduced to have a solvable system of equations.

4.3.2 Stoichiometry

The next step is to create the canonical stoichiometric matrix from the element abundance matrix. Again, this requires computing the reduced row echelon form of the transposed null space matrix for the element abundance matrix. The result of that procedure yields the matrix

	$SiO_{(g)}$	$CO_{2(g)}$	$CO_{(g)}$	C	SiC
Rx 1	1	0	−1	2	−1
Rx 2	0	1	−2	1	0

(121)

This produces a matrix with two independent rows that represent the two stoichiometric equations

$$CO_{(g)} + SiC = SiO_{(g)} + 2C \tag{122}$$

$$2CO_{(g)} = CO_{2(g)} + C \tag{123}$$

In this example, there are three gases and only two independent stoichiometric equations. This procedure has ensured that only $SiO_{(g)}$ is present in Equation 122 and $CO_{2(g)}$ is present in Equation 123, with $CO_{(g)}$ and the condensed species present in both equations. This allows $SiO_{(g)}$

and $CO_{2(g)}$ to be expressed in terms of the most abundant gas ($CO_{(g)}$) and the condensed species present (C and SiC).

4.3.3 Reaction Quotients and Equilibrium Constants

The stoichiometric equations are used to create additional constraint equations from the thermodynamic relations. Similar to the activity check procedure, using the positive and negative exponent convention with the ideal gas assumptions, yields the equilibrium reaction quotient expressions

$$K_{eq,SiO_g} = \frac{p_{SiO} a_C^2}{p_{CO} a_{SiC}} \tag{124}$$

$$K_{eq,CO_{2(g)}} = \frac{p_{CO_2} a_C}{p_{CO}^2} \tag{125}$$

corresponding to the stoichiometric equations given by Equations 122 and 123, respectively.

4.3.4 Gas Substitution Equations

Each reaction quotient expression can easily be transformed to isolate individual gas species partial pressures in terms of other gas partial pressures, condensed activities and the appropriate equilibrium constant. An analogous transformation expression to Equation 106, but for gas substitution is

$$K_{eq} \cdot \prod_{\substack{i \neq gas\ label \\ index}} (a\ or\ p)_i^{-v_i} = p_{\substack{gas\ label \\ index}} \tag{126}$$

where, the gas species used to label each equation is only present in one reaction and its stoichiometric coefficient is unity. The transformed equations for Equations 124 and 125 are

$$\frac{K_{eq,SiO_g} p_{CO} a_{SiC}}{a_C^2} = p_{SiO} \tag{127}$$

$$\frac{K_{eq,CO_{2(g)}} p_{CO}^2}{a_C} = p_{CO_2} \tag{128}$$

, respectively.

The next step in the process assumes that all condensed species in the regime are present and ideal, *i.e.* the activity is equal to unity. The assumption of ideal condensed species allows for the explicit elimination of a subset of gas species considered present. Some other assumption on the functional form for the condensed activities can be used, but the remainder of the procedure would have to be modified to account for the compositional dependences of the condensed species activities. Applying these assumptions to Equations 127 and 128 yield

$$K_{eq,SiO_g} p_{CO} = p_{SiO} \tag{129}$$

$$K_{eq,CO_{2(g)}} p_{CO}^2 = p_{CO_2} \tag{130}$$

By assuming that the gas species are ideal gases and using the ideal gas law, Equations 129 and 130 can be transformed into the *gas substitution equations*

$$K_{eq,SiO_{(g)}} n_{CO_{(g)}} = n_{SiO_{(g)}} \tag{131}$$

$$\frac{K_{eq,CO_{2(g)}} n_{CO_{(g)}}^2 RT}{V_{pore}} = n_{CO_{2(g)}} \tag{132}$$

A key feature is that for each gas species that has a substitution equation, the substitution expression will not contain any reference to any other gas species that also has a substitution equation. This feature allows explicit removal of these gas species because its dependence will not be reintroduced by another gas substitution equation.

4.3.5 Chemical Regime Equilibrium Constraints

A set of *chemical regime equilibrium constraints* are created by using gas substitution equations to explicitly eliminate unknown variables in the element abundance equations that satisfy the mass balance constraint. Equations 131 and 132 are substituted into the element abundance equations given by Equations 118, 119, and 120 to explicitly eliminate the unknown gas species concentrations for $n_{SiO_{(g)}}$ and $n_{CO_{2(g)}}$. A set of three chemical regime equilibrium constraints equations are

$$b_C = \frac{K_{eq,CO_{2(g)}} n_{CO_{(g)}}^2 RT}{V_{pore}} + n_{CO_{(g)}} + n_C + n_{SiC} \tag{133}$$

$$b_O = 2\frac{K_{eq,CO_{2(g)}} n_{CO_{(g)}}^2 RT}{V_{pore}} + n_{CO_{(g)}} + K_{eq,SiO_g} n_{CO_{(g)}} \tag{134}$$

$$b_{Si} = n_{CO_{(g)}} + K_{eq,SiO_{(g)}} n_{CO_{(g)}} \tag{135}$$

where, the pore volume is

$$V_{pore} = V_{total} - \frac{(n_C M_C)}{\rho_C} - \frac{(n_{SiC} M_{SiC})}{\rho_{SiC}} \tag{136}$$

The expression for the pore volume, Equation 136, should be explicitly substituted into Equations 133, 134, and 135 for the chemical regime equilibrium constraints.

Functions to evaluate the chemical equilibrium constants, $K_{eq,SiO_{(g)}}$ and $K_{eq,CO_{2(g)}}$, at a given temperature can be generated using the procedure in Appendix IV.ii and the Gibbs free energy of reaction for each stoichiometric equation:

$$\Delta G_{rx,SiO_{(g)}} = G_{SiO_{(g)}} + 2G_C - G_{SiC} - G_{CO_{(g)}} \tag{137}$$

$$\Delta G_{rx,CO_{2(g)}} = G_{CO_{2(g)}} + G_C - 2G_{CO_{(g)}} \quad (138)$$

The total volume, elemental composition and equilibrium constants are known from the starting constraints of the fixed size closed system, species composition, and temperature; while, the molecular mass and density are known material properties. Thus, $n_{CO_{(g)}}$, $n_{CO_{(g)}}$, and n_C are the only three unknown quantities in the chemical regime equilibrium constraint equations. This nonlinear system of equations can then be recast as a root finding problem by arranging all of the terms of Equations 133-135 onto the LHS of the equations and equating them to zero. The roots of this nonlinear system are then solved using numerical techniques, such as the Newton-Raphson method, for a real, positive root. Some difficulties of solving for the equilibrium chemical composition is discussed in the next section. The composition of the gas species eliminated from the constraint expressions are calculated by using Equations 38 and 39.

4.3.6 Difficulties Solving the Chemical Regime Equilibrium Constraint Equations

4.3.6.1 *Incorrect Chemical Regime Choice*

The ability to create chemical equilibrium constraint equations for a chemical regime does not ensure the equations have a physically reasonable solution. The validity of the choice of the chemical regime for a non-equilibrium starting composition is only checked after a solution has been found. If the regime choice is not correct, then there might be no solutions to the constraints that are physically reasonable, *i.e.* both real and positive.

4.3.6.2 *Existence and Uniqueness of a Solution*

A solution to the chemical equilibrium problem is known to exist for an ideal chemical system with multiple phases. However, there can be a degeneracy where the relative amount of each phase is not unique and an infinite number of solutions are possible. [68] This is the case for

both the nonlinear equation and free energy formulation of the chemical equilibrium problem. This complication is mitigated by starting any iterative procedure from a previous equilibrium composition, so the initial non-equilibrium composition is only a small perturbation from a known equilibrium solution. In the event of a multiplicity of solutions, it is assumed that the solution of the non-linear equations is the *nearest* root to a previous equilibrium composition.

4.3.6.3 *Fractional Power Nonlinearity*

Even if the regime choice is correct, the solution may be difficult to compute because of complications arising from nonlinearities in the constraint equations. Nonlinearities are introduced when the gas substitution equations are substituted into the element abundance equations to create the chemical regime equilibrium constraint equations. The nonlinearity can be a serious problem for any solution algorithm if the stoichiometric coefficient of any gas species is a fractional value. If any sub-expression evaluates to a negative value and is exponentiated to a fractional power, the result is almost always a complex number. The only exception is if the fractional exponent has a numerator equal to 1 and an odd denominator, will the exponentiation still produce a real number.

The nonlinearity in the gas substitution equations is a direct consequence of the coefficients of the stoichiometric equations used in the reaction quotients. A fractional value, from a stoichiometric coefficient, will be used to exponentiate the species composition variable as well as the pore volume sub-expression. If either the species composition variable or pore volume sub-expression becomes negative, then the exponentiation will produce a complex number. The exclusion of trial solutions that enforce positivity of species concentrations is trivial to introduce for most solution algorithms and not considered a serious problem. However, it is a non-trivial task to ensure the solution algorithm does not attempt positive trial solutions that cause the pore volume sub-expression, such as Equations 110 and 136, to become negative.

The failure of the solution algorithm can manifest itself in two different ways. First, when using gradient based solution algorithms (*i.e. Newton-Raphson Method*) it may not be able to reach a physically reasonable solution after producing a complex trial solution. This is due to the method trying to incrementally improve the previous trial solution, thus it is not likely to eliminate the imaginary part of the solution. Second, depending on the programming environment, the numeric type of the parameters used in the calculations must be defined prior to execution. If a complex number is produced when a real floating point number is expected, then a 'run-time' error will be produced and cause the program to fail.

4.3.7 Modified Chemical Regime Equilibrium Constraint Equations

To address problems solving the chemical regime equilibrium constraint equations, a slight reformulation of the constraint equations and solution method is needed. Due to the potential for the pore volume sub-expression to cause problems solving the constraint equations, the pore volume expression should not be substituted directly into the chemical regime equilibrium constraint equations. Instead, the pore volume is an input parameter that needs to be supplied along with the temperature and elemental composition when solving for the equilibrium species composition. The inclusion of the pore volume as a parameter mandates that the pore volume be calculated prior to solving for the equilibrium species composition. Some variables and parameters in the constraint equations are now indexed by an additional subscript to identify whether they are known before or after the iterant, given by 0 or 1, respectively.

The approximate pore volume is calculated from the total volume and the non-equilibrium condensed species composition. The initial iterant for the pore volume is

$$V_{pore,0} = V_{total} - \frac{\left(n_{C,0}M_C\right)}{\rho_C} - \frac{\left(n_{SiC,0}M_{SiC}\right)}{\rho_{SiC}} \quad (139)$$

The *modified chemical regime equilibrium constraint equations* are

$$b_C = \frac{K_{eq,CO_{2(g)}} n_{CO_{(g)},1}^2 RT}{V_{pore,0}} + n_{CO_{(g)},1} + n_{C,1} + n_{SiC,1} \quad (140)$$

$$b_O = 2\frac{K_{eq,CO_{2(g)}} n_{CO_{(g)},1}^2 RT}{V_{pore,0}} + n_{CO_{(g)},1} + K_{eq,SiO_g} n_{CO_{(g)},1} \quad (141)$$

$$b_{Si} = n_{SiC,1} + K_{eq,SiO_{(g)}} n_{CO_{(g)},1} \quad (142)$$

, in contrast to the unmodified version given by Equations 133-136.

The equilibrium species composition after solving the constraint equations will only be approximate because of the approximation used for the pore volume. An iterative approach to calculating the equilibrium species composition compensates for the approximation in the pore volume. The first iteration calculates the equilibrium species composition and is used to improve the approximate pore volume, allowing for the second iteration of the equilibrium species composition to be calculated and so on.

The choice to approximate the pore volume is appropriate for the current work because the non-equilibrium species composition will not be far away from the equilibrium species composition because small time steps are used. As a result, any changes in parameters are assumed to be small if used in an iterative scheme. The iterative process is fast to converge to the correct equilibrium composition, usually within two iterations. The fast convergence is mainly due to the small variation in pore volume that will take place during equilibration as condensed species either are consumed or deposited, into or from the gas phase, respectively. The first iteration mainly predicts the species composition to the correct order of magnitude (or

better). The second iteration then updates the pore volume to account for the more accurate prediction of the equilibrium species composition, allowing for a much more precise calculation of the equilibrium species composition on the second iteration.

4.3.8 Building Chemical Regime Equilibrium Solution Functions

The modified chemical regime equilibrium constraint equations shown in the previous section are generated as symbolic expressions using the outlined algorithmic procedure. The solution of these equations subject to the thermodynamic and mass balance constraints is the first step necessary to completely calculate the chemical equilibrium composition. Then using the solution to evaluate the gas substitution expressions to get the full equilibrium solution. An efficient solution method is the gradient based, Newton-Raphson algorithm for finding the roots of a nonlinear set of equations. To utilize this method, Equations 140-142 are recast as the vector valued function $\boldsymbol{f}$

$$\boldsymbol{f} = \begin{pmatrix} f_1 \\ f_2 \\ f_3 \end{pmatrix} = \begin{pmatrix} b_C - \dfrac{K_{eq,CO_{2(g)}} n_{CO_{(g)}}^2 RT}{V_{pore,0}} - n_{CO_{(g)}} - n_C - n_{SiC} \\ b_O - 2\dfrac{K_{eq,CO_{2(g)}} n_{CO_{(g)}}^2 RT}{V_{pore,0}} - n_{CO_{(g)}} - K_{eq,SiO_g} n_{CO_{(g)}} \\ b_{Si} - n_{SiC} - K_{eq,SiO_{(g)}} n_{CO_{(g)}} \end{pmatrix} = \mathbf{0} \tag{143}$$

to represent the root finding problem. The solution algorithm can be enhanced by generating the analytic jacobian matrix

$$\boldsymbol{J_f}\left(n_C, n_{SiC}, n_{CO_{(g)}}\right) = \begin{pmatrix} \dfrac{\partial f_1}{\partial n_C} & \dfrac{\partial f_1}{\partial n_{SiC}} & \dfrac{\partial f_1}{\partial n_{CO_{(g)}}} \\ \dfrac{\partial f_2}{\partial n_C} & \dfrac{\partial f_2}{\partial n_{SiC}} & \dfrac{\partial f_2}{\partial n_{CO_{(g)}}} \\ \dfrac{\partial f_3}{\partial n_C} & \dfrac{\partial f_3}{\partial n_{SiC}} & \dfrac{\partial f_3}{\partial n_{CO_{(g)}}} \end{pmatrix} \tag{144}$$

to provide the search directions. The explicit form of the jacobian matrix for $\boldsymbol{f}$ is

$$\boldsymbol{J_f}\left(n_C, n_{SiC}, n_{CO_{(g)}}\right) = \begin{pmatrix} -1 & -1 & \dfrac{-2K_{eq,CO_{2(g)}} n_{CO_{(g)}} RT}{V_{pore,0}} - 1 \\ 0 & 0 & \dfrac{-4K_{eq,CO_{2(g)}} n_{CO_{(g)}} RT}{V_{pore,0}} - K_{eq,SiO_g} - 1 \\ 0 & -1 & -K_{eq,SiO_g} \end{pmatrix} \tag{145}$$

Equations 143 and 145 are used to create the function *NLeqsetg2*, shown in Figure 4-4. *NLeqsetg2* is used in a gradient based root finding algorithm to evaluate $\boldsymbol{f}$ and $\boldsymbol{J_f}$, given by the variables *eqs* and *jac*, respectively.

```
function [eqs,jac] = NLeqsetg2(speciesIn)
%#codegen
global Keq elements T Vpore
%NLEQSETG2
%     [OUT1,OUT2] = NLEQSETG2(IN1,IN2,IN3,T,VPORE)

%    This function was generated by the Symbolic Math Toolbox version 6.0.
%    19-Sep-2014 14:48:58

C = speciesIn(:,1);
COg = speciesIn(:,3);
Ct = elements(:,1);
Keq1 = Keq(:,1);
Keq2 = Keq(:,2);
Ot = elements(:,2);
SiC = speciesIn(:,2);
Sit = elements(:,3);
t2 = COg.^2;
t3 = 1.0./Vpore;
eqs = [-C-COg+Ct-SiC-Keq2.*T.*t2.*t3.*8.205746000000001e1;-COg+Ot-COg.*...
    Keq1-Keq2.*T.*t2.*t3.*1.6411492e2;-SiC+Sit-COg.*Keq1];
if nargout > 1
    jac = reshape([-1.0,0.0,0.0,-1.0,0.0,-1.0,COg.*Keq2.*T.*t3.*...
        (-1.6411492e2)-1.0,-Keq1-COg.*Keq2.*T.*t3.*3.2822984e2-1.0,-Keq1],[3, 3]);
end
```

Figure 4-4: The NLeqsetg2 MATLAB function generated from symbolic expressions used for calculating the C, SiC, and CO_2. Global variables provide the additional constraints to respect the structure needed by root finding algorithms.

Equations 131 and 132, representing symbolic gas substitution expressions, are used to generate the function *TotalSol2* shown in Figure 4-5.

```
function speciesOut = TotalSol2(speciesIn,Keq,T,Vpore)%#codegen
%TOTALSOL2
%    SPECIESOUT = TOTALSOL2(SPECIESIN,KEQ,T,VPORE)

%    This function was generated by the Symbolic Math Toolbox version 6.0.
%    19-Sep-2014 14:48:59

C = speciesIn(:,1);
COg = speciesIn(:,4);
Keq1 = Keq(:,1);
Keq2 = Keq(:,2);
SiC = speciesIn(:,2);
speciesOut = [C,SiC,0.0,COg,(COg.^2.*Keq2.*T.*8.205746000000001e1)./Vpore,COg.*Keq1];
```

Figure 4-5: The TotalSol2 MATLAB function generated from symbolic expressions used for calculating the CO_2 and SiO gas composition. The speciesOut array is the complete equilibrium composition solution for Regime 2.

The solution to the modified chemical regime equilibrium constraint equations computed using *NLeqsetg2* is used as input into *TotalSol2* to compute the remaining gas species that were explicitly removed from the modified equations.

4.4 Generating Chemical Regime Equilibrium Functions: Method 2

Under certain circumstances it is possible to directly approximate the equilibrium composition for a chemical regime rather than having to solve a set of constraint equations. This is possible whenever the stoichiometric equations for a chemical regime can be written with only one gas species per reaction. The necessary and sufficient conditions for *a priori* prediction of when a chemical regime will satisfy these requirements is difficult to determine because of the interplay between the number of condensed and gas species and the elemental species of which they are comprised. However, a general heuristic is that the number of condensed species has to at least equal to the number of gas species. This may not hold generally, but is consistent with the chemical regimes discussed in this thesis.

This section will outline the procedure to generate the functions for direct approximation of the equilibrium composition for the chemical regime 1, {C, SiC, SiO_2, $CO_{(g)}$, $CO_{2(g)}$, $SiO_{(g)}$}. This chemical regime represents the chemical regime that is used in the section outlining the process for generating the activity checks. There are many

similarities between the previous method, Method 1, and this method, Method 2, for generating the chemical regime equilibrium functions, therefore some details will be omitted.

4.4.1 Element Abundance and Mass Balance Expressions

The goal of this process is to isolate one gas species per stoichiometric reaction. The chemical species should be ordered with the gas species preceding the condensed species. A suitable ordering of the chemical regime, ($SiO_{(g)}$, $CO_{2(g)}$, $CO_{(g)}$, C, SiC, SiO_2). The element abundance matrix for this species ordering is

	$SiO_{(g)}$	$CO_{2(g)}$	$CO_{(g)}$	C	SiC	SiO_2
C	0	1	1	1	1	0
O	1	2	1	0	0	2
Si	1	0	0	0	1	1

(146)

This element abundance matrix can be used to generate the same set of expressions representing the mass balance constraints given by Equations 118, 119, and 120.

4.4.2 Stoichiometry

The next step is create the canonical stoichiometric matrix from the element abundance matrix. Again, this requires computing the reduced row echelon form of the transposed null space matrix for the element abundance matrix. The result of that procedure yields the matrix

	$SiO_{(g)}$	$CO_{2(g)}$	$CO_{(g)}$	C	SiC	SiO_2
Rx 1	1	0	0	$\frac{1}{2}$	$-\frac{1}{2}$	$-\frac{1}{2}$
Rx 2	0	1	0	-2	1	-1
Rx 3	0	0	1	$-\frac{3}{2}$	$\frac{1}{2}$	$-\frac{1}{2}$

(147)

This produces a matrix with three independent rows that represent the three stoichiometric equations

$$\frac{1}{2}SiC + \frac{1}{2}SiO_2 = SiO_{(g)} + \frac{1}{2}C \tag{148}$$

$$2C + SiO_2 = CO_{2(g)} + SiC \tag{149}$$

$$\frac{3}{2}C + \frac{1}{2}SiO_2 = CO_{(g)} + \frac{1}{2}SiC \tag{150}$$

where, this procedure has ensured that each gas species is present in only one stoichiometric reaction.

4.4.3 Reaction Quotients and Equilibrium Constants

The stoichiometric equations are used to create additional constraint equations from thermodynamic relations, following the same conventions described earlier. The stoichiometric equations are used to create a set of reaction quotients for Equations 148, 149, and 150 are

$$K_{eq,SiO_{(g)}} = \frac{p_{SiO}a_C^{\frac{1}{2}}}{a_{SiC}^{\frac{1}{2}}a_{SiO_2}^{\frac{1}{2}}} \tag{151}$$

$$K_{eq,CO_{2(g)}} = \frac{p_{CO_2}a_{SiC}}{a_C^2 a_{SiO_2}} \tag{152}$$

$$K_{eq,CO_{(g)}} = \frac{p_{CO}a_{SiC}^{\frac{1}{2}}}{a_C^{\frac{3}{2}}a_{SiO_2}^{\frac{1}{2}}} \tag{153}$$

4.4.4 Gas Substitution Equations

Each reaction quotient expression can easily be transformed to isolate the individual gas species partial pressures in terms of the condensed activities and the appropriate equilibrium constant. An analogous transformation expression to Equations 106 and 126 is

$$K_{eq} \cdot \prod_{\substack{i \neq gas\ label \\ index}} (a)_i^{-v_i} = p_{\substack{gas\ label \\ index}} \tag{154}$$

The transformed equations corresponding to Equations 151, 152, and 153 are

$$\frac{K_{eq,SiO_{(g)}} a_{SiC}^{1/2} a_{SiO_2}^{1/2}}{a_C^{1/2}} = p_{SiO} \tag{155}$$

$$\frac{K_{eq,CO_{2(g)}} a_C^2 a_{SiO_2}}{a_{SiC}} = p_{CO_2} \tag{156}$$

$$\frac{K_{eq,CO_{(g)}} a_{SiC}^{3/2} a_{SiO_2}^{1/2}}{a_{SiC}^{1/2}} = p_{CO} \tag{157}$$

The assumption that all condensed species in the regime are present and ideal, *i.e.* the activity is equal to unity, yields a direct equality between each gas partial pressure and its associated equilibrium constant. Also applying the ideal gas law produces the *gas substitution equations*

$$n_{SiO_{(g)},1} = \frac{K_{eq,SiO_{(g)}} V_{pore,0}}{RT} \tag{158}$$

$$n_{CO_{2(g)},1} = \frac{K_{eq,SiO_{(g)}} V_{pore,0}}{RT} \tag{159}$$

$$n_{CO_{(g)},1} = \frac{K_{eq,CO_{(g)}} V_{pore,0}}{RT} \tag{160}$$

which can be used to explicitly calculate an approximation to gas species composition. The gas species composition is only an approximation to the true gas species composition because the pore volume used is an approximation based upon the non-equilibrium condensed species composition.

4.4.5 Iterative Chemical Equilibrium Approximation

This section outlines the construction of an iterative approach for calculating the equilibrium species composition for Regime 1. This approach directly approximates the gas species composition using the pore volume from the non-equilibrium condensed species composition and the gas substitution equations. The condensed species composition will change to account for an increase or decrease of elemental species in the gas phase. A change in the condensed species composition will correspondingly change the pore volume. In turn, the updated pore volume is used to iterate this process again to yield a better approximation for the gas and condensed species compositions. This process converges rapidly after a few iterations (one iteration for small deviations from equilibrium) to the equilibrium species composition, similar to Method 1, because the pore volume quickly approaches its correct value after just the first iteration.

The iterative process begins with the known information that includes the non-equilibrium species compositions, the total volume, and temperature, indicated by n_0, V_{total}, and T, respectively. The values for the associated equilibrium constants are calculated at the given temperature using the methods from Appendix IV.ii. The non-equilibrium composition is used to calculate the initial, zeroth approximation to the pore volume

$$V_{pore,0} = V_{total} - \frac{\left(n_{C,0}M_C\right)}{\rho_C} - \frac{\left(n_{SiC,0}M_{SiC}\right)}{\rho_{SiC}} - \frac{\left(n_{SiO_2,0}M_{SiO_2}\right)}{\rho_{SiO_2}} \tag{161}$$

The first approximation for the molar quantity of each gas species is calculated using Equations 158-160 with the initial pore volume approximation from Equation 161. If there is an increase (or decrease) in the molar quantity of the gas species predicted by the equilibrium approximation, this corresponds to an increase (or decrease) of the molar elemental quantities

in the gas phase. The change in gas moles between the first approximation and the initial composition are

$$\Delta n_{SiO_{(g)},1} = n_{SiO_{(g)},1} - n_{SiO_{(g)},0} \tag{162}$$

$$\Delta n_{CO_{2(g)},1} = n_{CO_{2(g)},1} - n_{CO_{2(g)},0} \tag{163}$$

$$\Delta n_{CO_{(g)},1} = n_{CO_{(g)},1} - n_{CO_{(g)},0} \tag{164}$$

The corresponding elemental change is

$$\Delta b_{C,1} = \Delta n_{CO_{(g)},1} + \Delta n_{CO_{2(g)},1} \tag{165}$$

$$\Delta b_{O,1} = \Delta n_{SiO_{(g)},1} + \Delta n_{CO_{(g)},1} + 2\Delta n_{CO_{2(g)},1} \tag{166}$$

$$\Delta b_{Si,1} = \Delta n_{SiO_{(g)},1} \tag{167}$$

The increase (or decrease) in the molar elemental quantities corresponds to a decrease (or increase) in the molar quantity of the condensed species due to chemical reaction in a closed system. The change in the molar quantity of the condensed species, to account for the elemental change, must satisfy

$$\Delta n_{C,1} + \Delta n_{SiC,1} = \Delta b_{C,1} \tag{168}$$

$$2\Delta n_{SiO_2,1} = \Delta b_{O,1} \tag{169}$$

$$\Delta n_{SiC,1} + \Delta n_{SiO_2,1} = \Delta b_{Si,1} \tag{170}$$

The system of Equations 168-170 is inverted to yield

$$\Delta n_{C,1} = \Delta b_{C,1} - \Delta b_{Si,1} + \frac{1}{2}\Delta b_{O,1} \tag{171}$$

$$\Delta n_{SiC,1} = \Delta b_{Si,1} - \frac{1}{2}\Delta b_{O,1} \tag{172}$$

$$\Delta n_{SiO_2,1} = \frac{1}{2}\Delta b_{O,1} \tag{173}$$

which represent the change in the condensed species in terms of the change in the elemental species. The first approximation of the condensed species composition is

$$n_{C,1} = n_{C,0} - \Delta n_{C,1} \tag{174}$$

$$n_{SiC,1} = n_{SiC,0} - \Delta n_{SiC,1} \tag{175}$$

$$n_{SiO_2,1} = n_{SiO_2,0} - \Delta n_{SiO_2,1} \tag{176}$$

Explicit expressions for the first approximation of the condensed species are generated by substitution of Equations 177-178, and subsequently Equations 168-170, into Equations 174-176 to yield

$$n_{C,1} = n_{C,0} - 2\Delta n_{CO_{2(g)},1} - \frac{3}{2}\Delta n_{CO_{(g)},1} + \frac{1}{2}\Delta n_{SiO_{(g)},1} \tag{179}$$

$$n_{SiC,1} = n_{SiC,0} + \frac{1}{2}\Delta n_{CO_{(g)},1} + \Delta n_{CO_{2(g)},1} - \frac{1}{2}\Delta n_{SiO_{(g)},1} \tag{180}$$

$$n_{SiO_2,1} = n_{SiO_2,0} - \frac{1}{2}\Delta n_{CO_{(g)},1} - \Delta n_{CO_{2(g)},1} - \Delta n_{SiO_{(g)},1} \tag{181}$$

Thus, Equations 158-160 and 179-181 are the first approximation for the equilibrium species compositions. These approximate values can be used update the pore volume using

$$V_{pore,1} = V_{total} - \frac{\left(n_{C,1}M_C\right)}{\rho_C} - \frac{\left(n_{SiC,1}M_{SiC}\right)}{\rho_{SiC}} - \frac{\left(n_{SiO_2,1}M_{SiO_2}\right)}{\rho_{SiO_2}} \tag{182}$$

This procedure can be iterated to refine the equilibrium species compositions as the pore volume converges to its true value.

The equations describing the step by step iterative approach to calculating equilibrium for this regime are only shown to describe the method. The necessary algebraic construction is only performed once using symbolic programming techniques to produce expressions, which are then used to generate functions to evaluate the pore volume and species compositions. The expression representing Equation 161 is used to generate the function, *VporeUpdate,* to calculate the pore volume.

```
function Vpore = VporeUpdate(speciesIn,Vtotal)%#codegen
%VPOREUPDATE
%    Vpore = VPOREUPDATE(speciesIn,VTOTAL)

%    This function was generated by the Symbolic Math Toolbox version 6.0.
%    19-Sep-2014 14:49:06

C = speciesIn(:,1);
SiC = speciesIn(:,2);
SiO2 = speciesIn(:,3);
Vpore = C.*(-5.719380952380952)-SiC.*1.249102803738318e1-SiO2.*2.731104545454545e1+Vtotal;
```

Figure 4-6: VporeUpdate is a MATLAB function generated from symbolic expressions to calculate the pore volume.

The expressions representing Equations 158-160 and 179-181 are used to generate the function, *TotalSol1,* to calculate the updated species compositions.

```
function speciesOut = TotalSol1(speciesIn,Keq,T,Vpore)%#codegen
%TOTALSOL1
%    SPECIESOUT = TOTALSOL1(SPECIESIN,KEQ,T,VPORE)
%    This function was generated by the Symbolic Math Toolbox version 6.0.
%    19-Sep-2014 14:48:58

C = speciesIn(:,1);
CO2g = speciesIn(:,5);
COg = speciesIn(:,4);
Keq1 = Keq(:,1);
Keq2 = Keq(:,2);
Keq3 = Keq(:,3);
SiC = speciesIn(:,2);
SiO2 = speciesIn(:,3);
SiOg = speciesIn(:,6);
t2 = 1.0./T;
t3 = Keq1.*Vpore.*t2.*6.093291213254712e-3;
t4 = SiOg.*(1.0./2.0);
t5 = Keq2.*Vpore.*t2.*1.218658242650942e-2;
t6 = Keq3.*Vpore.*t2.*6.093291213254712e-3;
speciesOut = [C+CO2g.*2.0+COg.*(3.0./2.0)-SiOg.*(1.0./2.0)+t3-Keq2.*Vpore.*t2.*...
    2.437316485301885e-2-Keq3.*Vpore.*t2.*1.827987363976413e-2,-CO2g-COg.*...
    (1.0./2.0)+SiC-t3+t4+t5+t6,CO2g+COg.*(1.0./2.0)+SiO2-t3+t4-t5-t6,Keq3.*...
    Vpore.*t2.*1.218658242650942e-2,t5,Keq1.*Vpore.*t2.*1.218658242650942e-2];
```

Figure 4-7: TotalSol1 is a MATLAB function generated from symbolic expressions to calculate updated species compositions for each iteration; speciesIn and speciesOut are the non-equilibrium and equilibrium species composition approximations, respectively.

VporeUpdate and *TotalSol1* are then evaluated sequentially to calculate the initial pore volume and use that value to get the updated species compositions.

4.5 Chemical Equilibrium Solution Algorithm

The previous sections of this chapter have shown how to construct the components (*i.e.* functions) necessary for computing and checking the thermodynamic chemical equilibrium composition of a closed chemical system by model reduction. Once the components for all the chemical regimes have been generated for a particular chemical system, they can be evaluated systematically, checking after each attempted solution if the proposed equilibrium composition satisfies the activity checks and the mass balance constraints. An outline of the procedure used for calculating the equilibrium species composition and pore volume, n_{eq} and V_{pore}, is shown in Figure 4-8, using the current temperature, total volume, and non-equilibrium species composition given by T, V_{total}, and $n_{non\text{-}eq}$, respectively.

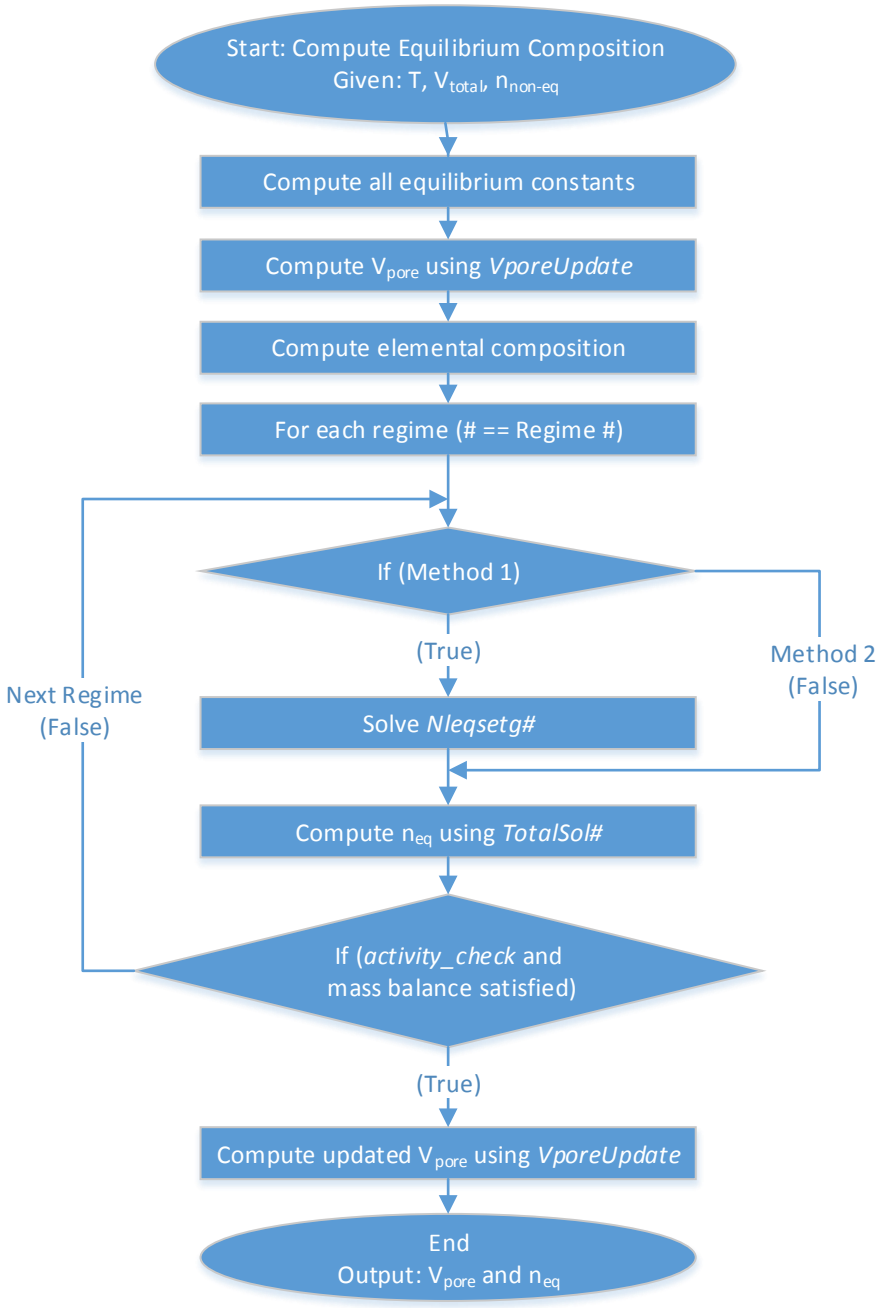

Figure 4-8: Flowchart outlining a procedure to calculate the equilibrium species composition using the chemical regimes for model reduction

The algorithm presented in Figure 4-8 is sufficient for calculating the equilibrium species composition for a closed chemical system. This process can be iterated using the output solution as the new input until the output converges to ensure the equilibrium composition is correct. Despite it being a sufficient algorithm, it is not an efficient algorithm for the large number of

evaluations needed for the gas transport model and does not handle numerical inaccuracies in the solution process. A more robust and complicated algorithm is actually implemented for the gas transport model. The additional features not presented include the caching of the output of computations and logic to handle inaccuracies inherent in numerical computations.

4.5.1.1 *Difficulties Coupling Chemical Equilibrium Reaction and Transport*

The solution algorithm shown in this chapter is applicable to most general chemical sets. However, there is the potential for numerical difficulties to arise when using any coupled sequentially iterated approach to calculating transport and reaction.[51, 78, 80] This problem is inherently linked to the large difference in the time scales of the transient behavior of the chemical species involved. For instance, the flux of gas happens at a much faster rate than the change in the condensed species composition. If an appropriately small time step is not used to calculate the numerical solution then oscillations in the solution may occur or a negative quantity of species may be predicted.

This type of problem arises when attempting to simulate the complete SiO_2 removal from a porous medium composed of species from the {C, SiC, SiO_2, $CO_{(g)}$, $CO_{2(g)}$, $SiO_{(g)}$} chemical set with an insufficient amount of C to fully reduce SiO_2. This results in regions with no free carbon and corresponds to regime 5 in Appendix I.vi. As some regions are depleted of C it produces local gradients in the gas behavior. If the time step is overestimated, then influx of gas to the region can cause oscillations in the behavior of the condensed species, where they may be precipitated or dissolved between successive time steps and is clearly a numerical artifact. Due to the rapid transient behavior of the gas flux, a small time step is mandated to fully resolve this behavior but the complete oxide removal still occurs over a much longer time scale. Due to computational limitations, the specific case of SiO_2 removal with insufficient C was not fully simulated using the current approach, although the chemical equilibrium model is able to

calculate the correct equilibrium composition when only SiC, SiO_2, $CO_{(g)}$, $CO_{2(g)}$, and $SiO_{(g)}$ are present.

The emergence of such problems can be handled in a few different ways. Firstly, a brute-force approach is to use appropriately small time steps which necessitates multiple parallel processors be used to solve the problem in a reasonable time frame.[50, 51, 78] Secondly, the coupled problem can be reformulated to take advantage of more advanced implicit time stepping algorithms, requiring the solution of large system of equations at each step.[80] Lastly, special knowledge about the system being studied can be used to explicitly hand modify a general solution algorithm to address numerical difficulties.

4.6 Chemical Equilibrium Model Conclusions

This chapter has presented a novel way to solve the problem of calculating the thermodynamic chemical equilibrium composition of a closed system by model reduction. Algorithms to construct and solve the equilibrium composition for the chemical regimes, representing the sub-problems, were presented using the chemical set {C, SiC, SiO_2, $CO_{(g)}$, $CO_{2(g)}$, $SiO_{(g)}$} as an example. A method was shown which generates functions for checking the activity of each condensed species using the proposed equilibrium gas species composition. Together with checking that mass was conserved during equilibration, the activity check ensures that the solution to the chemical regime sub-problem is the correct solution to the larger problem of the chemical set. The overall process is general enough for most chemical sets and designed to be automatically generated using symbolic programming techniques for use with the gas transport and reaction model.

5 Chemical Set 1 Simulations: {C, SiC, SiO_2, $CO_{(g)}$, $CO_{2(g)}$, $SiO_{(g)}$}

The results from simulations studying the transport and reaction in a porous medium comprised of condensed C, SiC, and SiO_2 are presented in this chapter. The chemical species modeled in the simulations are restricted to the chemical set {C, SiC, SiO_2, $CO_{(g)}$, $CO_{2(g)}$, $SiO_{(g)}$}. The porous medium was assumed to be reactive and the gas species produced from chemical reactions are limited to only $CO_{(g)}$, $CO_{2(g)}$, and $SiO_{(g)}$. This chemical set accounts for the initial condensed species present in the porous medium and the gas species with the three largest partial pressure in equilibrium with the condensed species. In reality, the reaction of the condensed and gas species will produce additional chemical species, but these will have only a minor effect on the qualitative and quantitative behavior observed during simulations. Figure 5-1 shows the partial pressures of several gas species in equilibrium with condensed C, SiC, and SiO_2 as a function of temperature. The study of the transport and reaction in porous medium for this chemical set is divided into two categories, those with a constant simulation temperature and those with a time-varying simulation temperature.

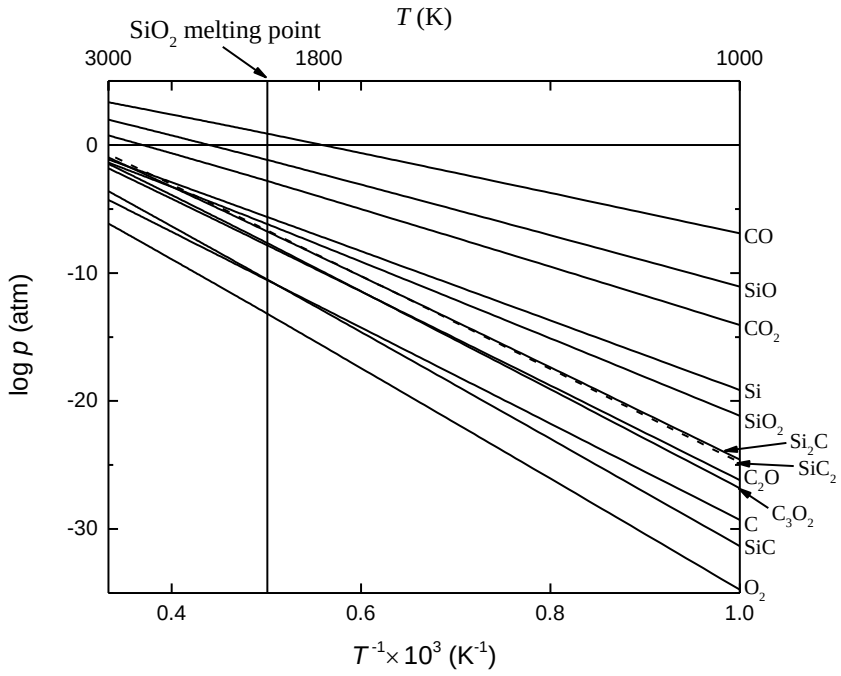

Figure 5-1: Gas pressures as a function of temperature for several species in equilibrium with solid SiC, C, and solid (T < 1996 K) or liquid (T > 1996 K).

The results of the simulations are presented by showing the compositional profile of the condensed species and the pressure profile of the gas species as time increases. It is helpful to represent the compositional profile of each condensed species, at a given time, as the relative percentage change of the condensed species with respect to its starting composition. This immediately quantifies the scale of the change of each species during a simulation, as opposed representing it as a molar composition. Also, by scaling the relative percentage change of each species by its starting molar composition, the overall magnitude of change of each condensed species compared to the others can be distinguished. Using this representation, the compositional profile for SiO_2 is denoted by ΔSiO_2 (%) and the *time for complete oxide removal*, t_c, is when ΔSiO_2 (%) = -100 across the whole porous medium.

The details of the numerical discretization and time stepping algorithm are not presented for each simulation. However, the results of the simulations were confirmed to converge to simulation results using the same parameters, but with a finer spatial and time

discretization. The size of the spatial discretization was kept uniform among the different simulations, that is, simulations corresponding to thicker samples had more discretization points to keep the size of the discretization uniform.

5.1 Physical Constants and Expressions

A number of constitutive models for describing the transport coefficients and constraint equations are used along with the DGM and CEM. Once a chemical set is chosen, the specific material properties associated with the chemical species are needed to complete the model description, excluding specific simulation parameters. These material properties are consistent for any simulation using a particular chemical set. They are separate from the simulation parameters, where the latter include the structure properties of the porous media, the initial chemical composition, and temperature.

For each condensed species, the molar mass (MM), density (ρ), and Gibbs free energy function is required. The Gibbs free energy function for each species is not explicitly listed, but the required data to construct them is provided in Appendix IV.iii. The relevant parameters for C, SiC, and SiO_2 are provide in Table 5-1.

Table 5-1: Material properties for the condensed chemical species from chemical set 1.

Condensed Species	MM ($g \cdot mol^{-1}$)	ρ ($g \cdot cm^{-3}$)
C	12.0107	2.10
SiC	40.0962	3.21
SiO_2	60.0843	2.20

For each gas species, the molecular mass (MM), Lennard-Jones collision diameter (σ), Lennard-Jones reduced potential well depth (ϵ/k_B) , and Gibbs free energy function is required. Again, the Gibbs free energy function for each species is not explicitly listed, but the required

data to construct them is provided in Appendix IV.iii. The relevant parameters for $CO_{(g)}$, $CO_{2(g)}$, and $SiO_{(g)}$ are provide in Table 5-2.

Table 5-2: Material properties for the gas chemical species from chemical set 1.

Gas Species	MM ($g \cdot mol^{-1}$)	σ (Å)	ϵ/k_B (K)
CO	28.0101	3.8	88
CO_2	44.0095	4.5	213
SiO	44.0849	3.6	88

5.2 Category 1: Constant Temperature Simulations (Model Validation)

The goal of this study is to not only to study oxide removal for this system, but to validate the generality of the current modelling framework by comparing the results of this model against the a model developed by Kaza *et al.* specifically for the {C, SiC, SiO_2, $CO_{(g)}$, $CO_{2(g)}$, $SiO_{(g)}$, $O_{2(g)}$} chemical set. The study of the first category, *i.e.* constant temperature simulations, systematically investigated the effect of individually varying the structure properties of the porous medium, the initial chemical composition, and the holding temperature. The individually varied structure properties of the porous medium include the starting porosity, tortuosity, pore radius, and sample thickness. The chemical composition of each species was varied on a mole fraction basis. The compositional variation was designed to have a constant starting molar ratio of C/SiO_2 (= 3.3), to ensure the complete reduction of SiO_2, *i.e.* enough carbon to ensure that it is not exhausted before the SiO_2 anywhere within the body. The simulations were assumed to take place under vacuum conditions, *i.e.* the external gas pressure on the boundary of the porous medium was equal to zero.

The common benchmark for these simulations was the time to remove all of the SiO_2 initially present in the porous medium. This benchmark was chosen because a negligible amount

of reaction and transport will occur after the depletion of all the oxide species since the remaining condensed species have extremely low vapor pressures. From a practical standpoint, it is desirable to identify the removal of all oxide species. An analogous study was conducted by Kaza *et al.*[90] for a similar chemical system. That work was used as a consistency check for comparing and validating the modeling framework designed for this thesis.

A standard set of simulation conditions was chosen to replicate the conditions used by Kaza *et al.* (except for temperature). These parameters are not representative of a particular powder compact nor optimized for sintering, but act as a reference point to which all other simulations could be compared. The parameters for the *standard simulation conditions* for chemical set 1 in category 1 (SSC1) are listed in Table 5-3.

Table 5-3: Standard simulation conditions (SSC1) reference parameter values for chemical set 1.

Parameter	Reference Value
C (X_{C})	3.3 mol %
SiC (X_{SiC})	95.7 mol %
SiO_2 ($X_{\mathrm{SiO_2}}$)	1.0 mol %
Porosity (ε)	0.4
Tortuosity (q)	5
Pore radius (r)	16 nm
Thickness (l)	1 cm
Temperature (T)	1673.15 K

Each of the parameter variations investigated was compared using the time for complete SiO_2 removal as the dependent variable when identifying any functional relationship. This follows the procedure outlined and performed on a similar chemical set by Kaza *et al.*[90] Other than the varied parameter for each systematic variation, the remaining parameters

correspond to the reference parameters; unless otherwise noted. The functional relationships identified were used to create a linearized function, around the SSC1 reference values, that could be used to predict the time for complete oxide removal without explicitly running the corresponding simulation. A set of simulations with multiple parameter variations were chosen and simulated to compare to the linearized model. Additionally, the functional relationships for the varied parameters were compared to the functional relationships observed by Kaza *et al.*[90]

5.2.1 Standard Reference Simulation (SRS1)

The qualitative and quantitative behavior of the standard reference simulation (SRS1) is presented in this section. SRS1 uses the SSC1 values from Table 5-3. The porous medium is assumed to be in a vacuum environment, evacuated of all gas, and heated instantaneously to 1673.15 K. The heating of the porous medium causes the condensed species, which make up the structure of the porous medium, to react and form gas. The reactions are assumed to be instantaneous and stop once the equilibrium composition is reached. Once gas is produced, it flows out of the porous medium due to the external vacuum. The flow of gas causes the local chemical equilibrium to be disturbed, prompting more reaction to occur, and initiating the transport and reaction cycle.

Table 5-4 shows the equilibrium partial pressures of $CO_{(g)}$, $CO_{2(g)}$, and $SiO_{(g)}$ at 1673.15 K for chemical set 1. The most abundant gas is $CO_{(g)}$, followed by $SiO_{(g)}$, and then $CO_{2(g)}$. The ratio of $CO_{(g)}/SiO_{(g)}$ and $CO_{(g)}/CO_{2(g)}$ are approximately 284 and 23133, respectively.

Table 5-4: Equilibrium partial pressures for chemical set 1 at 1673.15 K

Gas Species	p_{eq} (atm)
CO	0.25395
CO_2	1.09775×10^{-5}
SiO	8.92508×10^{-4}

After the initial reaction at the beginning of the simulation, the gas pressure of each species is uniform across the porous medium. It is only after the removal of gas, due to transport out of the porous surfaces, will any further reaction occur. The quantity of SiO_2 begins to deplete as the gas pressure returns to its equilibrium value, because the oxygen must come from the condensed species to replenish the oxygen containing gas species. Since the transport of gas out of the porous medium happens only at the surface and initially that is the only location with any pressure gradient, it is the surface that first is depleted of SiO_2. Figure 5-2 shows the growth of the regions depleted of SiO_2 as a function of time. The simulation stops at 1.06514 h, when all of the SiO_2 is depleted.

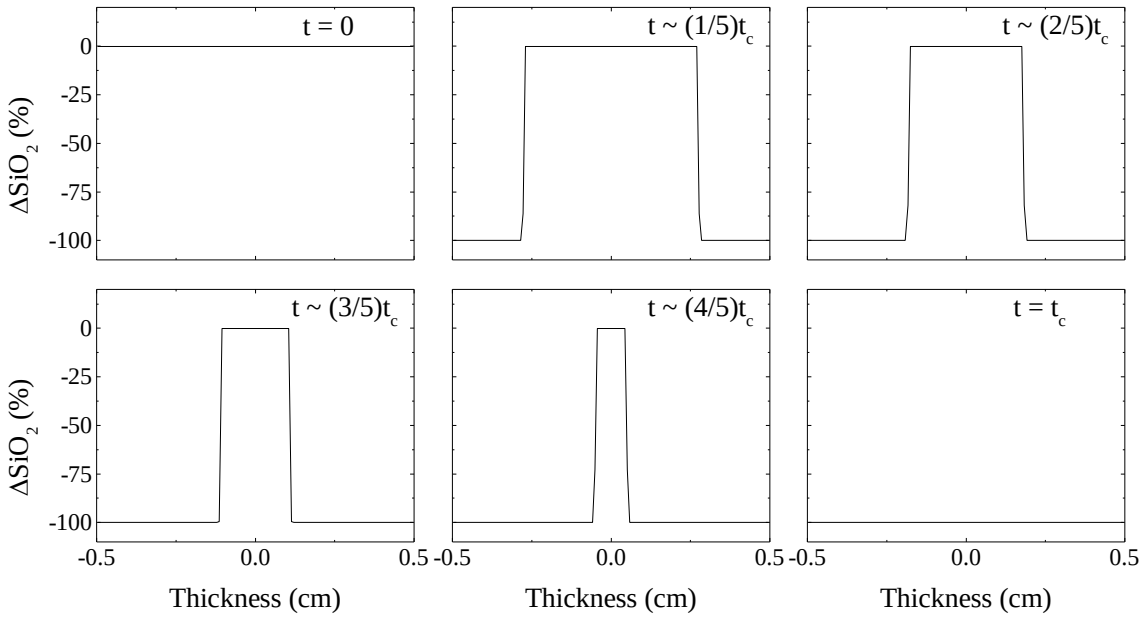

Figure 5-2: Compositional profile of SiO_2 across the porous medium as the simulation time increases up to t_c=1.06514 h. Times shown are in increments of t_c, where t ~ 0, 1/5, 2/5, 3/5, 4/5, and 1 t_c. Simulation conditions are SSC1.

Once the surface is depleted of SiO_2 and the region becomes oxygen deficient, the equilibrium partial pressures begin to vary from those in Table 5-4. The chemical equilibrium in this region corresponds to chemical regime 2 for chemical set 1 in the Appendix I.iii. At this point, the equilibrium gas pressure is no longer uniform across the sample, causing the transport of gas from inside the porous medium to the surface. This causes a local non-equilibrium composition to occur further inside the porous medium, instead of strictly at the surface. Thus, a *reaction front* forms and travels further into the center of the porous medium. There are actually two reaction fronts, each starting at one of the two surfaces.

The reaction front is the point where there is an inflection in the compositional profile of each chemical species. The behavior of the compositional profile before and after the reaction front varies drastically because the thermodynamics of each region is described by a different chemical regime. The change in behavior of the compositional and pressure profile at

the reaction front is specific to each chemical species. The abrupt interface where SiO_2 is depleted from the porous medium, seen in Figure 5-2, is the characteristic behavior of SiO_2 as the reaction front proceeds and there is a switch from chemical regime 1 to regime 2.

The depletion of SiO_2 is mainly attributed to the transport of $CO_{(g)}$ out of the surfaces of the porous medium. The time evolution of the $CO_{(g)}$ partial pressure profile is shown in Figure 5-3. There is an approximately linear variation in the $CO_{(g)}$ pressure from the surface up to the reaction front and then remains constant until reaching the reaction front originating from the opposite surface. The slow movement of the reaction front establishes approximately quasi-static diffusion conditions. Kaza *et al*.[90] observed that even though the DGM is non-Fickian, *i.e.* the effective diffusion coefficient of each species is not independent of pressure, the gas diffusion behavior is approximately Fickian. Analogous to quasi-static Fickian diffusion, the $CO_{(g)}$ pressure decreases linearly from that at the reaction front to the pressure at the surface. Comparing Figure 5-2 and Figure 5-3, it is clear that the region with the constant $CO_{(g)}$ pressure gradient coincides with the depleted SiO_2 region.

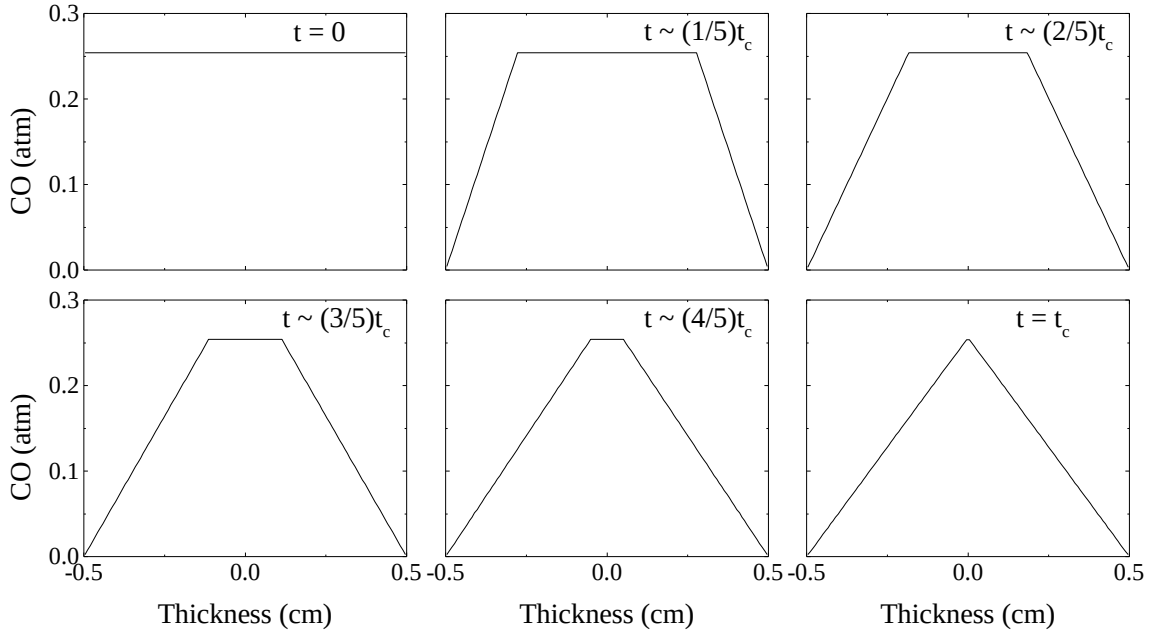

Figure 5-3: Partial pressure profile of $CO_{(g)}$ across the porous medium as the simulation time increases up to t_c=1.06514 h. Times shown are in increments of t_c, where t ~ 0, 1/5, 2/5, 3/5, 4/5, and 1 t_c. Simulation conditions are SSC1.

The pressure gradient is the driving force for the transport of $CO_{(g)}$ from inside the porous medium to the surface, where it is removed from the sample. As the reaction front proceeds with time, the depleted region becomes larger but the pressure at the center of the body remains constant, so the gradient is not as steep. The rate of gas removal is highly sensitive to the magnitude of the pressure gradient. Figure 5-4 shows the effusion rate of $CO_{(g)}$ as the simulation time increases. The effusion rate starts at 50.8 $mol \cdot m^{-2} \cdot h^{-1}$ and decreases to 2.3 $mol \cdot m^{-2} \cdot h^{-1}$ at the time all the SiO_2 is removed, followed by a rapid drop to zero. It may not be obvious, but the effusion rate is not asymptotically approaching some non-zero value; if the sample length was infinite, the effusion rate would approach zero.

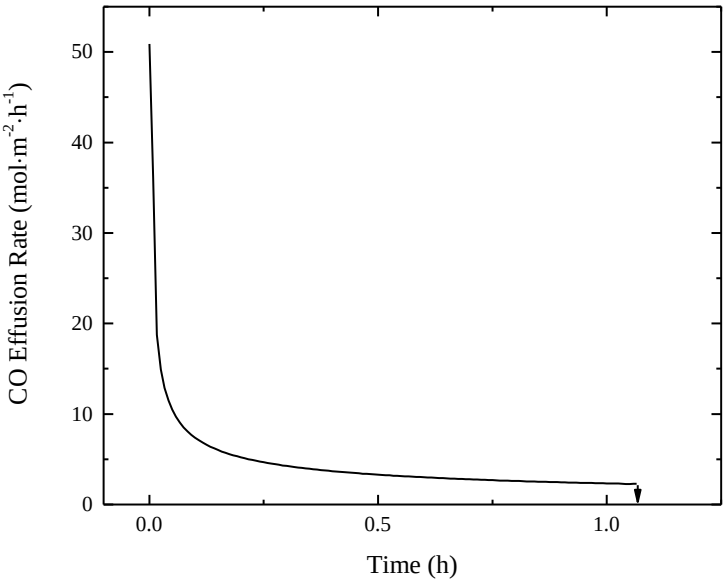

Figure 5-4: Effusion rate of $CO_{(g)}$ as the simulation time increases up to t_c=1.06514 h. Simulation conditions are SSC1.

The effusion rate behavior seen in Figure 5-4 is characteristic of constant temperature simulations which maintain the same maximum pressure throughout the simulation. But the size and location of the regions at the maximum pressure change with time. As a result, the effusion rate is dependent only on the length of the depleted region. Since the depleted region grows in time, the effusion rate always has a maximum at the beginning of the simulation and a minimum at the end of the simulation. It should be noted that if the temperature is not constant, the pressure will change along with the size and location of the depleted regions, resulting in more complicated effusion rate behavior.

Initially, the rate of SiO_2 removal is at a maximum because the effusion rate of $CO_{(g)}$ is at a maximum, resulting in a rapid advance of the reaction front. As the reaction front proceeds, the effusion rate of $CO_{(g)}$ drops and SiO_2 is removed at a slower rate. Accordingly, the rate of advance of the reaction front slows with increasing simulation time. This behavior is evident in Figure 5-2 and Figure 5-3 when comparing the rapid advance of the reaction front between t=0 and t~(1/5)t_c to the relatively slow advance of the reaction front between t~(4/5)t_c and t=t_c.

The rate of advance decreases in an approximately quadratic manner and this effect is shown more clearly later when analyzing the quadratic increase in t_c with sample thickness.

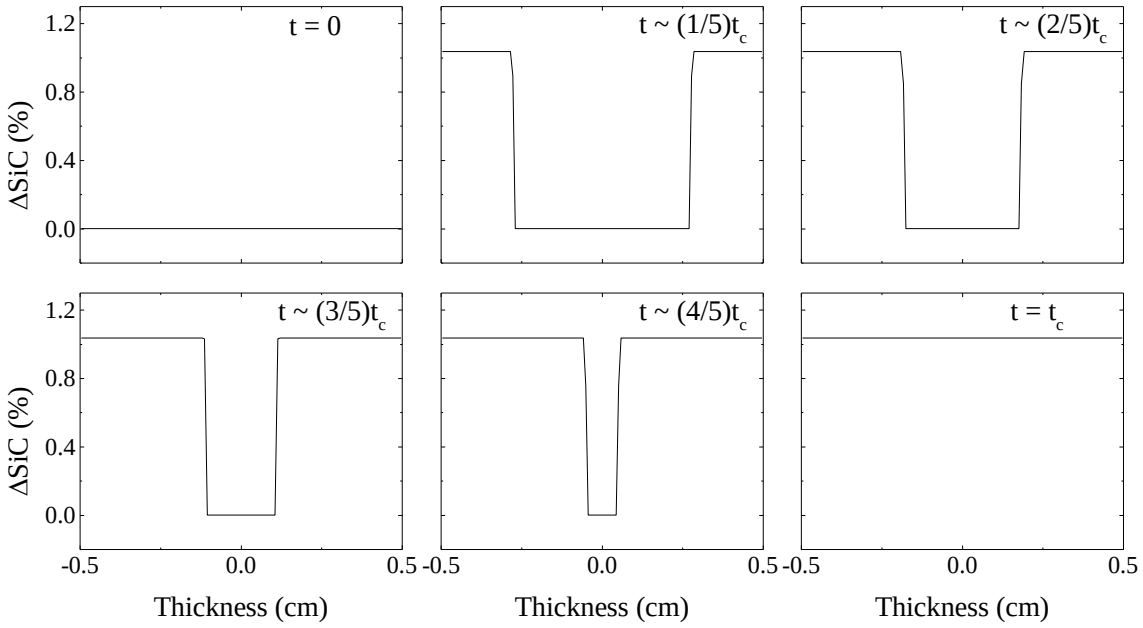

Figure 5-5: Compositional profile of SiC across the porous medium as the simulation time increases up to t_c=1.06514 h. Times shown are in increments of t_c, where t ~ 0, 1/5, 2/5, 3/5, 4/5, and 1 t_c. Simulation conditions are SSC1.

The chemical reaction that depletes SiO_2 and C to form $CO_{(g)}$ also deposits SiC. Figure 5-5 shows how the compositional profile of SiC changes in time as the reaction front proceeds and SiC is deposited. The deposition behavior of SiC in Figure 5-5 is, in a sense, opposite to the depletion behavior of SiO_2 in Figure 5-2. The relative percentage change of SiC was only 1.038 %. This is consistent with the large starting compositions of SiC compared to SiO_2, which were 95.7 and 1.0 mol %, respectively.

The time evolution of the compositional profiles of SiO_2 and SiC, shown frame by frame in Figure 5-2 and Figure 5-5, give a visualization of the reaction behavior. The compositional profiles for SiO_2, C, and SiC are shown concisely in Figure 5-6, with an arrow indicating the progression in time.

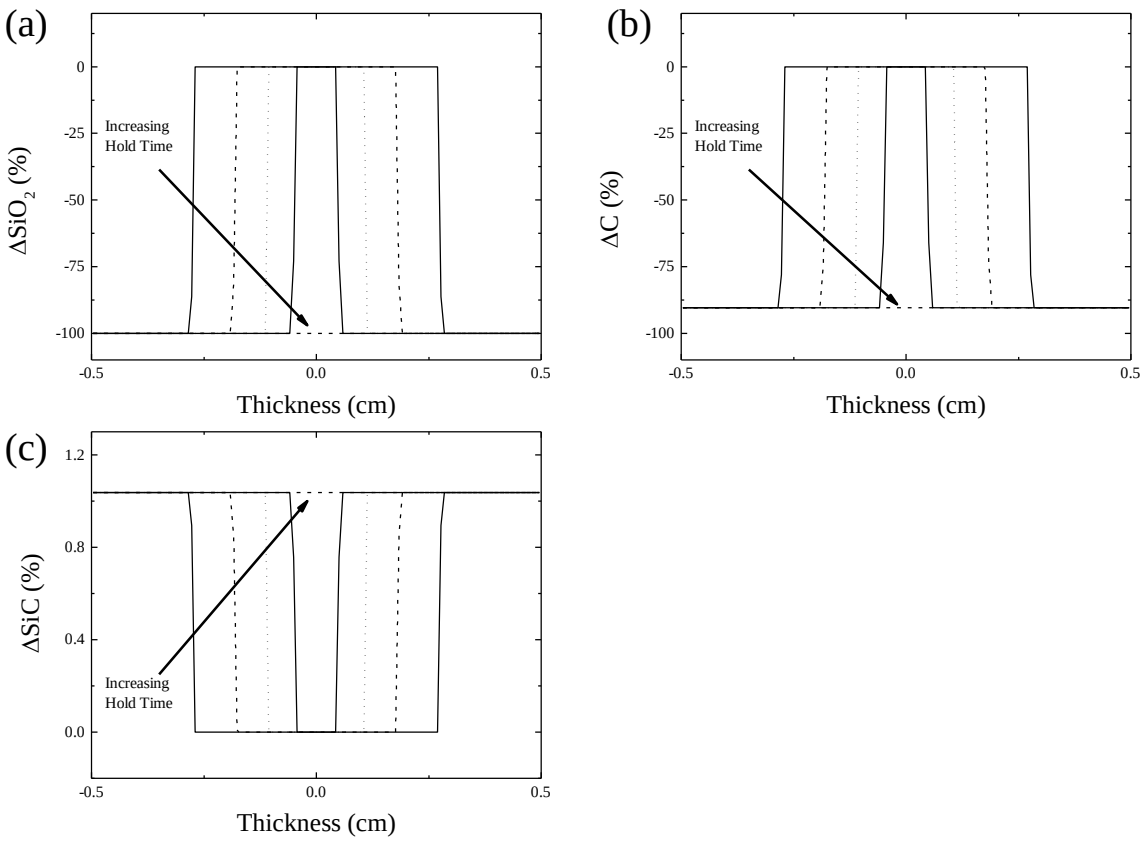

Figure 5-6: Compositional profile of (a) SiO_2, (b) C, and (c) SiC across the porous medium as simulation time increases up to t_c=1.06514 h. Times shown are in increments of t_c, where t ~ 1/5, 2/5, 3/5, 4/5, and 1 t_c. Simulation conditions are SSC1.

The initial amount of carbon, used to remove the SiO_2, was not completely depleted, as indicated in Figure 5-6(b). An initial composition of 3.3 mol % C was an excess amount to fully reduce the 1.0 mol % SiO_2. Figure 5-7(a) shows the residual C profile, as the relative percentage change of C. The amount of carbon was reduced by 90.490 and 90.482 % at the edge and center, respectively. The amount of C depleted, normalized by the starting SiO_2 content, is shown in Figure 5-7(b). Considering only the reaction given by Equation 150, leads to the prediction that the ratio of C/SiO_2, to remove all the SiO_2, should be 3.

The departure from the predicted C/SiO_2 ratio is due to the presence and reaction of the minor secondary gas species, $SiO_{(g)}$ and $CO_{2(g)}$; these effects are small because of the comparatively small partial pressures in relation to $CO_{(g)}$. In the oxygen rich region (regime 1),

SiC and SiO_2 can react to form $SiO_{(g)}$ and deposit C, as seen from the reaction in Equation 122. This acts to decrease the C/SiO_2 ratio slightly. Additionally, a slight reduction in the ratio is attributed to the small partial pressure of $CO_{2(g)}$, which only requires a C/SiO_2 ratio of 2 for SiO_2 removal, evident from the reaction in Equation 123. The $CO_{(g)}/SiO_{(g)}$ ratio is smaller than the $CO_{(g)}/CO_{2(g)}$ ratio, indicating that the $SiO_{(g)}$ has a greater effect on reducing the C/SiO_2 ratio.

The C/SiO_2 ratio is slightly higher at the edges of the sample. The edges of the sample are the first regions to become oxygen deficient (regime 2), as the SiO_2 is depleted. At this initial stage, the C/SiO_2 ratio at the edge is almost the same as the final C/SiO_2 ratio in the center. The $SiO_{(g)}$ from the center of the sample must travel through this region, before being evacuated, and continues to react with the remaining condensed and gas species. The feasible reaction for the oxygen deficient region, given by Equation 122, show that any reaction of $SiO_{(g)}$ consumes C. Thus explaining the slight increase in the C/SiO_2 ratio at the edges of the sample compared to the center.

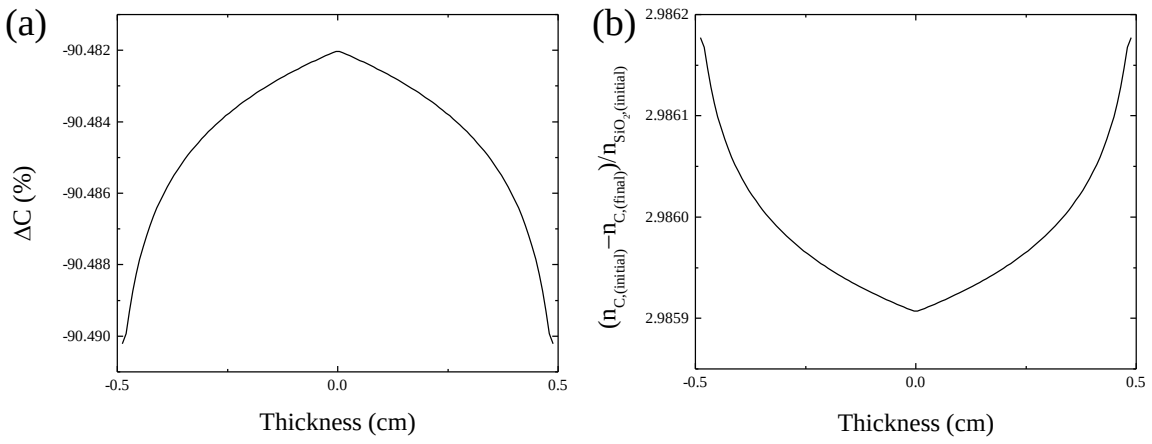

Figure 5-7: Residual C content profile after complete SiO_2 depletion, (a) ΔC (%) (b) C/SiO_2 ratio: change in the number of moles of C normalized by the initial number of moles of SiO_2. *Simulation conditions are SSC1.*

The time evolution of the partial pressure profile for $CO_{(g)}$ was shown frame by frame in Figure *5-3* to give a concrete visualization of transport and reaction behavior. The time evolution of the partial pressure profiles for $CO_{(g)}$, $CO_{2(g)}$, and $SiO_{(g)}$ are shown concisely in Figure 5-8, using

an arrow showing the progression of time. Both, $CO_{2(g)}$ and $SiO_{(g)}$ have a pressure gradient across the oxygen deficient region. The difference in curvature of these gradients can be explained by the thermodynamic conditions of chemical regime 2 for chemical set 1. Equation 131 shows that $n_{CO_{(g)}}^2 \propto n_{CO_{2(g)}}$, indicating the partial pressure profile of $CO_{2(g)}$ is quadratic compared to the $CO_{(g)}$ partial pressure profile. Similarly, Equation 132 shows that $n_{CO_{(g)}} \propto n_{SiO_{(g)}}$, indicating that the partial pressure profile of $SiO_{(g)}$ is linear because it is directly proportional to the $CO_{(g)}$ partial pressure profile.

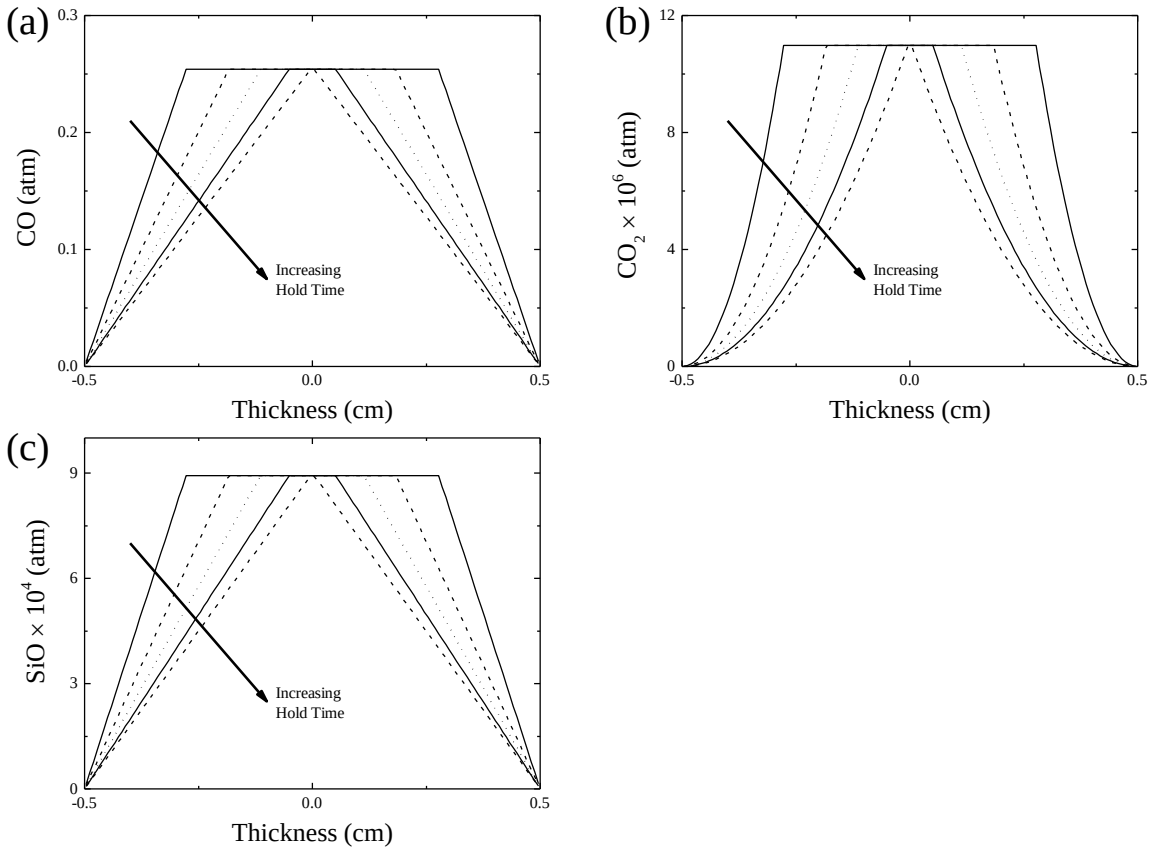

Figure 5-8: Partial pressure profile of (a) $CO_{(g)}$, (b) $CO_{2(g)}$, and (c) $SiO_{(g)}$ across the porous medium as simulation time increases up to t_c=1.06514 h. Times shown are in increments of t_c, where t ~ 1/5, 2/5, 3/5, 4/5, and 1 t_c. Simulation conditions are SSC1.

Characteristics of the condensed and gas species behavior for the standard reference simulation of chemical set 1 were shown in this section. The qualitative behavior associated with

the movement of the reaction front and a transition from chemical regime 1 to regime 2 is representative of simulations where C is present in excess to allow for complete reduction of SiO_2. The remaining simulations involving chemical set 1 were all designed to satisfy this condition. Consequently, the degree of the functional form (*i.e.* linear, quadratic, *etc.*) for each gas partial pressure profile, in the oxygen deficient region, is the same as this standard reference simulation. The rest of the simulations in category 1 investigate changing the simulation parameters and quantifying their effect on the time for complete oxide removal, in comparison to this standard reference simulation.

5.2.2 Effect of Porosity

The effect of porosity on the time for complete oxide removal was studied by varying the porosity, ε, while using the SSC1 in Table 5-3. The porosity was varied from 0.1 to 0.9 in increments of 0.05. Figure 5-9 shows the time required to completely remove all the SiO_2 from the porous medium, as a function of the porosity.

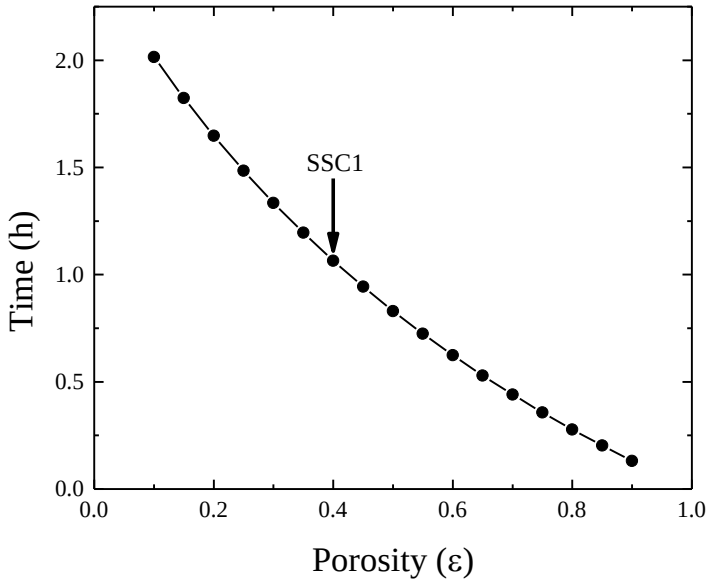

Figure 5-9: Time for complete SiO_2 removal, as a function of porosity.

The time for complete oxide removal was found to decrease as the porosity of the sample increased. This occurs for two reasons. Firstly, as the porosity is increased, the starting molar quantity of the SiO_2 is decreased. The molar amount of each condensed species is implicitly a function of porosity. Simulating a prescribed amount of porosity restricts the volume occupied by the condensed species. Reducing the volume occupied by the condensed species and keeping SiO_2 at 1.0 mol %, reduces the molar quantity of SiO_2. By itself, the reduction in the amount of SiO_2 validates the reduced time needed for complete oxide removal. Secondly, increasing the porosity causes the effective pore volume to increase and the permeability of a real porous medium increases. The DGM accounts for porosity by using effective diffusion coefficients (Equations 79-81), which are directly proportional to the porosity. Thus, increasing the porosity increases the gas diffusivity and subsequently the flux of gas out of the porous medium is increased. A faster removal rate of $CO_{(g)}$ causes the reaction front to advance faster and ultimately leads to shorter times for complete oxide removal.

An attempt was made to linearize the effect of the porosity on the time for complete oxide removal for the data represented by Figure 5-9. Kaza *et al.*[90] showed that the time for complete oxide removal depends linearly on $(1-\varepsilon)/\varepsilon$. However, that linearization expression did not properly linearize the simulation data. It can be seen from Figure 5-10 that the time for complete oxide removal is well described using the expression $(1-\varepsilon)^{3/2}$ to linearize the effect of porosity. The linear regression fit to Figure 5-10 satisfies the equation $y = y_o + a_\varepsilon(1-\varepsilon)^{3/2}$, where $y_o = 0.06116$ h and $a_\varepsilon = 2.22049$ h.

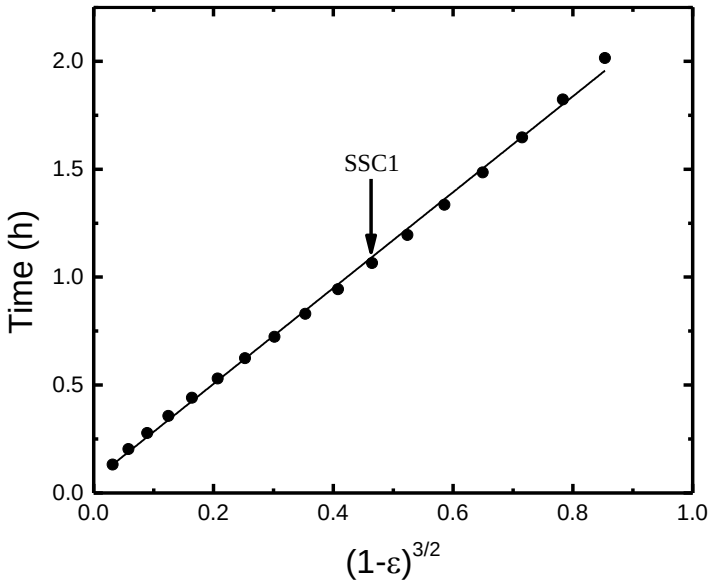

Figure 5-10: Time for complete SiO_2 removal, as a function of the linearized porosity.

It was initially expected that the linearization suggested by Kaza *et al.*[90] should be acceptable for the current model. However, a fundamental difference between the current model and that used by Kaza *et al.*[90] is the treatment of porosity after reaction takes place. The model used by Kaza *et al.*[90] assumes that the amount of porosity prescribed at the beginning of the simulation is constant, even after reaction. The current model accounts for the change in porosity due to reaction. As the reaction front proceeds across the porous medium, the porosity in the oxygen deficient region is increased. This occurs because the reaction of SiO_2 and C

primarily produces $CO_{(g)}$ and SiC. There is a net reduction in the volume of condensed species due to this reaction. It was already mentioned that an increase in porosity would increase the gas flux and shorten the time for oxide removal. It is believed that this effect may account for the discrepancy in the linearization of porosity between the two models.

5.2.3 Effect of Tortuosity

The effect of tortuosity on the time for complete oxide removal was studied by varying the tortuosity, q, while using the SSC1 in Table 5-3. The tortuosity was varied from 1 to 10 in increments of 1. Figure 5-11 shows the time required to completely remove all the SiO_2 from the porous medium, as a function of the tortuosity.

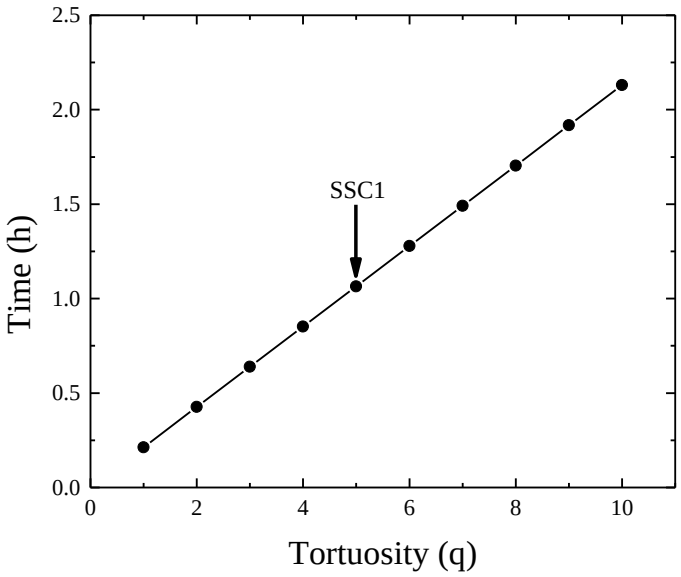

Figure 5-11: Time for complete SiO_2 removal, as a function of tortuosity.

The time for complete oxide removal was found to increase linearly as the tortuosity of the sample increased. The linear regression fit to Figure 5-11 satisfies the equation $y = y_o + a_q q$, where $y_o = 1.42 \times 10^{-7}$ h and $a_q = 0.21303$ h. This behavior is expected because the DGM accounts for the tortuosity by using effective diffusion coefficients (Equations 79-81),

which are inversely proportional to the tortuosity; similar results are shown by Kaza *et al.*[90] Thus, increasing the tortuosity decreases the gas diffusivity and subsequently the flux of gas out of the porous medium is decreased. A slower removal rate of $CO_{(g)}$ causes the reaction front to advance slower and ultimately leads to longer times for complete oxide removal.

5.2.4 Effect of Pore Radius

The effect of pore radius on the time for complete oxide removal was studied by varying the pore radius while using the SSC1 in Table 5-3. The pore radius was varied across the range of sizes including 4, 8, 12, 16, 20, 24, 32, and 40 nm. Figure 5-11 shows the time required to completely remove all the SiO_2 from the porous medium, as a function of the pore radius.

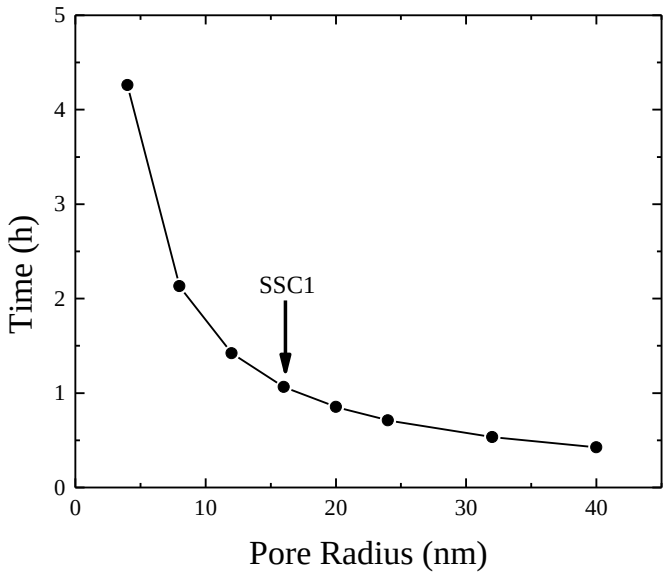

Figure 5-12: Time for complete SiO_2 removal, as a function pore radius.

The time for complete oxide removal was found to decrease non-linearly as the pore radius increases. The effect of the pore radius was linearized by plotting the time for complete oxide removal as a function of the inverse of the pore radius, shown in Figure 5-13 . The linear

regression fit to Figure 5-13 satisfies the equation $y = y_o + a_r r^{-1}$, where $y_o = -8.0928 \times 10^{-7}$ h and $a_r = 17.04363$ h·nm.

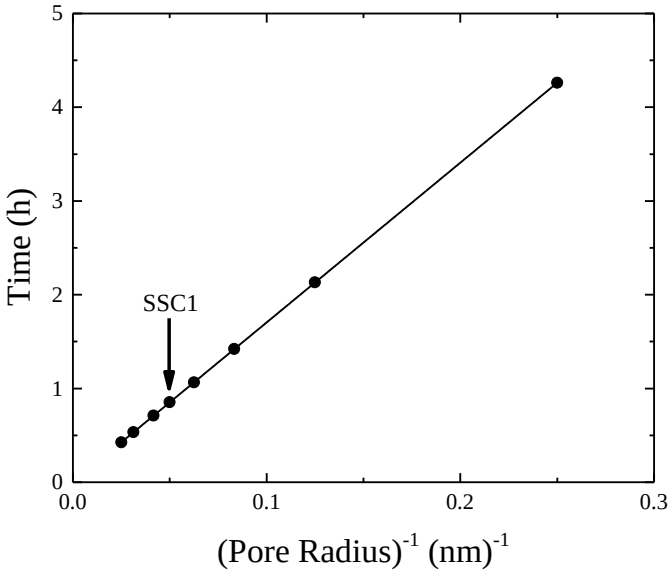

Figure 5-13: Time for complete SiO_2 removal, as a function inverse pore radius.

The effect of the pore radius was incorporated into the DGM using K_o(Equation 55) and B_o (Equation 65) for the Knudsen and viscous flow coefficients, respectively. K_o and B_o have a linear and quadratic dependence on pore radius for a cylindrical pore model, respectively. The inverse linear relationship between the pore radius and the time for complete oxide removal shows that Knudsen diffusion dominates compared to viscous flow for these simulation conditions; similar results are shown by Kaza *et al.*[90] Increasing the pore radius allows for more free-molecule $CO_{(g)}$ transport and subsequently the flux of gas out of the porous medium was increased. A faster removal rate of $CO_{(g)}$ causes the reaction front to advance faster and ultimately leads to shorter times for complete oxide removal.

5.2.5 Effect of Sample Thickness

The effect of sample thickness on the time for complete oxide removal was studied by varying the thickness while using the SSC1 in Table 5-3. The sample thickness was varied across the range of thicknesses including 0.25, 0.5, 0.75, 1, 2, 3, 4, and 6 cm. Figure 5-14 shows the time required to completely remove all the SiO_2 from the porous medium, as a function of the sample thickness.

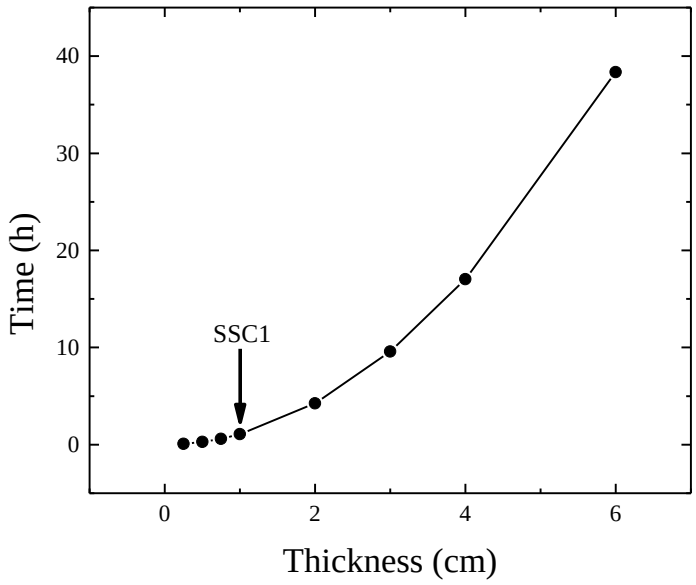

Figure 5-14: Time for complete SiO_2 removal, as a function of the sample thickness.

The time for complete oxide removal was found to increase non-linearly as the thickness increases. The effect of the sample thickness was linearized by plotting the time for complete oxide removal as a function of the square of the sample thickness, shown in Figure 5-13 . The linear regression fit to Figure 5-14 satisfies the equation $y = y_o + a_l l^2$, where $y_o = -1.04025 \times 10^{-7}$ h and $a_l = 1.06514$ h·cm^{-2}.

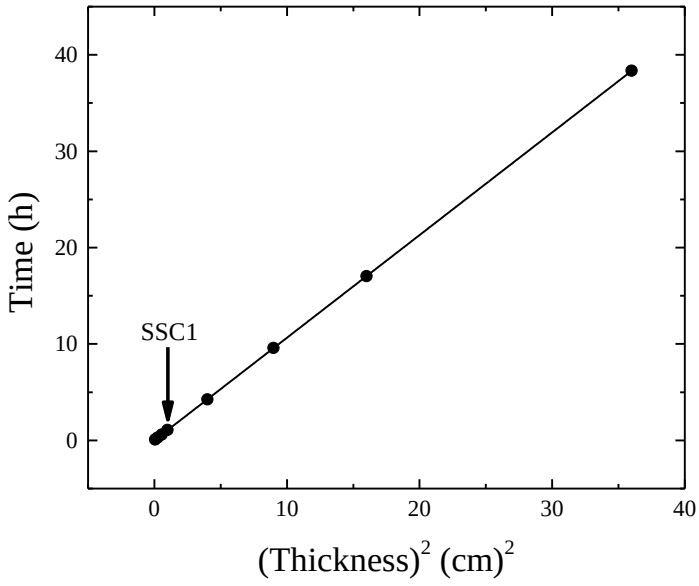

Figure 5-15: Time for complete SiO2 removal, as a function of the square of the sample thickness.

The quadratic dependence of the time for complete oxide removal on the sample thickness was similar to that which would be predicted by simple gas diffusion behavior; similar results are shown by Kaza *et al.*[90] The amount of SiO_2 to be removed increases linearly with sample thickness. However, the $CO_{(g)}$ formed during oxide removal has a greater barrier to evacuation as the sample thickness increases. As observed in the SRS1, the rate of advance of the reaction front decreases, because the pressure gradient reduces causing the effusion rate of $CO_{(g)}$ to decrease, as the front proceeds further into sample. The slowing rate of advance of the reaction front causes the time for complete oxide removal to increase drastically for thick samples.

5.2.6 Effect of Initial SiO_2 Content

The effect of the initial SiO_2 content on the time for complete oxide removal was studied by varying the starting amount of SiO_2. The SSC1 in Table 5-3 were used for all parameters, excluding the initial composition of each species. The initial SiO_2 content was varied across the range including 0.25, 0.5, 0.75, 1, 1.25, 1.5, 2, 2.5, and 3 mol %. The starting molar

ratio of C/SiO_2 was kept constant at 3.3, to ensure the complete reduction of all the starting oxide. The remaining mole percentage of material corresponds to SiC (to equal 100 %). Figure 5-16 shows the time required to completely remove all the SiO_2 from the porous medium, as a function of the initial SiO_2 content. The linear regression fit to Figure 5-16 satisfies the equation $y = y_o + a_{X_{\mathrm{SiO_2}}} X_{\mathrm{SiO_2}}$, where $y_o = 8.66 \times 10^{-3}$ h and $a_{X_{\mathrm{SiO_2}}} = 1.0543$ h (SiO_2 mol %)$^{-1}$.

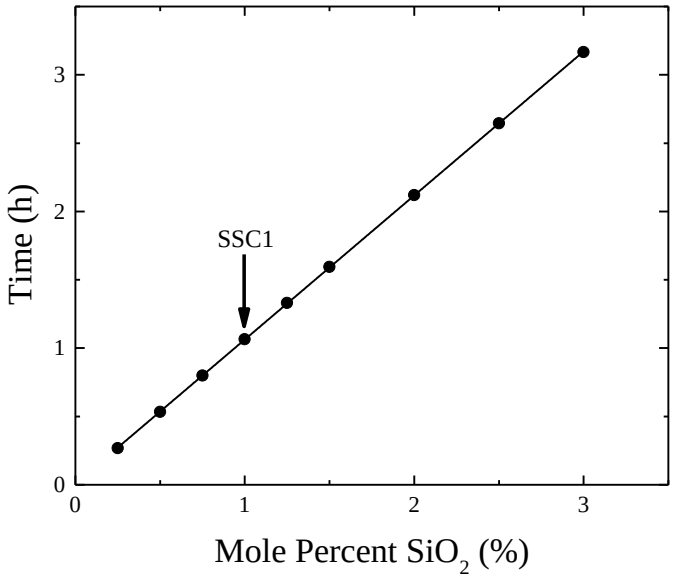

Figure 5-16: Time for complete SiO_2 removal, as a function of the initial SiO_2 content.

The time for complete oxide removal was found to increase linearly as a function of increasing initial SiO_2 content; similar results are shown by Kaza *et al.*[90] The equilibrium gas pressures, in regions of the porous medium described by regime 1, are not dependent on the SiO_2 content. Thus, the pressure gradient across the porous medium, as the reaction front proceeds, is the same as the SRS1. Since all other conditions are equal, the flux of $CO_{(g)}$ is approximately constant for any initial SiO_2 composition, when compared at any location where the reaction fronts between two simulations coincide. Finally, the linear relationship was expected because increasing the starting oxide content linearly scales the total amount of material to be removed (primarily as $CO_{(g)}$), while keeping the flux/reaction front location

correspondence approximately constant, so the time the reaction front spends at each location is linearly increased.

5.2.7 Effect of Holding Temperature

The effect of the holding temperature on the time for complete oxide removal was studied by varying the temperature while using the SSC1 in Table 5-3. The holding temperature was varied from 1573.15 K to 1973.15 K in increments of 50 K. Figure 5-17 shows the time required to completely remove all the SiO_2 from the porous medium, as a function of the holding temperature.

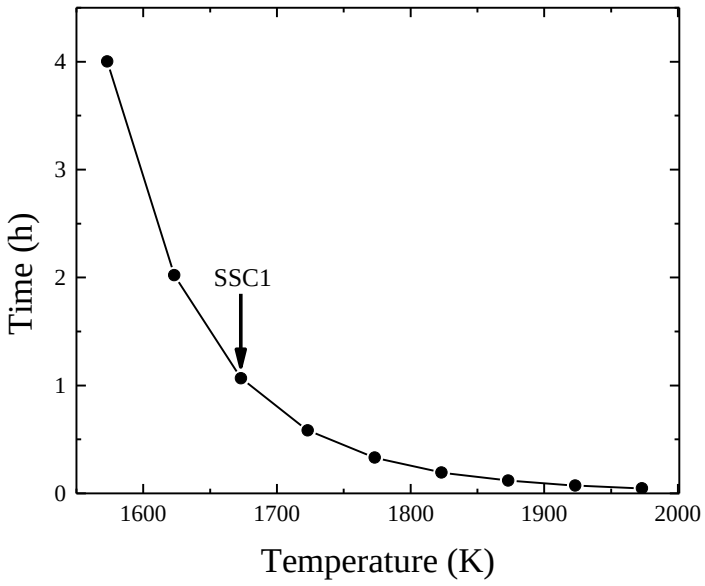

Figure 5-17: Time for complete SiO_2 removal, as a function of the holding temperature.

The time for complete oxide removal was found to decrease non-linearly as the holding temperature was increased. Figure 5-18(a) shows this behavior to be linear when the holding temperature is plotted on a reciprocal scale and the completion time is on a natural logarithm scale. The time for complete oxide removal is linearized by plotting the natural logarithm of the time for complete oxide removal as a function of inverse temperature, shown in Figure 5-18(b).

The linear regression fit to Figure 5-18(b) satisfies the equation $\ln t = \ln t_o + a_T T^{-1}$, where $\ln t_o = -20.6449$ and $a_T = 34651$ K.

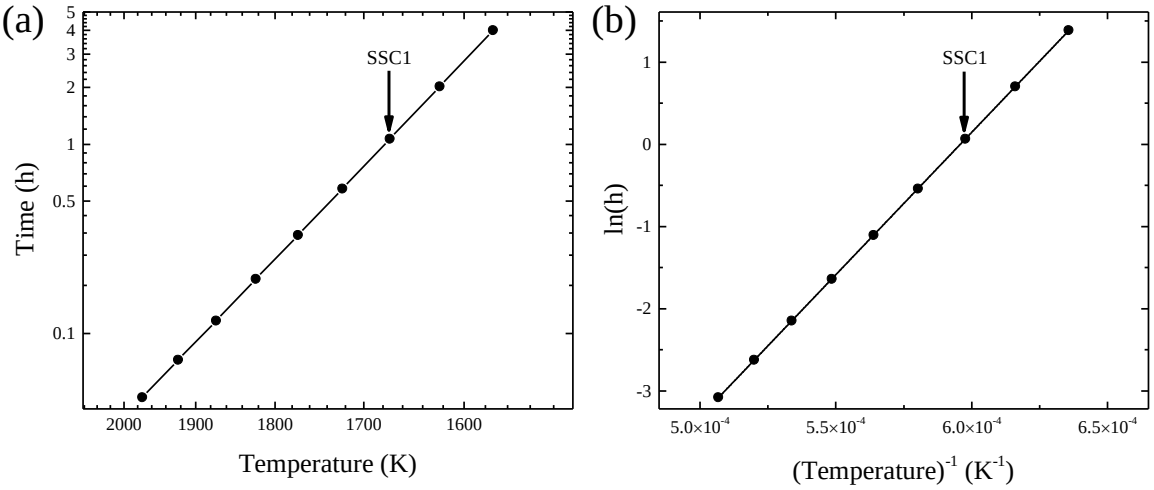

Figure 5-18: (a) Time for complete SiO_2 removal (natural logarithm scale), as a function of the holding temperature (reciprocal scale). (b) Natural logarithm of time for complete SiO_2 removal, as a function of inverse holding temperature.

Increasing the holding temperature does not qualitatively change any aspects of the partial pressure profiles. The equilibrium gas partial pressures at 1823.15 K are given in Table 5-5. Figure 5-19 shows the time evolution of the partial pressure profiles for $CO_{(g)}$, $CO_{2(g)}$, and $SiO_{(g)}$ at 1823.15 K, up to the time for complete oxide removal after 0.19388 h. Comparing Figure 5-8 and Figure 5-19 shows that the partial pressure profiles have the same shape despite being carried out at 1673.15 K and 1823.15 K, respectively. The two sets of plots are almost indistinguishable, up to a scaling of each partial pressure. At 1823.15 K, the ratio of $CO_{(g)}/SiO_{(g)}$ and $CO_{(g)}/CO_{2(g)}$ are approximately 177 and 10564, respectively; a decrease in both compared to 1673.15 K.

Table 5-5: Equilibrium partial pressures for chemical set 1 at 1823.15 K

Gas Species	p_{eq} (atm)
CO	1.45063
CO_2	1.37264×10^{-4}
SiO	8.17807×10^{-3}

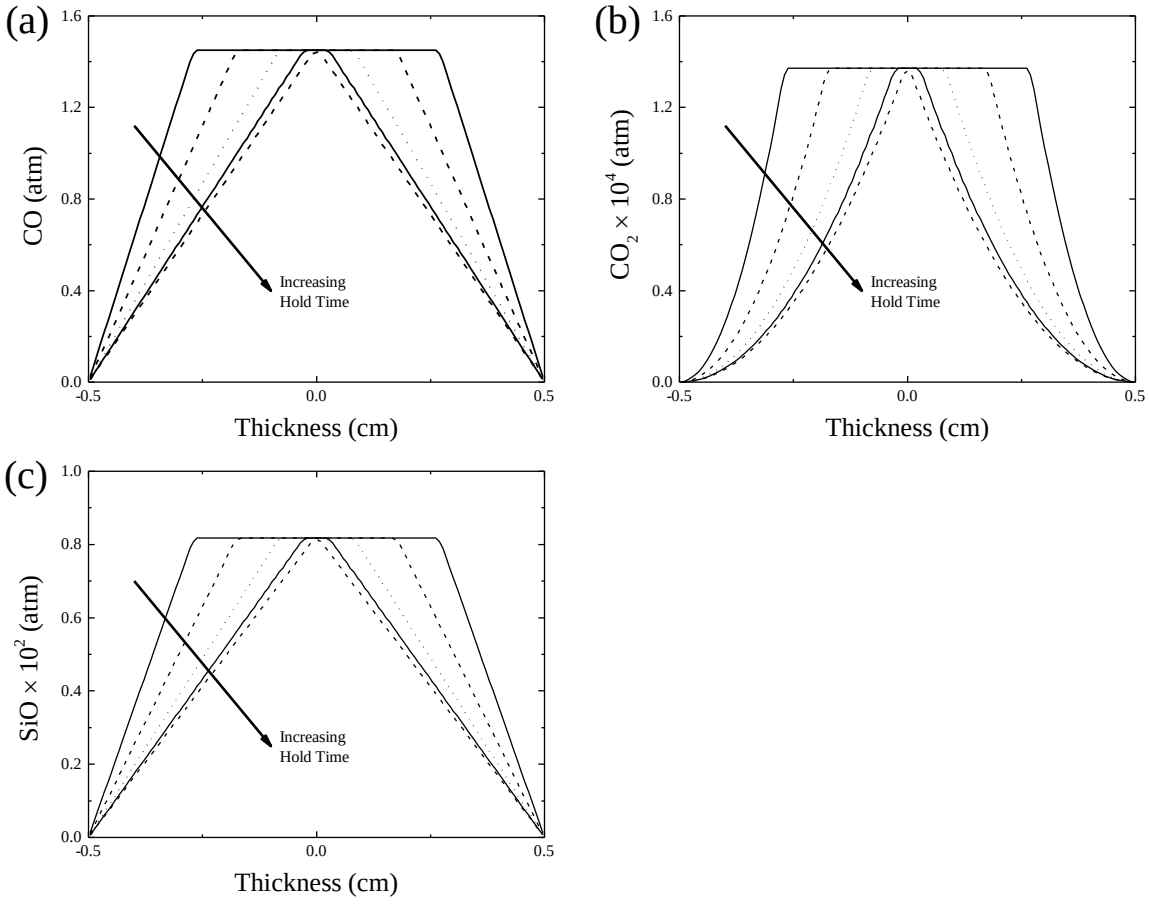

Figure 5-19: Partial pressure profile of (a) $CO_{(g)}$, (b) $CO_{2(g)}$, and (c) $SiO_{(g)}$ across the porous medium as simulation time increases up to t_c=0.19388 h. Times shown are in increments of t_c, where t ~1/5, 2/5, 3/5, 4/5, and 1 t_c. Simulation conditions are SSC1 at 1823.15 K.

Increasing the gas partial pressures results in a larger pressure gradient. Since the pressure gradient is the driving force for the transport $CO_{(g)}$ out of the porous medium, the effusion rate of $CO_{(g)}$ ($J_{CO_{(g)}}$) increases as the holding temperature increases. Figure 5-20 shows

$J_{CO_{(g)}}$ at 1873.15 K as the simulation time increases. The effusion rate starts at 119.2 mol·m^{-2}·h^{-1} and decreases to 12.5 mol·m^{-2}·h^{-1}, followed by a rapid drop to effectively zero. Figure 5-4 and Figure 5-20 allow for a comparison of $J_{CO_{(g)}}$ behavior at 1673.15 K and 1823.15 K, respectively. Both have an initial, very rapid drop in the effusion rate, followed by a very slow decrease of the effusion rate. At t_c, $J_{CO_{(g)}}$ and maximum pressure are 5.47 and 5.71 times greater at the higher temperature hold, respectively. There is no precise scaling relationship between the maximum pressure and the ending effusion rate, but there is a close connection between these two properties.

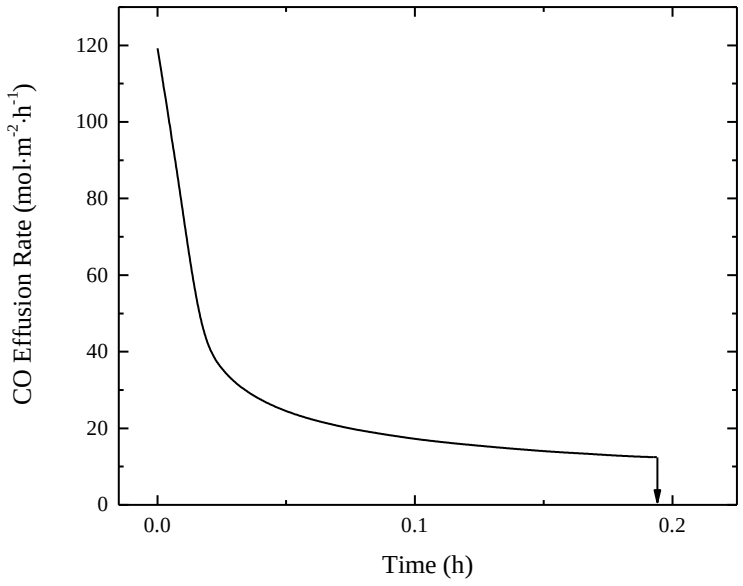

Figure 5-20: Effusion rate of $CO_{(g)}$ as the simulation time increases up to t_c=*0.19388 h*. Simulation conditions are SSC1 at 1823.15 K.

Increasing the holding temperature does not qualitatively change any aspects of the time evolution of the condensed species compositional profiles. Figure 5-21 shows the time evolution of the compositional profile for SiO_2, C, and SiC at 1823.15 K. Comparing Figure 5-6 and Figure 5-21 shows that the compositional profiles are almost quantitatively the same, despite being carried out at 1673.15 K and 1823.15 K, respectively. The relative percentage

change of carbon was −90.49 % and −90.24 % for simulations at 1673.15 K and 1823.15 K, respectively.

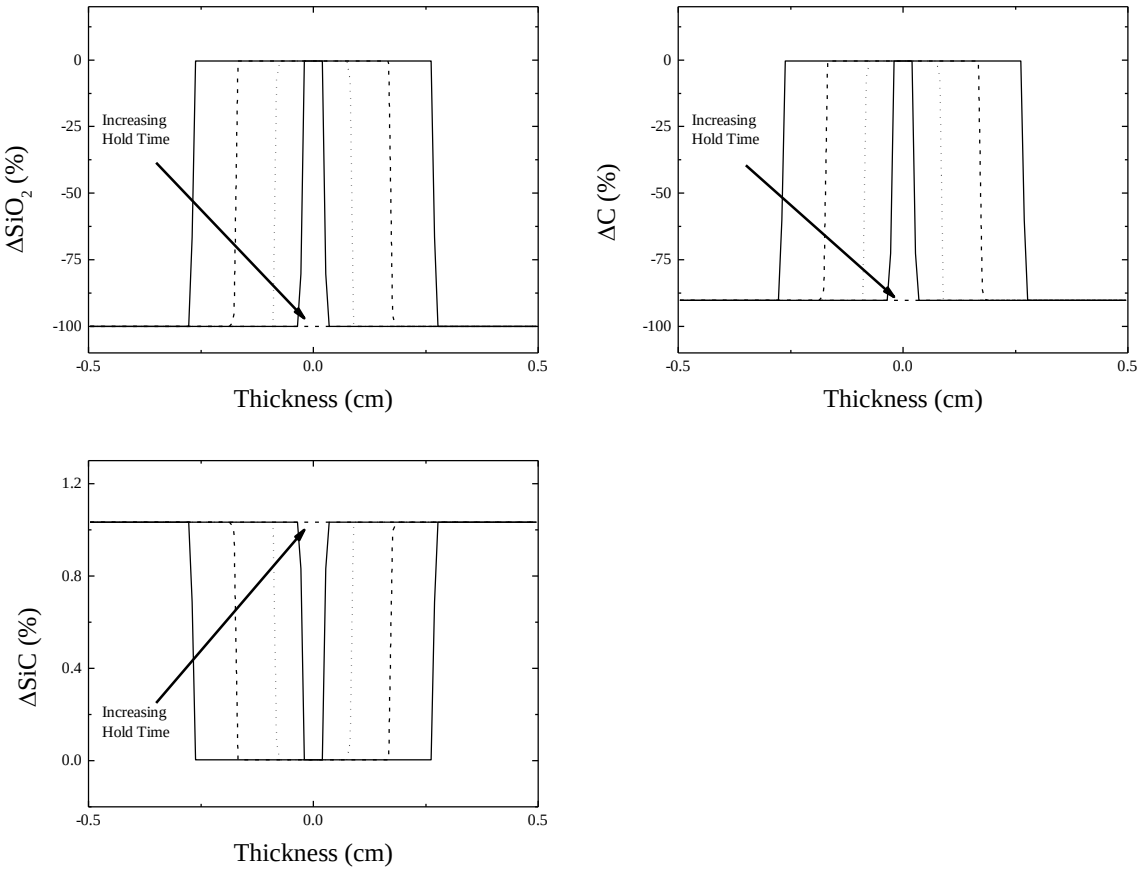

Figure 5-21: Compositional profile of (a) SiO_2, (b) C, and (c) SiC across the porous medium as simulation time increases up to t_c=0.19388 h. Times shown are in increments of t_c, where t ~ 1/5, 2/5, 3/5, 4/5, and 1 t_c. Simulation conditions are SSC1 at 1823.15 K.

For this chemical set, a decrease in the amount of carbon consumed at higher temperatures is mainly a consequence of the decrease in the $CO_{(g)}/SiO_{(g)}$ ratio from 284 to 177 at 1673.15 K and 1823.15 K, respectively. As the $CO_{(g)}/SiO_{(g)}$ ratio decreases, less C is needed to fully reduce all of the starting oxide. Additionally, as the $CO_{(g)}/CO_{2(g)}$ ratio decreases, the amount of C consumed decreases, but to a lesser extent. Even though the $CO_{(g)}/SiO_{(g)}$ ratio is reduced at higher temperatures, the effect on the final carbon content is almost negligible because the $CO_{(g)}/SiO_{(g)}$ ratio is still large.

The C/SiO_2 ratio profile across each sample, at each temperature, resembles the profile shown in Figure 5-7(b). Figure 5-22 shows the variation in the C/SiO_2 ratio at different holding temperatures. The difference between the minimum and maximum C/SiO_2 ratio increases with increasing temperature. Additionally, the standard deviation about the mean C/SiO_2 ratio is skewed toward the minimum. This reflects the higher uniformity near the center (location of the minimum ratio) and sharper gradients towards the edges (location of the maximum ratio).

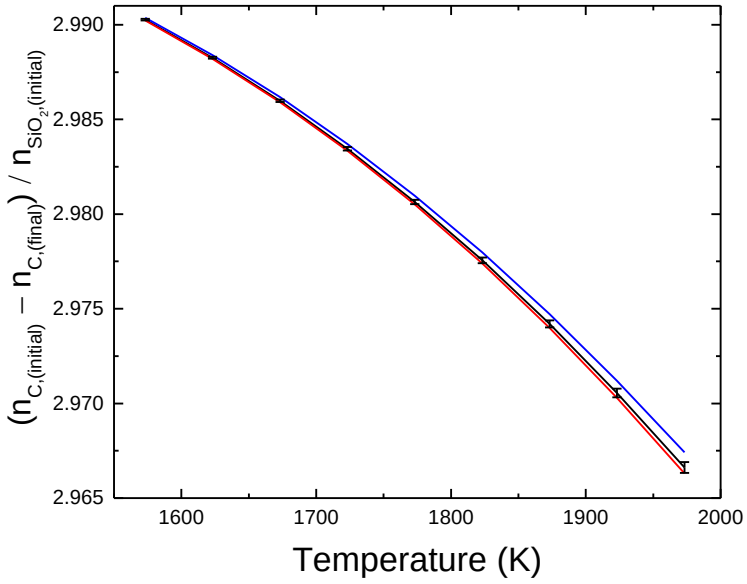

Figure 5-22: C/SiO_2 ratio variation as function of holding temperature: Maximum [Blue, Upper], Mean [Black, Middle], Minimum [Red, Lower], Standard deviation [Range] of the C/SiO_2 ratio across each sample

The change in the $CO_{(g)}/SiO_{(g)}$ ratio also has an effect on the final amount of SiC. The relative percentage change of SiC was 1.038 and 1.033 % for simulations at 1673.15 K and 1823.15 K, respectively. The decrease in the amount of SiC produced was a consequence of consuming more SiC to deplete SiO_2 (regime 1) as $SiO_{(g)}$ was produced. The difference in the relative percentage change was even smaller for SiC compared to C, because the initial amount of SiC was in considerable excess to initial amount of C.

In summary, the time for complete oxide removal appears to have an Arrhenius behavior ($\ln(t_c)$ vs. $1/\mathrm{T}$) with the holding temperature. This result is consistent with the

equilibrium gas pressures also roughly having an Arrhenius dependence ($\ln(p_{eq})$ vs. $1/\mathrm{T}$) on temperature. Increasing the maximum gas pressure, by increasing the hold temperature, results in higher $CO_{(g)}$ effusion rates and faster SiO_2 removal rates. The time for complete oxide removal is mainly controlled by the production and removal of $CO_{(g)}$. The time for complete oxide removal can be modeled effectively by including only $CO_{(g)}$, because the $CO_{(g)}$ pressure dominates over $SiO_{(g)}$ and $CO_{2(g)}$. However, secondary effects, such as the decrease in the C/SiO_2 ratio with increasing holding temperature, are only evident due to the inclusion of minor gas species. The chemical set chosen for these simulations allowed for and provided evidence that varying the holding temperature changed the ratio of the equilibrium gas partial pressures, resulting in a quantifiable change in the final condensed species compositions as shown in Figure 5-22. This is consistent with the experimental observations of property gradients.

5.2.8 Parameter Linearization

The previous sections of category 1 for chemical set 1 have established a standard reference simulation (SRS1) and described the effects of varying the simulation parameters. In all cases, a suitable transformation was found to linearize the dependence of the time for complete oxide removal on each parameter. The slope of the least squares linear regression for each linearized form is proportional to t_c and used to describe the sensitivity to each parameter. Following the approach by Kaza *et al.*[90], a semi-empirical equation can be constructed using a sensitivity parameter based upon the linearization of each model parameter. The t_c for SRS1, t_o, was used to center the linearization using the SSC1 given by Table 5-3. For example, for the dependence on porosity, t_c is proportional to $(1-\varepsilon)^{3/2}$. Its parameter sensitivity is given by b_ε, where $b_\varepsilon = a_\varepsilon/t_o$. This results in an expression of the form $t_o\left(1 + b_\varepsilon \Delta\left[(1-\varepsilon)^{3/2}\right]\right)$ where $\Delta\left[(1-\varepsilon)^{3/2}\right]$ is the difference between $(1-\varepsilon)^{3/2}$ and $(1-\varepsilon_o)^{3/2}$, with ε_o given in Table 5-3.

The linearized forms and parameter sensitivities for all of the independent parameter variations are shown in Table 5-6. Only the temperature sensitivity parameter is not scaled by t_o.

Except for ε and T, all of the linearized expressions coincide with those of Kaza *et al.*[90] The current study and Kaza *et al.*[90] both show an exponential dependence on T with the functional forms given by $t_o \exp\left(b_T \Delta\left[\frac{1}{T}\right]\right)$ and $t_o \exp(b_T \Delta[T])$, respectively. If the functional form of Kaza *et al.*[90] was used in the current study it would only result in a minor deviation because the transformed data was close to linear (with slight systematic curvature). This was not the case with the porosity and using $(1-\varepsilon)/\varepsilon$ to transform the data resulted in a highly nonlinear behavior, instead prompting the use of $(1-\varepsilon)^{3/2}$ to linearize the data.

Table 5-6: Linearized expressions relating the time for complete oxide removal, t_c, to each parameter for chemical set 1

Parameter	Expression for t_c	b_i
Porosity (ε)	$t_o\left(1 + b_\varepsilon \Delta\left[(1-\varepsilon)^{3/2}\right]\right)$	2.0847
Tortuosity (q)	$t_o\left(1 + b_q \Delta[q]\right)$	0.2000
Pore radius (r)	$t_o\left(1 + b_r \Delta\left[\frac{1}{r}\right]\right)$	16.00 nm
Thickness (l)	$t_o(1 + b_l \Delta[l^2])$	1.000 cm^{-2}
SiO_2 (X_{SiO_2})	$t_o\left(1 + b_{X_{SiO_2}} \Delta\left[X_{SiO_2}\right]\right)$	0.9898
Temperature (T)	$t_o \exp\left(b_T \Delta\left[\frac{1}{T}\right]\right)$	34651 K

t_c, takes a value of t_o=*1.06514* h for the SSC1 listed in Table 5-3

Assuming the various parameter dependencies of t_c are weakly coupled allows the linearized expressions from Table 5-6 to be combined into a single equation. The resulting semi-empirical equation describing the simultaneous variation of multiple parameters is given by Equation 183.

$$t_c = t_o\left(1 + b_\varepsilon \Delta\left[(1-\varepsilon)^{3/2}\right]\right) \cdot \left(1 + b_q \Delta[q]\right) \cdot \left(1 + b_r \Delta\left[\frac{1}{r}\right]\right) \times \left(1 + b_l \Delta[l^2]\right) \cdot \left(1 + b_{X_{\mathrm{SiO_2}}} \Delta\left[X_{\mathrm{SiO_2}}\right]\right) \cdot \exp\left(b_T \Delta\left[\frac{1}{T}\right]\right) \quad (183)$$

The assumption that the parameters are weakly coupled was checked by creating sets of simulation conditions that simultaneously vary all of the six parameters. The amount of C was implicitly changed as the amount of starting oxide changed, designed to start at 3.3 times the initial amount of SiO_2. Each parameter was changed such that the t_c was scaled by the same proportion. For example, changing each parameter by an amount such that t_c = 0.5t_o, would mean that the combined effect would reduce the t_c by a factor of 64. Under these conditions, the predicted t_c would be reduced to t_o/64 = 1.66×10^{-2} h; the actual simulation gives a value of 1.74×10^{-2} h. This shows Equation 183 gives a good prediction of t_c even when all the parameters were changed by a large amount, confirming the assumption that the individual parameters are weakly coupled. The sets of simulation conditions, actual simulation times, and the predicted t_c are given in Table 5-7; parameter changes to increase and decrease t_c are both well represented by Equation 183.

Table 5-7: Semi-empirical equation sensitivity test for chemical set 1

Parameter	Reference Value	1.25t_o	0.8t_o	0.5t_o	0.25t_o
SiO_2 ($X_{\mathrm{SiO_2}}$) (%)	1.0	1.2526	0.7979	0.4949	0.2423
Porosity	0.4	0.3008	0.4857	0.6302	0.7774
Tortuosity	5	6.250	4.000	2.500	1.250
Pore radius (nm)	16	12.80	20.00	32.00	63.98
Thickness (cm)	1	1.1180	0.8944	0.7071	0.5000
Temperature (K)	1673.15	1655.3	1691.4	1731.1	1793.2
Actual t_c (h)	1.06514	4.0702	0.2815	1.74×10^{-2}	2.89×10^{-4}
Predicted t_c (h)	1.06514	4.0632	0.2792	1.66×10^{-2}	2.60×10^{-4}

Equation 183 can be used to gain insight into the effect of changing any of the simulation parameters on t_c. This allows for t_c to be predicted without need to explicitly calculate the simulation for every set of experimental parameters. The overall form of the semi-empirical equation is very similar to that of Kaza *et al.*[90] (despite the differences already mentioned) and validates the modeling framework correctly simulates oxide removal behavior for this chemical system. This validation provides confidence that simulations with other process variations can be accurately modeled, some of which are explored in Category 2 (Chapter 5.3).The functional relationships identified also provide guidance when designing the adequate processing conditions needed to account for industrial scaling and/or changing processing parameters resulting from differences in raw materials.

The functional relationships representing each parameter variation's effect on t_c can be used to understand the oxide removal from green bodies made using different powders. Trends for how powder variation changes the porous media parameters were described in Chapter 1.3. In general, using a smaller particle size distribution will cause the porosity and tortuosity to increase while decreasing the pore radius. Additionally, there will tend to be a higher oxide content for smaller particles because the surface area to volume ratio increases. The combined effects due to a decreasing particle size distribution cause t_c to increase. Ultimately, a practitioner can use the functional relationships to predict how the time for complete oxide removal will change when using different powders.

5.3 Category 2: Time-varying Temperature Simulations

The study of the second category, *i.e.* time-varying temperature simulations, investigated the effect of various heating profiles, sample thicknesses, and initial SiO_2 concentrations on the gas effusion behavior during oxide removal. The actual heat treatment of

a sample requires that it undergo some heating cycle to reach the desired temperature. This is in contrast to the previous category of simulations which assumed the porous medium was instantaneously at the holding temperature; a reasonable assumption when the time for complete oxide removal is much longer than the actual amount of time required to heat a sample to the holding temperature. However, instantaneously starting at the holding temperature leads to the artificial characteristic phenomenon of having the highest gas effusion rate at the beginning of the simulation. Samples undergoing a heating cycle that goes from room temperature up to the holding temperature will always have an initial effusion rate close to zero; a consequence of the almost negligible equilibrium gas pressure of $CO_{(g)}$, $CO_{2(g)}$, and $SiO_{(g)}$ at room temperature.

The simulations in category 2 were aimed to produce the same effects of using a real heating cycle by ramping the sample temperature according to pre-defined heating rates. The starting temperature of each simulation was 1173.15 K instead of room temperature. It was observed at this temperature the gas pressures were low enough to keep the gas effusion rate at a negligible level, at which almost no SiO_2 depletion occurs prior to reaching this temperature. Pragmatically, it was computationally efficient to avoid simulating lower temperatures which were determined to be inconsequential to the final outcome.

5.3.1 Practical Considerations and Limitations

A practitioner trying to design a heating schedule to remove all of the oxide from a porous medium will be subject to several constraints when trying to optimize the process. Some of these constraints place limits on the processing of individual samples, while others have a greater impact during the batch processing of numerous samples. It was previously demonstrated that the time for oxide removal can be decreased by using a higher holding

temperature. Possible drawbacks related to using a higher temperature heat treatment include larger internal pressures and pressure gradients, onset of densification, and higher gas effusion rates. Additionally, a constant temperature hold can be an inefficient use of resources when trying to remove all of the oxide.

The green body characteristics and powder properties will determine the maximum internal pressure and pressure gradients that can be sustained before green body rupture and/or the formation of defects. Additionally, the reactivity of the powder will determine the temperature at which the onset of densification will eliminate gas removal pathways, halting the oxide removal process. The furnace used for the heat treatment needs to be of sufficient size to accommodate the gas effusion rate with a vacuum pump capable of keeping the desired vacuum pressure. The vacuum pump capabilities become progressively more important as the number of samples processed in each batch increases, because the overall amount of gas to be removed increases. Due to the complex and varying nature of these constraints, there are no explicit tolerance levels set on these constraints. Rather, the approach is to, at times, assume artificial tolerances and demonstrate simulations can be used to stay within the acceptable range.

Once a heating schedule is optimized for the characteristics of a particular green body, any deviation from these characteristics will change the effectiveness of the heating schedule. These deviations manifest themselves in different ways. For example, if the powder used to produce a green body has a higher initial SiO_2 content, the effusion rate of $CO_{(g)}$ will increase more rapidly than otherwise expected. Furthermore, if the heating schedule is used on a thicker sample, the effusion rate and internal pressure will increase dramatically as the sintering temperature is reached. A change in the porosity, pore radius, and/or tortuosity of a green body will also modify the effectiveness of a heating schedule. While these effects will not be

investigated; the effect of these properties can be inferred from the constant temperature simulations in category 1. Understanding how green body characteristics influence the gas effusion rate and the time for complete oxide removal provides insight into identifying and addressing problems with heating schedules.

5.3.2 Common Simulation Conditions

All of the simulations were started at an initial temperature (T_i) of 1173.15 K with an initial heating rate (HR_i) of 10 K/min up to the holding temperature. The two holding temperature (T_h) choices were 1673.15 K and 1723.15 K. The *holding temperature* is used to indicate the temperature at the end of the initial heating segment. The *holding temperature* may then be qualified by including the description of the new heating rate to be used once the *holding temperature* is reached. For example, this includes scenarios where upon reaching the *holding temperature*, instead of continuing at 10 K/min, the heating rate is changed to 0 K/min, 5 K/min, or even 10 K/min, etc. This provides a consistent way to reference and group the simulations. Table 5-8 lists the equilibrium gas pressures at the starting temperature, holding temperature 1 ($T_{h,1}$), and holding temperature 2 ($T_{h,2}$).

Table 5-8: Equilibrium gas pressures at starting temperature, holding temperature 1, and holding temperature 2

Gas Species	p_{eq} at 1173.15 K (atm)	p_{eq} at 1673.15 K (atm)	p_{eq} at 1723.15 K (atm)
CO	2.686×10^{-5}	0.2540	0.4701
CO_2	2.009×10^{-11}	1.0978×10^{-5}	2.6787×10^{-5}
SiO	8.012×10^{-9}	8.9251×10^{-4}	1.9520×10^{-3}

The initial SiO_2 concentration (X_{SiO_2}) was varied across the range including 1.0 ($X_{SiO_2,1}$) and 1.5 mol % SiO_2 ($X_{SiO_2,2}$). The compositional variation was designed to have a constant starting molar ratio of C/SiO_2 (= 3.3), to ensure the complete reduction of SiO_2. The sample

thicknesses (l) was varied across the range including 1 (l_1), 2 (l_2), and 4 (l_3) cm. The simulations were assumed to take place under vacuum conditions, i.e. the external gas pressure on the boundary of the porous medium was equal to zero. The remaining parameters used to describe the simulation conditions for category 2 of chemical set 1 (SSC1b) are listed in Table 5-9.

Table 5-9: Standard simulation conditions (SSC1b) reference parameter values for category 2 of chemical set 1

Parameter	Reference Value
Porosity (ε)	0.4
Tortuosity (q)	5
Pore radius (r)	16 nm
Initial Temperature (T_i)	1173.15 K
Initial Heating Rate (HR_i)	10 K/min

5.3.3 Standard Reference Simulation - Constant Temperature Hold (SRS1b)

The following simulation was designed to replicate a prototypical heating cycle for SiC production which rapidly heats to an intermediate hold temperature, dwells for a period of time, and then rapidly heats to the sintering temperature. A set of simulation conditions was selected to act as a reference simulation to illustrate the characteristic features of a time-varying temperature simulation. The reference simulation conditions were set to l = 1 cm, X_{SiO_2} = 1.0 %, and T_h = 1673.15 K, with the remaining initial conditions given by SSC1b in Table 5-9. The simulation began at 1173.15 K with a heating rate of 10 K/min for 50 minutes (0.833$\bar{3}$ hours), until T_h was reached. Next, the heating rate was continued at 0 K/min (*i.e.* held at 1673.15 K) for 0.5 hour. Finally, once the hold time had elapsed, the heating rate was continued at 10 K/min until all of the oxide was removed. The simulation conditions were selected so the

hold time was “non-optimized” and inefficient at removing all the oxide, resulting in higher pressures and effusion rates than may be desired.

The simulation was completed after 1.5338 hours, reaching a final temperature of 1793.43 K and maximum $p_{CO_{(g)}}$ of 1.05 atm. The heating profile for the simulation is shown in Figure 5-23. The equilibrium gas partial pressures increase with temperature, $p_{CO_{(g)}}$ increasing by the greatest amount of all the gases. Figure 5-24 shows the time evolution of $p_{CO_{(g)}}$ at the center of the sample during the simulation. The inset graph of Figure 5-24 shows that the initial $p_{CO_{(g)}}$ is extremely low in comparison to later stages of the simulation. The low initial gas pressure lead to there being little gas effusion during the initial stage which, in turn, lead to a negligible amount of oxide removal. Because of this, starting the simulation at a lower temperature would result in a negligible change in the observed behavior. This validates using 1173.15 K as the initial temperature, rather than room temperature.

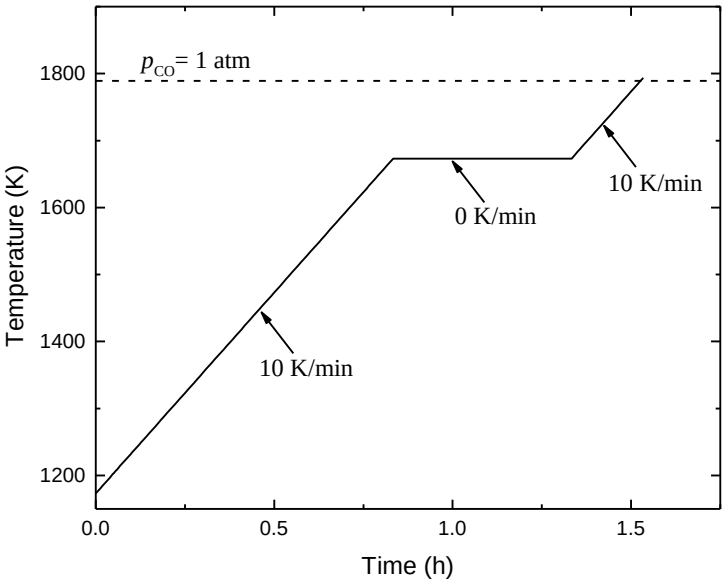

Figure 5-23: Heating profile. Uses SSC1b. A 1 cm sample with 1.0 mol % SiO_2. Initial Temperature: 1173.15 K. Hold Temperature: 1673.15 K. Heating Cycle: 10 K/min (to 1673.15 K); 0 K/min (for 0.5 h); 10 K/min (until t_c).

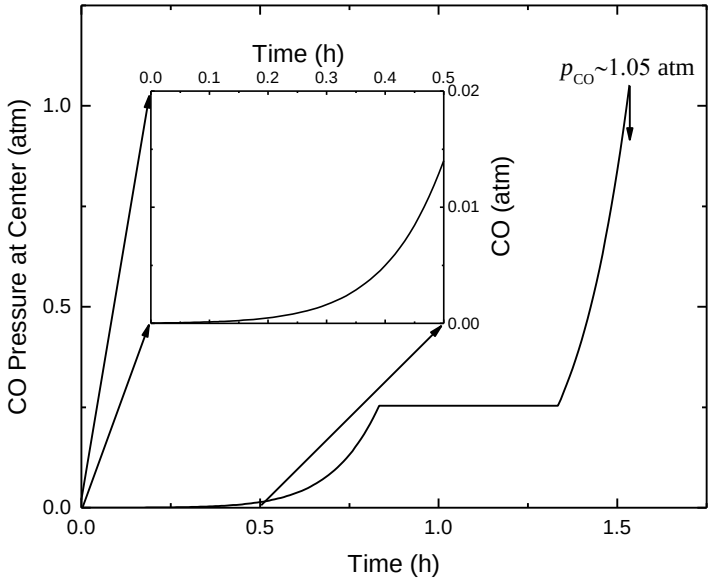

Figure 5-24: Pressure evolution of $CO_{(g)}$ at the center of the sample. Inset: $CO_{(g)}$ pressure between t=0 h and t= ½ h. A 1 cm sample with 1.0 mol % SiO_2. Initial Temperature: 1173.15 K. Hold Temperature: 1673.15 K. Heating Cycle: 10 K/min (to 1673.15 K); 0 K/min (for 0.5 h); 10 K/min (until t_c).

As the temperature increased to 1673.15 K, the maximum internal $p_{CO_{(g)}}$ increased to 0.2540 atm (Figure 5-24). Figure 5-25 shows the $p_{CO_{(g)}}$ at the time the T_h is reached, at the end of the 0.5 hour hold, and at t_c. In this simulation, the movement of the reaction front is drastically different than the simulations in category 1; where all of the simulations in category 1 had the fastest progression of the reaction front at the beginning of the simulation. Here, the

reaction front initially proceeds very slowly, speeding up as the holding temperature is approached. This behavior is confirmed by the first peak in the effusion rate of $CO_{(g)}$ ($J_{CO_{(g)}}$), shown in Figure 5-26, since the removal rate of $CO_{(g)}$ is directly correlated with the rate of progression of the reaction front.

Upon reaching T_h, the reaction front behavior of the category 1 and 2 begin to coincide. At a constant T, the maximum $p_{CO_{(g)}}$ plateaus and pressure gradient decreases as the reaction front proceeds. Figure 5-26 shows the $J_{CO_{(g)}}$ rapidly declines during the hold. Similar to category 1, the rate of decrease of $J_{CO_{(g)}}$ begins to slow because the rate of advance of the reaction front also slows. However, once the 0.5 hour hold is over and heating resumes at 10 K/min, $p_{CO_{(g)}}$ increases exponentially, resulting in a larger pressure gradient which increases $J_{CO_{(g)}}$. It should be noted that the increase in $J_{CO_{(g)}}$ is a consequence of the rate of increase of the pressure gradient, not just the increase in the maximum $p_{CO_{(g)}}$. The pressure and effusion rate continue to increase until all the oxide is removed, followed by a rapid drop in both. At t_c, the temperature, maximum $p_{CO_{(g)}}$, and $J_{CO_{(g)}}$ reach 1793.43 K, 1.05 atm, and 9.05 mol·m^{-2}·h^{-1}. Since the internal pressure and effusion rate are both greater than that at T_h, this simulation is not considered to be optimized.

From this simulation it is evident that each segment of the heating cycle corresponds directly to a change in effusion rate behavior. The time spent dwelling at the intermediate hold temperature is inefficient at removing all of the oxide because the effusion rate decreases as dwell time increases. Since all of the oxide was not removed during the dwell, subsequent heating of the sample results in an increase in the effusion rate and internal pressure until the time at which all the oxide is removed.

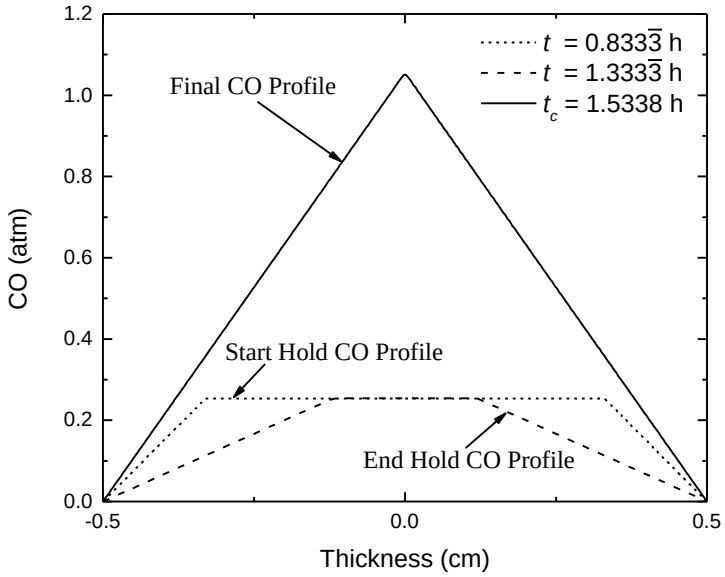

Figure 5-25: Pressure Profile of $CO_{(g)}$ at the start of the hold temperature, at the end of the 0.5 h hold, and at the time of complete oxide removal. A 1 cm sample with 1.0 mol % SiO_2. Initial Temperature: 1173.15 K. Hold Temperature: 1673.15 K. Heating Cycle: 10 K/min (to 1673.15 K); 0 K/min (for 0.5 h); 10 K/min (until t_c).

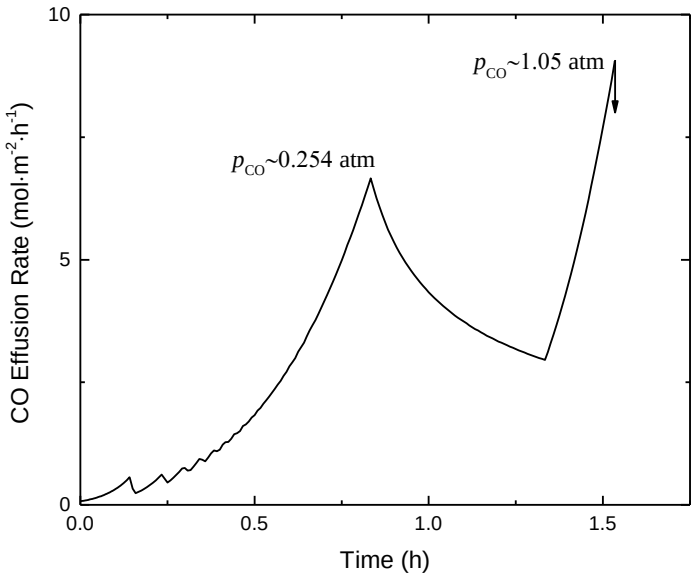

Figure 5-26: Effusion rate of $CO_{(g)}$. Sample with l=1 cm and X_{SiO_2}= 1.0 mol %. Initial Temperature: 1173.15 K. Hold Temperature: 1673.15 K. Heating Cycle: 10 K/min (to 1673.15 K); 0 K/min (for 0.5 h); 10 K/min (until t_c).

The simulation was solved by numerically discretizing the physically relevant algebraic and partial differential equations for thermodynamic equilibrium and gas transport. The gradients in the partial differential equations are represented by difference equations using the discretized grid. A consequence of the discretization procedure can be seen in Figure 5-26. At the beginning of the simulation the pressure gradient is essentially a step function between the ambient pressure and the pressure inside the sample at the first discretized point. This sharp jump at the boundary results in the discretized derivative not being precisely representative of the true behavior. This manifests itself as small steps in the effusion rate as the reaction front expands to include the next discretized point. However, as the reaction front proceeds the pressure gradient is calculated using a progressively larger number of discretized points and the accuracy of the computed effusion rate is increased. Eventually, the irregularity becomes indiscernible as more of the computational grid is used. This artifact in the numerical solution was studied using both larger and smaller discretization grids, with all simulations converging to the same solution. This artifact is therefore of no significance.

5.3.4 Constant Temperature Hold Simulations

The goal of this section is to further study the effect of introducing a constant temperature hold. The sample length, initial SiO_2 concentration, heating rates, holding temperature, and hold duration greatly influence the range of effusion rates, pressure gradients, and maximum internal pressures exhibited while heating a sample to the densification temperature. A number of sets of simulations were designed to illustrate the sensitivity of the effusion rate and internal pressure to variations in the processing conditions. The simulations are grouped in order to highlight the difference between “optimized” and “non-optimized” simulation conditions.

5.3.4.1 *1 cm thick samples with a 0.5 hour hold time*

This set of simulations investigates how the oxide content and holding temperature effect the effusion rate behavior and internal pressure during oxide removal. Four simulations are shown, each with a sample thickness of l = 1 cm and a 0.5 hour hold time. The varied parameters were $X_{\mathrm{SiO_2}}$ and T_h, each varying between 1.0 ($X_{\mathrm{SiO_2},1}$) or 1.5 mol % ($X_{\mathrm{SiO_2},2}$) and 1673.15 ($T_{h,1}$) or 1723.15 K ($T_{h,2}$), respectively. These parameters were selected so only the sample with ($X_{\mathrm{SiO_2},1}$, $T_{h,2}$) was optimized to exhaust all of the oxide during the hold time. The time evolution of the $CO_{(g)}$ effusion rates ($J_{CO_{(g)}}$), the $CO_{(g)}$ pressure ($p_{CO_{(g)}}$) in the center of the sample, and the heating profile are shown in Figure 5-28 (a),(b), and (c), respectively. Additionally, the SiO_2 concentration profile of each sample upon reaching the holding temperature is shown in Figure 5-27. Lastly, Table 5-10 provides t_c, T, maximum $p_{CO_{(g)}}$, and $J_{CO_{(g)}}$ at the end of each simulation, in order of increasing time for complete oxide removal.

For each of the simulations, the reaction fronts proceeded to different depths within the interior of the samples by the time T_h was reached (Figure 5-28). The samples with $X_{\mathrm{SiO_2},2}$ have reaction fronts that didn't proceeded as far into the interior of the samples when the T_h was reached. Thus, $J_{CO_{(g)}}$ at T_h is higher for $X_{\mathrm{SiO_2},2}$ samples compared to $X_{\mathrm{SiO_2},1}$ samples, because the pressure gradient is larger for the former (for the same T_h). The samples with $T_{h,2}$ have reaction fronts that proceeded further into the samples because the samples were heated for an additional 5 minutes at 10 K/min. The $J_{CO_{(g)}}$ is higher for the $T_{h,2}$ samples compared to the $T_{h,1}$ samples, because the pressure and pressure gradient is larger for the former (for the same $X_{\mathrm{SiO_2}}$). The effusion rates of $CO_{(g)}$ upon reaching the holding temperature are listed in Table 5-11.

If the hold temperature was introduced to limit the effusion rate and pressure, only the sample with ($X_{\mathrm{SiO_2},1}$, $T_{\mathrm{h},2}$) was successful. The remaining simulations end up with a higher pressure and effusion rate because all of the oxide was not removed during the hold. The most drastic difference is between the sample with ($X_{\mathrm{SiO_2},2}$, $T_{\mathrm{h},1}$) compared to the optimized sample; $J_{CO_{(g)}}$ was ~4x greater and $p_{CO_{(g)}}$ was ~5x larger at t_c. The sample with ($X_{\mathrm{SiO_2},2}$, $T_{\mathrm{h},2}$) has roughly the same $J_{CO_{(g)}}$ at $T_{\mathrm{h},2}$ and t_c, but $p_{CO_{(g)}}$ is more than 2.5x greater. An increase in the temperature is needed to increase $p_{CO_{(g)}}$, which is necessary to maintain or increase $J_{CO_{(g)}}$ as more oxide is removed. Therefore, it is not possible to maintain both $p_{CO_{(g)}}$ and $J_{CO_{(g)}}$ at a constant level. Though not analyzed, the pressure gradient can be maintained at a specified level by increasing the temperature as the reaction front proceeds into the sample.

These four simulations show that different powder compacts (of the same thickness) can have higher effusion rates and internal pressures than expected. Samples with higher oxide content have a more rapid rise in effusion rate during heating. However, there is also more oxide to be removed so longer holding times are needed. Using a higher temperature hold results in a greater effusion rate at the onset of the hold and as a result oxide removal during the hold occurs more rapidly.

Table 5-10: Simulation results from 1 cm samples with a ½ hour hold time.

Varied Parameters (In order of oxide removal)	t_c (h)	T (K)	$p_{CO_{(g)}}$ (atm)	$J_{CO_{(g)}}$ (mol·m^{-2}·h^{-1})
$X_{SiO_2,1}$= 1.0 mol %; $T_{h,2}$=1723.15 K	1.3703	1723.13	0.47	4.14
$X_{SiO_2,1}$= 1.0 mol %; $T_{h,1}$=1673.15 K	1.5338	1793.43	1.05	9.05
$X_{SiO_2,2}$= 1.5 mol %; $T_{h,2}$=1723.15 K	1.5604	1809.39	1.25	10.78
$X_{SiO_2,2}$= 1.5 mol %; $T_{h,1}$=1673.15 K	1.6297	1850.97	1.94	16.52

Table 5-11: Effusion rates for 1 cm samples upon reaching the holding temperature

Varied Parameters (In order of oxide removal)	$J_{CO_{(g)}}$ at T_h (mol·m^{-2}·h^{-1})
$X_{SiO_2,1}$= 1.0 mol %; $T_{h,2}$=1723.15 K	8.73
$X_{SiO_2,1}$= 1.0 mol %; $T_{h,1}$=1673.15 K	6.66
$X_{SiO_2,2}$= 1.5 mol %; $T_{h,2}$=1723.15 K	10.74
$X_{SiO_2,2}$= 1.5 mol %; $T_{h,1}$=1673.15 K	8.19

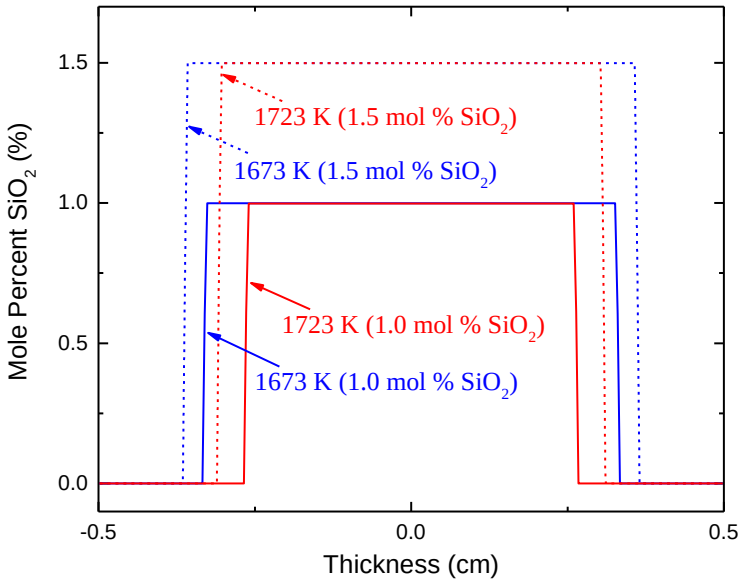

Figure 5-27: SiO_2 concentration profile upon reaching the holding temperature. Four samples with l=1 cm, X_{SiO_2}=1.0 or 1.5 mol %, T_i = 1173.15 K, and T_h= 1673.15 K or 1723.15 K. Heating Cycle: 10 K/min to T_h.

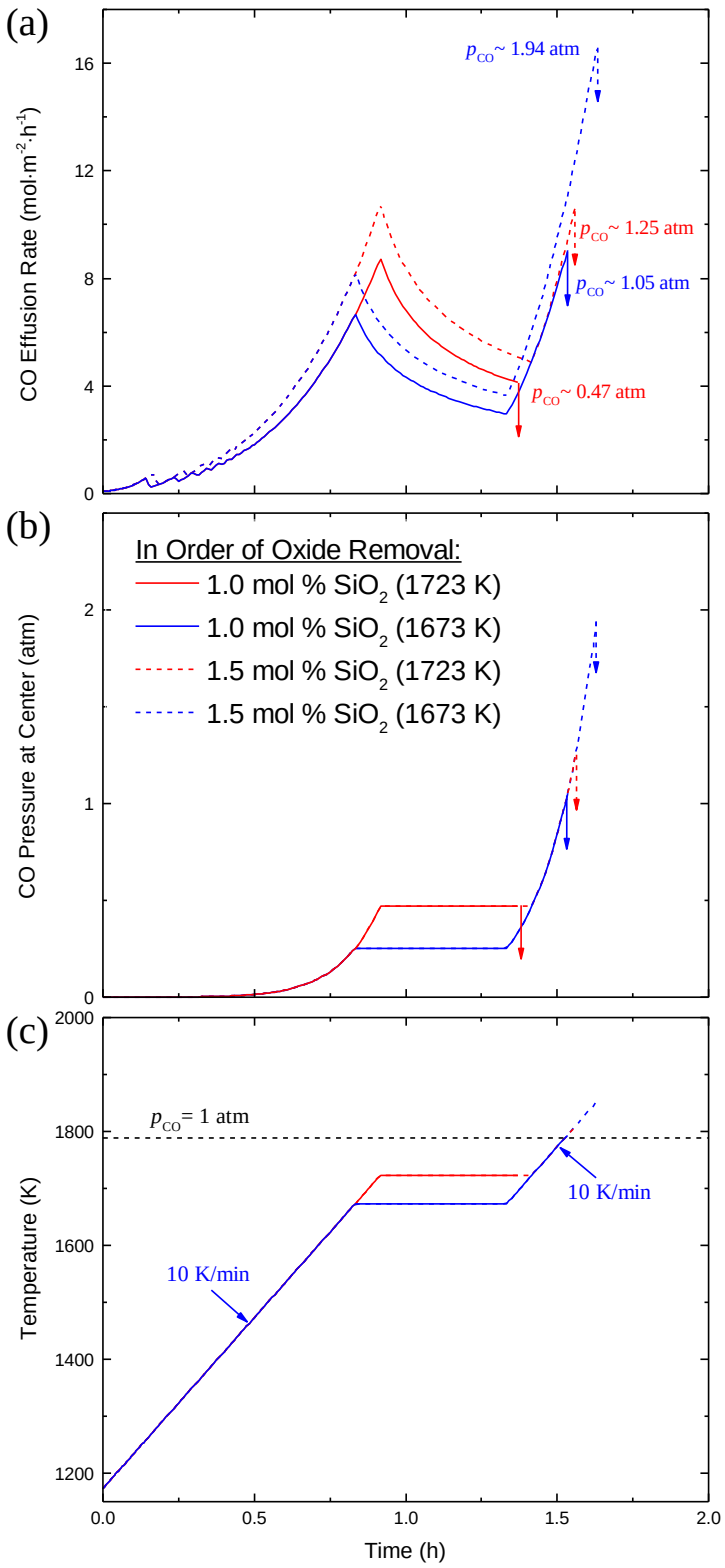

Figure 5-28: Four samples with l=1 cm and X_{SiO_2}=1.0 or 1.5 mol %. Initial Temperature: 1173.15 K. Hold Temperature(s): 1673.15 K or 1723.15 K. Heating Cycle: 10 K/min (to holding temperature); 0 K/min (for 0.5 h); 10 K/min (until t_c).(a) Effusion rate of $CO_{(g)}$ (max p_{CO} indicated). (b) Pressure of $CO_{(g)}$ at the center of the sample. (c) Heating Profile.

5.3.4.2 *1.0 mol % SiO_2 samples with 0.5 hour hold time*

This set of simulations investigates how the sample length and holding temperature effect the effusion rate behavior and internal pressure during oxide removal. Four simulations are shown, each with an initial oxide content of $X_{\mathrm{SiO_2}}$ = 1.0 mol % and a 0.5 hour hold time. The varied parameters were l and T_h, each varying between 1 (l_1) or 2 cm (l_2) and 1673.15 ($T_{h,1}$) or 1723.15 K ($T_{h,2}$), respectively. The thicker sample simulations were used to study the effect of using the same heating profiles when trying to manufacture larger parts. These parameters were selected so only the sample with (l_1, $T_{h,2}$) was optimized to exhaust all of the oxide during the hold time. The time evolution of the $CO_{(g)}$ effusion rates ($J_{CO_{(g)}}$), the $CO_{(g)}$ pressure ($p_{CO_{(g)}}$) in the center of the sample, and the heating profile are shown in Figure 5-29 (a),(b), and (c), respectively. Table 5-12 provides t_c, T, maximum $p_{CO_{(g)}}$, and $J_{CO_{(g)}}$ at the end of each simulation, in order of increasing time for complete oxide removal.

If the hold temperature was introduced to limit the effusion rate and pressure, only the sample with (l_1, $T_{h,2}$) was successful. Even though the sample with (l_1, $T_{h,1}$) did not completely exhaust all of the oxide during the hold, $J_{CO_{(g)}}$ rose to ~1.5x that at T_h and $p_{CO_{(g)}}$ quadrupled to 1.05 atm, but only for a short time. Up to t_c for the $l_1$samples, both the l_1 and $l_2$samples have the same time evolution of $p_{CO_{(g)}}$ and $J_{CO_{(g)}}$. However, once the $l_1$samples reached t_c, $p_{CO_{(g)}}$ and $J_{CO_{(g)}}$ for the l_2 samples continued to rise quickly, with the $p_{CO_{(g)}}$ exceeding 5 atm. Comparing the l_1 and l_2 samples shows that using the same heating cycle for thicker samples leads to much higher effusion rates and internal pressures than might be acceptable.

These four simulations show that powder compacts of different thicknesses have the same effusion rate behavior until all the oxide is removed from the shorter samples. As the sample thickness increases, using a constant temperature hold becomes increasingly inefficient

at removing all of the oxide. As the samples are heated to the sintering temperature, a thicker sample will experience much higher pressures and effusion rates.

Table 5-12: Ending simulation conditions results from l = 1 or 2 cm and X_{SiO_2} = 1.0 mol % samples with a ½ hour hold time.

Varied Parameters (In order of oxide removal)	t_c (h)	T (K)	$p_{CO_{(g)}}$ (atm)	$J_{CO_{(g)}}$ (mol·m^{-2}·h^{-1})
l_1 = 1 cm; $T_{h,2}$=1723.15 K	1.3703	1723.13	0.47	4.14
l_1 = 1 cm; $T_{h,1}$=1673.15 K	1.5338	1793.43	1.05	9.05
l_2 = 2 cm; $T_{h,2}$=1723.15 K	1.8056	1956.47	5.41	22.16
l_2 = 2 cm; $T_{h,1}$=1673.15 K	1.8251	1968.2	6.02	24.6

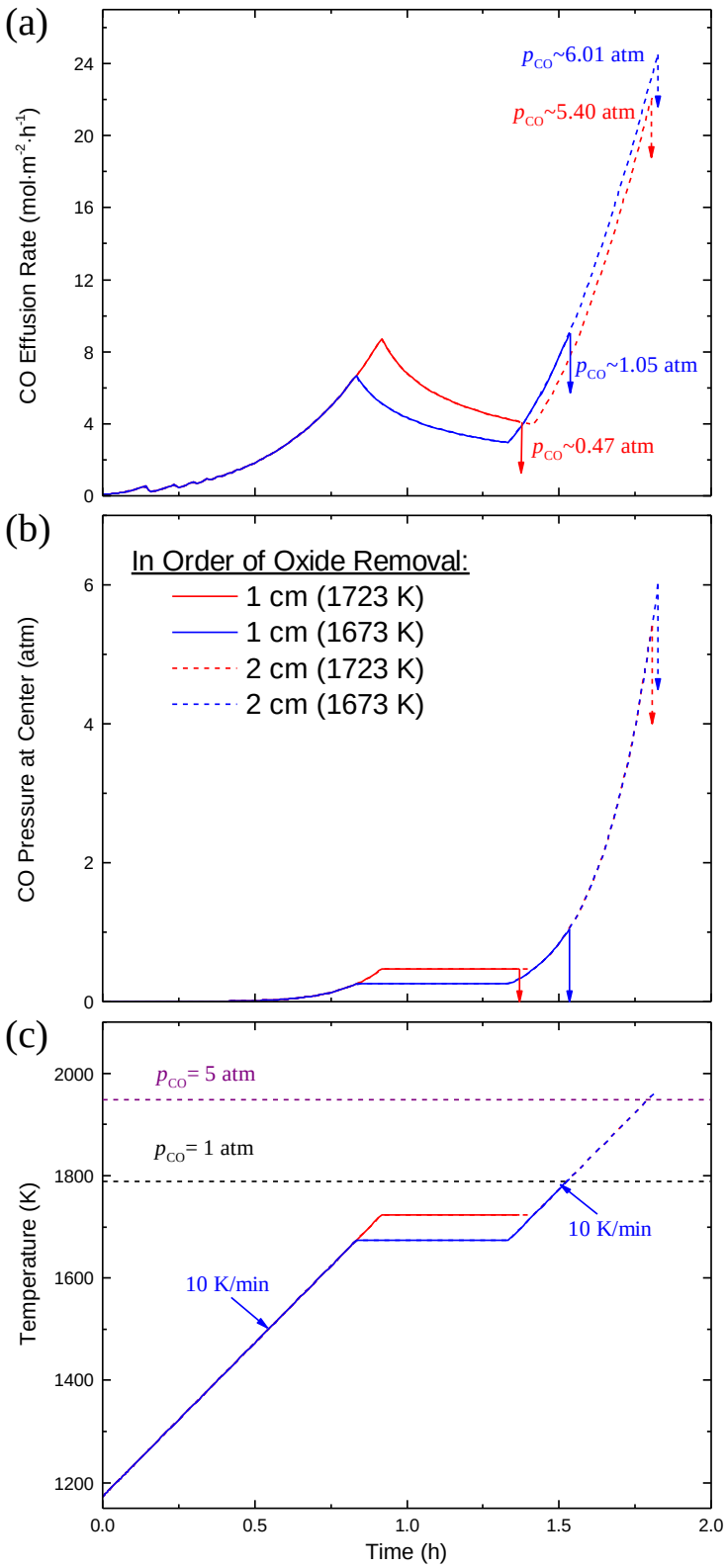

Figure 5-29: Four samples with l=1 or 2 cm and X_{SiO_2}= 1.0 mol %. Initial Temperature: 1173.15 K. Hold Temperature(s): 1673.15 K or 1723.15 K. Heating Cycle: 10 K/min (to holding temperature); 0 K/min (for 0.5 h); 10 K/min (until t_c). (a) Effusion rate of $CO_{(g)}$ (max p_{CO} indicated). (b) Pressure of $CO_{(g)}$ at the center of the sample. (c) Heating Profile.

5.3.4.3 *1.5 mol % SiO_2 samples with 0.5 hour hold time*

This set of simulations investigates how the sample length and holding temperature effect the effusion rate behavior and internal pressure during oxide removal when starting with a higher oxide content. Four simulations are shown, each with an initial oxide content of $X_{\mathrm{SiO_2}}$ = 1.5 mol % and a 0.5 hour hold time. The varied parameters were l and T_h, each varying between 1 (l_1) or 2 cm (l_2) and 1673.15 ($T_{h,1}$) or 1723.15 K ($T_{h,2}$), respectively. The thicker sample simulations are used to study the effect of using the same heating profiles when trying to manufacture larger parts. These parameters were selected so only the sample with (l_1, $T_{h,2}$) was optimized to exhaust all of the oxide without greatly exceeding the effusion rate at T_h, no restriction is placed on the $p_{CO_{(g)}}$. The time evolution of the $CO_{(g)}$ effusion rates ($J_{CO_{(g)}}$), the $CO_{(g)}$ pressure ($p_{CO_{(g)}}$) in the center of the sample, and the heating profile are shown in Figure 5-30 (a),(b), and (c), respectively. Table 5-13 provides t_c, T, maximum $p_{CO_{(g)}}$, and $J_{CO_{(g)}}$ at the end of each simulation, in order of increasing time for complete oxide removal.

If the hold temperature was introduced to limit the effusion rate, only the sample with (l_1, $T_{h,2}$) was optimized successfully. Even though the sample with (l_1, $T_{h,2}$) did not completely exhaust all of the oxide during the hold, $J_{CO_{(g)}}$ at T_h and t_c are roughly the equal, but $p_{CO_{(g)}}$ is more than 2.5x greater. Increasing $p_{CO_{(g)}}$, by increasing T, is necessary to maintain or increase $J_{CO_{(g)}}$ while removing the oxide, so it is not possible to maintain both below a given level. Similar to the last section, up to t_c for the $l_1$samples, both the l_1 and $l_2$samples have the same time evolution of $p_{CO_{(g)}}$ and $J_{CO_{(g)}}$. Once the $l_1$samples reached t_c, the $p_{CO_{(g)}}$ and $J_{CO_{(g)}}$ for the l_2 samples continued to rise quickly with the $p_{CO_{(g)}}$ exceeding 8 atm. Comparing the l_1 and l_2 samples shows that using the same heating cycle for thicker samples leads to much higher effusion rates and internal pressures than might be acceptable. Additionally, comparing the two

sets of simulations with $X_{\mathrm{SiO_2},1}$ and $X_{\mathrm{SiO_2},2}$ shows that the higher the initial oxide content, the more severe the variation in $p_{CO_{(g)}}$ and $J_{CO_{(g)}}$ will be when increasing the sample thickness for a set heating cycle.

These four simulations show the same trends in effusion rate behavior as the previous set of simulations comparing different sample thicknesses. The constant temperature hold remains inefficient at removing all of the oxide. The higher oxide content samples experience much higher effusion rates and internal pressures than the lower oxide content samples in the previous study.

Table 5-13: Ending simulation conditions results from l = 1 or 2 cm and $X_{\mathrm{SiO_2}}$ = 1.5 mol % samples with a ½ hour hold time.

Varied Parameters (In order of oxide removal)	t_c (h)	T (K)	$p_{\mathrm{CO}_{(g)}}$ (atm)	$J_{CO_{(g)}}$ (mol·m^{-2}·h^{-1})
l_1 = 1 cm; $T_{h,2}$=1723.15 K	1.5604	1809.39	1.25	10.78
l_1 = 1 cm; $T_{h,1}$=1673.15 K	1.6297	1850.97	1.94	16.52
l_2 = 2 cm; $T_{h,2}$=1723.15 K	1.8897	2006.94	8.48	34.47
l_2 = 2 cm; $T_{h,1}$=1673.15 K	1.9026	2014.69	9.06	36.79

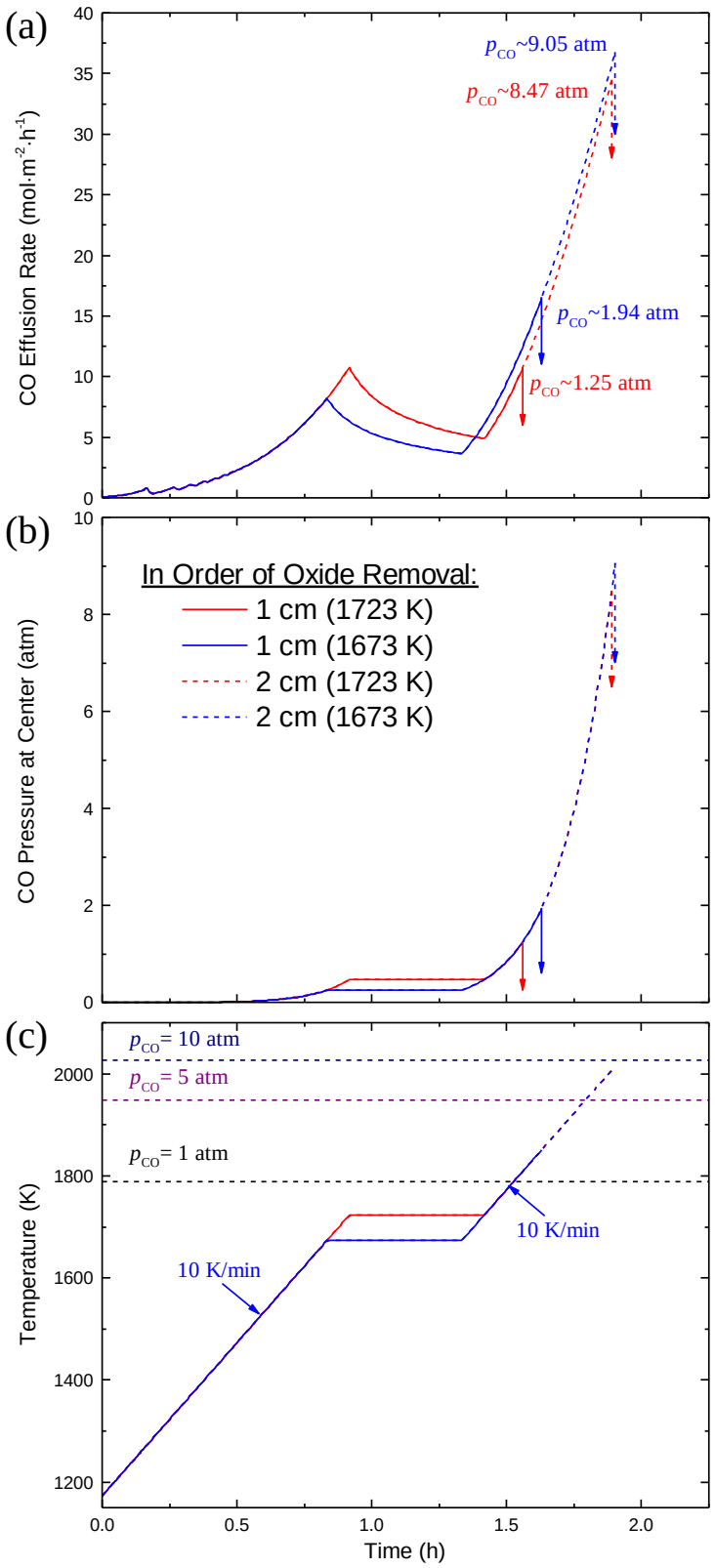

Figure 5-30: Four samples with l=1 or 2 cm and X_{SiO_2}= 1.5 mol %. Initial Temperature: 1173.15 K. Hold Temperature(s): 1673.15 K or 1723.15 K. Heating Cycle: 10 K/min (to holding temperature); 0 K/min (for 0.5 h);

10 K/min (until t_c). (a) Effusion rate of $CO_{(g)}$ (max p_{CO} indicated). (b) Pressure of $CO_{(g)}$ at the center of the sample. (c) Heating Profile.

5.3.4.4 *2 cm thick samples with a 2.5 hour hold time*

This set of simulations investigates how the oxide content and holding temperature effect the effusion rate behavior and internal pressure for thicker samples with an extended hold time. Four simulations are shown, each with a constant sample thickness of l = 2 cm and a 2.5 hour hold time are presented. The varied parameters were X_{SiO_2} and T_h, each varying between 1.0 ($X_{SiO_2,1}$) or 1.5 mol % ($X_{SiO_2,2}$) and 1673.15 ($T_{h,1}$) or 1723.15 K ($T_{h,2}$), respectively. These parameters were selected so only the ($X_{SiO_2,1}$, $T_{h,2}$) sample was optimized to exhaust all of the oxide during the hold time. The time evolution of the $CO_{(g)}$ effusion rates ($J_{CO_{(g)}}$), the $CO_{(g)}$ pressure ($p_{CO_{(g)}}$) in the center of the sample, and the heating profile are shown in Figure 5-31 (a),(b), and (c), respectively. Table 5-14 provides t_c, T, maximum $p_{CO_{(g)}}$, and $J_{CO_{(g)}}$ at the end of each simulation, in order of increasing time for complete oxide removal.

If the hold temperature was introduced to limit the effusion rate and pressure, only the sample with ($X_{SiO_2,1}$, $T_{h,2}$) was optimized successfully. The remaining simulations end up with a higher pressure and effusion rate because all of the oxide was not removed during the hold. The most drastic difference was between the ($X_{SiO_2,2}$, $T_{h,1}$) sample compared to the optimized sample; $J_{CO_{(g)}}$ was ~12x greater and $p_{CO_{(g)}}$ was ~13x larger at t_c. The ($X_{SiO_2,2}$, $T_{h,2}$) sample has a $J_{CO_{(g)}}$ only ~1.3x greater at t_c than $T_{h,2}$, but $p_{CO_{(g)}}$ is more than 6x greater; there is more variation in $J_{CO_{(g)}}$ and $p_{CO_{(g)}}$ for the l_2 sample than the corresponding l_1 sample in a previous section. For thicker samples, a constant temperature hold becomes much less effective at removing oxide because $J_{CO_{(g)}}$ decreases as the reaction front proceeds into the sample and the total distance traveled by the reaction front increases with sample thickness.

These four simulations clearly show that for thicker powder compacts extending the hold time becomes exceedingly inefficient at removing all of the oxide. For thicker samples with an optimized heating profile, any sample variation tends to produce more extreme deviations from the tolerable effusion rates and internal gas pressures. Thus, it is generally more difficult and time consuming to process thicker samples using constant temperature holds.

Table 5-14: Simulation results from 2 cm samples with a 2.5 hour hold time.

Varied Parameters (In order of oxide removal)	t_c (h)	T (K)	$p_{CO_{(g)}}$ (atm)	$J_{CO_{(g)}}$ (mol·m^{-2}·h^{-1})
$X_{SiO_2,1}$= 1.0 mol %; $T_{h,2}$=1723.15 K	3.1228	1723.13	0.47	2.06
$X_{SiO_2,1}$= 1.0 mol %; $T_{h,1}$=1673.15 K	3.7015	1894.05	2.99	12.45
$X_{SiO_2,2}$= 1.5 mol %; $T_{h,2}$=1723.15 K	3.706	1896.74	3.07	12.84
$X_{SiO_2,2}$= 1.5 mol %; $T_{h,1}$=1673.15 K	3.8304	1971.35	6.19	25.42

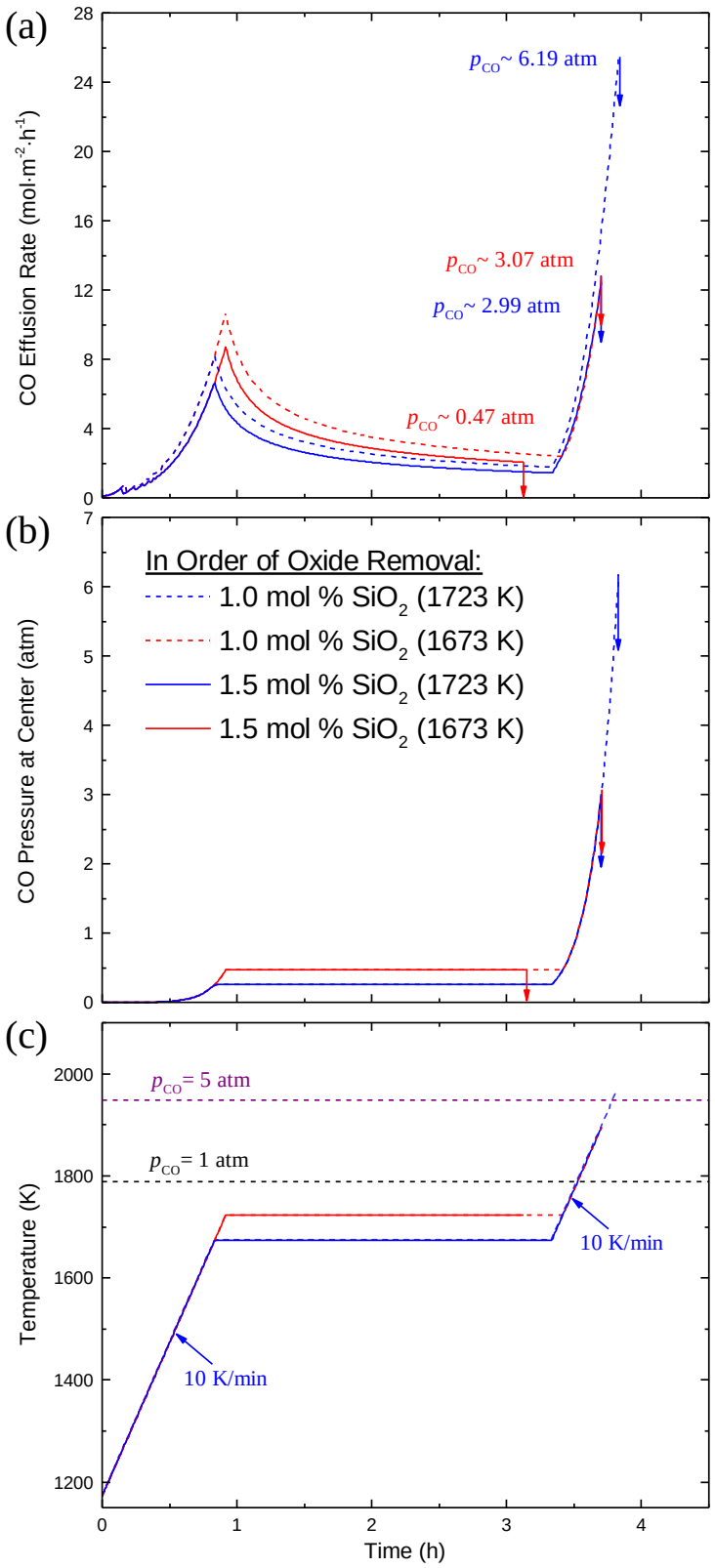

Figure 5-31: Four simulations: l= 2 cm, X_{SiO_2}= 1.0 or 1.5mol %, T_i=1173.15 K, and T_h=1673.15 K or 1723.15 K. Heating Cycle: 10 K/min (to T_h); 0 K/min (for 5/2 h); 10 K/min (until t_c). (a) Effusion rate of $CO_{(g)}$ (max p_{CO} indicated). (b) Pressure of $CO_{(g)}$ at the center of the sample. (c) Heating Profile.

5.3.5 Variable Ramping Rate Simulations

The goal of this section is to study the effect of changing the heating rate once a threshold temperature (T_h) is reached. These simulations are in response to observing that using a constant temperature hold necessitates very long hold times to remove all of the oxide from thick samples due to a decreasing effusion rate. The constant temperature hold simulations can be optimized to maintain both the pressure and effusion rate below a specified level. However, changing the heating rate indicates that the simulations can only be optimized to maintain the effusion rate below a specified level, because the maximum internal pressure increases with temperature. A number of sets of simulations were designed to illustrate the difference in effusion rate, pressure, and time for complete oxide removal when using different heating rates.

5.3.5.1 *1 cm thick, 1.0 mol % SiO_2, and T_h = 1673.15 K samples*

This set of simulations investigates how changing the heating rate at the hold temperature effects the effusion rate behavior, internal pressure, and time for complete oxide removal. Four simulations are shown, each with a sample thickness of 1 cm (l_1), oxide content of 1.0 mol % ($X_{\mathrm{SiO_2},1}$), and threshold temperature of 1673.15 K ($T_{h,1}$). The heating rate (HR_1) was varied after reaching T_h. The heating rate for the simulations was varied between 10, 5, 2.5, or 0 K/min; alternatively labeled as $HR_{1,1a}$, $HR_{1,2a}$, $HR_{1,3a}$, and $HR_{1,4a}$, respectively. The time evolution of the $CO_{(g)}$ effusion rates ($J_{CO_{(g)}}$), the $CO_{(g)}$ pressure ($p_{CO_{(g)}}$) in the center of the sample, and the heating profile are shown in Figure 5-32 (a),(b), and (c), respectively. Table 5-15 provides t_c, T, maximum $p_{CO_{(g)}}$, and $J_{CO_{(g)}}$ at the end of each simulation, in order of increasing time for complete oxide removal.

Changing the heating rate at T_h can help to maintain $J_{CO_{(g)}}$ below a desired level. For $HR_{1,3}$, there is an initial decrease in $J_{CO_{(g)}}$ at T_h, followed by a minimum in $J_{CO_{(g)}}$, and finally an

increase in $J_{CO_{(g)}}$. This behavior is interesting because even though $p_{CO_{(g)}}$ is monotonically increasing, $J_{CO_{(g)}}$ experiences a minimum. The minimum in $J_{CO_{(g)}}$ occurs because $J_{CO_{(g)}}$ is controlled by the pressure gradient which is a function of pressure and the depleted layer thickness. After T_h and using $HR_{1,3a}$, the reaction front proceeds at a rate faster than the pressure is rising, which leads to a decrease in $J_{CO_{(g)}}$. Eventually, the two rates become commensurate at the $J_{CO_{(g)}}$ minimum. Finally, $J_{CO_{(g)}}$ begins to increase, until t_c, because the pressure rises faster than the reaction front is proceeding. The 2.5 K/min heating rate for $HR_{1,3a}$ was chosen to keep $J_{CO_{(g)}}$ at t_c below $J_{CO_{(g)}}$ at T_h. After T_h and using $HR_{1,2a}$, the pressure rise and reaction front progression are already commensurate, leading to only an increase in $J_{CO_{(g)}}$ upon heating.

If the heating rate change was introduced to limit the effusion rate, only the samples with $HR_{1,3a}$ and $HR_{1,4a}$ were successful. However, $HR_{1,4a}$ is a constant temperature hold and t_c is long because $J_{CO_{(g)}}$ continually decreases. $HR_{1,3a}$ is effective at keeping the $J_{CO_{(g)}}$ below the $J_{CO_{(g)}}$ value at T_h. The t_c for $HR_{1,3a}$ is ~22 % less than $HR_{1,4a}$, while having a $p_{CO_{(g)}}$ of 0.69 atm and maintaining the effusion rate below the level specified at T_h. Thus, $HR_{1,3a}$ is a more efficient optimization because $J_{CO_{(g)}}$ is closer to the threshold $J_{CO_{(g)}}$ level.

These simulations show that lowering the heating rate can be used to decrease the time for complete oxide removal compared to an isothermal hold. Depending on the new heating rate, the effusion rate behavior will differ. If the heating rate is only slightly lowered, the effusion rate will continue to rise with heating. However, if the heating rate is significantly lower, the effusion rate will initially decrease. This decrease in effusion rate is only temporary and will begin to increase again, provided that all of the oxide is not exhausted.

Table 5-15: Simulation results from l = 1 cm, X_{SiO_2}= 1.0 mol % samples with variable heating rates after T_h=1673.15 K.

Varied Parameters (In order of oxide removal)	t_c (h)	T (K)	$p_{CO_{(g)}}$ (atm)	$J_{CO_{(g)}}$ (mol·m^{-2}·h^{-1})
$HR_{1,1a}$= 10 K/min	1.1257	1848.56	1.89	16.04
$HR_{1,2a}$= 5 K/min	1.2487	1797.72	1.1	9.49
$HR_{1,3a}$= 2.5 K/min	1.385	1755.88	0.69	6.01
$HR_{1,4a}$= 0 K/min	1.7762	1673.13	0.25	2.27

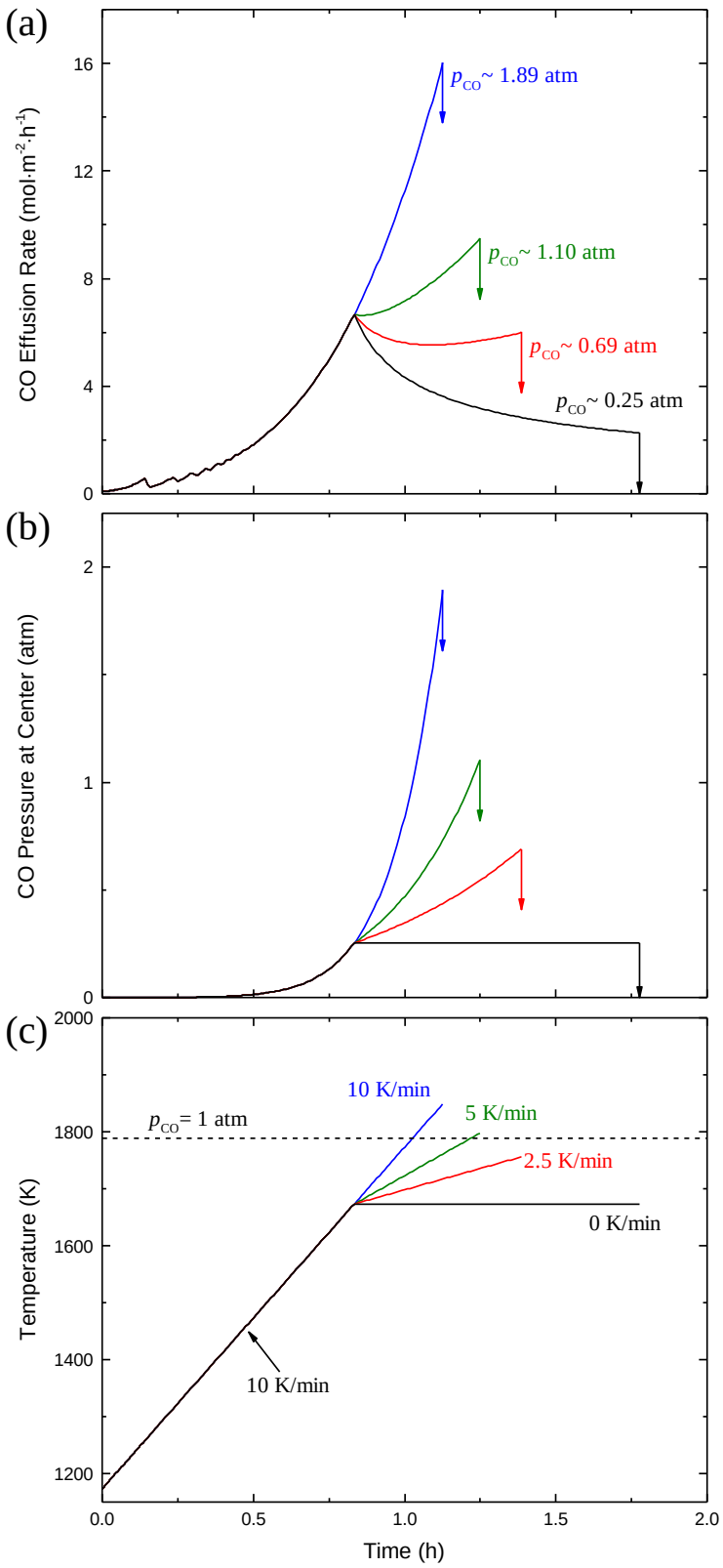

Figure 5-32: Four simulations: l= 1 cm, X_{SiO_2}= 1.0, T_i=1173.15 K, and T_h=1673.15 K. Heating Cycle: 10 K/min (to T_h); HR_1 = 0, 2.5, 5, or 10 K/min (until t_c). (a) Effusion rate of $CO_{(g)}$ (max p_{CO} indicated). (b) Pressure of $CO_{(g)}$ at the center of the sample. (c) Heating Profile.

5.3.5.2 *1 cm thick, 1.0 mol % SiO_2, and T_h = 1723.15 K samples*

This set of simulations investigates how changing the heating rate at a higher holding temperature effects the effusion rate behavior, internal pressure, and time for complete oxide removal. Four simulations are shown, each with a sample thickness of 1 cm (l_1), oxide content of 1.0 mol % ($X_{\mathrm{SiO_2},1}$), and threshold temperature of 1723.15 K ($T_{\mathrm{h},1}$). The heating rate (HR_1) was varied after reaching T_h. The heating rate for the simulations was varied between 10, 5, 3, or 0 K/min; alternatively labeled as $HR_{1,1b}$, $HR_{1,2b}$, $HR_{1,3b}$, and $HR_{1,4b}$, respectively. The time evolution of the $CO_{(g)}$ effusion rates ($J_{CO_{(g)}}$), the $CO_{(g)}$ pressure ($p_{CO_{(g)}}$) in the center of the sample, and the heating profile are shown in Figure 5-33 (a),(b), and (c), respectively. Table 5-16 provides t_c, T, maximum $p_{CO_{(g)}}$, and $J_{CO_{(g)}}$ at the end of each simulation, in order of increasing time for complete oxide removal.

This set of simulations shows the same trends in the $J_{CO_{(g)}}$ behavior as the previous section. The difference between two sets of simulations is that $HR_{1,3}$ is 3.0 K/min, instead of 2.5 K/min. The faster heating rate is possible for two reasons. First, the threshold $J_{CO_{(g)}}$ at $T_{\mathrm{h},2}$ is greater than at $T_{\mathrm{h},1}$. Second, the reaction front has proceeded further into the sample upon reaching $T_{\mathrm{h},2}$, therefore the amount of additional oxide removal is less than in the previous section. The t_c for $HR_{1,3b}$ is ~10 % less than $HR_{1,4b}$, while having a $p_{CO_{(g)}}$ of 0.92 atm and maintaining the effusion rate below the level specified at T_h. From this set of simulations, $HR_{1,3b}$ is the most efficient because $J_{CO_{(g)}}$ is kept closest to the threshold $J_{CO_{(g)}}$ level.

These simulations show that changing the heating rate at a higher temperature does not fundamentally change any of the gas effusion behavior compared to previous simulations for which it is changed at a lower temperature. When using a higher hold temperature it is possible to use a higher heating rate without exceeding the effusion rate exhibited at the onset of the

temperature change. Additionally, after the hold temperature is reached, the amount of time needed to deplete all of the oxide is diminished because overall the effusion rate is higher.

Table 5-16: Simulation results from l = 1 cm, X_{SiO_2}= 1.0 mol % samples with variable heating rates after T_h=1723.15 K.

Varied Parameters (In order of oxide removal)	t_c (h)	T (K)	$p_{CO_{(g)}}$ (atm)	$J_{CO_{(g)}}$ (mol·m^{-2}·h^{-1})
$HR_{1,1b}$= 10 K/min	1.1257	1848.56	1.89	16.04
$HR_{1,2b}$= 5 K/min	1.1915	1805.57	1.2	10.31
$HR_{1,3b}$= 3 K/min	1.2373	1780.84	0.92	7.91
$HR_{1,4b}$= 0 K/min	1.3703	1723.13	0.47	4.14

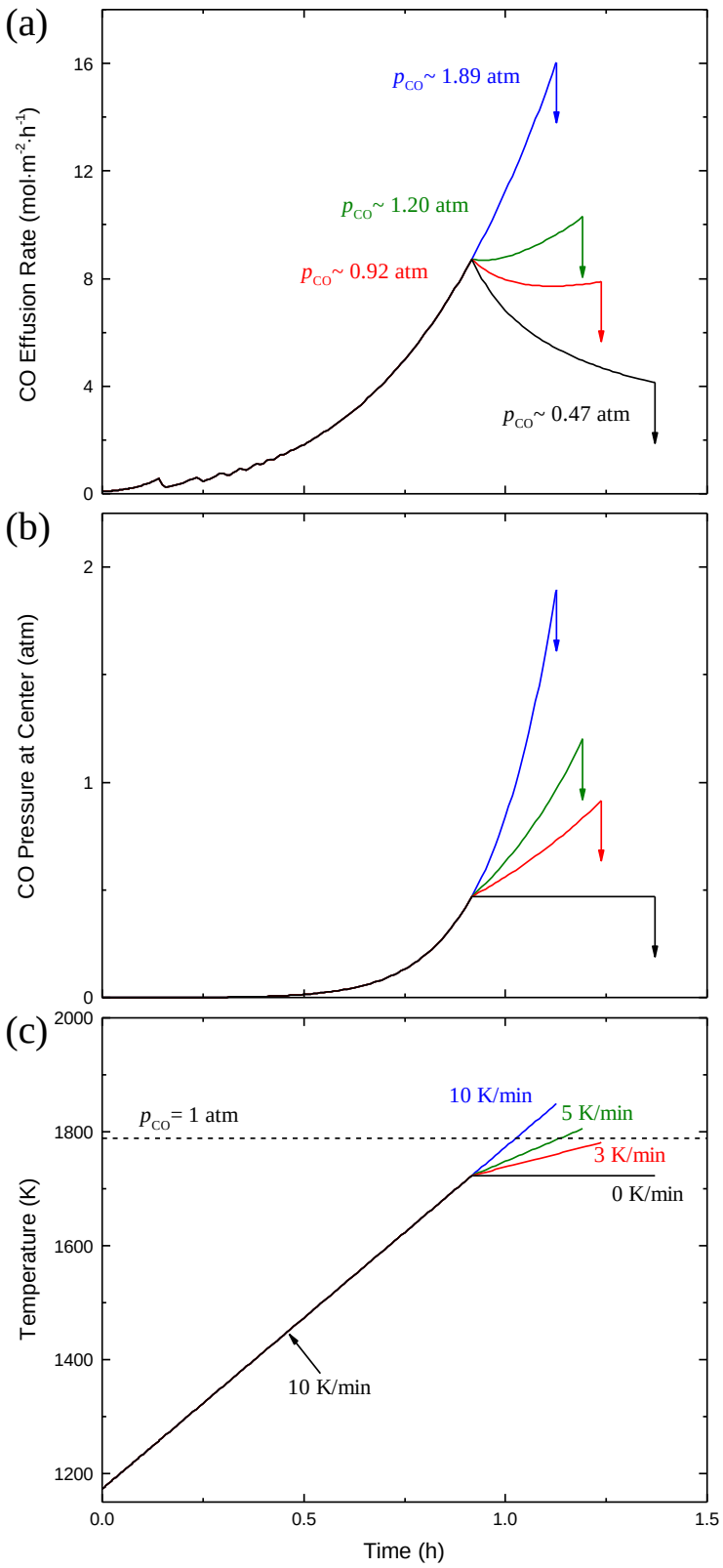

Figure 5-33: Four simulations: l= 1 cm, X_{SiO_2}= 1.0, T_i=1173.15 K, and T_h=1723.15 K. Heating Cycle: 10 K/min (to T_h); HR_1 = 0, 3, 5, or 10 K/min (until t_c). (a) Effusion rate of $CO_{(g)}$ (max p_{CO} indicated). (b) Pressure of $CO_{(g)}$ at the center of the sample. (c) Heating Profile.

5.3.5.3 *1 cm thick, 1.5 mol % SiO_2, and T_h = 1673.15 K or 1723.15 K samples*

These two sets of simulations investigate the effect of changing the heating rate at the hold temperature for samples with a higher initial oxide content. Two sets of four simulations are shown, each with a sample thickness of 1 cm (l_1), oxide content of 1.5 mol % ($X_{\mathrm{SiO_2},2}$), and threshold temperature of 1673.15 K ($T_{\mathrm{h},1}$) or 1723.15 K ($T_{\mathrm{h},2}$). The heating rate (HR_1) was varied after reaching T_{h}. The heating rate for the $T_{\mathrm{h},1}$ simulations was varied between 10, 5, 2.5, or 0 K/min; alternatively labeled as $HR_{1,1a}$, $HR_{1,2a}$, $HR_{1,3a}$, and $HR_{1,4a}$, respectively. The heating rate for the $T_{\mathrm{h},2}$ simulations was varied between 10, 5, 3, or 0 K/min; alternatively labeled as $HR_{1,1b}$, $HR_{1,2b}$, $HR_{1,3b}$, and $HR_{1,4b}$, respectively. The time evolution of the $CO_{(g)}$ effusion rates ($J_{CO_{(g)}}$), the $CO_{(g)}$ pressure ($p_{CO_{(g)}}$) in the center of the sample, and the heating profiles for $T_{\mathrm{h},1}$ and $T_{\mathrm{h},2}$ are shown in Figure 5-34 and Figure 5-35 (a),(b), and (c), respectively. Table 5-17 and Table 5-18 provide t_c, T, maximum $p_{CO_{(g)}}$, and $J_{CO_{(g)}}$ at the end of each simulation, in order of increasing time for complete oxide removal for $T_{\mathrm{h},1}$ and $T_{\mathrm{h},2}$, respectively.

These sets of simulations show the same trends in the $J_{CO_{(g)}}$ behavior as the previous sections. The difference between these simulations and previous simulations is that the reaction front does not proceed as far into the sample by the time T_{h} is reached due to the higher oxide content. This results in the $J_{CO_{(g)}}$ being higher at T_{h} for the $X_{\mathrm{SiO_2},2}$ simulations compared to $X_{\mathrm{SiO_2},1}$ simulations. Again, the $HR_{1,3a}$ and $HR_{1,3b}$ simulations are the most efficient optimizations. The time savings for $HR_{1,3a}$ is ~32% and $HR_{1,3b}$ is ~17% compared to the t_c for $HR_{1,4a}$ and $HR_{1,4b}$, respectively.

These two sets of simulations show that lowering the heating rate considerably reduces t_c compared to an isothermal hold. For the higher oxide content samples there is more time spent after the holding temperature which leads to more heating and higher effusion rates than

the previous simulations. In general, samples with a higher initial oxide content benefit more from maintaining the effusion rate by lowering the heating rate compared to an isothermal hold.

Table 5-17: Simulation results from l = 1 cm, X_{SiO_2}= 1.5 mol % samples with variable heating rates after T_h=1673.15 K.

Varied Parameters (In order of oxide removal)	t_c (h)	T (K)	$p_{CO_{(g)}}$ (atm)	$J_{CO_{(g)}}$ (mol·m^{-2}·h^{-1})
$HR_{1,1a}$= 10 K/min	1.1872	1885.44	2.75	23.19
$HR_{1,2a}$= 5 K/min	1.3547	1829.53	1.55	13.31
$HR_{1,3a}$= 2.5 K/min	1.5571	1781.69	0.92	8.03
$HR_{1,4a}$= 0 K/min	2.3052	1673.13	0.25	2.28

Table 5-18: Simulation results from l = 1 cm, X_{SiO_2}= 1.5 mol % samples with variable heating rates after T_h=1723.15 K.

Varied Parameters (In order of oxide removal)	t_c (h)	T (K)	$p_{CO_{(g)}}$ (atm)	$J_{CO_{(g)}}$ (mol·m^{-2}·h^{-1})
$HR_{1,1b}$= 10 K/min	1.1872	1885.44	2.75	23.19
$HR_{1,2b}$= 5 K/min	1.2903	1835.22	1.65	14.11
$HR_{1,3b}$= 3 K/min	1.3699	1804.7	1.19	10.27
$HR_{1,4b}$= 0 K/min	1.6602	1723.13	0.47	4.16

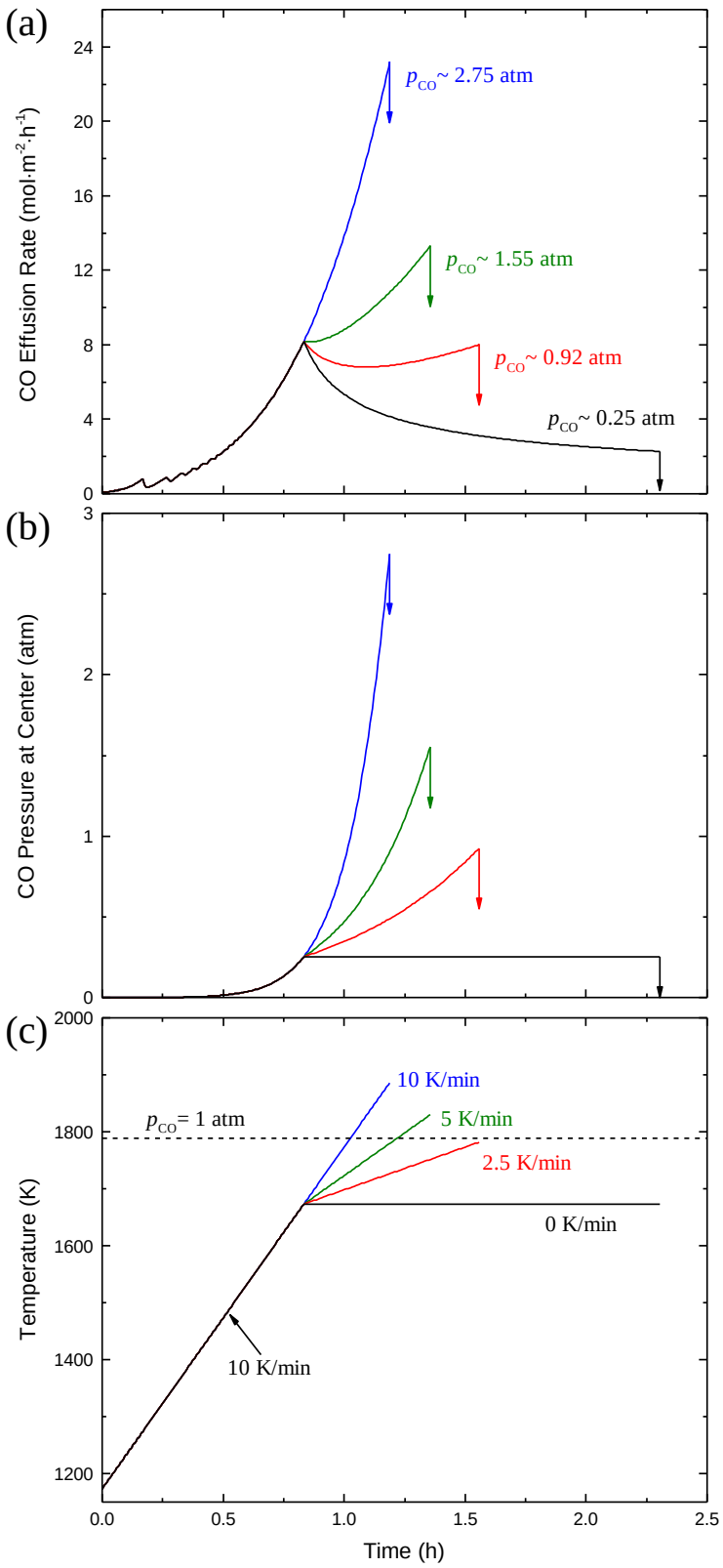

Figure 5-34: Four simulations: l= 1 cm, X_{SiO_2}= 1.5, T_i=1173.15 K, and T_h=1623.15 K. Heating Cycle: 10 K/min (to T_h); HR_1 = 0, 2.5, 5, or 10 K/min (until t_c). (a) Effusion rate of $CO_{(g)}$ (max p_{CO} indicated). (b) Pressure of $CO_{(g)}$ at the center of the sample. (c) Heating Profile.

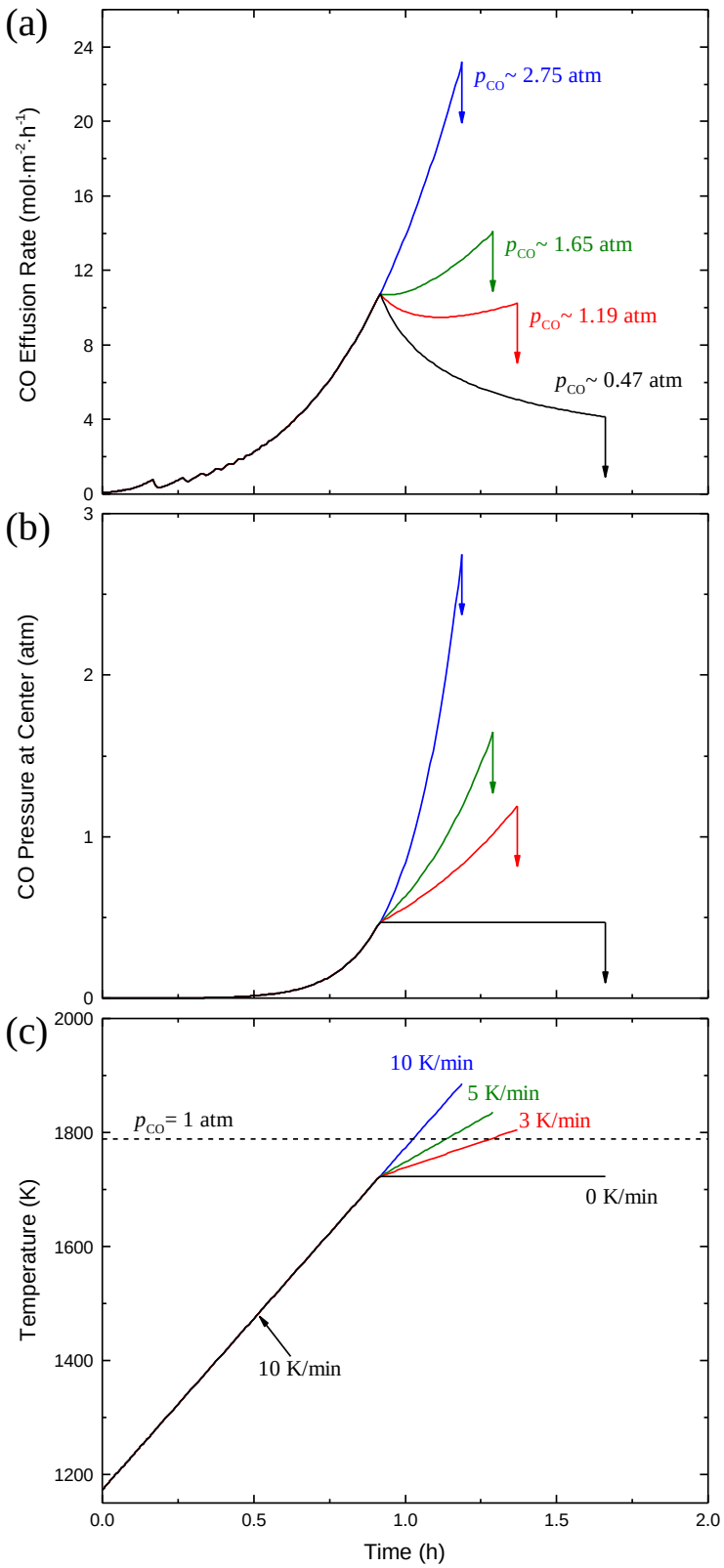

Figure 5-35: Four simulations: l= 1 cm, X_{SiO_2}= 1.5, T_i=1173.15 K, and T_h=1723.15 K. Heating Cycle: 10 K/min (to T_h); HR_1 = 0, 3, 5, or 10 K/min (until t_c). (a) Effusion rate of $CO_{(g)}$ (max p_{CO} indicated). (b) Pressure of $CO_{(g)}$ at the center of the sample. (c) Heating Profile.

5.3.5.4 *2 or 4 cm thick, 1.0 or 1.5 mol % SiO_2, and T_h = 1673.15 K or 1723.15 K samples*

These next eight sets of simulations are used to compare the effect of changing the heating rate on samples of increasing thickness. Eight sets of simulations are shown, each with a sample thickness of 2 (l_2) or 4 cm (l_3), oxide content of 1.0 ($X_{\mathrm{SiO_2},1}$) or 1.5 mol % ($X_{\mathrm{SiO_2},2}$), and threshold temperature of 1673.15 K ($T_{h,1}$) or 1723.15 K ($T_{h,2}$). The heating rate (HR_1) was varied after reaching T_h. The heating rate for the $T_{h,1}$ simulations was varied between 10, 5, 2.5, or 0 K/min; alternatively labeled as $HR_{1,1a}$, $HR_{1,2a}$, $HR_{1,3a}$, and $HR_{1,4a}$, respectively. The heating rate for the $T_{h,2}$ simulations was varied between 10, 5, 3, or 0 K/min; alternatively labeled as $HR_{1,1b}$, $HR_{1,2b}$, $HR_{1,3b}$, and $HR_{1,4b}$, respectively. The time evolution of the $CO_{(g)}$ effusion rates ($J_{CO_{(g)}}$), the $CO_{(g)}$ pressure ($p_{CO_{(g)}}$) in the center of the sample, and the heating profiles for eight sets of simulations are shown in Figure 5-36 through Figure 5-43(a),(b), and (c), respectively. Table 5-19 through Table 5-26 provide t_c, T, maximum $p_{CO_{(g)}}$, and $J_{CO_{(g)}}$ at the end of each simulation, in order of increasing time for complete oxide removal.

These sets of simulations show the same trends in the $J_{CO_{(g)}}$ behavior as the previous sections. As the sample thickness increases, it is evident that simulations with $HR_{1,4a}$ and $HR_{1,4b}$ are increasingly inefficient at removing all of the oxide. This effect is worse for $X_{\mathrm{SiO_2},2}$ simulations, because more oxide is being removed with a progressively lower $J_{CO_{(g)}}$. The main difference between these sets of simulations and the previous sets of l_1 simulations is that $HR_{1,3a}$ and $HR_{1,3b}$ simulations are no longer effective at maintain $J_{CO_{(g)}}$ below the threshold reached at T_h. This is a result of the thicker samples reaching higher temperatures and internal $p_{CO_{(g)}}$ by the time t_c is reached. Though the $HR_{1,3a}$ and $HR_{1,3b}$ simulations exceed the desired $J_{CO_{(g)}}$ level, they provide a much greater time saving compared to the isothermal holds.

Additional modifications to the heating cycle to maintain the desired $J_{CO_{(g)}}$ level are shown in the following section.

Simulations from all sets with heating rates of $HR_{1,1a}$, $HR_{1,1b}$, $HR_{1,2a}$, and $HR_{1,2b}$ reach unrealistic temperatures by the time t_c is reached. The inclusion of these simulations was to show that at these heating rates, even if the internal $p_{CO_{(g)}}$ would not causes rupture of the sample and $J_{CO_{(g)}}$ could be tolerated by the processing equipment, the temperature reached at t_c would cause changes in the sample that violate the model assumptions. At elevated temperatures, real samples will begin to densify and close the pore network hence impeding or even stopping gas effusion. These secondary effects were not modeled and can be expected to drastically change the oxide removal process.

These simulations show that reducing the heating rate can greatly reduce the time for complete oxide removal compared to isothermal holds. The time savings becomes more significant for thicker samples. However, for even the lowest heating rate the effusion rate will rise to considerably higher levels than the effusion rate at the hold temperature. This effect was not seen for thinner samples because all the oxide was exhausted before the effusion rate rose significantly. Ultimately, despite reducing the time for oxide removal, a single reduction in the heating rate may not always be a practical processing solution.

Table 5-19: Simulation results from l = 2 cm, X_{SiO_2}= 1.0 mol % samples with variable heating rates after T_h=1673.15 K.

Varied Parameters (In order of oxide removal)	t_c (h)	T (K)	$p_{CO_{(g)}}$ (atm)	$J_{CO_{(g)}}$ (mol·m^{-2}·h^{-1})
$HR_{1,1a}$= 10 K/min	1.3464	1980.97	6.75	27.52
$HR_{1,2a}$= 5 K/min	1.6407	1915.32	3.68	15.26
$HR_{1,3a}$= 2.5 K/min	2.0525	1856.01	2.04	8.63
$HR_{1,4a}$= 0 K/min	4.9761	1673.13	0.25	1.13

Table 5-20: Simulation results from l = 2 cm, X_{SiO_2}= 1.0 mol % samples with variable heating rates after T_h=1723.15 K.

Varied Parameters (In order of oxide removal)	t_c (h)	T (K)	$p_{CO_{(g)}}$ (atm)	$J_{CO_{(g)}}$ (mol·m^{-2}·h^{-1})
$HR_{1,1b}$= 10 K/min	1.3464	1980.97	6.75	27.52
$HR_{1,2b}$= 5 K/min	1.5656	1917.81	3.76	15.48
$HR_{1,3b}$= 3 K/min	1.7671	1876.21	2.51	10.52
$HR_{1,4b}$= 0 K/min	3.1228	1723.13	0.47	2.06

Table 5-21: Simulation results from l = 2 cm, X_{SiO_2}= 1.5 mol % samples with variable heating rates after T_h=1673.15 K.

Varied Parameters (In order of oxide removal)	t_c (h)	T (K)	$p_{CO_{(g)}}$ (atm)	$J_{CO_{(g)}}$ (mol·m^{-2}·h^{-1})
$HR_{1,1a}$= 10 K/min	1.4172	2023.45	9.75	39.53
$HR_{1,2a}$= 5 K/min	1.7696	1954.02	5.29	21.86
$HR_{1,3a}$= 2.5 K/min	2.2837	1890.68	2.9	12.17
$HR_{1,4a}$= 0 K/min	7.0959	1673.13	0.25	1.14

Table 5-22: Simulation results from l = 2 cm, X_{SiO_2}= 1.5 mol % samples with variable heating rates after T_h=1723.15 K.

Varied Parameters (In order of oxide removal)	t_c (h)	T (K)	$p_{CO_{(g)}}$ (atm)	$J_{CO_{(g)}}$ (mol·m^{-2}·h^{-1})
$HR_{1,1b}$= 10 K/min	1.4172	2023.45	9.75	39.53
$HR_{1,2b}$= 5 K/min	1.6922	1955.77	5.37	22.2
$HR_{1,3b}$= 3 K/min	1.9575	1910.48	3.51	14.68
$HR_{1,4b}$= 0 K/min	4.2803	1723.13	0.47	2.08

Table 5-23: Simulation results from l = 4 cm, X_{SiO_2}= 1.0 mol % samples with variable heating rates after T_h=1673.15 K.

Varied Parameters (In order of oxide removal)	t_c (h)	T (K)	$p_{CO_{(g)}}$ (atm)	$J_{CO_{(g)}}$ (mol·m^{-2}·h^{-1})
$HR_{1,1a}$= 10 K/min	1.599	2132.48	23.22	45.37
$HR_{1,2a}$= 5 K/min	2.106	2054.93	12.66	25.27
$HR_{1,3a}$= 2.5 K/min	2.9003	1983.17	6.89	14.03
$HR_{1,4a}$= 0 K/min	17.7556	1673.13	0.25	0.57

Table 5-24: Simulation results from l = 4 cm, X_{SiO_2}= 1.0 mol % samples with variable heating rates after T_h=1723.15 K.

Varied Parameters (In Order of Oxide Removal)	t_c (h)	T (K)	$p_{CO_{(g)}}$ (atm)	$J_{CO_{(g)}}$ (mol·m^{-2}·h^{-1})
$HR_{1,1b}$= 10 K/min	1.599	2132.48	23.22	45.37
$HR_{1,2b}$= 5 K/min	2.0252	2055.67	12.73	25.42
$HR_{1,3b}$= 3 K/min	2.4719	2003.07	8.2	16.62
$HR_{1,4b}$= 0 K/min	10.1226	1723.13	0.47	1.03

Table 5-25: Simulation results from l = 4 cm, X_{SiO_2}= 1.5 mol % samples with variable heating rates after T_h=1673.15 K.

Varied Parameters (In order of oxide removal)	t_c (h)	T (K)	$p_{CO_{(g)}}$ (atm)	$J_{CO_{(g)}}$ (mol·m^{-2}·h^{-1})
$HR_{1,1a}$= 10 K/min	1.6823	2182.5	33.5	65.1
$HR_{1,2a}$= 5 K/min	2.2588	2100.78	18.22	36.18
$HR_{1,3a}$= 2.5 K/min	3.1792	2025	9.88	20.02

Table 5-26: Simulation results from l = 4 cm, X_{SiO_2}= 1.5 mol % samples with variable heating rates after T_h=1723.15 K.

Varied Parameters (In order of oxide removal)	t_c (h)	T (K)	$p_{CO_{(g)}}$ (atm)	$J_{CO_{(g)}}$ (mol·m^{-2}·h^{-1})
$HR_{1,1b}$= 10 K/min	1.6823	2182.5	33.5	65.1
$HR_{1,2b}$= 5 K/min	2.1773	2101.3	18.3	36.33
$HR_{1,3b}$= 3 K/min	2.7075	2045.48	11.72	23.61

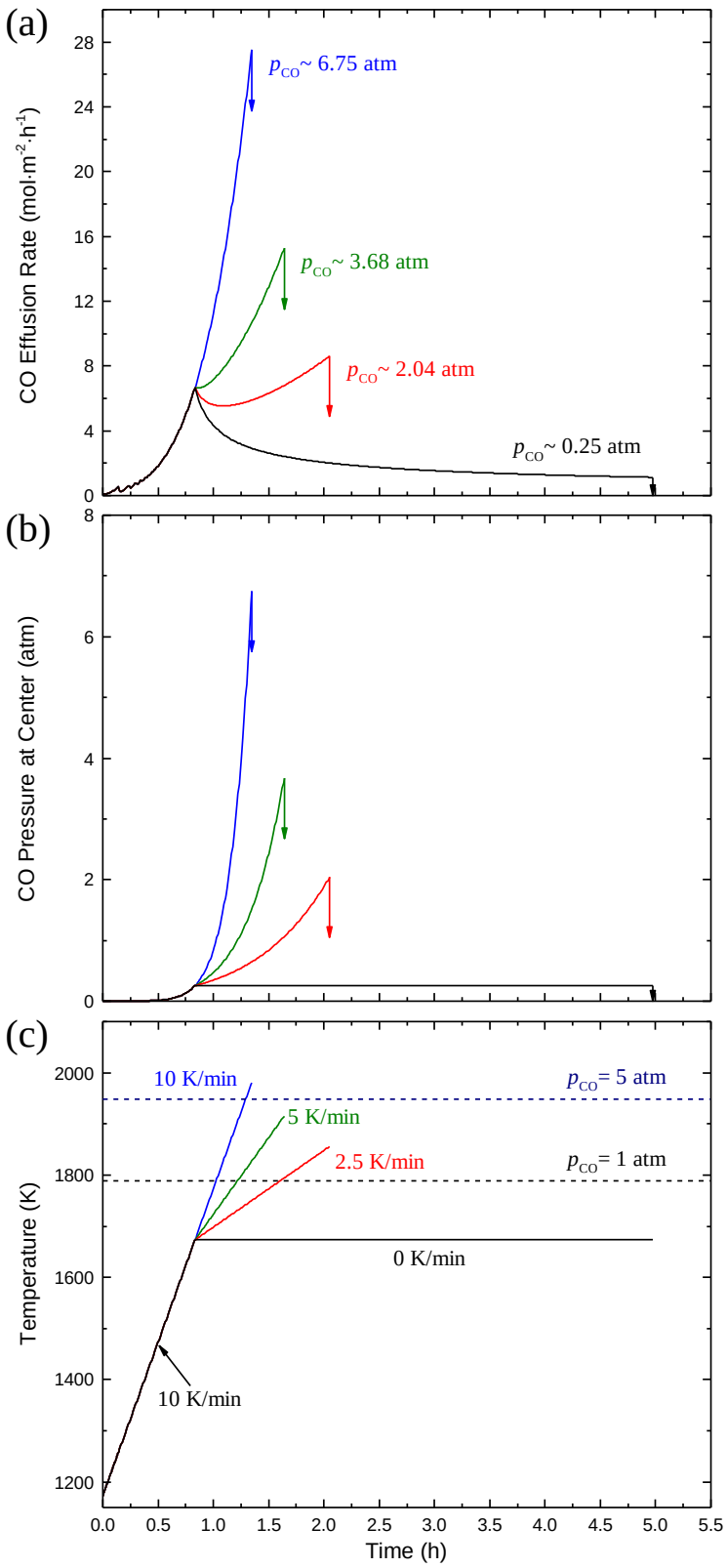

Figure 5-36: Four simulations: l= 2 cm, X_{SiO_2}= 1.0, T_i=1173.15 K, and T_h=1673.15 K. Heating Cycle: 10 K/min (to T_h); HR_1 = 0, 2.5, 5, or 10 K/min (until t_c). (a) Effusion rate of $CO_{(g)}$ (max p_{CO} indicated). (b) Pressure of $CO_{(g)}$ at the center of the sample. (c) Heating Profile.

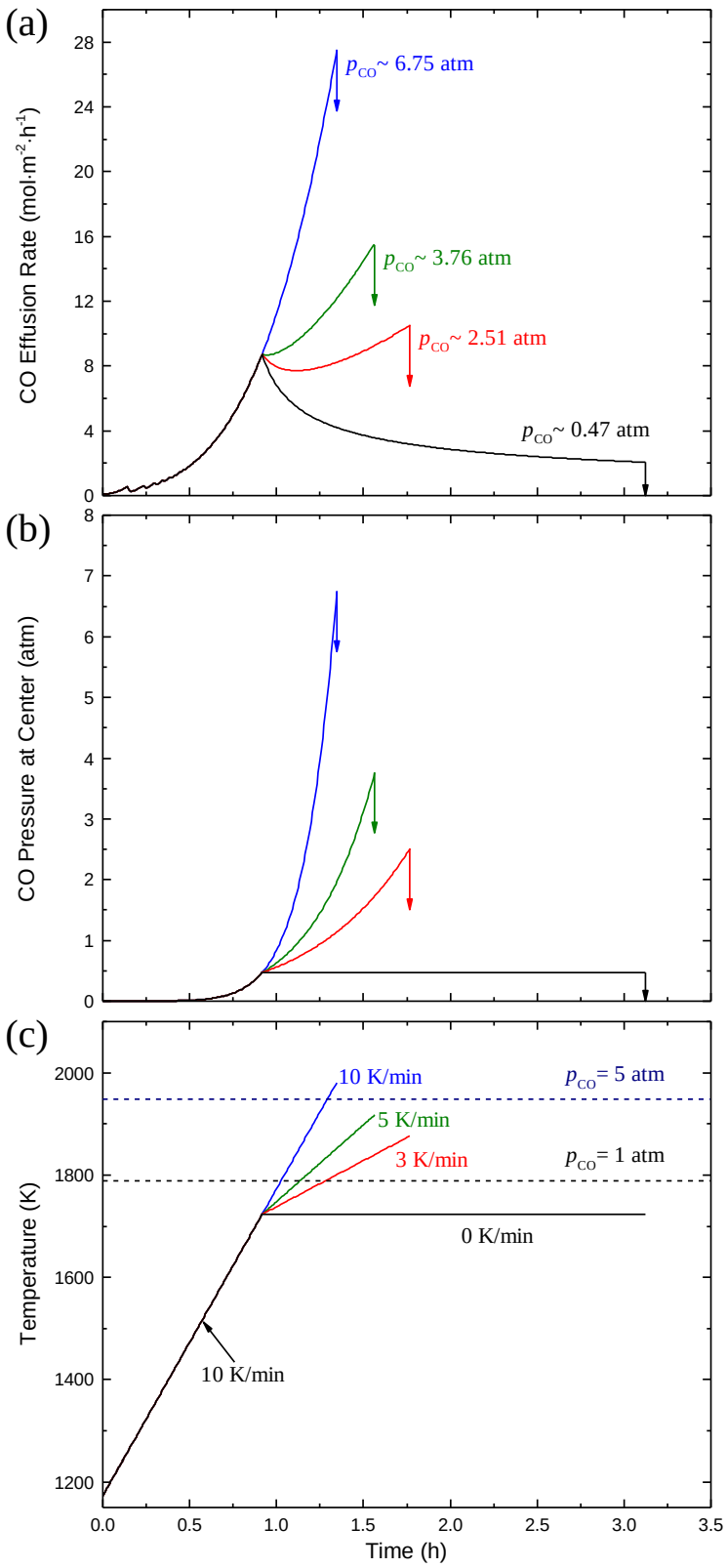

Figure 5-37: Four simulations: l= 2 cm, X_{SiO_2}= 1.0, T_i=1173.15 K, and T_h=1723.15 K. Heating Cycle: 10 K/min (to T_h); HR_1 = 0, 3, 5, or 10 K/min (until t_c). (a) Effusion rate of $CO_{(g)}$ (max p_{CO} indicated). (b) Pressure of $CO_{(g)}$ at the center of the sample. (c) Heating Profile.

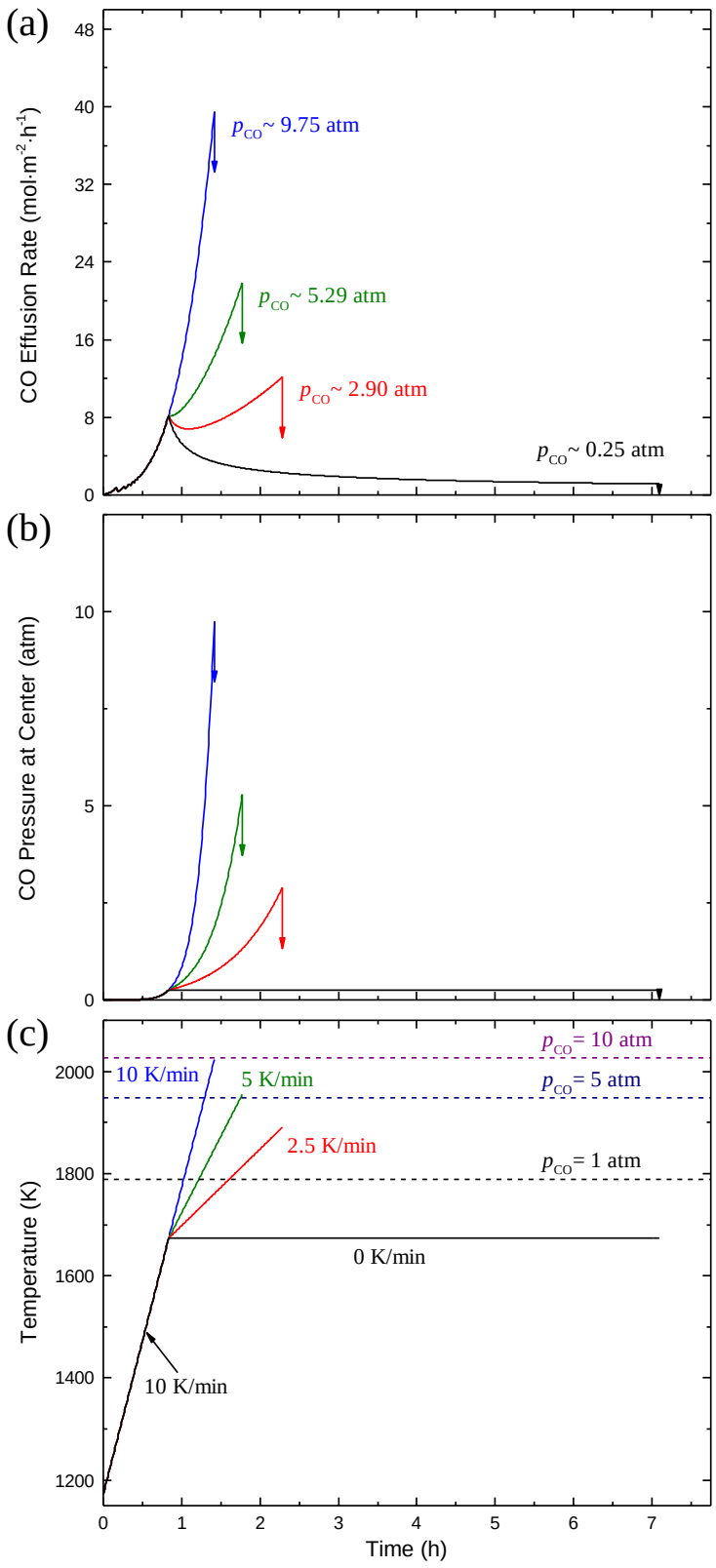

Figure 5-38: Four simulations: l= 2 cm, X_{SiO_2}= 1.5 mol %, T_i=1173.15 K, and T_h=1673.15 K. Heating Cycle: 10 K/min (to T_h); HR_1 = 0, 2.5, 5, or 10 K/min (until t_c). (a) Effusion rate of $CO_{(g)}$ (max p_{CO} indicated). (b) Pressure of $CO_{(g)}$ at the center of the sample. (c) Heating Profile.

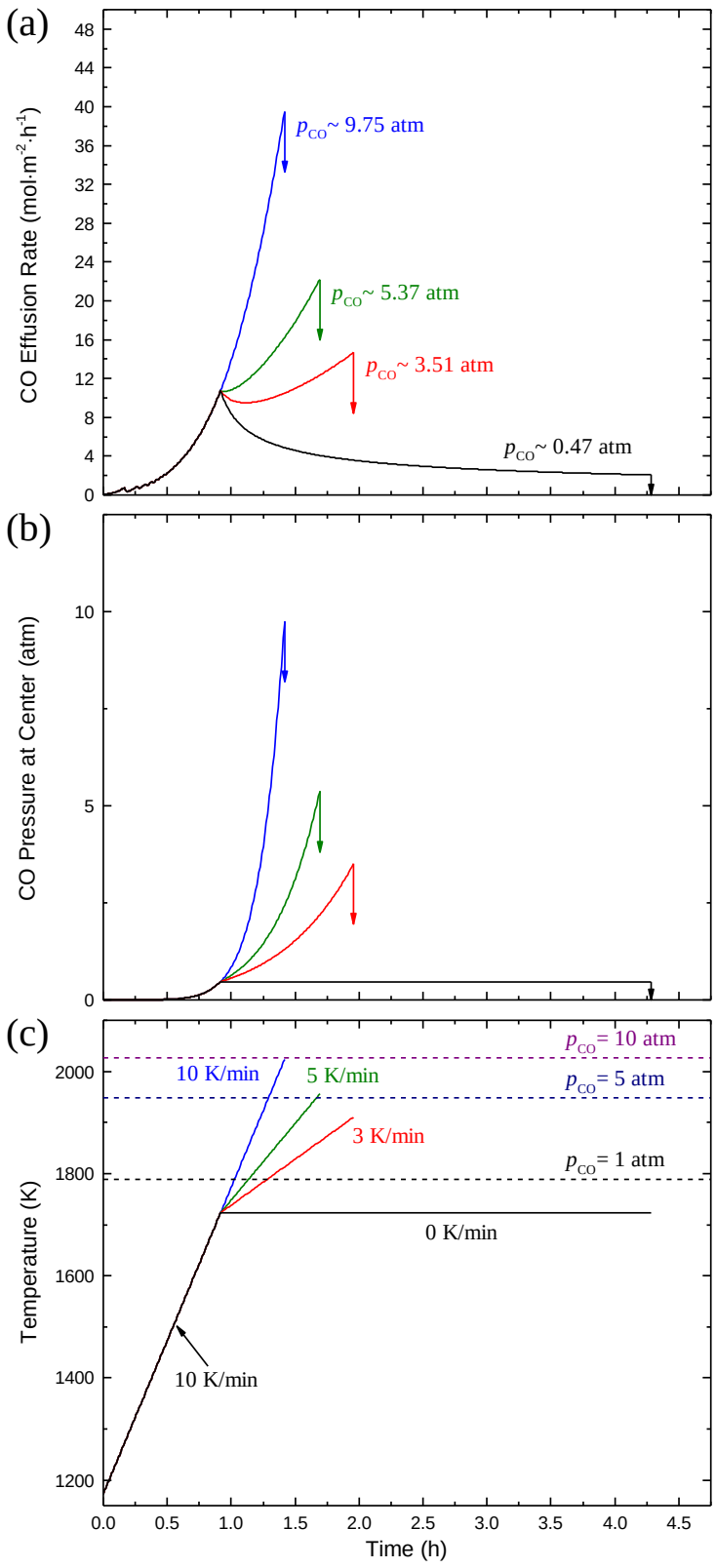

Figure 5-39: Four simulations: l= 2 cm, X_{SiO_2}= 1.5 mol %, T_i=1173.15 K, and T_h=1723.15 K. Heating Cycle: 10 K/min (to T_h); HR_1 = 0, 3, 5, or 10 K/min (until t_c). (a) Effusion rate of $CO_{(g)}$ (max p_{CO} indicated). (b) Pressure of $CO_{(g)}$ at the center of the sample. (c) Heating Profile.

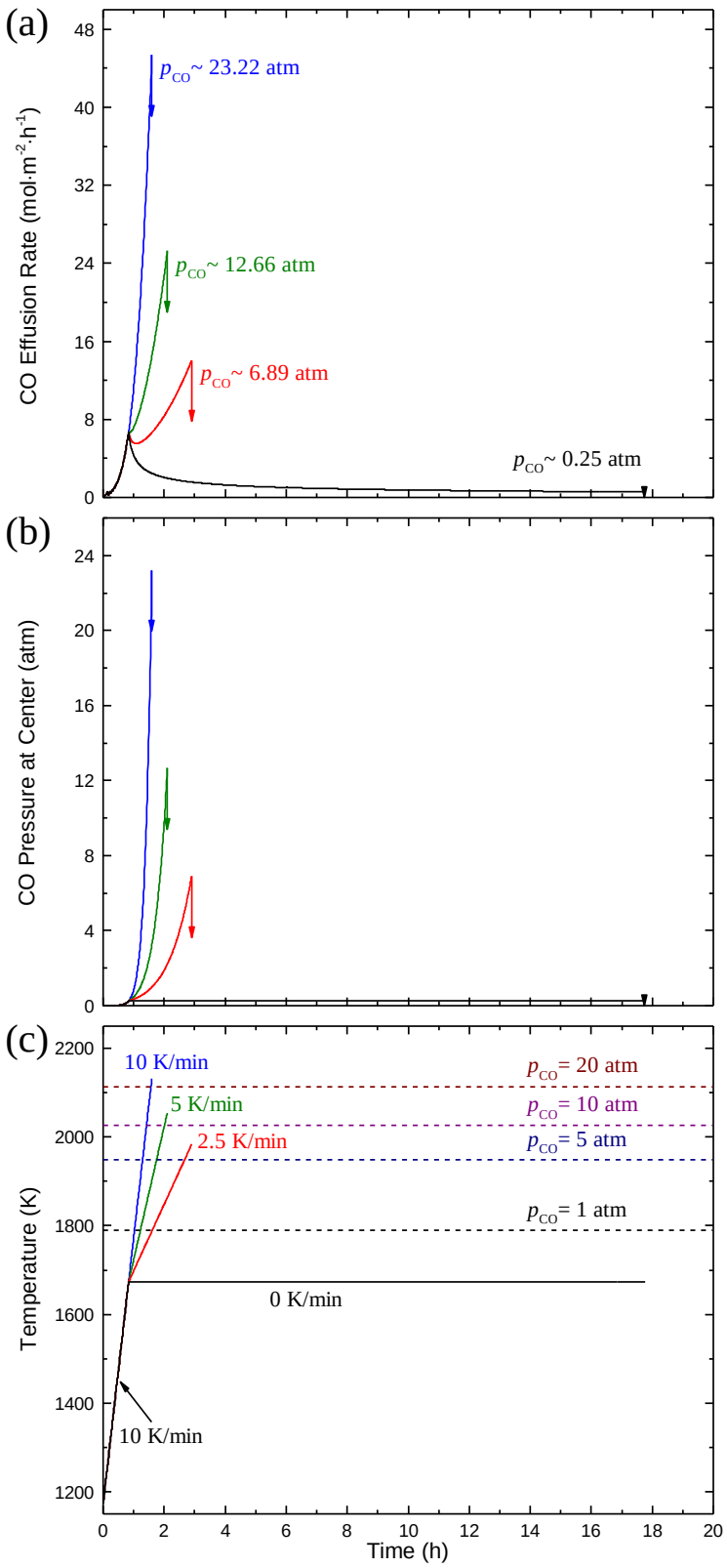

Figure 5-40: Four simulations: l= 4 cm, X_{SiO_2}= 1.0 mol %, T_i=1173.15 K, and T_h=1673.15 K. Heating Cycle: 10 K/min (to T_h); HR_1 = 0, 2.5, 5, or 10 K/min (until t_c). (a) Effusion rate of $CO_{(g)}$ (max p_{CO} indicated). (b) Pressure of $CO_{(g)}$ at the center of the sample. (c) Heating Profile.

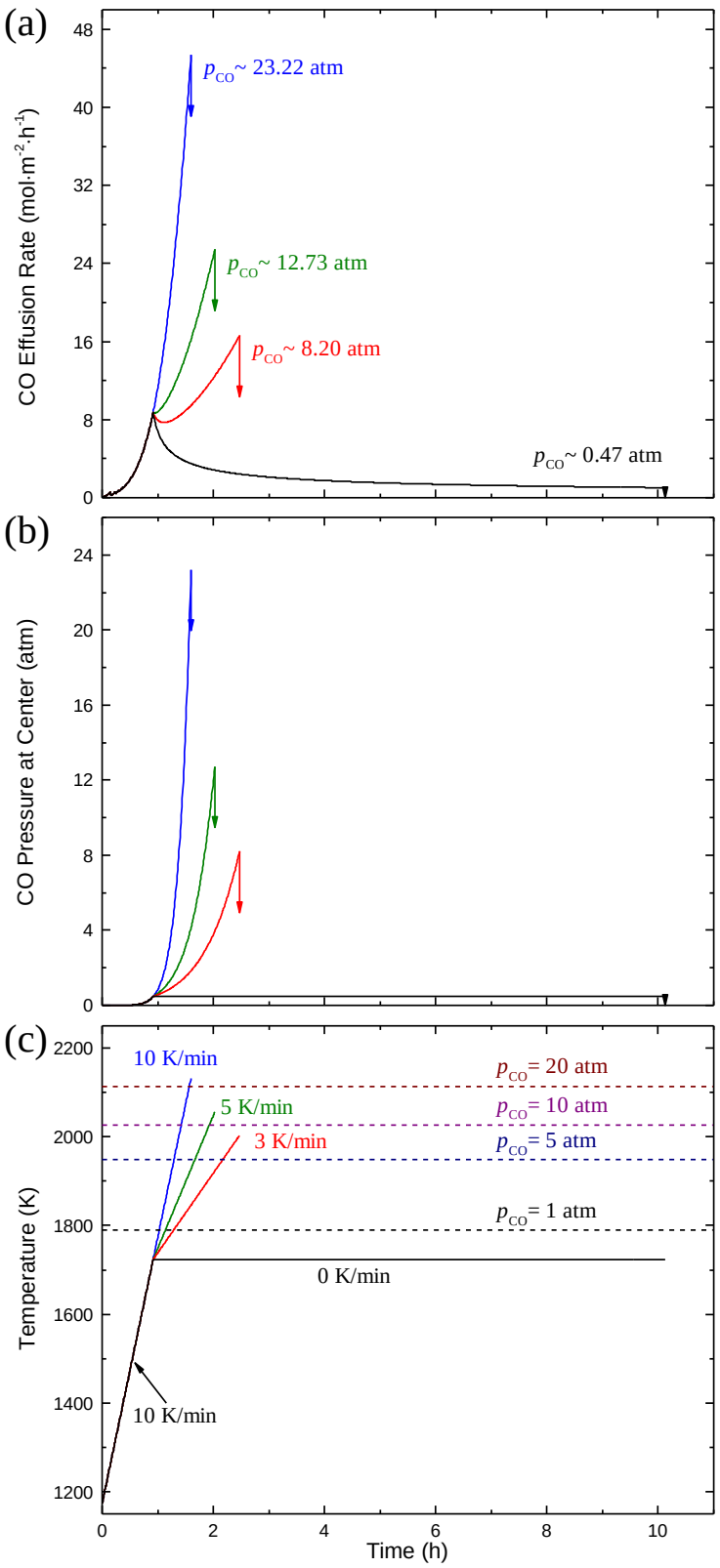

Figure 5-41: Four simulations: l= 4 cm, X_{SiO_2}= 1.0 mol %, T_i=1173.15 K, and T_h=1723.15 K. Heating Cycle: 10 K/min (to T_h); HR_1 = 0, 3, 5, or 10 K/min (until t_c). (a) Effusion rate of $CO_{(g)}$ (max p_{CO} indicated). (b) Pressure of $CO_{(g)}$ at the center of the sample. (c) Heating Profile.

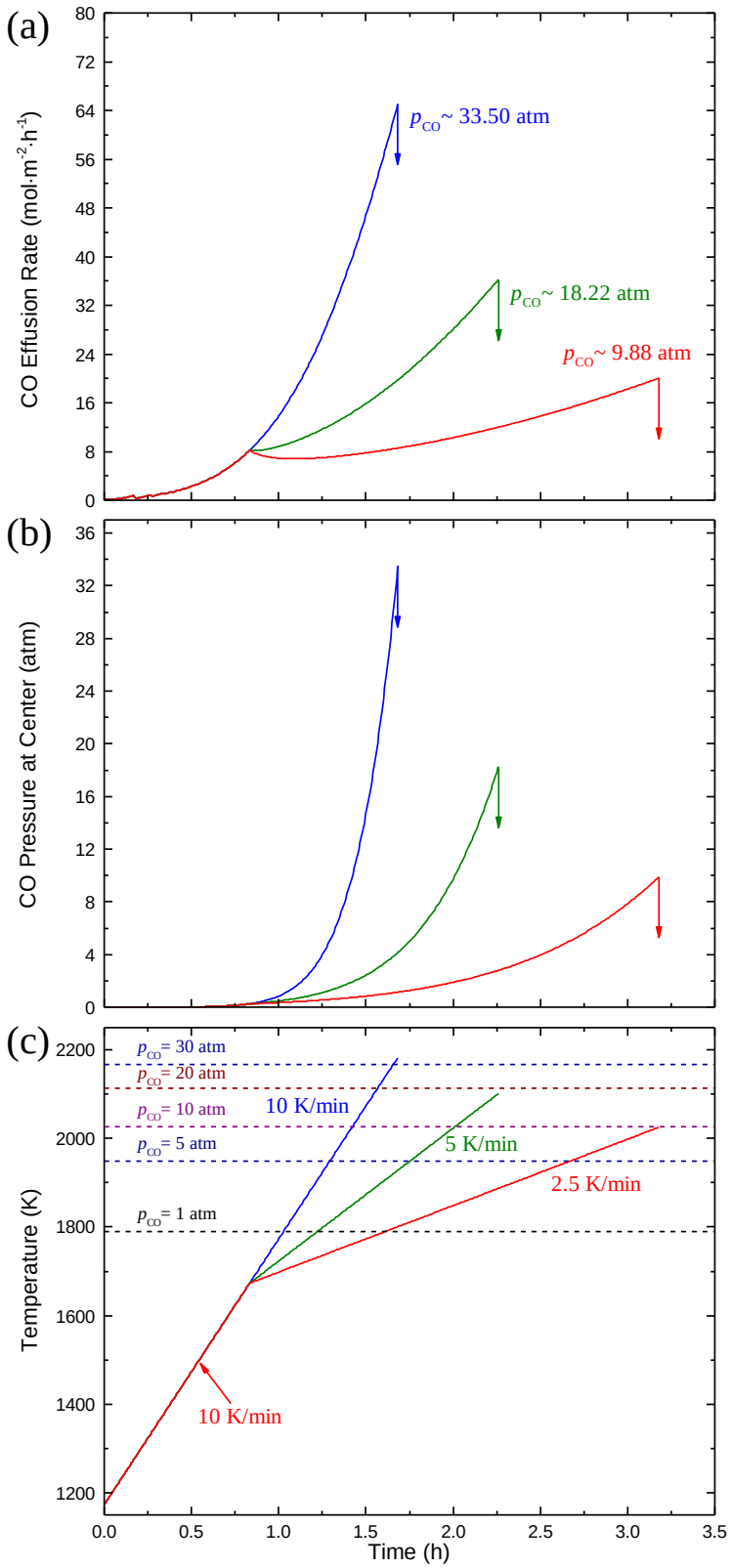

Figure 5-42: Three simulations: l= 4 cm, X_{SiO_2}= 1.5 mol %, T_i=1173.15 K, and T_h=1673.15 K. Heating Cycle: 10 K/min (to T_h); HR_1= 2.5, 5, or 10 K/min (until t_c). (a) Effusion rate of $CO_{(g)}$ (max p_{CO} indicated). (b) Pressure of $CO_{(g)}$ at the center of the sample. (c) Heating Profile.

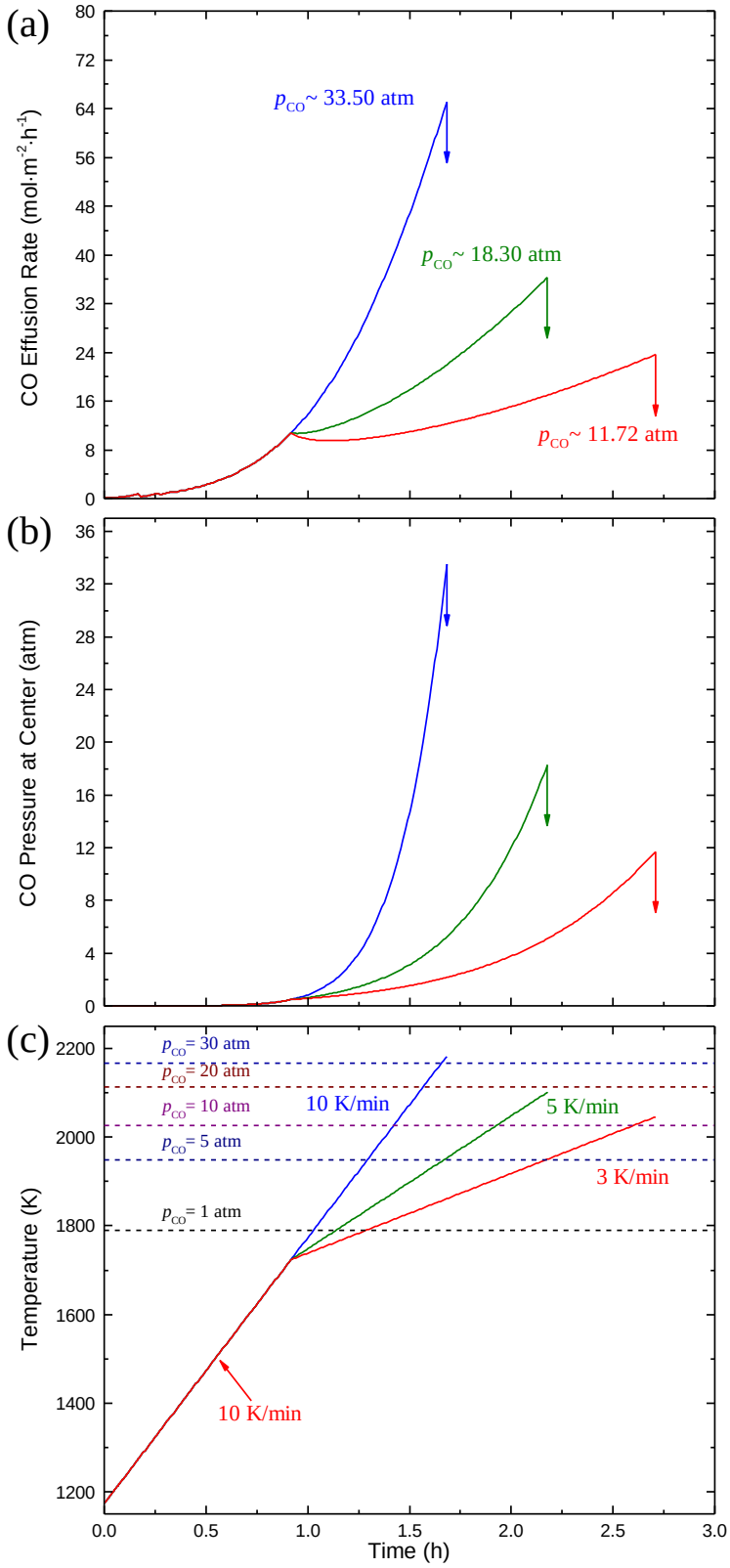

Figure 5-43: Three simulations: l= 4 cm, X_{SiO_2}= 1.5 mol %, T_i=1173.15 K, and T_h=1673.15 K. Heating Cycle: 10 K/min (to T_h); HR_1= 3, 5, or 10 K/min (until t_c). (a) Effusion rate of $CO_{(g)}$ (max p_{CO} indicated). (b) Pressure of $CO_{(g)}$ at the center of the sample. (c) Heating Profile.

5.3.6 Effusion Controlled Ramping Rates Simulations

The goal of this section is to study the effect of making multiple adjustments to the heating rate in an attempt to maintain the effusion rate below a specified level. These simulations were in response to observing that a single adjustment of the heating rate at the threshold temperature (T_h) is only effective at controlling the gas effusion rate for thin samples. If the sample is heated above T_h the maximum internal pressure will increase, therefore any heating rate changes are only effective at maintaining the effusion rate below a specified level and not the pressure. A number of sets of simulations were designed to illustrate the difference in effusion rate, pressure, and time for complete oxide removal when using different heating rates.

5.3.6.1 *2 and 4 cm thick, 1.0 mol % SiO_2, and T_h = 1673.15 K samples*

This set of simulations investigates the effect of incorporating multiple heating rate reductions to control the gas effusion rate during oxide removal. Five simulations are shown, each with sample thicknesses of 2 (l_2) and 4 cm (l_3), oxide content of 1.0 mol % ($X_{\mathrm{SiO_2},1}$), and threshold temperature of 1673.15 K ($T_{h,1}$) are presented. The heating rate was varied after reaching T_h. The heating rates for the simulations were varied between 2.5, 1, and 0.5 K/min; alternatively labeled as HR_{1a}, HR_{2a}, and HR_{3a}, respectively. The simulations were designed to progressively add heating rate modifications to keep $J_{CO_{(g)}}$ below the threshold $J_{CO_{(g)}}$ reached at T_h. The time evolution of the $CO_{(g)}$ effusion rates ($J_{CO_{(g)}}$), the $CO_{(g)}$ pressure ($p_{CO_{(g)}}$) in the center of the sample, and the heating profile are shown in Figure 5-44 (a),(b), and (c), respectively. Table 5-27 provides t_c, T, maximum $p_{CO_{(g)}}$, and $J_{CO_{(g)}}$ at the end of each simulation, in order of increasing time for complete oxide removal.

This set of simulations shows how the $J_{CO_{(g)}}$ behavior can be modified by making multiple heating rate modifications. Both the l_2 and l_3 samples heated at HR_{1a} have a higher $J_{CO_{(g)}}$ at t_c than the threshold $J_{CO_{(g)}}$. After heating at $HR_{1,a}$ for 0.6$\bar{6}$ h (40 min), if the heating rate is changed to HR_{2a} then the l_2 sample successfully stays below the threshold $J_{CO_{(g)}}$. However, the l_3 sample will still exceed the threshold $J_{CO_{(g)}}$ upon reaching t_c. To successfully optimize the l_3 sample, after heating at HR_{2a} for 1.75 h the heating rate should be changed to HR_{3a}. The addition of modifications which progressively slow the heating rate can modulate $J_{CO_{(g)}}$ to be kept below a specified level

Each reduction in the heating rate results in $J_{CO_{(g)}}$ reaching a minimum before increasing again; provided that the reduction in the heating rate is large enough. The curvature of $J_{CO_{(g)}}$ at the HR_{1a} minimum is the largest of the $J_{CO_{(g)}}$ minimums. The curvature of $J_{CO_{(g)}}$ at the HR_{2a} minimum is lower than HR_{1a}. If the HR_{3a} minimum would have been reached (as it would have for thicker samples), it would have had the lowest curvature. The trend of reduced $J_{CO_{(g)}}$ curvature for successive heating rate modifications indicates that each progressive heating rate reduction is effective for a longer time at maintaining $J_{CO_{(g)}}$ below a given level. Thus, the time interval between requiring heating rate modifications to maintain a specified $J_{CO_{(g)}}$ becomes progressively longer. Ultimately, slowing the heating rate allows $J_{CO_{(g)}}$ to be maintained below a maximum level.

Table 5-27: Simulation results for l = 2 and 4 cm, X_{SiO_2}= 1.0 mol % samples with variable heating rates after $T_{h,1}$=1673.15 K.

Varied Parameters (In order of oxide removal)	t_c (h)	T (K)	$p_{CO_{(g)}}$ (atm)	$J_{CO_{(g)}}$ (mol·m^{-2}·h^{-1})
l_2=2 cm; HR_{1a}= 2.5 K/min	2.0525	1856.01	2.04	8.63
l_2=2 cm; HR_{1a}= 2.5 K/min (0.6$\bar{6}$ h), HR_{2a}= 1 K/min	2.2012	1815.2	1.33	5.69
l_3=4 cm; HR_{1a}= 2.5 K/min	2.9003	1983.17	6.89	14.03
l_3=4 cm; HR_{1a}= 2.5 K/min (0.6$\bar{6}$ h), HR_{2a}= 1 K/min	3.7307	1906.97	3.4	7.05
l_3=4 cm; HR_{1a}= 2.5 K/min (0.6$\bar{6}$ h), HR_{2a}= 1 K/min (1.75 h), HR_{3a}= 0.5 K/min	3.7649	1893.57	2.98	6.22

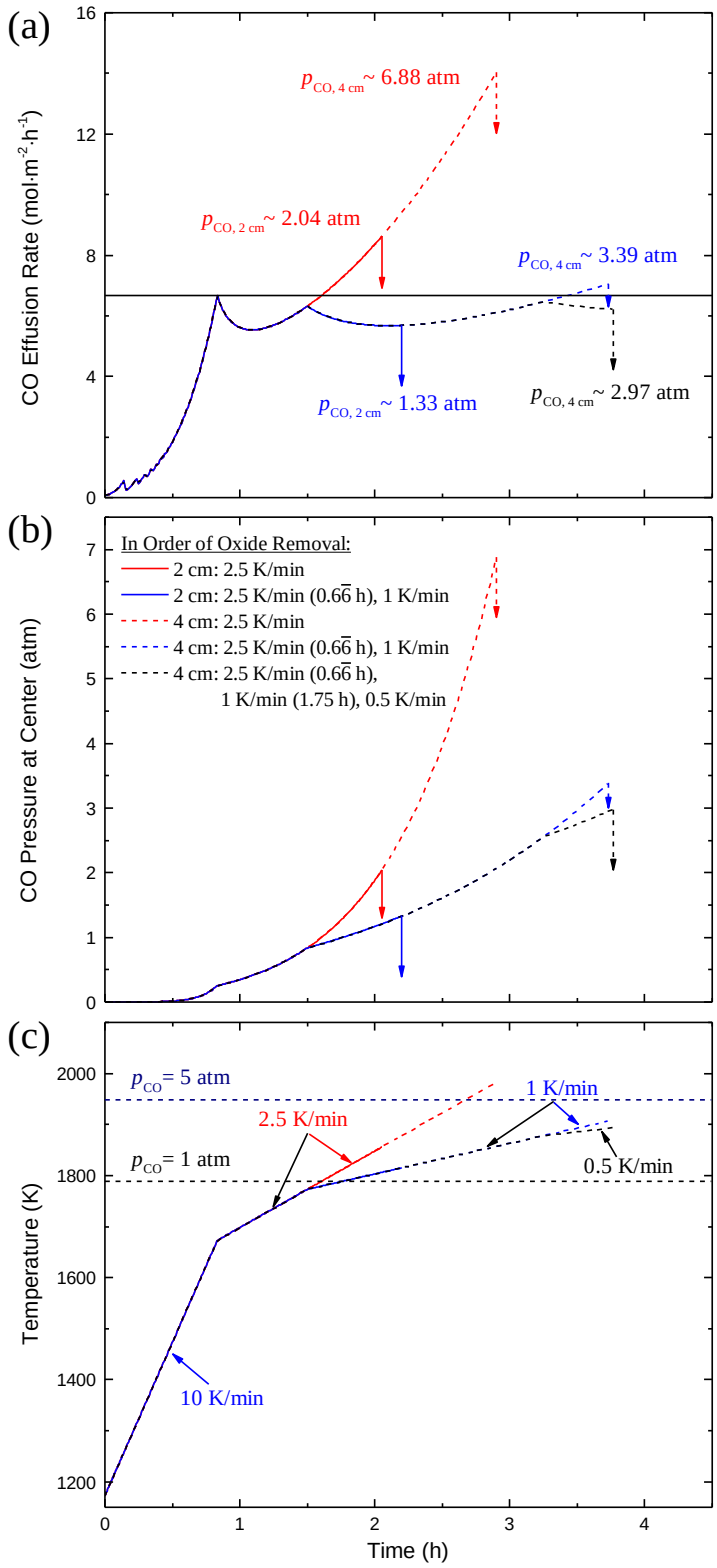

Figure 5-44: Five simulations: l= 2 or 4 cm, X_{SiO_2}= 1.0 mol %, T_i= 1173.15 K, and T_h= 1673.15 K. Heating Cycle: 10 K/min (to T_h); HR_1= 2.5 K/min (0.66̄ h or until t_c); HR_2= 1 K/min (1.75 h or until t_c); HR_3= 0.5 K/min (until t_c). (a) Effusion rate of $CO_{(g)}$ (max p_{CO} and threshold $J_{CO_{(g)}}$ indicated). (b) Pressure of $CO_{(g)}$ at the center of the sample. (c) Heating Profile.

5.3.6.2 *2 and 4 cm thick, 1.0 mol % SiO_2, and T_h = 1723.15 K samples*

This set of simulations investigates the effect of incorporating multiple heating rate reductions starting at a higher holding temperature to control the gas effusion rate during oxide removal. Four simulations are shown, each with sample thicknesses of 2 (l_2) and 4 cm (l_3), oxide content of 1.0 mol % ($X_{\mathrm{SiO}_2,1}$), and threshold temperature of 1723.15 K ($T_{\mathrm{h},2}$) are presented. The heating rate was varied after reaching T_{h}. The heating rates for the simulations were varied between 3 and 1 K/min; alternatively labeled as HR_{1b} and HR_{2b}, respectively. The simulations were designed to progressively add heating rate modifications to keep $J_{CO_{(g)}}$ below the threshold $J_{CO_{(g)}}$ reached at T_{h}. The time evolution of the $CO_{(g)}$ effusion rates ($J_{CO_{(g)}}$), the $CO_{(g)}$ pressure ($p_{CO_{(g)}}$) in the center of the sample, and the heating profile are shown in Figure 5-45 (a),(b), and (c), respectively. Table 5-28 provides t_c, T, maximum $p_{CO_{(g)}}$, and $J_{CO_{(g)}}$ at the end of each simulation, in order of increasing time for complete oxide removal.

This set of simulations shows the same trends in the $J_{CO_{(g)}}$ behavior as the previous section. A difference between these two sets of simulations is that the ($T_{\mathrm{h},2}$, l_3) sample only requires 2 heating rate modifications rather than 3 needed for the ($T_{\mathrm{h},1}$, l_3) sample. This is a consequence of accepting a higher threshold $J_{CO_{(g)}}$ at $T_{\mathrm{h},2}$. The use of HR_{1b} results in a larger $J_{CO_{(g)}}$ curvature than when using HR_{1a}. Due to the higher curvature, the transition to HR_{2b} was required after 0.5 h at HR_{1b} to avoid exceeding the threshold $J_{CO_{(g)}}$. Since $HR_{1b} > HR_{1a}$, $J_{CO_{(g)}}$ remained closer to the threshold $J_{CO_{(g)}}$, but the time interval between heating rate modifications was decreased. Ultimately, there is a tradeoff between the magnitude of heating rate modifications, the heating rate duration, and the ability to keep $J_{CO_{(g)}}$ close to the threshold $J_{CO_{(g)}}$.

Table 5-28: Simulation results for l = 2 and 4 cm, $X_{SiO_{2,1}}$ = 1.0 mol % samples with variable heating rates after $T_{h,2}$=1723.15 K.

Varied Parameters (In order of oxide removal)	t_c (h)	T (K)	$p_{CO_{(g)}}$ (atm)	$J_{CO_{(g)}}$ (mol·m^{-2}·h^{-1})
l_2=2 cm; HR_{1b}= 3 K/min	1.7671	1876.21	2.51	10.52
l_2=2 cm; HR_{1b}= 3 K/min (0.5 h), HR_{2b}= 1 K/min	1.847	1838.95	1.71	7.27
l_3=4 cm; HR_{1b}= 3 K/min	2.4719	2003.07	8.2	16.62
l_3=4 cm; HR_{1b}= 3 K/min (0.5 h), HR_{2b}= 1 K/min	3.1519	1917.24	3.74	7.77

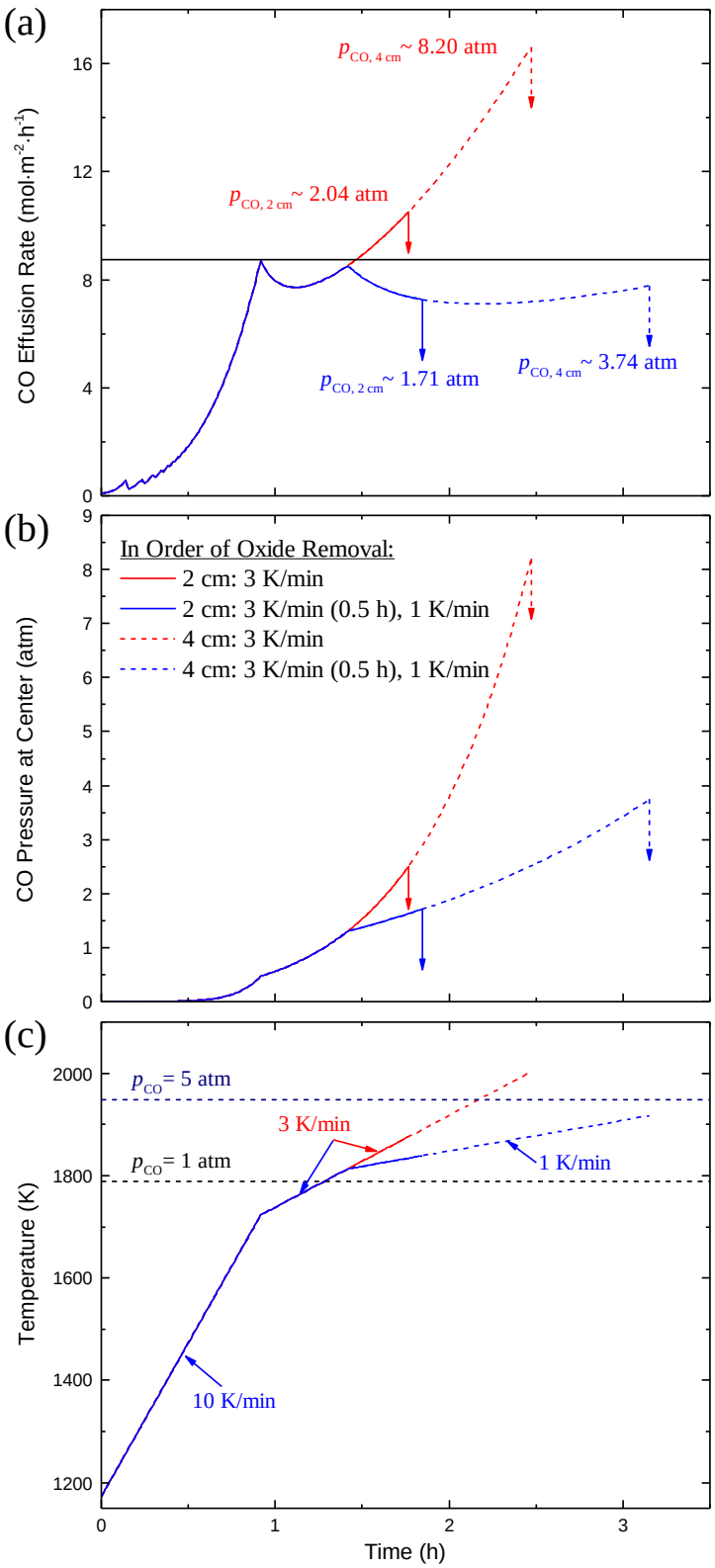

Figure 5-45: Four simulations: l= 2 or 4 cm, X_{SiO_2}= 1.0 mol %, T_i= 1173.15 K, and T_h= 1723.15 K. Heating Cycle: 10 K/min (to T_h); HR_1= 3 K/min (0.5 h or until t_c); HR_2= 1 K/min (until t_c). (a) Effusion rate of $CO_{(g)}$ (max p_{CO} and threshold $J_{CO_{(g)}}$ indicated). (b) Pressure of $CO_{(g)}$ at the center of the sample. (c) Heating Profile.

5.3.6.3 *2 and 4 cm thick, 1.5 mol % SiO_2, and T_h = 1673.15 K samples*

This set of simulations investigates the effect of incorporating multiple heating rate reductions to control the gas effusion rate during oxide removal when starting with a higher initial oxide content. Five simulations are shown, each with sample thicknesses of 2 (l_2) and 4 cm (l_3), oxide content of 1.5 mol % ($X_{\mathrm{SiO}_2,2}$), and threshold temperature of 1673.15 K ($T_{\mathrm{h},1}$) are presented. The heating rate was varied after reaching T_{h}. The heating rates for the simulations were varied between 2.5, 1, and 0.5 K/min; alternatively labeled as HR_{1a}, HR_{2a}, and HR_{3a}, respectively. The simulations were designed to progressively add heating rate modifications to keep $J_{CO_{(g)}}$ below the threshold $J_{CO_{(g)}}$ reached at T_{h}. The time evolution of the $CO_{(g)}$ effusion rates ($J_{CO_{(g)}}$), the $CO_{(g)}$ pressure ($p_{CO_{(g)}}$) in the center of the sample, and the heating profile are shown in Figure 5-46 (a),(b), and (c), respectively. Table 5-29 provides t_c, T, maximum $p_{CO_{(g)}}$, and $J_{CO_{(g)}}$ at the end of each simulation, in order of increasing time for complete oxide removal.

This set of simulations shows the same trends in the $J_{CO_{(g)}}$ behavior as the previous sections. These simulations are comparable to the ($T_{\mathrm{h},1}$, $X_{\mathrm{SiO}_2,1}$) simulations, but the threshold $J_{CO_{(g)}}$ is higher for the current simulations because the depleted layer is thinner at $T_{\mathrm{h},1}$. Both sets of simulations require 3 heating rate modifications to keep $J_{CO_{(g)}}$ below the threshold level for the l_3 sample. The (l_3, $X_{\mathrm{SiO}_2,2}$) simulations spend more time heating at HR_{3a} before reaching t_c than the (l_3, $X_{\mathrm{SiO}_2,1}$) simulation. Generally, higher oxide content samples need and/or benefit more from heating rate modifications because the pressure gradient increases more rapidly during the same heating cycle compared to lower oxide content samples.

Table 5-29: Simulation results for l = 2 and 4 cm, $X_{SiO_{2,2}}$= 1.5 mol % samples with variable heating rates after $T_{h,1}$=1673.15 K.

Varied Parameters (In order of oxide removal)	t_c (h)	T (K)	$p_{CO_{(g)}}$ (atm)	$J_{CO_{(g)}}$ (mol·m^{-2}·h^{-1})
l_2=2 cm; HR_{1a}= 2.5 K/min	2.2837	1890.68	2.9	12.17
l_2=2 cm; HR_{1a}= 2.5 K/min (0.6$\bar{6}$ h), HR_{2a}= 1 K/min	2.5734	1837.53	1.69	7.21
l_3=4 cm; HR_{1a}= 2.5 K/min	3.1792	2025	9.88	20.02
l_3=4 cm; HR_{1a}= 2.5 K/min (0.6$\bar{6}$ h), HR_{2a}= 1 K/min	4.3006	1941.16	4.69	9.73
l_3=4 cm; HR_{1a}= 2.5 K/min (0.6$\bar{6}$ h), HR_{2a}= 1 K/min (1.75 h), HR_{3a}= 0.5 K/min	4.4561	1914.31	3.64	7.61

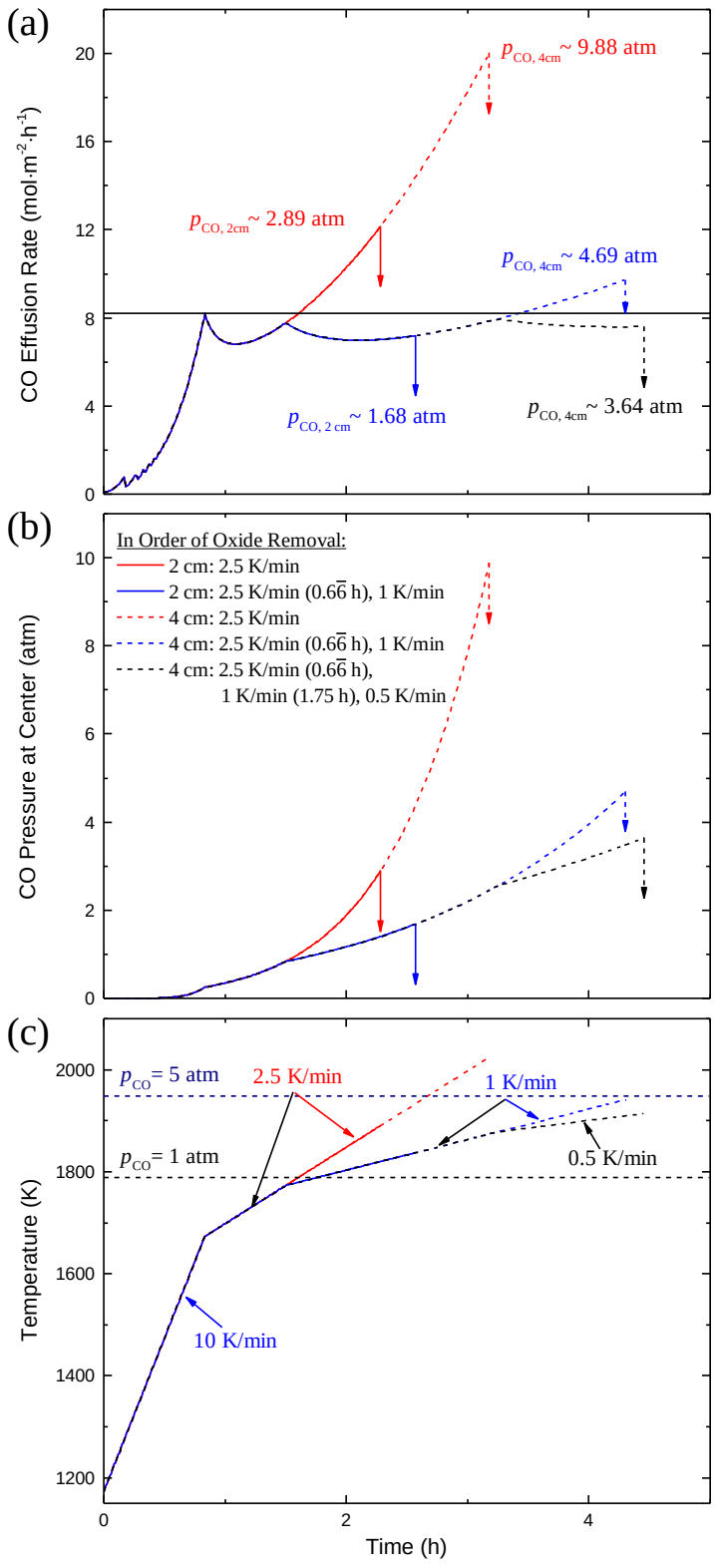

Figure 5-46: Five simulations: l= 2 or 4 cm, X_{SiO_2}= 1.5 mol %, T_i= 1173.15 K, and T_h= 1673.15 K. Heating Cycle: 10 K/min (to T_h); HR_1= 2.5 K/min (0.6$\bar{6}$ h or until t_c); HR_2= 1 K/min (1.75 h or until t_c); HR_3= 0.5 K/min (until t_c). (a) Effusion rate of $CO_{(g)}$ (max p_{CO} and threshold $J_{CO_{(g)}}$ indicated). (b) Pressure of $CO_{(g)}$ at the center of the sample. (c) Heating Profile.

5.3.6.4 *2 and 4 cm thick, 1.5 mol % SiO_2, and T_h = 1723.15 K samples*

This set of simulation investigates the effect of incorporating multiple heating rate reductions when starting at a higher holding temperature and greater initial oxide content. Four simulations are shown, each with sample thicknesses of 2 (l_2) and 4 cm (l_3), oxide content of 1.5 mol % ($X_{\mathrm{SiO_2},2}$), and threshold temperature of 1723.15 K ($T_{\mathrm{h},2}$) are presented. The heating rate was varied after reaching T_{h}. The heating rates for the simulations were varied between 3 and 1 K/min; alternatively labeled as HR_{1b} and HR_{2b}, respectively. The simulations were designed to progressively add heating rate modifications to keep $J_{CO_{(g)}}$ below the threshold $J_{CO_{(g)}}$ reached at T_{h}. The time evolution of the $CO_{(g)}$ effusion rates ($J_{CO_{(g)}}$), the $CO_{(g)}$ pressure ($p_{CO_{(g)}}$) in the center of the sample, and the heating profile are shown in Figure 5-47 (a),(b), and (c), respectively. Table 5-30 provides t_c, T, maximum $p_{CO_{(g)}}$, and $J_{CO_{(g)}}$ at the end of each simulation, in order of increasing time for complete oxide removal.

This set of simulations shows the same trends in the $J_{CO_{(g)}}$ behavior as the previous sections. These simulations are comparable to the ($T_{\mathrm{h},2}$, $X_{\mathrm{SiO_2},2}$) simulations, but the threshold $J_{CO_{(g)}}$ is higher for the current simulations because the depleted layer is thinner at $T_{\mathrm{h},2}$. Both sets of simulations require 2 heating rate modifications to keep $J_{CO_{(g)}}$ below the threshold level for the l_2 and l_3 samples. The (l_2 and l_3, $X_{\mathrm{SiO_2},2}$) simulations spend more time heating at HR_{2b} before reaching t_c than the (l_2 and l_3, $X_{\mathrm{SiO_2},1}$) simulation. This is consistent with the inference of the previous sections stating higher oxide content samples need and/or benefit more from heating rate modifications. A comparison of the effusion controlled simulations shows that introducing the heating rate reductions at a higher hold temperature reduces the number of modifications need; while increasing the oxide content causes a greater variation in the effusion rate during each heating cycle segment.

Table 5-30: Simulation results for l = 2 and 4 cm, X_{SiO_2}= 1.5 mol % samples with variable heating rates after T_h=1723.15 K.

Varied Parameters (In order of oxide removal)	t_c (h)	T (K)	$p_{CO_{(g)}}$ (atm)	$J_{CO_{(g)}}$ (mol·m^{-2}·h^{-1})
l_2=2 cm; HR_{1b}= 3 K/min	1.8897	2006.94	8.48	34.47
l_2=2 cm; HR_{1b}= 3 K/min (0.5 h), HR_{2b}= 1 K/min	2.146	1856.89	2.06	8.76
l_3=4 cm; HR_{1b}= 3 K/min	2.7075	2045.48	11.72	23.61
l_3=4 cm; HR_{1b}= 3 K/min (0.5 h), HR_{2b}= 1 K/min	3.6772	1948.75	5.04	10.42

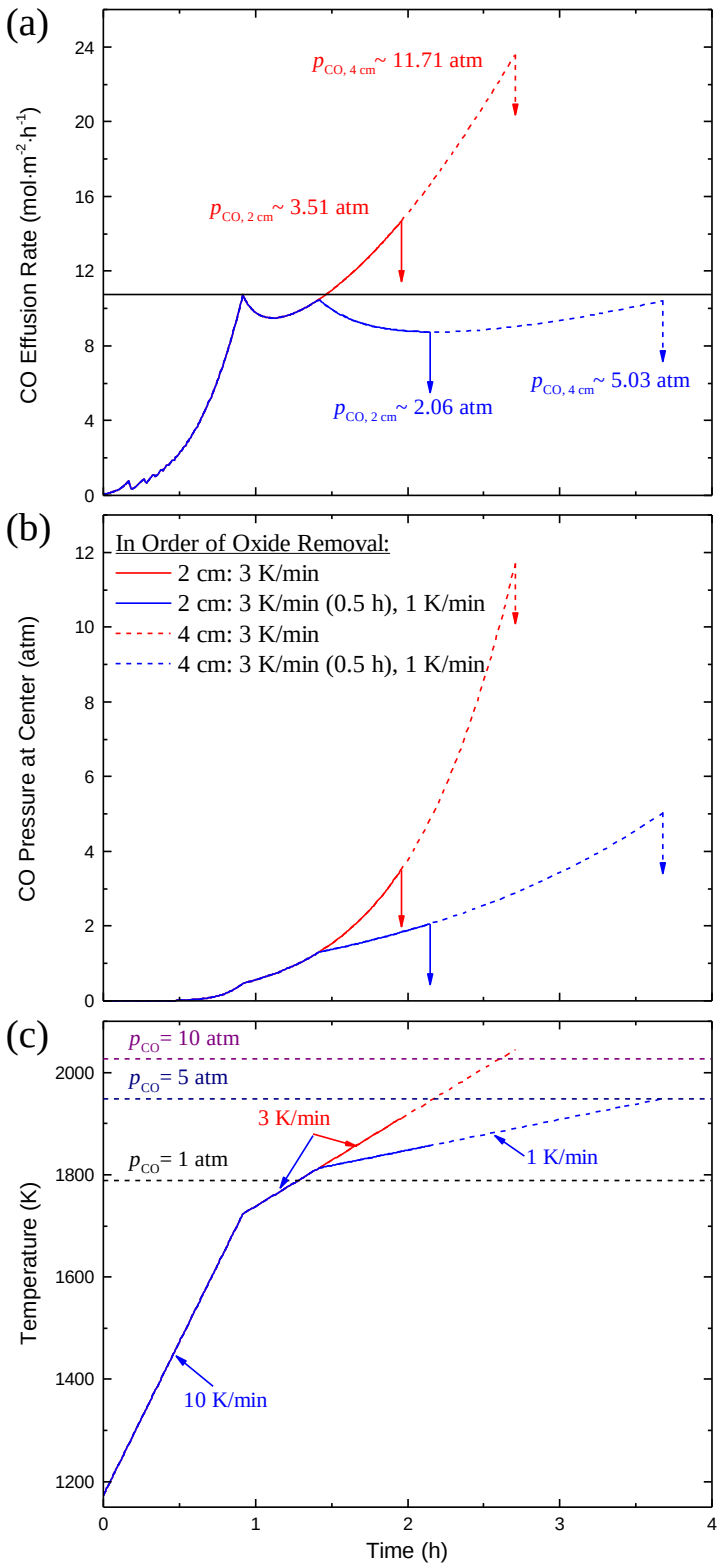

Figure 5-47: Four simulations: l= 2 or 4 cm, X_{SiO_2}= 1.5 mol %, T_i= 1173.15 K, and T_h= 1723.15 K. Heating Cycle: 10 K/min (to T_h); HR_1= 3 K/min (0.5 h or until t_c); HR_2= 1 K/min (until t_c). (a) Effusion rate of $CO_{(g)}$ (max p_{CO} and threshold $J_{CO_{(g)}}$ indicated). (b) Pressure of $CO_{(g)}$ at the center of the sample. (c) Heating Profile.

5.4 Summary of Chemical Set 1

Chemical set 1 consists of simulations designed to analyze the removal of SiO_2 from porous media comprised of C, SiC, and SiO_2. The reaction between SiO_2 and C produces mainly $CO_{(g)}$ and SiC, along with minor amounts of $SiO_{(g)}$ and $CO_{2(g)}$. The removal of SiO_2 is limited by the ability to remove $CO_{(g)}$ from the porous medium, subsequently removing more SiO_2 to replenish the $CO_{(g)}$ that was removed. This creates a reaction front, at each surface, which proceeds towards the center of the sample as SiO_2 is depleted. The time for complete oxide removal (t_c) is when the two reaction fronts meet and all the SiO_2 is depleted. The time for complete oxide removal was studied by dividing constant temperature and time-varying temperature simulations into two categories labeled category 1 and 2, respectively.

The constant temperature simulations in category 1 were simulated using an isothermal hold temperature and individually varying the model parameters for porosity, tortuosity, pore radius, thickness, holding temperature, and initial oxide content. A characteristic feature of the constant temperature simulations was that the gas effusion rate was always highest at the start of the simulation, followed by a rapid drop, and then slowly declined until t_c. Consequently, the rate of progression of the reaction front slows, causing t_c to increase quadratically with the sample thickness. The linearized functional dependence of t_c on each parameter was found and used to create a semi-empirical equation that can be used to predict t_c for isothermal holds. A comparison of t_c from simulations that simultaneously varied all of the simulation parameters and t_c predicted using the semi-empirical equation showed good agreement. Compacts made from different powders take on different values for the simulation parameters for which the semi-empirical equation can be used to predict trends in the time for oxide removal due to powder variation. These tools can be used to improve processing by guiding and reducing the amount of experimentation needed.

Modeling the minor gas species $SiO_{(g)}$ and $CO_{2(g)}$ produced secondary effects during the oxide removal process. It was found that a non-uniform amount of carbon was consumed while reducing the initially uniform SiO_2 content. Both the center and edges consumed less carbon than the C/SiO_2 ratio of 3 predicted if only $CO_{(g)}$ was produced during oxide removal. More carbon was depleted from the edges of the sample compared to the center. These secondary effects were relatively minor because they were considerably lower in concentration compared to $CO_{(g)}$, with $CO_{(g)}/SiO_{(g)}$ and $CO_{(g)}/CO_{2(g)}$ being approximately 284 and 23133, respectively. These secondary effects increase at higher temperatures because the relative amount of $SiO_{(g)}$ and $CO_{2(g)}$ increases compared to $CO_{(g)}$.Time-varying temperature simulations in category 2 were conducted to analyze the effect of temperature ramping, hold time duration, initial oxide content, and sample thickness on the time for complete oxide removal and the gas effusion rates. The simulations in category 2 were started at a low enough temperature where a negligible amount of reaction occurs, so $p_{CO_{(g)}}$ was also negligible. A characteristic feature of the time-varying temperature simulations was that the effusion rate of $CO_{(g)}$ ($J_{CO_{(g)}}$) started close to zero and reached a local maximum at the onset of a constant temperature hold. The local peak $J_{CO_{(g)}}$ was dependent on the starting oxide content and hold temperature, but not the sample thickness. It was found that only a constant temperature hold was effective at keeping both $p_{CO_{(g)}}$ and $J_{CO_{(g)}}$ below a desired level.

Four sets of simulations were conducted to observe the effect of changing the simulation parameters when using a constant temperature hold. It was found that thinner samples with lower oxide content and a higher holding temperature are the best candidates for using a constant temperature hold. However, any constant temperature hold is inefficient at removing all of the SiO_2, because $J_{CO_{(g)}}$ decreases as SiO_2 is removed. If the hold time is too

short to remove all of the SiO_2, then $p_{CO_{(g)}}$ and $J_{CO_{(g)}}$ may reach undesirable levels as the sintering temperature is reached. It was found that ending the hold too early caused a more drastic increase in the internal pressure and effusion rate for thicker samples with higher oxide contents and lower hold temperatures.

Relaxing the condition limiting the maximum $p_{CO_{(g)}}$ and focusing only on limiting $J_{CO_{(g)}}$ expands the range of heating schedules available to remove all of the SiO_2. Simulations were conducted which lowered the heating rate after reaching the holding temperature to control the effusion rate and reduce the time needed for oxide removal. For thin samples, lowering the heating rate to 2.5 K/min or 3 K/min, upon reaching a threshold $J_{CO_{(g)}}$, was effective at keeping $J_{CO_{(g)}}$ below the threshold level and reducing t_c. For thick samples, a single reduction in the heating rate was not effective at maintaining the threshold $J_{CO_{(g)}}$ because, after going through a minimum, $J_{CO_{(g)}}$ began to increase again.

It was observed that each lowering of the heating rate helped limit the growth of the effusion rate. As the sample thickness increased, multiple heating rate reductions, each after progressively longer time intervals, were needed to keep $J_{CO_{(g)}}$ below the specified threshold level. When starting with a higher oxide content there will be more variation in the effusion rate behavior between heating segments. By starting the heating rate reductions at a higher hold temperature, fewer heating segments are needed. In summary, the information from category 1 on how porous media parameter variation affects t_c and category 2 on how heating rates can be used to limit $J_{CO_{(g)}}$, provides a practitioner useful insight into how to design and optimize heating schedules to remove SiO_2 from porous SiC green bodies.

6 Chemical Set 2 Simulations: {B_4C, B_2O_3, C, $CO_{(g)}$, $B_2O_{3(g)}$, $B_2O_{2(g)}$}

The results from simulations studying the transport and reaction in a porous medium comprised of condensed B_4C, B_2O_3, and C are presented in this chapter. The chemical species modeled in the simulations are restricted to the chemical set {B_4C, B_2O_3, C, $CO_{(g)}$, $B_2O_{3(g)}$, $B_2O_{2(g)}$}. The porous medium were assumed to be reactive and the gas species produced from chemical reactions are limited to only $CO_{(g)}$, $B_2O_{3(g)}$, and $B_2O_{2(g)}$. This chemical set accounts for the initial condensed species present in the porous medium and the gas species with the three largest partial pressures in equilibrium with the condensed species. In reality, the reaction of the condensed and gas species will produce additional chemical species, but these will have only a minor effect on the qualitative and quantitative behavior observed during simulations. Figure 6-1 shows the partial pressures of various gas species in equilibrium with condensed B_4C, B_2O_3, and C. The study of the transport and reaction in porous medium for this chemical set is restricted to constant temperature simulations.

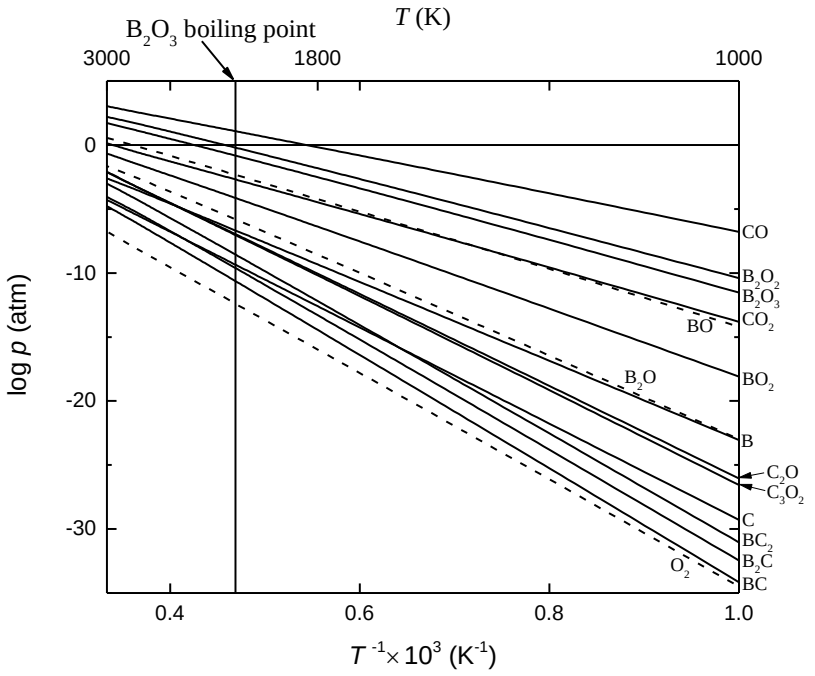

Figure 6-1: Gas pressures as a function of temperature for several species in equilibrium with solid B_4C, C, and liquid ($T > 1723$ K) B_2O_3.

Similar to the procedure for SiC in Chapter 5, the compositional profiles of the condensed species are represented by their percentage change. The compositional profile for B_2O_3 is denoted by ΔB_2O_3 (%) and the *time for complete oxide removal*, t_c, is when ΔB_2O_3 (%) = -100 across the whole porous medium. Additionally, the same numerical scheme and simulations checks were used to verify the convergence of the numerical solution.

6.1 Physical Constants and Expressions

The same collection of physical constants and simulation parameters as chemical set 1 (Chapter 5.1) are needed for the current chemical set. The relevant parameters for B_4C, B_2O_3, and C are provide in Table 6-1 and those for $CO_{(g)}$, $B_2O_{3(g)}$, and $B_2O_{2(g)}$ are provide in Table 6-2. The Gibbs free energy function for each species is not explicitly listed, but the required data to construct them is provided in Appendix IV.iii.

Table 6-1: Material properties for the condensed chemical species from chemical set 2.

Condensed Species	MM (g·mol^{-1})	ρ (g·cm^{-3})
B_4C	55.2547	2.50
B_2O_3	69.6202	2.55
C	12.0107	2.10

Table 6-2: Material properties for the gas chemical species from chemical set 2.

Gas Species	MM (g·mol^{-1})	σ (Å)	ϵ/k_B (K)
CO	28.0101	3.80	88
B_2O_3	69.6202	4.1605	2092
B_2O_2	53.6208	4.79	350

6.2 Constant Temperature Simulations (Model Validation)

The goal of this study is to not only to study oxide removal from this system, but to further validate the generality of the current modeling framework by comparing the results of this model against the a model developed by Rossi *et al.* specifically for the {B_4C, B_2O_3, C, $CO_{(g)}$, $B_2O_{2(g)}$, $BO_{(g)}$, $B_2O_{3(g)}$, $O_{2(g)}$} chemical set.[91] This study of constant temperature simulations systematically investigated the effect of individually varying the structure properties of the porous medium, the initial chemical composition, and the holding temperature. The individually varied structure properties of the porous medium include the starting porosity, tortuosity, pore radius, and sample thickness. The chemical composition of each species was varied on a mole fraction basis. The compositional variations were designed to have a constant starting molar ratio of C/B_2O_3 (= 6), to ensure complete reduction of B_2O_3, *i.e.* enough carbon to ensure that it is not exhausted before the B_2O_3 anywhere within the body. The remaining mole fraction of material consists of B_4C. The simulations were assumed to take place under vacuum conditions, *i.e.* the external gas pressure on the boundary of the porous medium was equal to zero.

The common benchmark for these simulations was the time to remove all of the B_2O_3 initially present in the porous media. This benchmark was chosen because a negligible amount of reaction and transport will occur after the depletion of all the oxide species since the remaining condensed species have extremely low vapor pressures. From a practical standpoint, it is desirable to identify the removal of all oxide species. The results from Rossi *et al.* were used as a consistency check for comparing and validating the modeling framework designed for this thesis.[91]

A standard set of simulation conditions was chosen to be comparable to the SiC system studied in Chapter 6.2 and acts as a reference point to which all other simulations could be compared. These parameters are not optimized for sintering or mechanical properties. The parameters for the *standard simulation conditions* for chemical set 2 (SSC2) are listed in Table 6-3.

Table 6-3: Standard simulation conditions (SSC2) reference parameter values for chemical set 2.

Parameter	Reference Value
B_4C (X_{B_4C})	92.3 mol %
B_2O_3 ($X_{B_2O_3}$)	1.1 mol %
C (X_C)	6.6 mol %
Porosity (ε)	0.4
Tortuosity (q)	5
Pore radius (r)	16 nm
Thickness (l)	1 cm
Temperature (T)	1713.15 K

The same parameter variation for chemical set 1 (Chapter 5.2) was conducted for this chemical set to investigate the time for complete B_2O_3 removal. This follows the procedure outlined by Kaza *et al.*[90] and performed on a similar chemical set by Rossi *et al,* allowing for a comparison between the two systems and previous modeling results.[91] The functional relationships identified from the parameter variations were used to create a linearized function, centered at the SSC2 reference values, which can be used to predict the time for complete oxide removal without explicitly running the corresponding simulation. A set of simulations with multiple parameter variations was chosen to compare with the predictions from the linearized model. The oxide removal behavior and parameter dependence for the two systems are very similar because C is the reducing agent and $CO_{(g)}$ is the dominate gas species in both chemical sets.

6.2.1 Standard Reference Simulation

The qualitative and quantitative behavior of the standard reference simulation for chemical set 2 (SRS2) is presented in this section. SRS2 uses the SSC2 values from Table 6-3. The porous medium is assumed to be in a vacuum environment, evacuated of all gas, and heated instantaneously to 1713.15 K. Table 6-4 shows the equilibrium partial pressures of $CO_{(g)}$, $B_2O_{3(g)}$, and $B_2O_{2(g)}$ at 1713.15 K for chemical set 2. The most abundant gas is $CO_{(g)}$, followed by $B_2O_{2(g)}$, and then $B_2O_{3(g)}$. The ratio of $CO_{(g)}/B_2O_{2(g)}$ and $CO_{(g)}/B_2O_{3(g)}$ are approximately 59 and 306, respectively. The temperature of 1713.15 K was chosen because at this temperature the $CO_{(g)}$ pressure is similar (< 3% Δ) to the $CO_{(g)}$ pressure in equilibrium with SiC system at 1673.15 K (Table 5-4). The minor gas species pressure for $B_2O_{2(g)}$ is an order of magnitude greater than $SiO_{(g)}$ in the SiC system, indicating that secondary effects leading to non-uniform compositions will be more prevalent in the B_4C system. By using a similar maximum $CO_{(g)}$ equilibrium pressure it emphasizes the many qualitative similarities between the two systems.

Table 6-4: Equilibrium partial pressures for chemical set 2 at 1713.15 K

Gas Species	P_{eq} (atm)
CO	0.26172
B_2O_2	4.4612×10^{-3}
B_2O_3	8.5450×10^{-4}

After the initial reaction at the beginning of the simulation, the gas pressure of each species is uniform across the porous medium. It is only after the removal of gas, due to transport out of the porous surfaces, will any further reaction occur. Qualitatively the same as SiO_2 removal, the quantity of B_2O_3 begins to deplete as the gas pressure returns to its equilibrium value, because the oxygen must come from the condensed species to replenish the oxygen containing gas species. Since the transport of gas out of the porous medium happens only at the surface and initially that is the only location with any pressure gradient, it is the surface that first is depleted of B_2O_3. Figure 6-2 shows the growth of the regions depleted of B_2O_3 as a function of time. The simulation stops at 0.9950 h, when all of the B_2O_3 is depleted.

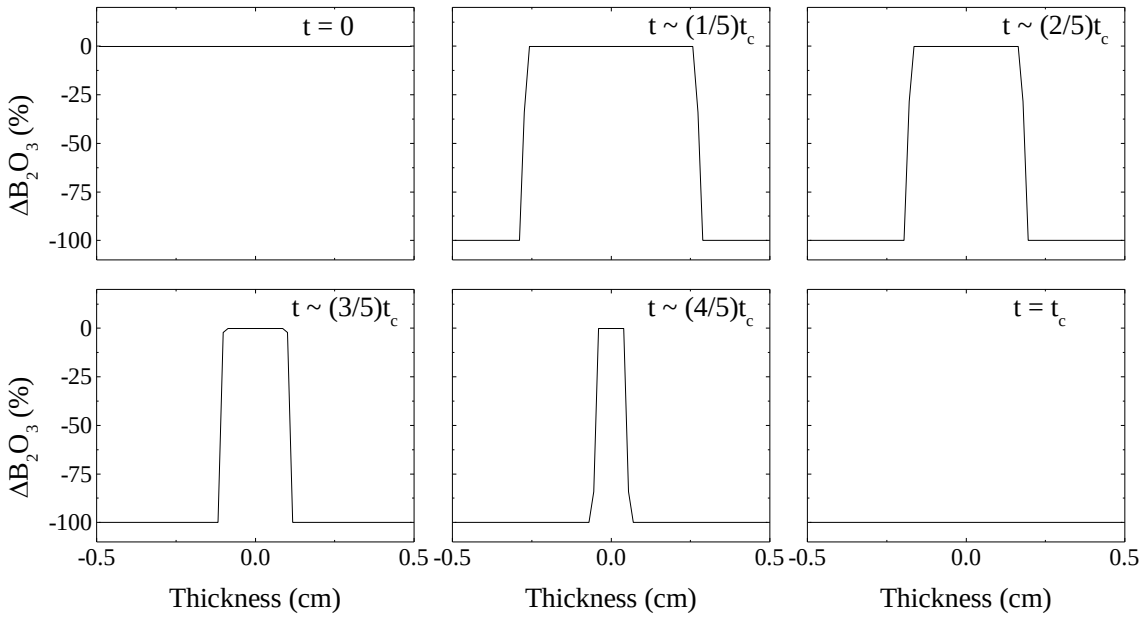

Figure 6-2: Compositional profile of B_2O_3 across the porous medium as the simulation time increases up to t_c=0.9950 h. Times shown are in increments of t_c, where t ~ 0, 1/5, 2/5, 3/5, 4/5, and 1 t_c. Simulation conditions are SSC2.

Once the surface is depleted of B_2O_3 and the region becomes oxygen deficient, the equilibrium partial pressures begin to vary from those in Table 6-4. The chemical equilibrium in this region is corresponds to chemical regime 3 for chemical set 2 in the Appendix II.iv. Similar to SiO_2 removal (Chapter 6.2.1), a reaction front forms at the interface between regimes, with an abrupt change where B_2O_3 is depleted at the interface. This characteristic behavior of B_2O_3 removal is shown in Figure 6-2 and is qualitatively the same as SiO_2 removal shown in Figure 5-2.

The depletion of B_2O_3 is mainly attributed to the transport of $CO_{(g)}$ out of the surfaces of the porous medium. The time evolution of the $CO_{(g)}$ partial pressure profile is shown in Figure 6-3 and is the same behavior for $CO_{(g)}$ in chemical set 1 shown in Figure 5-3. Since there is a similar slow movement of the reaction front for both chemical sets, there is also approximately linear variation in the $CO_{(g)}$ pressure in the depleted regime due to the quasi-static diffusion conditions. This similarity was seen by Rossi *et al*.[91] They observed that even though the DGM is

non-Fickian, *i.e.* the effective diffusion coefficient of each species is not independent of pressure, the gas diffusion behavior for this chemical set is approximately Fickian (similar to that described by Kaza *et al.*[90]) causing the $CO_{(g)}$ pressure to decrease linearly from that at the reaction front to the pressure at the surface. Comparing Figure 6-2 and Figure 6-3, it is clear that the region with the linear $CO_{(g)}$ pressure gradient coincides with the depleted B_2O_3 region.

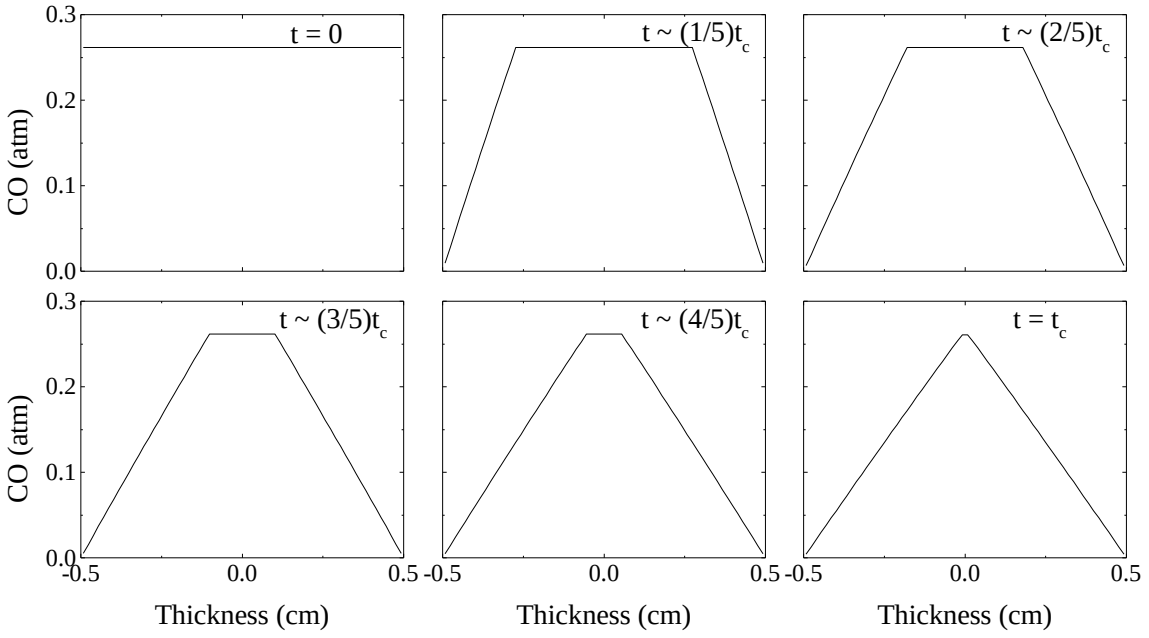

Figure 6-3: Partial pressure profile of $CO_{(g)}$ across the porous medium as the simulation time increases up to t_c= 0.9950 h. Times shown are in increments of t_c, where t ~ 0, 1/5, 2/5, 3/5, 4/5, and 1 t_c. Simulation conditions are SSC2.

As was shown for chemical set 1, the pressure gradient is the driving force for the transport of $CO_{(g)}$ and the rate of gas removal is highly sensitive to the magnitude of the pressure gradient. Figure 6-4 shows the effusion rate of $CO_{(g)}$ as the simulation time increases. The effusion rate starts at 50.3 $mol \cdot m^{-2} \cdot h^{-1}$ and decreases to 2.4 $mol \cdot m^{-2} \cdot h^{-1}$ at the time all the B_2O_3 is removed, followed by a rapid drop to zero. Because the $CO_{(g)}$ pressures for chemical set 1 and 2 are similar, the effusion rate behavior shown in Figure 5-4 and Figure 6-4 also almost

identical, with the former having an effusion rate of 50.8 mol·m^{-2}·h^{-1} and decreases to 2.3 mol·m^{-2}·h^{-1}.

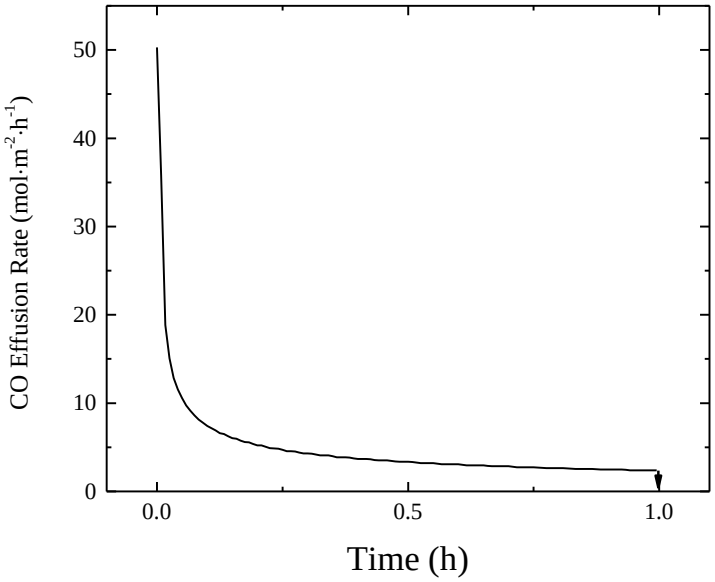

Figure 6-4: Effusion rate of $CO_{(g)}$ as the simulation time increases up to t_c=0.9950 h. Simulation conditions are SSC2.

Initially, the rate of B_2O_3 removal is at a maximum because the effusion rate of $CO_{(g)}$ is at a maximum, resulting in a rapid advance of the reaction front. As the reaction front proceeds, the effusion rate of $CO_{(g)}$ drops and B_2O_3 is removed at a slower rate. Accordingly, the rate of advance of the reaction front slows with increasing simulation time. This behavior is evident in Figure 6-2 and Figure 6-3 when comparing the rapid advance of the reaction front between t=0 and t~(1/5)t_c to the relatively slow advance of the reaction front between t~(4/5)t_c and t=t_c. The rate of advance decreases in an approximately quadratic manner and this effect is shown more clearly later when analyzing the quadratic increase in t_c with sample thickness.

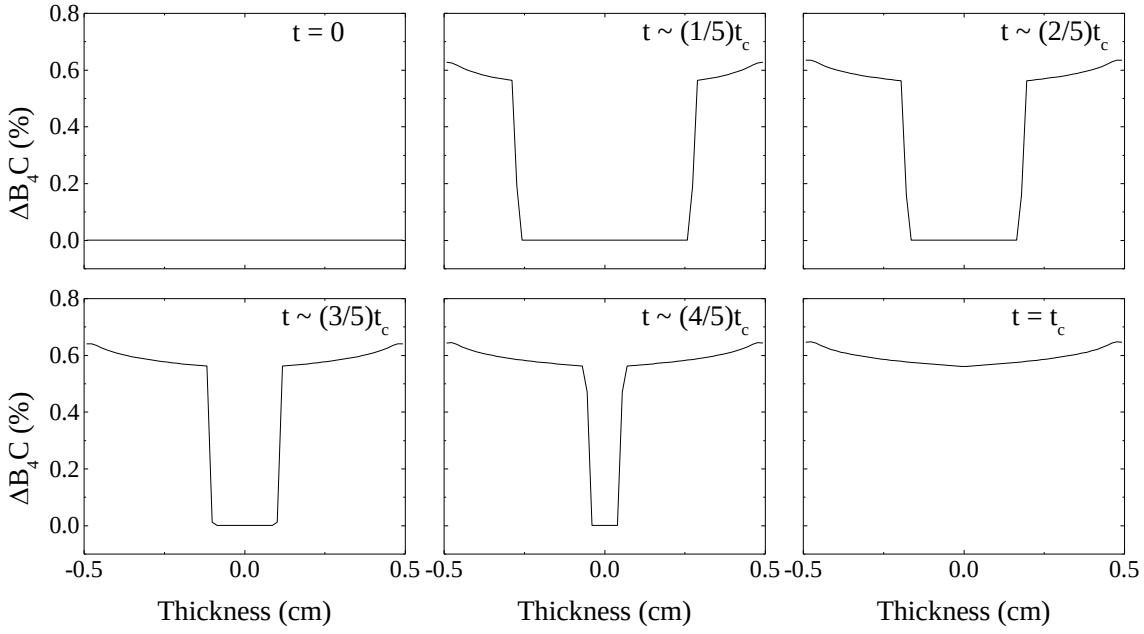

Figure 6-5: Compositional profile of B_4C across the porous medium as the simulation time increases up to t_c=0.9950 h. Times shown are in increments of t_c, where t ~ 0, 1/5, 2/5, 3/5, 4/5, and 1 t_c. Simulation conditions are SSC2.

The chemical reaction that depletes B_2O_3 and C to form $CO_{(g)}$ also deposits B_4C. Figure 6-5 shows how the compositional profile of B_4C changes in time as the reaction front proceeds and B_4C is deposited during the complete reduction of B_2O_3. The deposition behavior of B_4C in Figure 6-5 is, in a sense, opposite to the depletion behavior of B_2O_3 in Figure 6-2. The ΔB_4C at the edge and the center was only 0.648 and 0.562 %, respectively. The small overall change in ΔB_4C is consistent with a large starting composition of B_4C compared to B_2O_3, which were 92.3 and 1.1 mol %, respectively. There is a noticeable trend for more B_4C to be deposited at the edges of the sample due to the continued reaction of $B_2O_{2(g)}$ and $B_2O_{3(g)}$ with C as the gas flows over the oxide depleted region. Comparing Figure 5-5 and Figure 6-5 shows that the amount of B_4C deposited is much more significant than for the analogous situations with SiC deposition.

The time evolution of the compositional profiles of B_2O_3 and B_4C, shown frame by frame in Figure 6-2 and Figure 6-5, give a visualization of the reaction behavior. The compositional

profiles of C, B_2O_3, and B_4C are shown concisely in Figure 6-6, with an arrow indicating the progression in time.

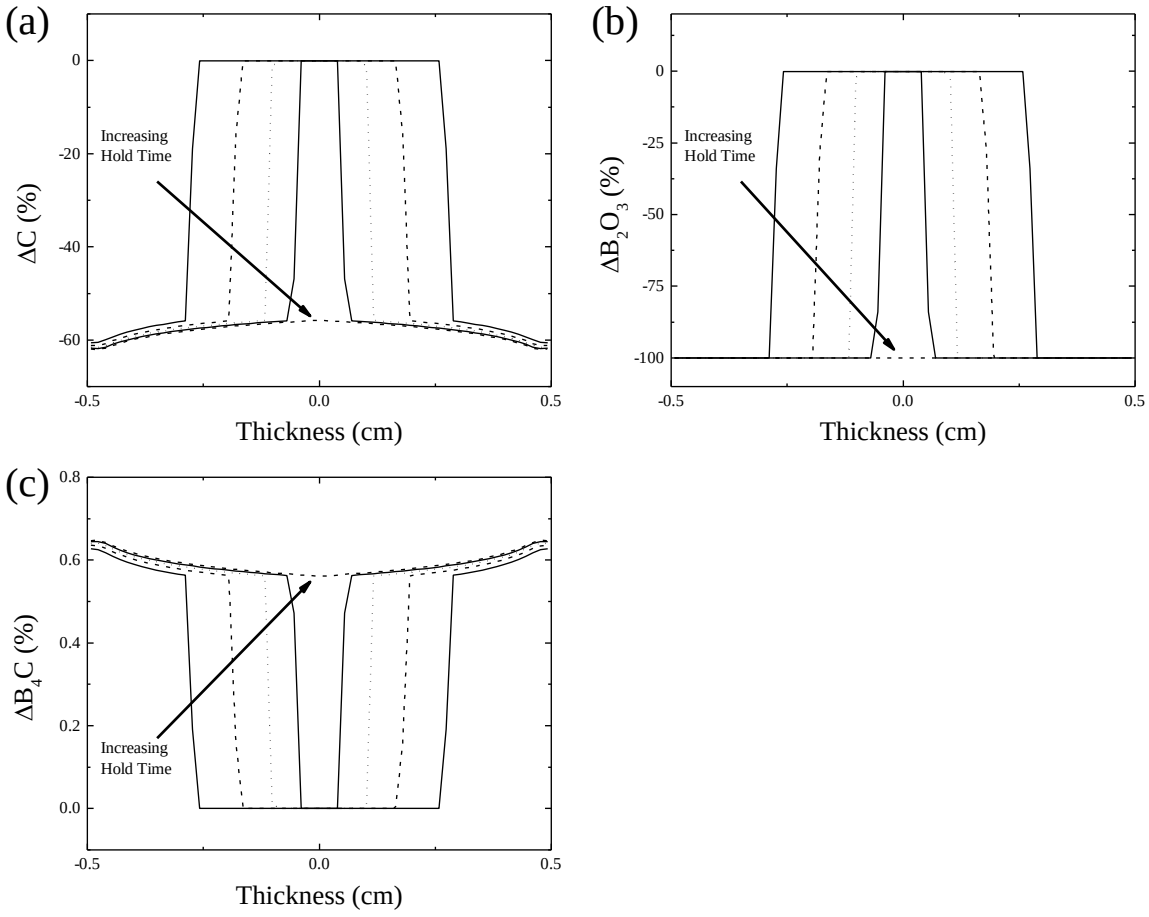

Figure 6-6: Compositional profile of (a) C, (b) B_2O_3, and (c) B_4C across the porous medium as simulation time increases up to t_c=0.9950 h. Times shown are in increments of t_c, where t ~ 1/5, 2/5, 3/5, 4/5, and 1 t_c. Simulation conditions are SSC2.

The initial amount of carbon used to remove the B_2O_3 was not completely depleted, as indicated in Figure 6-6(a). An initial composition of 6.6 mol % C was an excess amount to fully reduce the 1.1 mol % B_2O_3. Figure 6-7(a) shows the residual C profile, as the relative percentage change of C. The amount of carbon was reduced by 62.06 and 55.79 % at the edge and center, respectively. The amount of carbon depleted, normalized by the starting B_2O_3 content, is shown in Figure 6-7(b). Considering only the reaction given by Equation 226 leads to the prediction that the ratio of C/B_2O_3, to remove all the B_2O_3, should be 3.5.

The departure from the predicted C/B_2O_3 ratio is due to the presence and reaction of the minor secondary gas species, $B_2O_{2(g)}$ and $B_2O_{3(g)}$; these effects are small because of the comparatively small partial pressures in relation to $CO_{(g)}$. In the oxygen rich region (regime 1), SiC and B_2O_3 can react to form $B_2O_{2(g)}$ and deposit C, as seen from the reaction in Equation 224. This acts to decrease the C/B_2O_3 ratio slightly. Additionally, the sublimation of B_2O_3 to $B_2O_{3(g)}$ occurs without carbon, further reducing the C/B_2O_3 ratio. The $CO_{(g)}/B_2O_{2(g)}$ ratio is smaller than the $CO_{(g)}/B_2O_{3(g)}$ ratio, indicating that the $B_2O_{2(g)}$ has a greater effect on reducing the C/B_2O_3 ratio.

The C/B_2O_3 ratio is higher at the edges of the sample. The edges of the sample are the first regions to become oxygen deficient (regime 3), as the B_2O_3 is depleted. At this initial stage, the C/B_2O_3 ratio at the edge is almost the same as the final C/B_2O_3 ratio in the center. The $B_2O_{2(g)}$ and $B_2O_{3(g)}$ from the center of the sample must travel through this region, before being evacuated, and continue to react with the remaining condensed and gas species. The feasible reactions for the oxygen deficient region, given by Equations 258 and 259, show that any reaction of $B_2O_{2(g)}$ and/or $B_2O_{3(g)}$ consumes C. Thus explaining the increase in the C/B_2O_3 ratio at the edges of the sample compared to the center. This effect on the C/B_2O_3 ratio of SRS2 of chemical set 2 is much greater than on the C/SiO_2 ratio of SRS1 of chemical set 1, due to the much smaller $CO_{(g)}/B_2O_{2(g)}$ ratio (~59) compared the $CO_{(g)}/SiO_{(g)}$ ratio (~287), respectively. This results in a much greater non-uniformity in the residual carbon composition for chemical set 2 compared to chemical set 1.

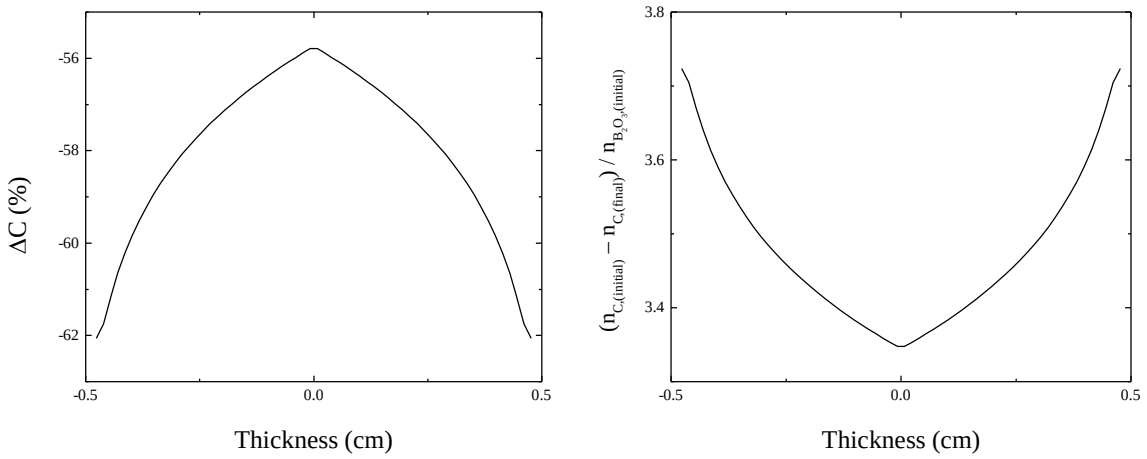

Figure 6-7: Residual C content profile after complete B_2O_3 depletion, (a) ΔC (%) (b) Change in the number of moles of C normalized by the initial number of moles of B_2O_3. Simulation conditions are SSC2.

The time evolution of the partial pressure profile for $CO_{(g)}$ was shown frame by frame in Figure 6-3 to give a concrete visualization of transport and reaction behavior. The time evolution of the partial pressure profiles for $CO_{(g)}$, $B_2O_{3(g)}$, and $B_2O_{2(g)}$ are shown concisely in Figure 6-8, with an arrow indicating the progression in time. Both, $B_2O_{2(g)}$ and $B_2O_{3(g)}$ have a pressure gradient across the oxygen deficient region. The difference in curvature of these gradients can be explained by the thermodynamic conditions of chemical regime 3 for chemical set 2. Equation 264 shows that $n^2_{CO_{(g)}} \propto n_{B_2O_{2(g)}}$, indicating the partial pressure profile of $B_2O_{2(g)}$ is quadratic (Figure 6-8(b)) compared to the $CO_{(g)}$ partial pressure profile. Similarly, Equation 265 shows that $n^3_{CO_{(g)}} \propto n_{B_2O_{3(g)}}$, indicating that the partial pressure profile of $B_2O_{3(g)}$ is cubic (Figure 6-8(c)) compared to the $CO_{(g)}$ partial pressure profile.

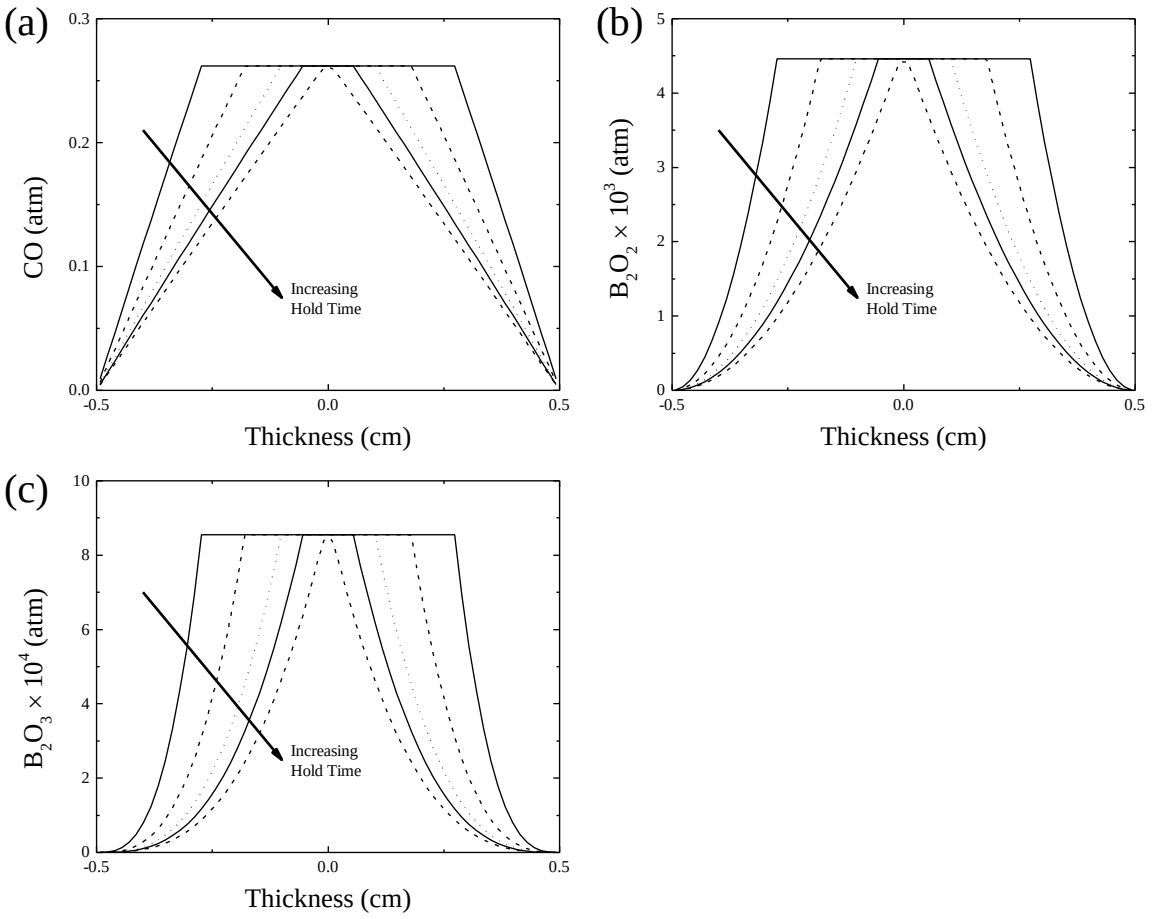

Figure 6-8: Partial pressure profile of (a) $CO_{(g)}$, (b) $B_2O_{2(g)}$, and (c) $B_2O_{3(g)}$ across the porous medium as simulation time increases up to t_c=0.9950 h. Times shown are in increments of t_c, where t ~ 1/5, 2/5, 3/5, 4/5, and 1 t_c. Simulation conditions are SSC2.

Characteristics of the condensed and gas species behavior for the standard reference simulation of chemical set 2 were shown in this section. The qualitative behavior associated with the movement of the reaction front and a transition from chemical regime 1 to regime 3 is representative of simulations where C is present in excess to allow for complete reduction of B_2O_3. The remaining simulations involving chemical set 2 were all designed to satisfy this condition. Consequently, the degree of the functional form (*i.e.* linear, quadratic, *etc.*) for each gas partial pressure profile, in the oxygen deficient region, is the same as this standard reference simulation. The rest of the simulations investigate changing the simulation parameters and quantifying their effect on the time for complete oxide removal, in comparison

to this standard reference simulation. As would be expected, the result of changing the simulation parameters for this chemical set is highly analogous to that of chemical set 1 because $CO_{(g)}$ is the dominant gas species, at a similar pressure, and the other processing parameters are not affected by the choice of chemical set.

6.2.2 Effect of Porosity

The effect of porosity on the time for complete oxide removal was studied by varying the porosity, ε, while using the SSC2 in Table 6-3. The porosity was varied from 0.1 to 0.9 in increments of 0.1. Figure 6-9 shows the time required to completely remove all the B_2O_3 from the porous medium, as a function of the porosity.

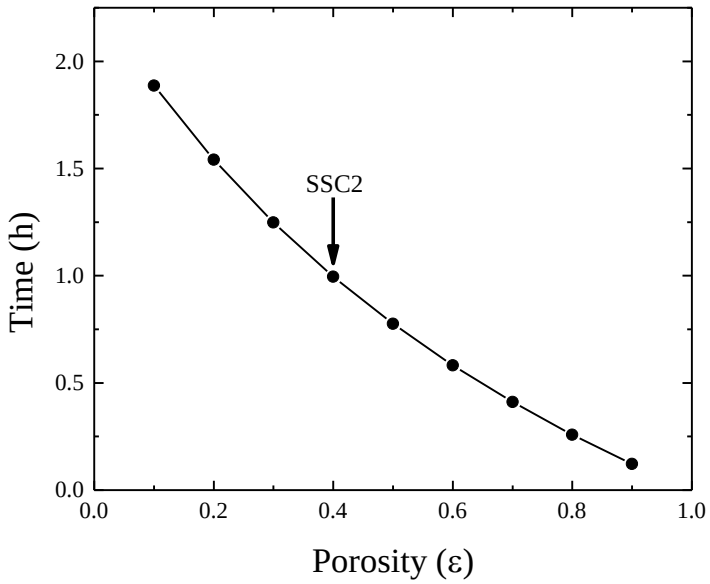

Figure 6-9: Time for complete B_2O_3 removal, as a function porosity.

The time for complete oxide removal was found to decrease as the porosity of the sample increased. An explanation for the reduction in t_c due to porosity was presented in Chapter 5.2.2 for the removal SiO_2 and is analogous to the removal B_2O_3. An attempt was made to linearize the effect of the porosity on the time for complete oxide removal for the data represented by Figure 6-9. Rossi *et al.* showed that the time for complete oxide removal

depends linearly on $(1-\varepsilon)/\varepsilon$.[91] However, similar to chemical set 1, that expression does not properly linearize the simulation data. It can be seen from Figure 6-10 that the time for complete oxide removal is well described using the expression $(1-\varepsilon)^{3/2}$ to linearize the effect of porosity. The linear regression fit to Figure 6-10 satisfies the equation $y = y_o + a_\varepsilon(1-\varepsilon)^{3/2}$, where $y_o = 0.05148$ h and $a_\varepsilon = 2.09503$ h.

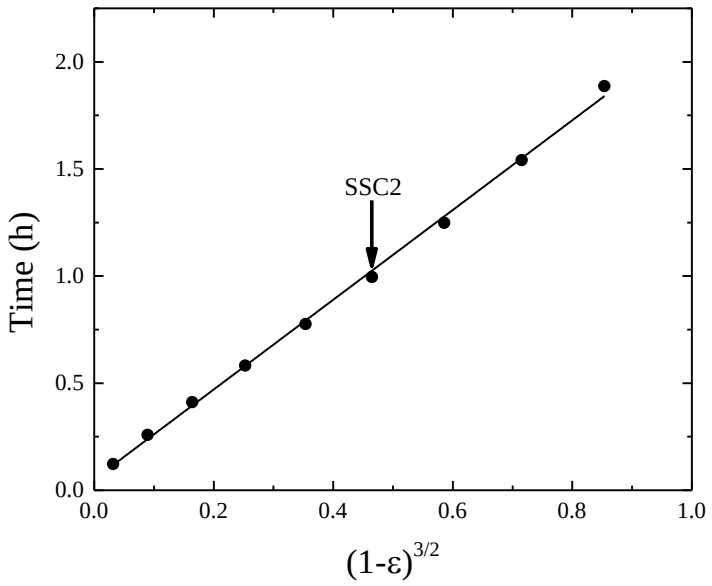

Figure 6-10: Time for complete B_2O_3 removal, as a function of the linearized porosity.

It was initially expected that the linearization suggested by Rossi *et al*. should be acceptable for the current model.[91] However, a notable difference between the current model and that used by Rossi *et al.*[91] is the treatment of porosity after reaction takes place. The model used by Rossi *et al.* assumes that the amount of porosity prescribed at the beginning of the simulation is constant, even after reaction.[91] The current model accounts for the change in porosity due to reaction. As the reaction front proceeds across the porous medium, the porosity in the oxygen deficient region is increased. This occurs because the reaction of B_2O_3 and C primarily produces $CO_{(g)}$ and B_4C. There is a net reduction in the volume of condensed species due to this reaction. It was already mentioned that an increase in porosity would increase the

gas flux and shorten the time for oxide removal. It is believed that this effect may account for the discrepancy in the linearization of porosity between the two models.

6.2.3 Effect of Tortuosity

The effect of tortuosity on the time for complete oxide removal was studied by varying the tortuosity, q, while using the SSC2 in Table 6-3. The tortuosity was varied from 1 to 10 in increments of 1. Figure 6-11 shows the time required to completely remove all the B_2O_3 from the porous medium, as a function of the tortuosity.

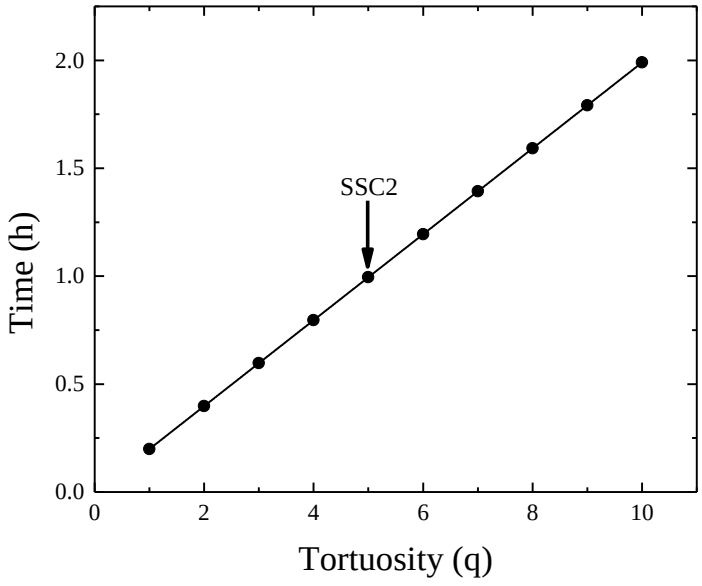

Figure 6-11: Time for complete B_2O_3 removal, as a function tortuosity.

The time for complete oxide removal was found to increase linearly as the tortuosity of the sample increased. The linear regression fit to Figure 6-11 satisfies the equation $y = y_o + a_q q$, where $y_o = -2.68 \times 10^{-13}$ h and $a_q = 0.19901$ h. This behavior is expected because the DGM accounts for the tortuosity by using effective diffusion coefficients (Equations 79-81), which are inversely proportional to the tortuosity; similar results are shown by Rossi *et al.* and in Chapter 5.2.3 for chemical set 1.[91] Thus, increasing the tortuosity decreases the gas diffusivity

and subsequently the flux of gas is decreased leading to longer times for complete oxide removal.

6.2.4 Effect of Pore Radius

The effect of pore radius on the time for complete oxide removal was studied by varying the pore radius while using the SSC2 in Table 6-3. The pore radius was varied across the range of sizes including 4, 8, 12, 16, 20, 24, 32, and 40 nm. Figure 6-12 shows the time required to completely remove all the SiO_2 from the porous medium, as a function of the pore radius.

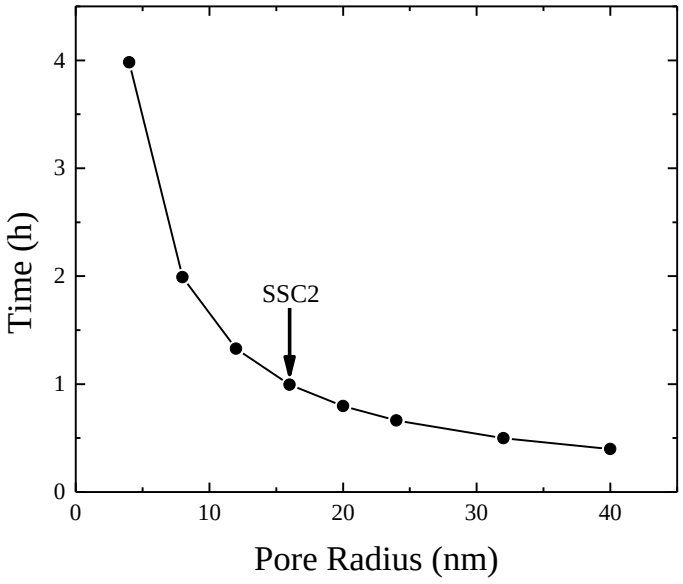

Figure 6-12: Time for complete B_2O_3 removal, as a function pore radius.

The time for complete oxide removal was found to decrease non-linearly as the pore radius increases. The effect of the pore radius is linearized by plotting the time for complete oxide removal as a function of the inverse of the pore radius, shown in Figure 6-13 . The linear regression fit to Figure 6-13 satisfies the equation $y = y_o + a_r r^{-1}$, where $y_o = -4.29144 \times 10^{-7}$ h and $a_r = 15.92042$ h·nm.

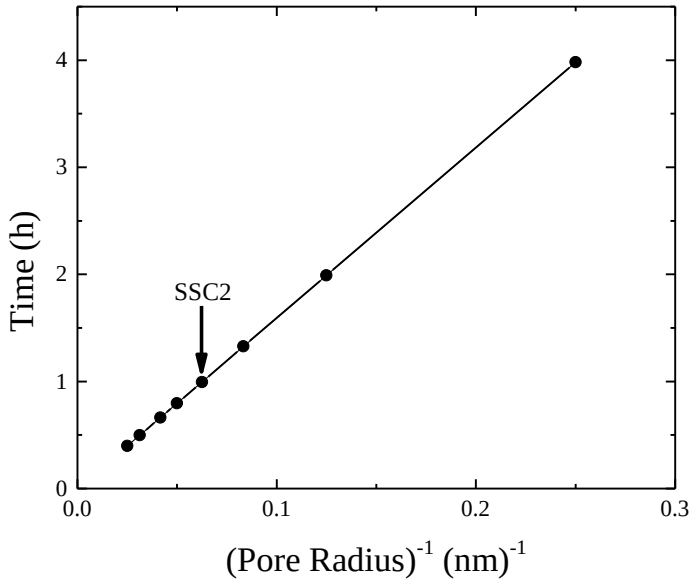

Figure 6-13: Time for complete B_2O_3 removal, as a function inverse pore radius.

The inverse linear relationship between the pore radius and the time for complete oxide removal shows that Knudsen diffusion dominates compared to viscous flow for these simulation conditions; similar results are shown by Rossi *et al* and in Chapter 5.2.4 for chemical set 1. Increasing the pore radius allows for more free-molecule $CO_{(g)}$ transport and subsequently the flux of gas out of the porous medium is increased leading to shorter times for complete oxide removal.

6.2.5 Effect of Sample Thickness

The effect of sample thickness on the time for complete oxide removal was studied by varying the thickness while using the SSC2 in Table 6-3. The sample thickness was varied across the range of thicknesses including 0.25, 0.5, 0.75, 1, 2, 3, and 4 cm. Figure 6-14 shows the time required to completely remove all the SiO_2 from the porous medium, as a function of the sample thickness.

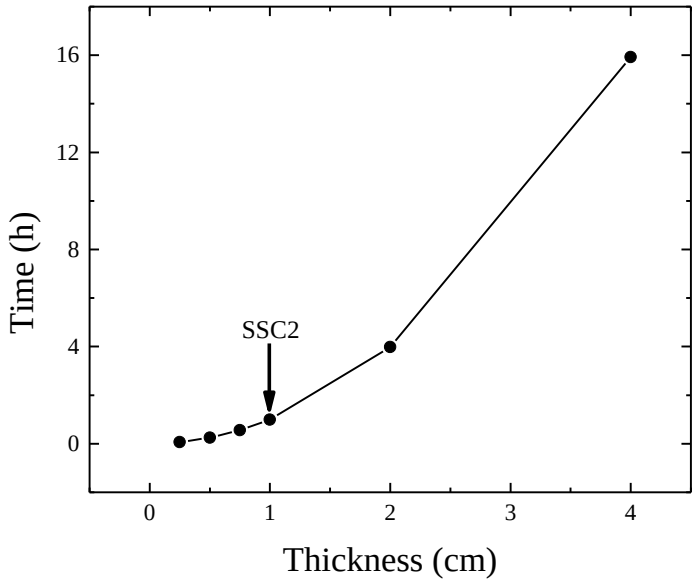

Figure 6-14: Time for complete B_2O_3 removal, as a function of the sample thickness.

The time for complete oxide removal was found to increase non-linearly as the thickness increases. The effect of the sample thickness was linearized by plotting the time for complete oxide removal as a function of the square of the sample thickness, shown in Figure 6-15 . The linear regression fit to Figure 6-15 satisfies the equation $y = y_o + a_l l^2$, where $y_o = -1.4168 \times 10^{-11}$ h and $a_l = 0.99503$ h·cm^{-2}.

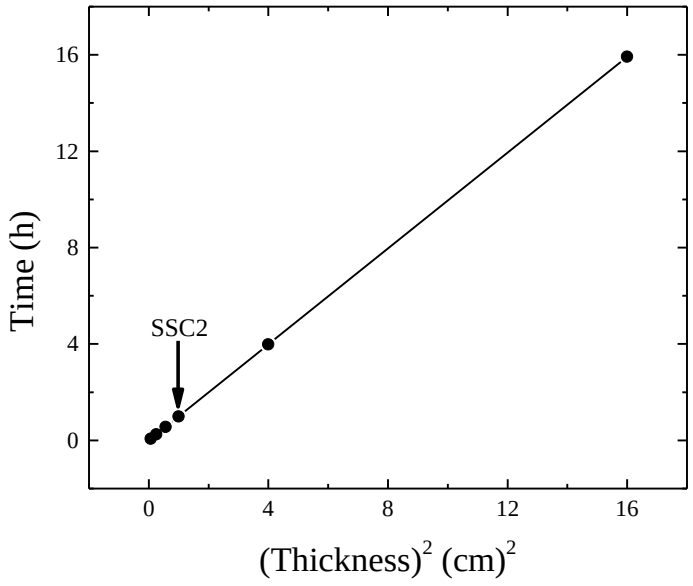

Figure 6-15: Time for complete B_2O_3 removal, as a function of the square of the sample thickness.

The quadratic dependence of the time for complete oxide removal on the sample thickness is similar to results are shown by Rossi *et al* and in Chapter 5.2.5 for chemical set 1. The slowing rate of advance of the reaction front causes the time for complete oxide removal to increase drastically for thick samples.

6.2.6 Effect of Initial B_2O_3 Content

The effect of the initial B_2O_3 content on the time for complete oxide removal was studied by varying the starting amount of B_2O_3. The SSC2 in Table 6-3 were used for all parameters, excluding the initial composition of each species. The initial B_2O_3 content was varied across the range including 0.275, 0.55, 0.825, 1.1, 1.65, 2.2, 2.75, and 3.3 mol %. The starting molar ratio of C/B_2O_3 was kept constant at 6, to ensure the complete reduction of all the starting oxide. The remaining mole percentage of material corresponds to B_4C (to equal 100 %). Figure 6-16 shows the time required to completely remove all the B_2O_3 from the porous medium, as a function of the initial B_2O_3 content. The linear regression fit to Figure 6-16 satisfies

the equation $y = y_o + a_{X_{B_2O_3}} X_{B_2O_3}$, where $y_o = -7.335 \times 10^{-2}$ h and $a_{X_{B_2O_3}} = 0.99155$ h·(B_2O_3 mol %)$^{-1}$.

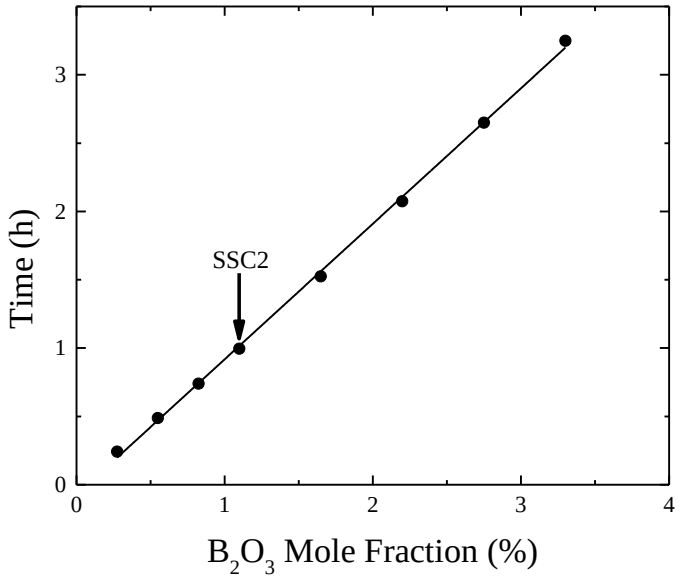

Figure 6-16: Time for complete B_2O_3 removal, as a function of the initial B_2O_3 content.

The time for complete oxide removal was found to increase linearly as a function of increasing initial B_2O_3 content; similar results are shown by Rossi *et al.* and for SiO_2 removal from chemical set 1 in Chapter 5.2.2.

6.2.7 Effect of Holding Temperature

The effect of the holding temperature on the time for complete oxide removal was studied by varying the temperature while using the SSC2 in Table 6-3. The holding temperature was varied across the range of temperatures including 1473.15, 1573.15, 1673.15, 1713.15, 1773.15, 1873.15, and 1973.15 K. Figure 6-17 shows the time required to completely remove all the B_2O_3 from the porous medium, as a function of the holding temperature.

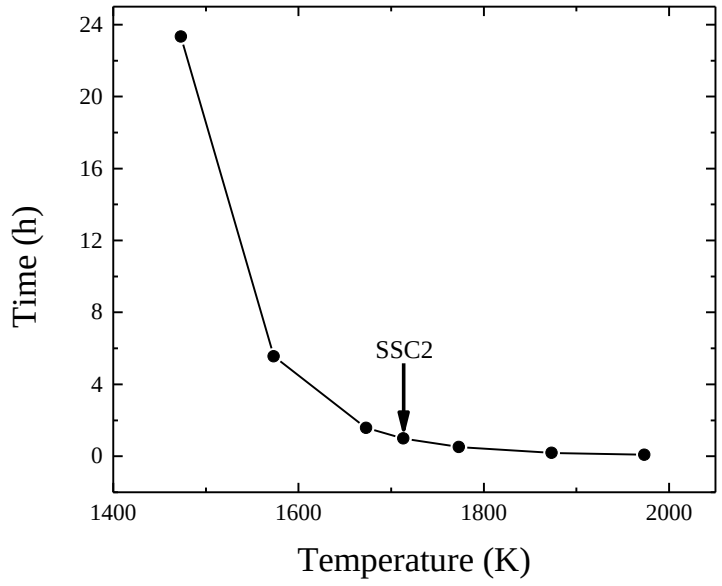

Figure 6-17: Time for complete B_2O_3 removal, as a function of the holding temperature.

The time for complete oxide removal was found to decrease non-linearly as the holding temperature was increased. Figure 6-18(a) shows this behavior to be linear when the holding temperature is plotted on a reciprocal scale and the completion time is on a natural logarithm scale. The time for complete oxide removal is linearized by plotting the natural logarithm of the time for complete oxide removal as a function of inverse temperature, shown in Figure 6-18(b). The linear regression fit to Figure 6-18(b) satisfies the equation $\ln t = \ln t_o + a_T T^{-1}$, where $\ln t_o = -19.30721$ when time is in hours and $a_T = 33074$ K.

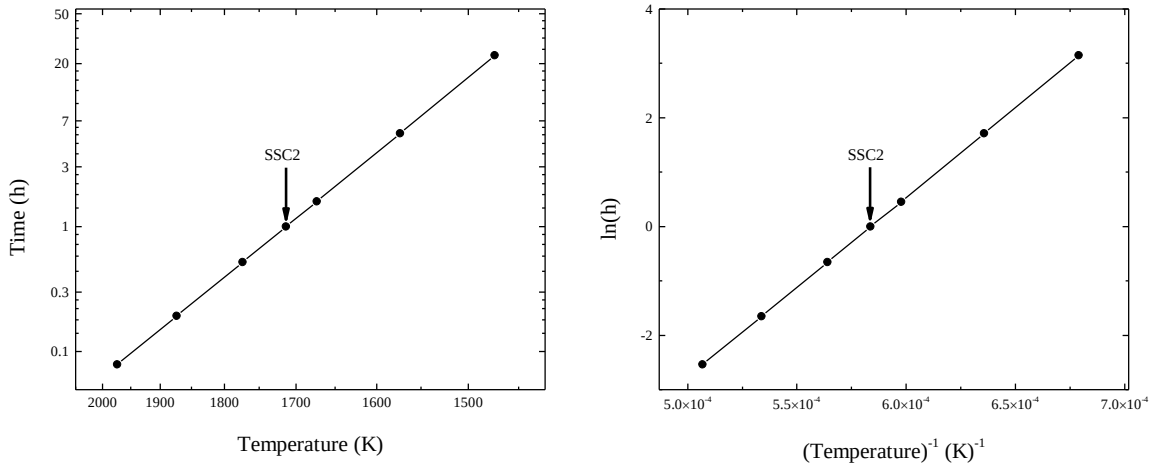

Figure 6-18: (a) Time for complete B_2O_3 removal (natural logarithm scale), as a function of the holding temperature (reciprocal scale). (b) Natural logarithm of time for complete B_2O_3 removal, as a function of inverse holding temperature.

Increasing the holding temperature does not qualitatively change any aspects of the partial pressure profiles. The equilibrium gas partial pressures at 1873.15 K are given in Table 6-5. Figure 6-19 shows the time evolution of the partial pressure profiles for $CO_{(g)}$, $B_2O_{3(g)}$, and $B_2O_{2(g)}$ at 1873.15 K, up to the time for complete oxide removal after 0.19226 h. Comparing Figure 6-8 and Figure 6-19 shows that the partial pressure profiles have the same shape despite being carried out at 1713.15 K and 1873.15 K, respectively. The two sets of plots are almost indistinguishable, up to a scaling of each partial pressure. At 1873.15 K, the $CO_{(g)}/B_2O_{2(g)}$ and $CO_{(g)}/B_2O_{3(g)}$ ratios are approximately 36 and 170, respectively; a decrease in both compared to 1713.15 K.

Table 6-5: Equilibrium partial pressures for chemical set 2 at 1873.15 K

Gas Species	p_{eq} (atm)
CO	1.3886
B_2O_2	3.8595×10^{-2}
B_2O_3	8.1374×10^{-3}

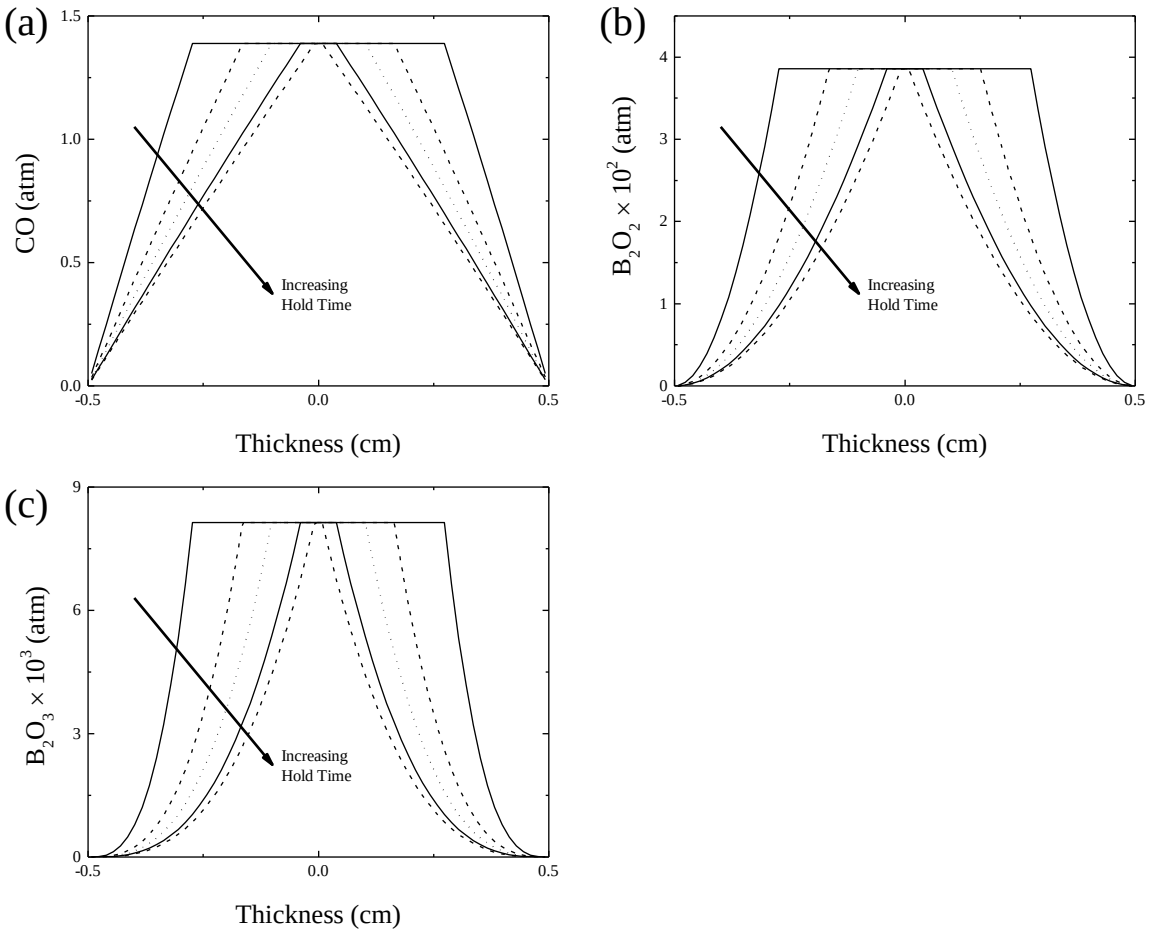

Figure 6-19: Partial pressure profile of (a) $CO_{(g)}$, (b) $B_2O_{2(g)}$, and (c) $B_2O_{3(g)}$ across the porous medium as simulation time increases up to t_c=0.19226 h. Times shown are in increments of t_c, where t ~1/5, 2/5, 3/5, 4/5, and 1 t_c. Simulation conditions are SSC2 at 1873.15 K.

Increasing the gas partial pressures results in a larger pressure gradient. Since the pressure gradient is the driving force for the transport $CO_{(g)}$ out of the porous medium, the effusion rate of $CO_{(g)}$ increases as the holding temperature increases. Figure 6-20 shows the effusion rate of $CO_{(g)}$ at 1873.15 K as the simulation time increases. The effusion rate starts at 114.64 mol·m^{-2}·h^{-1} and decreases to 12.36 mol·m^{-2}·h^{-1}, followed by a rapid drop to effectively zero. Figure 6-4 and Figure 6-20 allow for a comparison of the effusion rate behavior of $CO_{(g)}$ at 1713.15 K and 1873.15 K, respectively. Both have an initial, very rapid drop in the effusion rate, followed by a very slow decrease of the effusion rate. At the time for complete oxide removal, the effusion rate and maximum pressure are 5.16 and 5.31 times greater at the higher

temperature hold, respectively. There is no precise scaling relationship between the maximum pressure and the ending effusion rate, but there is a close connection between these two properties.

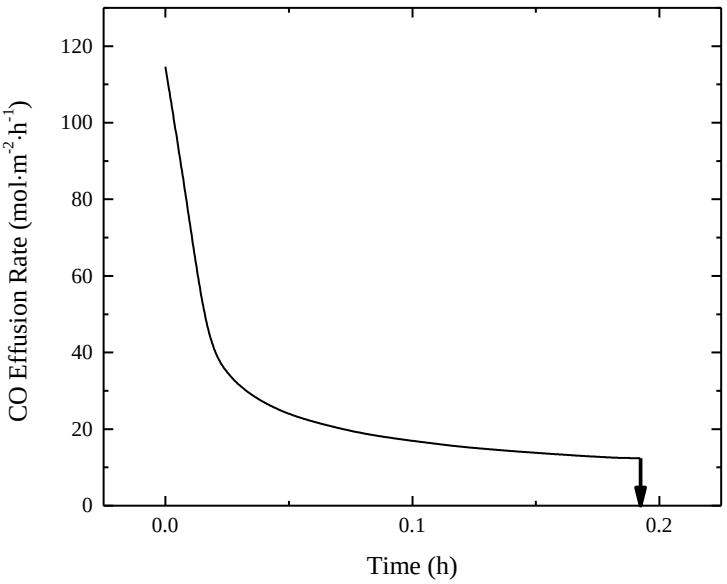

Figure 6-20: Effusion rate of $CO_{(g)}$ as the simulation time increases up to t_c=0.19226 h. Simulation conditions are SSC2 at 1873.15 K.

Increasing the holding temperature does not qualitatively change any aspects of the time evolution of the condensed species compositional profiles. Figure 6-21 shows the time evolution of the compositional profile for B_4C, B_2O_3, and C at 1873.15 K. Comparing Figure 6-6 and Figure 6-21 shows that the compositional profiles are almost quantitatively the same, despite being carried out at 1713.15 K and 1873.15 K, respectively. The relative percentage change of carbon was −62.06 % and −64.48 % for simulations at 1713.15 K and 1873.15 K, respectively.

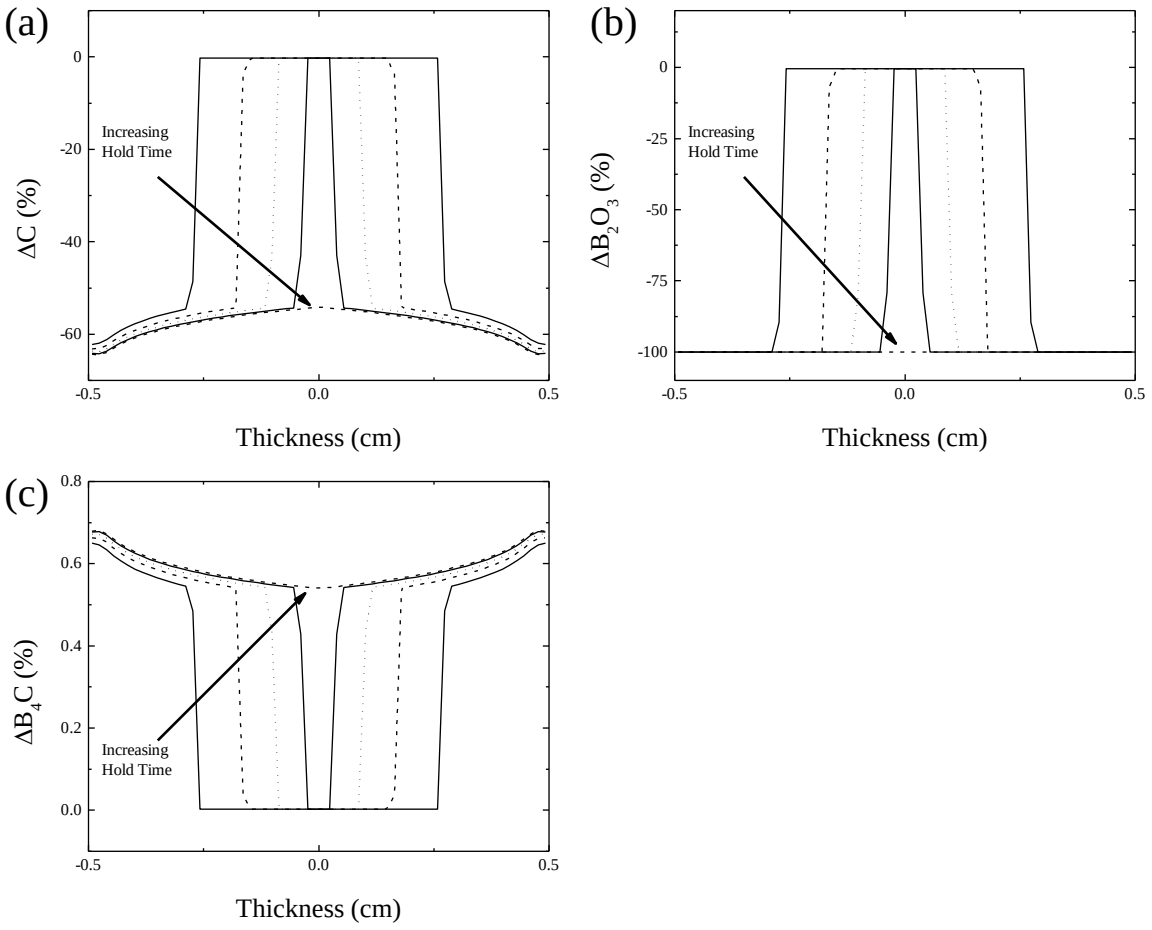

Figure 6-21: Compositional profile of (a) C, (b) B_2O_3, and (c) B_4C across the porous medium as simulation time increases up to t_c=0.19226 h. Times shown are in increments of t_c, where t ~ 1/5, 2/5, 3/5, 4/5, and 1 t_c. Simulation conditions are SSC2 at 1873.15 K.

For this chemical set, the decrease in the amount of carbon consumed in the center of samples at higher temperatures is mainly a consequence of the decrease in the $CO_{(g)}/B_2O_{2(g)}$ ratio from 59 to 36 at 1673.15 K and 1873.15 K, respectively. As the $CO_{(g)}/B_2O_{2(g)}$ ratio decreases, less C is needed to fully reduce all of the starting oxide (regime 1). Additionally, as the $CO_{(g)}/B_2O_{3(g)}$ ratio decreases, the amount of C consumed in the center of samples decreases, but to a lesser extent. However, the increased amounts of $B_2O_{2(g)}$ and $B_2O_{3(g)}$ cause a higher consumption of C at the edges of the sample (regime 3). Because at higher temperatures $CO_{(g)}$ and $B_2O_{2(g)}$ become commensurate in scale, larger deviations from the predicted C/B_2O_3 ratio of 3.5 occur across the length of the sample.

The C/B_2O_3 ratio profile across each sample, for select hold temperatures, is shown in Figure 6-22(a). The amount of C consumed at the surface increases and at the center decreases as the holding temperature is increased. Figure 6-22(b) shows the variation in the C/B_2O_3 ratio at different holding temperatures. The difference between the minimum and maximum C/B_2O_3 ratio increases with increasing temperature. There is slight decrease in the mean amount of C needed and the standard deviation about the mean C/B_2O_3 ratio is skewed toward the minimum. This reflects the higher uniformity near the center (location of the minimum ratio) and sharper gradients towards the edges (location of the maximum ratio).

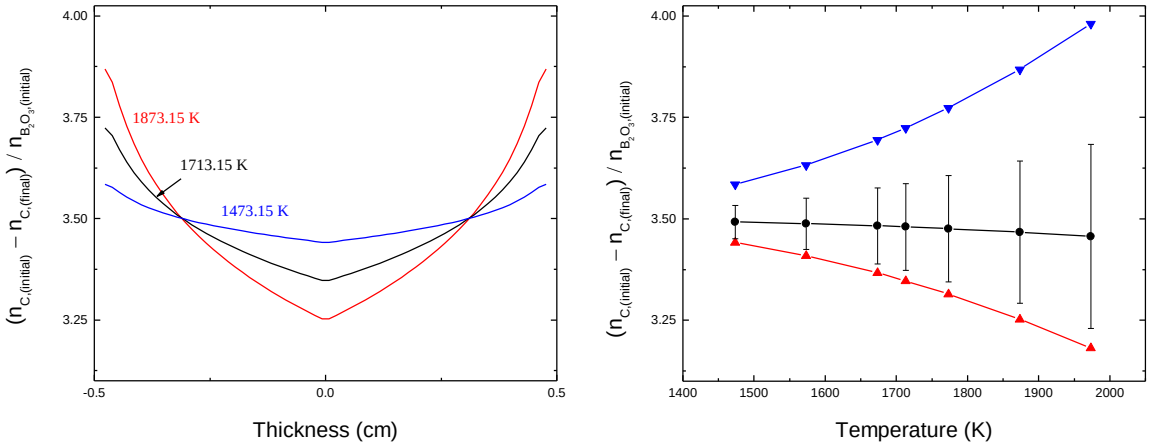

Figure 6-22: C/B_2O_3 ratio (a) Profile across samples at 1873.15 K [Red], 1713.15 K [Black], 1473.15 K [Blue]. (b) Variation as function of holding temperature: Maximum [Blue, Upper], Mean [Black, Middle], Minimum [Red, Lower], Standard deviation [Range] of the C/B_2O_3 ratio across each sample.

The change in the $B_2O_{2(g)}/CO_{(g)}$ and $B_2O_{3(g)}/CO_{(g)}$ ratios also have an effect on the final amount of B_4C, similar to C. In the center of the samples, the relative percentage change of B_4C decreases from 0.562 % to 0.541 % for simulations at 1713.15 K and 1873.15 K, respectively The decrease in the amount of B_4C produced is a consequence of consuming more B_4C to remove B_2O_3 (regime 1) as higher amounts of $B_2O_{2(g)}$ and $B_2O_{3(g)}$ are produced. At the edges of the samples, the relative percentage change of B_4C increases from 0.648 % to 0.681 % for simulations at 1713.15 K and 1873.15 K, respectively. The increase in B_4C is the result of higher

internal amounts of $B_2O_{2(g)}$ and $B_2O_{3(g)}$, which consume more C and producing more B_4C, as the gas evacuates through the oxygen deficient region (regime 3). The difference in the relative percentage change is much smaller for B_4C compared to C, because the initial amount of B_4C is in considerable excess to initial amount C.

In summary, the time for complete oxide removal appears to have an Arrhenius behavior ($\ln(t_c)$ vs. $1/\mathrm{T}$) with the holding temperature. This result is consistent with the equilibrium gas pressures also roughly having an Arrhenius dependence ($\ln(p_{eq})$ vs. $1/\mathrm{T}$) on temperature. Increasing the maximum gas pressure, by increasing the hold temperature, results in higher $CO_{(g)}$ effusion rates and faster B_2O_3 removal rates. The time for complete oxide removal is mainly controlled by the production and removal of $CO_{(g)}$. The time for complete oxide removal can be modeled effectively by including only $CO_{(g)}$, because the $CO_{(g)}$ pressure dominates over $B_2O_{2(g)}$ and $B_2O_{3(g)}$. However, secondary effects, such as the increased variation in the C/B_2O_3 ratio with increasing holding temperature, are only evident due to the inclusion of minor gas species. The chosen chemical set provides evidence that varying the holding temperature changes the ratio of the equilibrium gas partial pressures, resulting in a quantifiable change in the final condensed species compositions as seen in Figure 6-22. This is consistent with the experimental observations of property gradients.

6.2.8 Parameter Linearization

The previous sections for chemical set 2 have established a standard reference simulation (SRS2) and described the effects of varying the simulation parameters. Following the approach outlined by Kaza *et al.*[90] (shown in Chapter 6.2.8) and performed by Rossi *et al.* on a similar chemical set, a semi-empirical equation was constructed using a sensitivity parameter based upon the linearization of each model parameter. The t_c for SRS2, t_o, was used to center

the linearization using the SSC2 given by Table 6-3 and used to scale the slope of each linearization (*e.g.* $b_\varepsilon = a_\varepsilon / t_o$). The linearized forms and parameter sensitivities for all of the independent parameter variations are shown in Table 6-6. Only the temperature sensitivity parameter is not scaled by t_o.

Except for ε and T, all of the linearized expressions coincide with those of Rossi *et al.* These are the same two deviations from the work of Kaza *et al.*[90] that was observed for chemical set 1. The current study and Rossi *et al.* both show an exponential dependence on T with the functional forms given by $t_o \exp\left(b_T \Delta\left[\frac{1}{T}\right]\right)$ and $t_o \exp(b_T \Delta[T])$, respectively.[91] If the functional form of Rossi *et al.* was used in the current study it would only result in a minor deviation because the transformed data was close to linear (with slight systematic curvature).[91] This was not the case with the porosity and using $(1-\varepsilon)/\varepsilon$ to transform the data resulted in a highly nonlinear behavior, instead prompting the use of $(1-\varepsilon)^{3/2}$ to linearize the data.

Table 6-6: Linearized expressions relating the time for complete oxide removal, t_c, to each parameter for chemical set 2

Parameter	Expression for t_c	b_i
Porosity (ε)	$t_o\left(1 + b_\varepsilon \Delta\left[(1-\varepsilon)^{3/2}\right]\right)$	2.1056
Tortuosity (q)	$t_o\left(1 + b_q \Delta[q]\right)$	0.2000
Pore radius (r)	$t_o\left(1 + b_r \Delta\left[\frac{1}{r}\right]\right)$	16.00 nm
Thickness (l)	$t_o(1 + b_l \Delta[l^2])$	1.000 cm^{-2}
B_2O_3 ($X_{B_2O_3}$)	$t_o\left(1 + b_{X_{B_2O_3}} \Delta\left[X_{B_2O_3}\right]\right)$	0.9965
Temperature (T)	$t_o \exp\left(b_T \Delta\left[\frac{1}{T}\right]\right)$	33075 K

t_c, takes a value of t_o=*0.9950* h for the SSC2 listed in Table 5-3

It is very interesting to compare the parameter sensitivities from chemical set 1 and 2 given by Table 5-6 and Table 6-6, respectively. The corresponding sensitivity values are either very similar or identical for the two chemical sets. The tortuosity, pore radius, and thickness are parameters that are independent of an influence of the chemical set chosen and have identical

values. Those parameters are essentially independent of the chemical set chosen and solely properties of the DGM. The porosity, mole fraction of oxide (SiO_2 and B_2O_3), and the temperature parameter sensitivities for the two systems are very close in scale, but there are some differences.

It is not surprising that there is a difference in the temperature dependence because t_c is highly sensitive to the $CO_{(g)}$ pressure and the $CO_{(g)}$ pressure increases at different rates for the two chemical sets. The current modeling framework accounts for changes in porosity due to reaction. Thus, the increase in the final porosity is coupled to the amount of oxide to be depleted. This is a small effect due to the small percentage of oxide and carbon, but would slightly increase the ε/q scaling of the diffusion coefficients in the DGM. Any coupling between the initial porosity and oxide content would be weakly dependent on the oxide species and the amount of carbon needed to fully reduce them. For these reasons, it would not be expected that the parameter sensitivity of porosity, initial oxide content, and temperature to be exactly coincident across chemical sets as tortuosity, pore radius, and thickness are shown to be in these two chemical sets.

Assuming the various parameter dependencies of t_c are weakly coupled, allows the linearized expression from Table 6-6 to be combined into a single equation. The resulting semi-empirical equation describing the simultaneous variation of multiple parameters is given by

$$t_c = t_o\left(1 + b_\varepsilon \Delta\left[(1-\varepsilon)^{3/2}\right]\right) \cdot \left(1 + b_q \Delta[q]\right) \cdot \left(1 + b_r \Delta\left[\frac{1}{r}\right]\right) \times \left(1 + b_l \Delta[l^2]\right) \cdot \left(1 + b_{X_{\mathrm{SiO_2}}} \Delta\left[X_{\mathrm{SiO_2}}\right]\right) \cdot \exp\left(b_T \Delta\left[\frac{1}{T}\right]\right) \tag{184}$$

The assumption that the parameters are weakly coupled was checked by creating sets of simulation conditions that simultaneously vary all of the six parameters. The amount of C implicitly changes as the amount of starting oxide changes and is designed to start at 6 times the initial amount of B_2O_3. Each parameter is changed such that the t_c is scaled by the same proportion. For example, changing each parameter by an amount such that $t_c = 0.5t_o$, would mean that the combined effect would reduce the t_c by a factor of 64. Under these conditions, the predicted t_c would be reduced to $t_o/64 = 1.55\times10^{-2}$ h; the actual simulation gives a value of 1.77×10^{-2} h. This shows Equation 183 gives a good prediction of t_c even when all the parameters are changed by a large amount, confirming that the assumption that the individual parameters are weakly coupled. The sets of simulation conditions, actual simulation times, and the predicted t_c are given in Table 6-7; parameter changes that increase and decrease t_c are both well represented by Equation 183.

Table 6-7: Semi-empirical equation sensitivity test for chemical set 2

Parameter	Reference Value	$1.25t_o$	$0.8t_o$	$0.5t_o$	$0.25t_o$
B_2O_3 ($X_{B_2O_3}$) (mol %)	1.1	1.3509	0.8993	0.5982	0.3474
Porosity	0.4	0.3017	0.4848	0.6276	0.7724
Tortuosity	5	6.250	4.000	2.500	1.250
Pore radius (nm)	16	12.80	20.00	32.00	63.99
Thickness (cm)	1	1.1180	0.8944	0.7071	0.5000
Temperature (K)	1713.15	1693.6	1733.2	1776.9	1845.7
Actual t_c (h)	0.9950	3.7581	0.2680	1.77×10^{-2}	2.43×10^{-4}
Predicted t_c (h)	0.9950	3.7956	0.2608	1.55×10^{-2}	2.60×10^{-4}

Equation 183 can be used to gain insight into the effect of changing any of the simulation parameters on t_c. This allows for t_c to be predicted without recourse to explicitly

calculating the simulation for every set of experimental parameters. The functional relationships identified also provide guidance when designing adequate processing conditions to account for industrial scaling and/or changing parameters due to raw material characteristics.

6.3 Summary of Chemical Set 2

Chemical set 2 consists of simulations designed to analyze the removal of B_2O_3 from porous media comprised of B_4C, B_2O_3, and C. The reaction between B_2O_3 and C produces predominantly $CO_{(g)}$ and B_4C. The removal of B_2O_3 is limited by the ability to remove $CO_{(g)}$ from the porous medium, subsequently removing more B_2O_3 to replenish the $CO_{(g)}$ that was removed. This behavior is qualitatively the same as chemical set 1, where SiO_2 is removed by the formation and removal of the dominate gas $CO_{(g)}$. Similar to chemical set 1, a reaction front is created at each surface, which proceed towards the center of the sample as B_2O_3 is depleted, and mark the time for complete oxide removal (t_c). The time for complete oxide removal was studied for constant temperature simulations.

The constant temperature simulations were simulated using an isothermal hold temperature and individually varying the model parameters for porosity, tortuosity, pore radius, thickness, holding temperature, and initial oxide content. The linearized functional dependence of t_c on each parameter was found and used to create a semi-empirical equation that can be used to predict t_c for isothermal holds. A comparison of t_c from simulations that simultaneously varied all of the simulation parameters and t_c predicted using the semi-empirical equation showed good agreement. The overall form of the semi-empirical equation is very similar to that of Rossi *et al.* (despite the differences already mentioned) and validates the modeling framework correctly simulates oxide removal behavior for chemical set 2. Additionally, this shows that the general modeling framework is adaptable to different chemical sets and

confirms it is able to successfully replicates the major findings of two previously studied chemical sets (chemical set 1 and 2).

Chemical set 1 and 2 are highly comparable because the oxide removal mechanism for both sets are the same. Both chemical sets have the same functional dependence on t_c for all of the model parameters. The parameter sensitivities for thickness, pore radius, and tortuosity are exactly the same for both chemical sets. This indicates that these parameters that only affect the transport aspect of simulation are independent of the chemical set. Thus, varying these parameters for any other chemical set should have the same effect on the oxide removal rate as it does for chemical set 1 and 2.

Additional similarities are seen when comparing the parameter sensitivities for porosity and initial oxide content. The parameter sensitivity for each differ by only a few percent between the two sets. The dependence on the porosity and initial oxide content are coupled because the change in the porosity is dependent on the amount and density of the oxide. However, this overall effect is small because only a small percentage of the starting composition is oxide. It is expected that this effect will also be seen in chemical sets other than chemical set 1 and 2. The temperature sensitivity between the two sets is different because it depends on the thermodynamics of the each set. However, because $CO_{(g)}$ controls the transport properties and oxide removal for both chemical sets, the effusion rate behavior for similar equilibrium pressures is almost identical.

The main difference between the two chemical sets is the extent of secondary reactions that occurs due to the minor gas species. Chemical set 1 has a C/SiO_2 that closely reflects the ratio of 3 predicted by the dominate reaction (Equation 150), because a $CO_{(g)}/SiO_{(g)}$ ratio of 284 (at 1673.15 K) limits the amount of secondary reactions that can occur. Chemical set 2 shows a

significant variation from the C/B_2O_3 ratio of 3.5 predicted by the dominate reaction (Equation 226), because a $CO_{(g)}/B_2O_{2(g)}$ ratio of 59 (at 1713.15 K) allows for a greater amount of secondary reactions to occur. It was observed that there is more carbon depleted from the edges of the sample and less is depleted from the center than would be simply predicted. The difference in the amount of C consumed between the edge and the center exceeds 10 % at 1713.15 K. This deviation from the predicted C/B_2O_3 ratio and the residual C non-uniformity increases with the holding temperature because the $CO_{(g)}/B_2O_{2(g)}$ ratio decreases. Chemical set 2 shows that the presence of a significant quantity of secondary gas species can result in a large amount of non-uniformity in the residual solids compositions.

The parameter sensitivities between chemical set 1 and 2 were compared and showed that in both cases the parameter sensitivities were either close or identical. The similarity of oxide removal mechanism (i.*e.* $CO_{(g)}$ formation and transport) and of the parameter sensitives indicates that the same trends of behavior are likely to be seen in chemical sets that have a similar oxide removal mechanism. Additionally, the same effusion rate behavior would be expected for chemical set 2, when using a heating cycle, as was seen for chemical set 1 in Chapter 5.3. In summary, understanding how porous media parameter variation affects t_c and the residual solids compositions provides a practitioner useful insight into how to design heating schedules to remove B_2O_3 from porous B_4C green bodies.

7 Chemical Set 3 Simulations: {C, SiC, SiO_2, B_4C, $CO_{(g)}$, $SiO_{(g)}$, $B_2O_{3(g)}$, $B_2O_{2(g)}$}

There is a practical need to include sintering additives to facilitate the full densification of SiC. For sintering additives to be effective, they need to be present in sufficient quantity and uniformly distributed throughout a green body at the time of densification. Chemical set 3 is used to study the effect of including B_4C, representative of a sintering additive, in addition to the condensed species studied in chemical set 1. During the removal of SiO_2, the inclusion of B_4C increases the complexity of the equilibrium gas species mixture and the ability for redistribution of condensed species. The objective of this chapter is to identify and quantify factors producing a variation in the initial B_4C distribution during the removal of SiO_2. After all the SiO_2 is removed, the quantity of all the gas species falls quickly due to the low vapor pressure of the remaining condensed species, eliminating any further condensed species redistribution. Therefore, the resultant condensed species distribution should be a good representative of the distribution present at the time of densification.

The results from simulations studying the transport and reaction in a porous medium comprised of condensed C, SiC, SiO_2, and B_4C are presented in this chapter. The chemical species modeled in the simulations are restricted to the chemical set {C, SiC, SiO_2, B_4C, $CO_{(g)}$, $SiO_{(g)}$, $B_2O_{3(g)}$, $B_2O_{2(g)}$}. The porous medium is assumed to be reactive and the gas species produced from chemical reactions are limited to only $CO_{(g)}$, $SiO_{(g)}$, $B_2O_{3(g)}$, and $B_2O_{2(g)}$. This chemical set accounts for the initial condensed species present in the porous medium and the gas species with the four largest partial pressure in equilibrium with the condensed species. In reality, the reaction of the condensed and gas species will produce additional chemical species, but these will have only a minor effect on the qualitative and quantitative behavior observed during

simulations. Figure 7-1 shows the partial pressures of various gas species in equilibrium with condensed C, SiC, SiO_2, and B_4C.The study of the transport and reaction in porous media for this chemical set is restricted to constant temperature simulations.

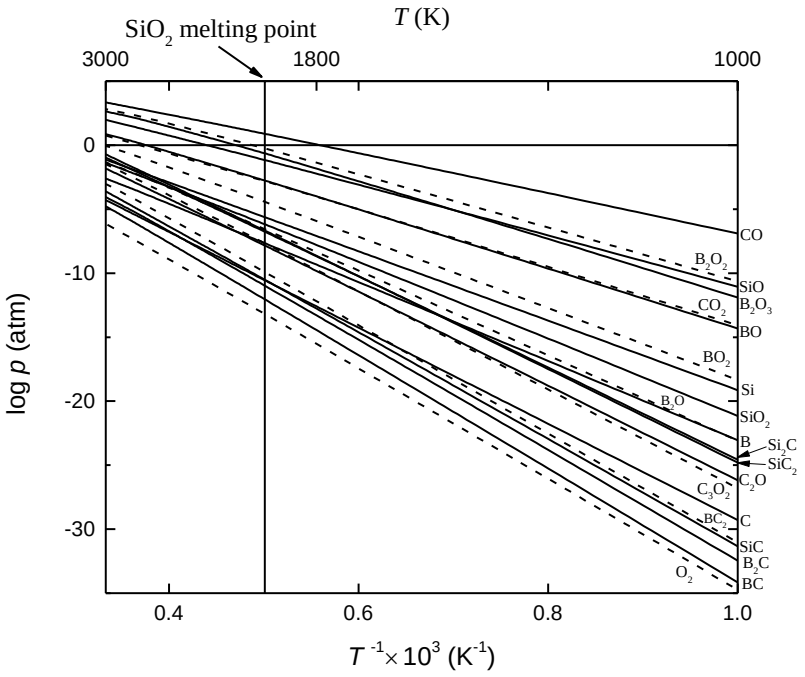

Figure 7-1: Gas pressures as a function of temperature for several species in equilibrium with solid SiC, C, B_4C and solid (T < 1996 K) or liquid (T > 1996 K) SiO_2.

Similar to the procedure for SiC in Chapter 5, the compositional profiles of the condensed species are represented by their percentage change. The compositional profile for B_2O_3 is denoted by ΔB_2O_3 (%) and the *time for complete oxide removal*, t_c, is when ΔB_2O_3 (%) = -100 across the whole porous medium. Additionally, the same numerical scheme and simulations checks were used to verify the convergence of the numerical solution

7.1 Physical Constants and Expressions

The same collection of physical constants and simulation parameters as chemical set 1 (Chapter 5.1) are needed for the current chemical set. The relevant parameters for C, SiC, SiO_2, and B_4C are provide in Table 7-1 and those for $CO_{(g)}$, $SiO_{(g)}$, $B_2O_{3(g)}$, and $B_2O_{2(g)}$ are provided in

Table 7-2. The Gibbs free energy function for each species is not explicitly listed, but the required data to construct them is provided in Appendix IV.iii.

Table 7-1: Material properties for the condensed chemical species from chemical set 3.

Condensed Species	MM ($g \cdot mol^{-1}$)	ρ ($g \cdot cm^{-3}$)
C	12.0107	2.10
SiC	40.0962	3.21
SiO_2	60.0843	2.20
B_4C	55.2547	2.50

Table 7-2: Material Properties for the Gas Chemical Species from Chemical Set 3.

Gas Species	MM ($g \cdot mol^{-1}$)	σ (Å)	ϵ/k_B (K)
CO	28.0101	3.8	88
SiO	44.0849	3.6	88
B_2O_3	69.6202	4.1605	2092
B_2O_2	53.6208	4.79	350

7.2 Constant Temperature Simulations

This study of constant temperature simulations systematically investigates the effect of individually varying the length of the porous medium, the initial chemical composition, and the holding temperature. The chemical composition of each species was varied on a mole fraction basis. These variations were designed to have a constant 0.25 mol % of B_4C, a molar ratio of C/SiO_2 (= 4.4), to ensure the complete reduction of SiO_2, *i.e.* enough carbon to ensure that it is not exhausted before the B_2O_3 anywhere within the body. The remaining mole percent of material consisted of SiC. Similar to the conditions for chemical set 1 in Chapter 5.2, the samples are in a vacuum and the simulations stop when all the SiO_2 is removed. A standard set of simulation conditions was chosen as a reference point to which all other simulations could be

compared. The parameters for the *standard simulation conditions* for chemical set 3 (SSC3) are listed in Table 7-3.

Table 7-3: Standard simulation conditions (SSC3) reference parameter values for chemical set 3.

Parameter	Reference Value
C (X_{C})	4.4 mol %
SiC (X_{SiC})	94.35 mol %
SiO_2 ($X_{\mathrm{SiO_2}}$)	1.0 mol %
B_4C ($X_{\mathrm{B_4C}}$)	0.25 mol %
Porosity (ε)	0.4
Tortuosity (q)	5
Pore radius (r)	16 nm
Thickness (l)	1 cm
Temperature (T)	1673.15 K

7.2.1 Standard Reference Simulation (SRS3)

The qualitative and quantitative behavior of the standard reference simulation (SRS3) is presented in this section. SRS3 uses the SSC3 values from Table 7-3. Similar to SRS1 (Chapter 5.2.1), the porous medium is assumed evacuated of all gas and heated instantaneously to 1673.15 K, initiating the reaction and transport cycle of behavior. Table 7-4 lists the equilibrium partial pressures of $CO_{(g)}$, $SiO_{(g)}$, $B_2O_{3(g)}$, and $B_2O_{2(g)}$ at 1673.15 K for chemical set 3. The most abundant gas is $CO_{(g)}$, followed by $B_2O_{2(g)}$, $B_2O_{3(g)}$, and then $SiO_{(g)}$. The ratio of $CO_{(g)}/SiO_{(g)}$, $CO_{(g)}/B_2O_{3(g)}$ and $CO_{(g)}/B_2O_{2(g)}$ are approximately 284, 150, and 43, respectively.

Table 7-4: Equilibrium partial pressures for chemical set 1 at 1673.15 K

Gas Species	P_{eq} (atm)
CO	0.25395
SiO	8.92508×10^{-4}
B_2O_3	1.69033×10^{-3}
B_2O_2	5.84830×10^{-3}

Similar to chemical set 1 and 2, since the transport of gas out of the porous medium happens only at the surface and initially that is the only location with any pressure gradient, it is the surface that is first depleted of SiO_2. Figure 7-2 shows the growth of the regions depleted of SiO_2 as a function of time. The simulation stops at 1.02832 h, when all of the SiO_2 is depleted.

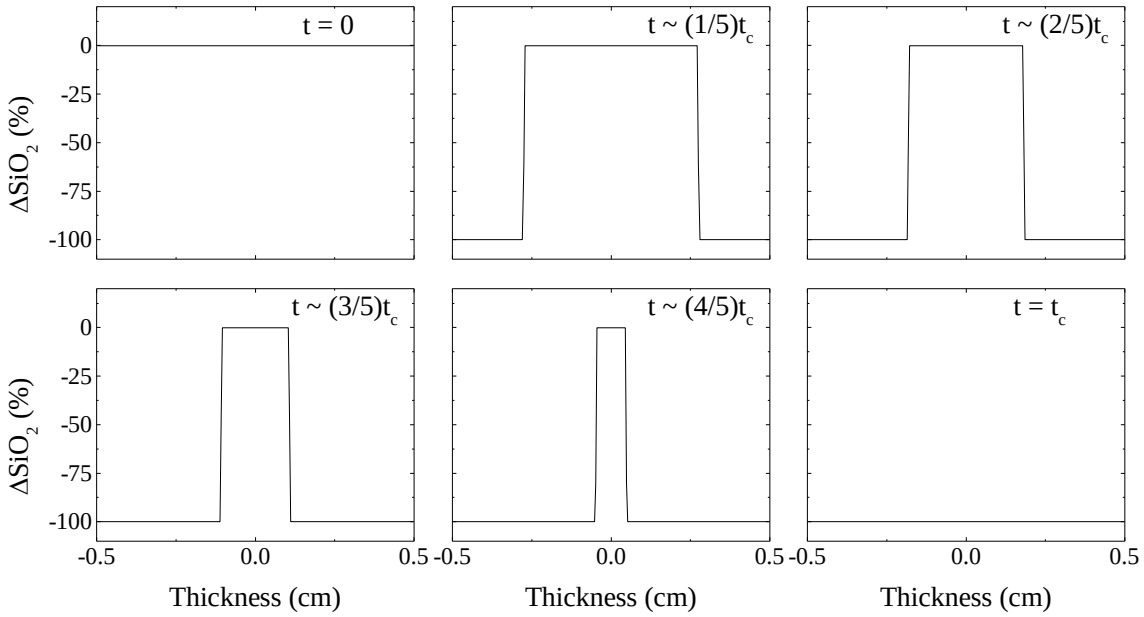

Figure 7-2: Compositional profile of SiO_2 across the porous medium as the simulation time increases up to t_c=1.02832 h. Times shown are in increments of t_c, where t ~ 0, 1/5, 2/5, 3/5, 4/5, and 1 t_c. Simulation conditions are SSC3.

Once the surface is depleted of SiO_2 and the region becomes oxygen deficient, the equilibrium partial pressures begin to vary from those in Table 7-4. The chemical equilibrium in this region corresponds to chemical regime 3 for chemical set 3 in the Appendix III.iv. Similar to

SiO_2 removal in chemical set 1 (Chapter 5.2.1), a reaction front forms at the interface between regimes 1 and 3. The change in behavior of the compositional and pressure profile at the reaction front is specific to each chemical species. This characteristic behavior during SiO_2 removal for SRS3 shown in Figure 7-2 is the same is that for SRS1 shown in Figure 5-2 and qualitatively similar to B_2O_3 removal for SRS2 shown in Figure 6-2. The change in behavior of the compositional and pressure profile at the reaction front is specific to each chemical species.

The depletion of SiO_2 is mainly attributed to the transport of $CO_{(g)}$ out of the surfaces of the porous medium. The time evolution of the $CO_{(g)}$ partial pressure profile is shown in Figure 7-3 and is the same behavior for $CO_{(g)}$ in chemical set 1 shown in Figure 5-3. Since there is a similar slow movement of the reaction front for both chemical sets, there is also approximately linear variation in the $CO_{(g)}$ pressure in the depleted regime due to the quasi-static diffusion conditions. As described earlier for chemical system 1 and 2, Kaza *et al*.[90] and Rossi *et al.* observed that even though the DGM is non-Fickian, *i.e.* the effective diffusion coefficient of each species is not independent of pressure, the gas diffusion behavior is approximately Fickian, respectively. Analogous to quasi-static Fickian diffusion, the $CO_{(g)}$ pressure decreases linearly from that at the reaction front to the pressure at the surface. Comparing Figure 7-2 and Figure 7-3, it is clear that the region with the linear $CO_{(g)}$ pressure gradient coincides with the depleted SiO_2 region.

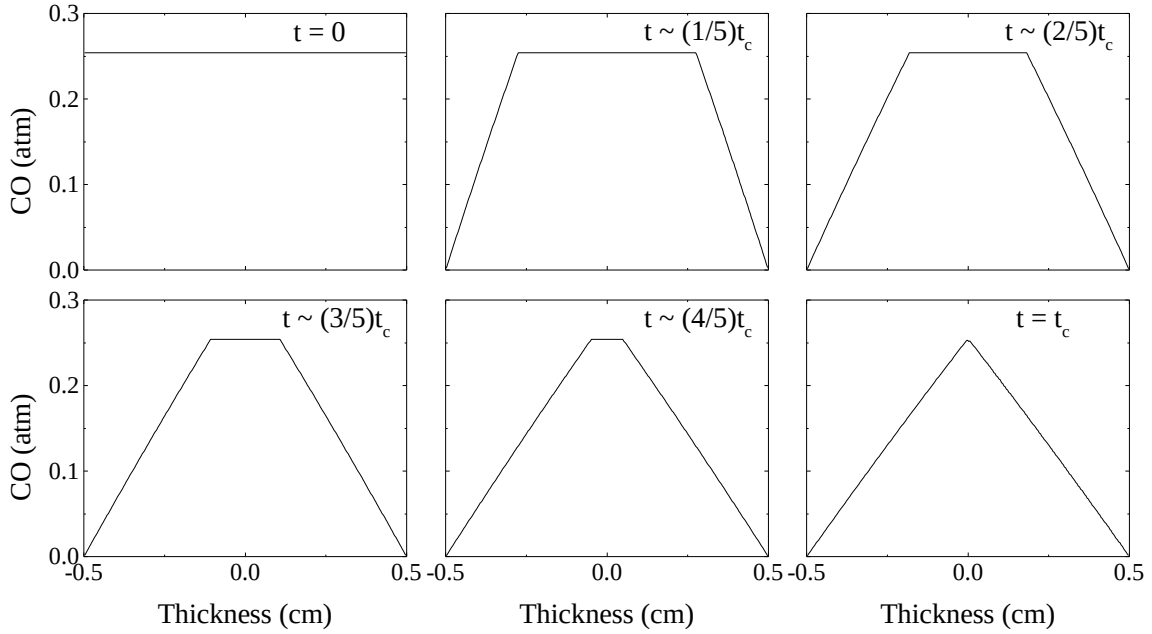

Figure 7-3: Partial pressure profile of $CO_{(g)}$ across the porous medium as the simulation time increases up to t_c=1.02832 h. Times shown are in increments of t_c, where t ~ 0, 1/5, 2/5, 3/5, 4/5, and 1 t_c. Simulation conditions are SSC3.

As was shown for chemical set 1, the pressure gradient is the driving force for the transport of $CO_{(g)}$ and the rate of gas removal is highly sensitive to the magnitude of the pressure gradient. Figure 7-4 shows the effusion rate of $CO_{(g)}$ as the simulation time increases. The effusion rate starts at 51.6 $mol \cdot m^{-2} \cdot h^{-1}$ and decreases to 2.6 $mol \cdot m^{-2} \cdot h^{-1}$ at the time all the SiO_2 is removed, followed by a rapid drop to zero. Because the $CO_{(g)}$ pressures for chemical set 1 and 3 are the same in regime 1, the effusion rate behavior shown in Figure 7-4 and Figure 6-4 also almost identical.

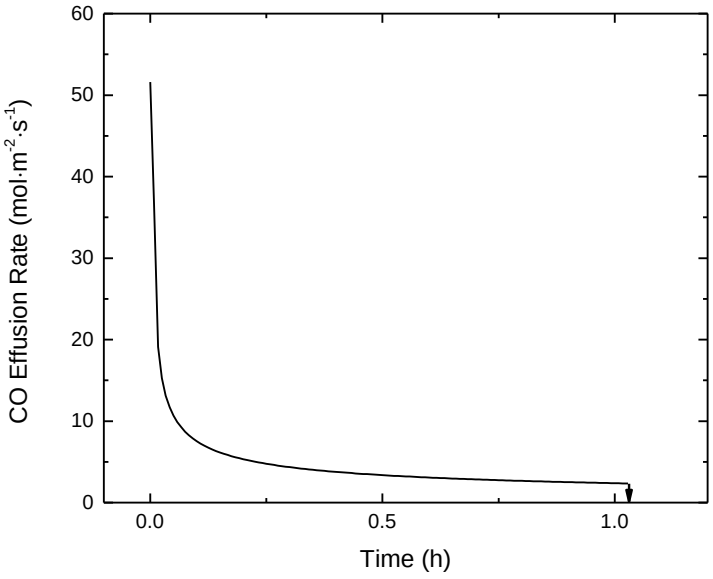

Figure 7-4: Effusion rate of $CO_{(g)}$ as the simulation time increases up to t_c=1.02832 h. Simulation conditions are SSC3.

Initially, the rate of SiO_2 removal is at a maximum because the effusion rate of $CO_{(g)}$ is at a maximum, resulting in a rapid advance of the reaction front. As the reaction front proceeds, the effusion rate of $CO_{(g)}$ drops and SiO_2 is removed at a slower rate. Accordingly, the rate of advance of the reaction front slows with increasing simulation time. This behavior is evident in Figure 7-2 and Figure 7-3 when comparing the rapid advance of the reaction front between t=0 and t~(1/5)t_c to the relatively slow advance of the reaction front between t~(4/5)t_c and t=t_c. The rate of advance decreases in an approximately quadratic manner, similar to reaction front behavior observed in chemical sets 1 and 2.

The inclusion of B_4C opens up alternative SiO_2 reduction pathways. Initially, the sample is assumed to be evacuated of all gas species. However, thermodynamic equilibrium insists that there is some non-zero quantity of $B_2O_{2(g)}$ and $B_2O_{3(g)}$. Two plausible equilibrium reactions are represented by Equation 311 and 312. These reactions show that B_4C and C will reduce SiO_2 to produce $B_2O_{2(g)}$ and $B_2O_{3(g)}$ as well as SiC. Consequently, in regime 1, B_4C and C are less stable

than SiC and will be consumed as the reaction front proceeds. Figure 7-5 shows how the compositional profile of B_4C changes in time as the reaction front proceeds.

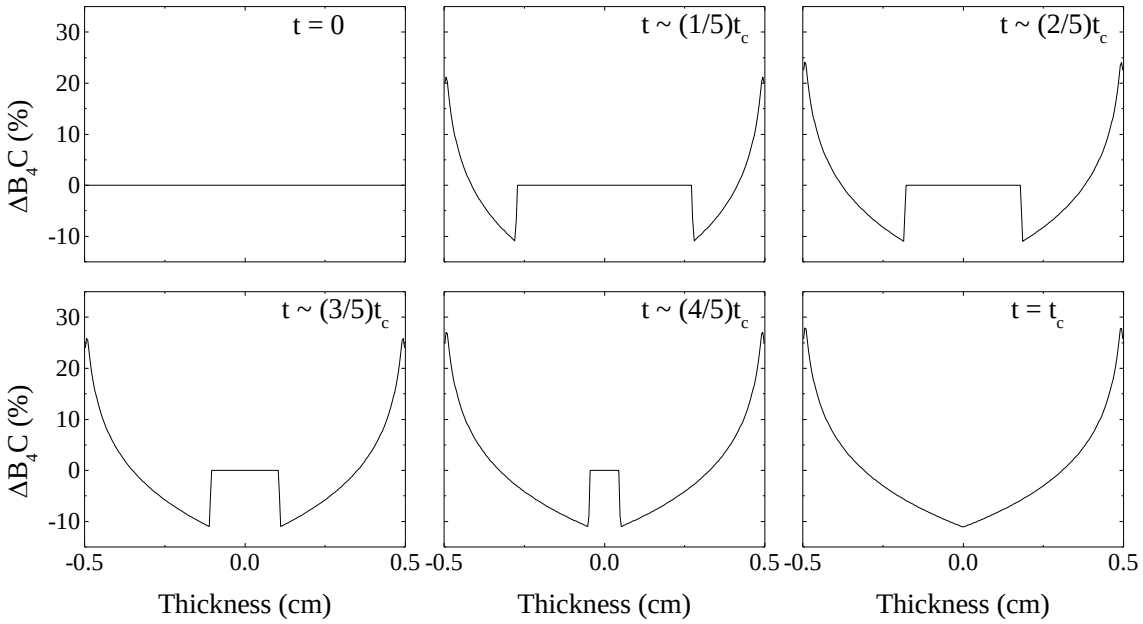

Figure 7-5: Compositional profile of B_4C across the porous medium as the simulation time increases up to t_c=0.9950 h. Times shown are in increments of t_c, where t ~ 0, 1/5, 2/5, 3/5, 4/5, and 1 t_c. Simulation conditions are SSC3.

Figure 5-6 and Figure 6-6 show that the time evolution of the species in chemical sets 1 and 2 are all characterized by a sharp gradient at the reaction front. Additionally, if a species gets deposited, it only continues to get deposited and if a species is depleted by reaction, it only further gets depleted. The time evolution of B_4C has a more complicated behavior than the other condensed species. There is a clear reduction in the amount of B_4C at the reaction front, consistent with the previous argument regarding the stability of B_4C in the oxygen rich region. However, in the oxygen deficient region (regime 3), the amount of B_4C increases at the edges of the sample with time. Two plausible chemical reactions for the deposition of B_4C are given by Equations 354 and 355. These reactions show that $B_2O_{2(g)}$ and $B_2O_{3(g)}$ can react with C to produce B_4C and $CO_{(g)}$. In this regime, the less stable carbide is dependent upon the relative partial

pressures of the gas species. But, for SRS3, the equilibrium calculations show that B_4C is deposited as $B_2O_{2(g)}$ and $B_2O_{3(g)}$ are removed due to gas transport.

The time evolution of the compositional profiles of SiO_2 and B_4C, shown frame by frame in Figure 7-2 and Figure 7-5, give a visualization of the reaction behavior. The time evolution of the compositional profiles for SiO_2, C, SiC, and B_4C are shown concisely in Figure 7-6, with an arrow indicating the progression in time. Comparing the time evolution the species in SRS1, SRS2, and SRS3 corresponding to Figure 5-6, Figure 6-6, and Figure 7-6 shows that they all have similar features, including the behavior of B_4C for SRS3 in the oxygen depleted region. The residual carbon profile in Figure 6-6(a) and Figure 7-6(a) are qualitatively similar. For SRS2 this was attributed to the increased deposition of B_4C at the edges of the sample as shown in Figure 6-6(c). This same deposition behavior is seen for B_4C in SRS3 in the oxygen depleted region, but at the reaction front B_4C is actually consumed while SiO_2 is removed.

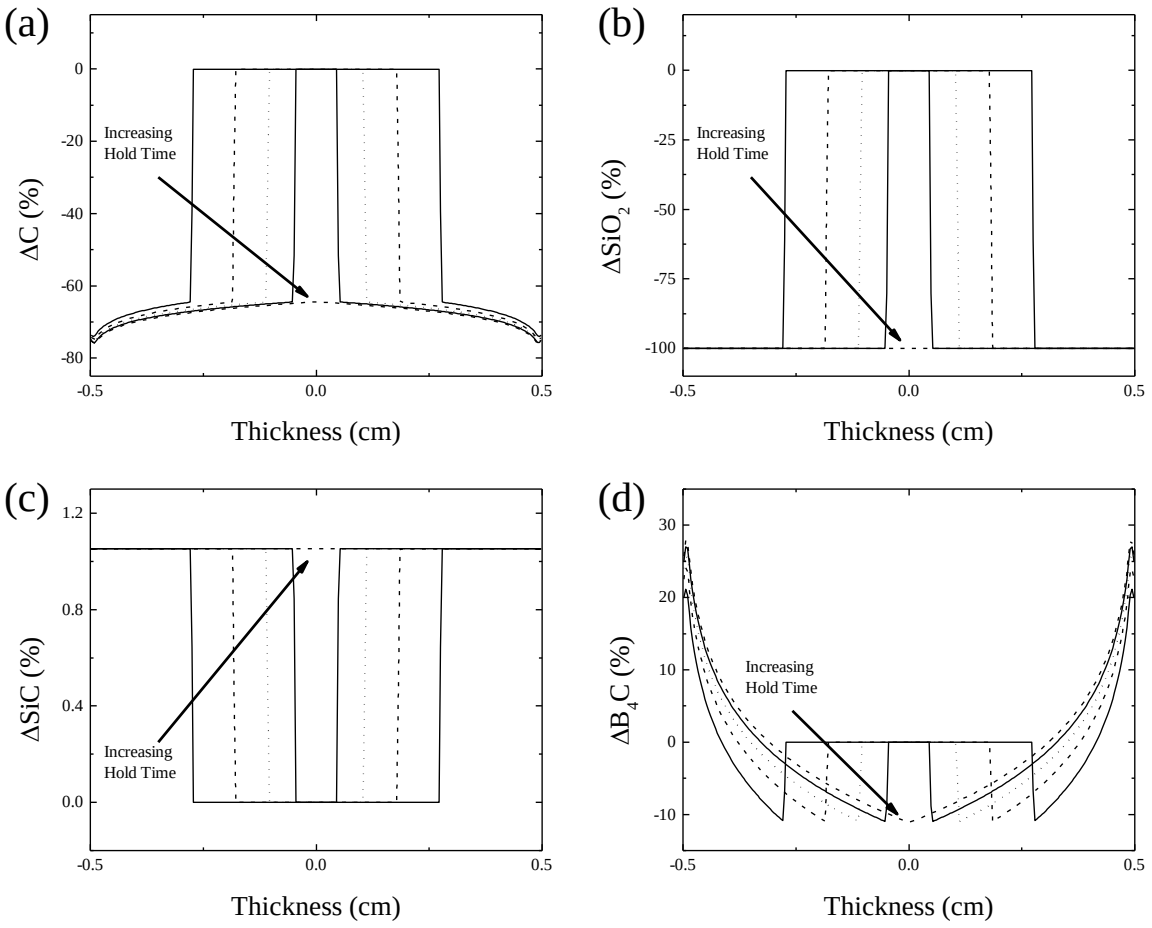

Figure 7-6: Compositional profile of (a) C, (b) SiO_2, (c) SiC, and (d) B_4C across the porous medium as simulation time increases up to t_c=0.9950 h. Times shown are in increments of t_c, where t ~ 1/5, 2/5, 3/5, 4/5, and 1 t_c. Simulation conditions are SSC3.

The initial amount of carbon, used to remove the SiO_2, was not completely depleted, as indicated in Figure 7-6(a). An initial composition of 4.4 mol % C was an excess amount to fully reduce the 1.0 mol % SiO_2. Figure 7-7(a) shows the residual C profile, as the relative percentage change of C. The amount of carbon was reduced by 75.95 and 64.46 % at the edge and center, respectively. The amount of carbon depleted, normalized by the starting SiO_2 content, is shown in Figure 7-7(b). Considering only the reaction given by Equation 314, leads to the prediction that the ratio of C/SiO_2, to remove all the SiO_2, should be 3.

The departure from the predicted C/SiO_2 ratio is due to the presence and reaction of the minor secondary gas species. The deviation from the predicted C/SiO_2 ratio is much more

pronounced in chemical set 3 compared to chemical set 1, mainly because the $CO_{(g)}/B_2O_{2(g)}$ ratio (~43) is much smaller than the $CO_{(g)}/SiO_{(g)}$ ratio (~284). In the oxygen rich region (regime 1), B_4C and C both contribute to reducing SiO_2. This acts to decrease the C/SiO_2 ratio in the center of the sample, since C is not the main reducing agent responsible for the formation of $B_2O_{2(g)}$ and $B_2O_{2(g)}$.

In contrast, the C/SiO_2 ratio is higher at the edges of the sample. The edges of the sample are the first regions to become oxygen deficient (regime 3), as the SiO_2 is depleted. At this initial stage, the C/SiO_2 ratio at the edge is almost the same as the final C/SiO_2 ratio in the center. The $B_2O_{2(g)}$, $B_2O_{3(g)}$, and $SiO_{(g)}$ from the center of the sample must travel through this region, before being evacuated, and continue to react with the remaining condensed and gas species. As explained earlier, these species consume C and act to increase the C/SiO_2 ratio at the edges.

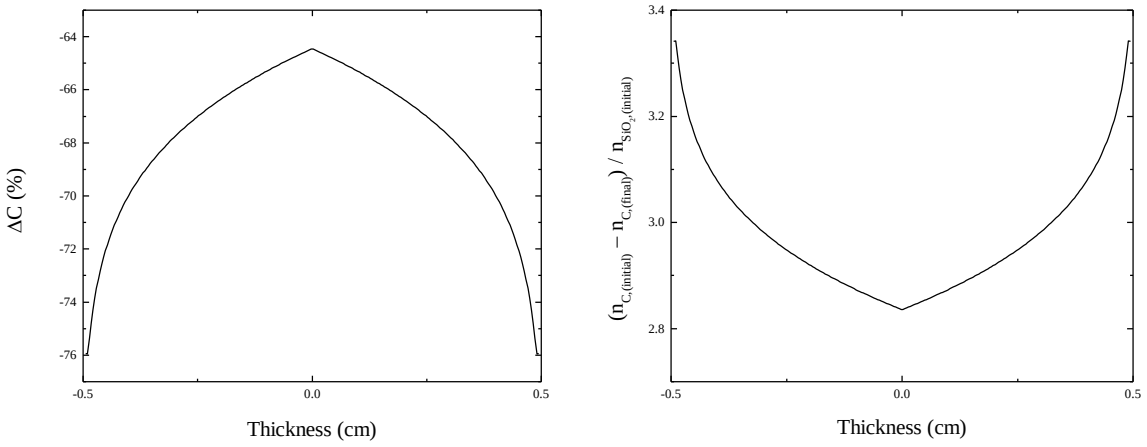

Figure 7-7: Residual C content profile after complete SiO_2 depletion, (a) ΔC (%) (b) C/SiO_2 ratio: change in the number of moles of C normalized by the initial number of moles of SiO_2. Simulation conditions are SSC3.

The time evolution of the partial pressure profile for $CO_{(g)}$ was shown frame by frame in Figure 7-3 to give a concrete visualization of transport and reaction behavior. The time evolution of the partial pressure profiles for $CO_{(g)}$,$SiO_{(g)}$, $B_2O_{2(g)}$, and $B_2O_{3(g)}$ are shown concisely in Figure 7-8, using an arrow showing the progression of time. The pressure gradient of the minor gases

across the oxygen deficient region is influenced by $CO_{(g)}$. The difference in curvature of these gradients can be explained by the thermodynamic conditions of chemical regime 3 for chemical set 3. Equation 365 shows that $n_{CO_{(g)}} \propto n_{SiO_{(g)}}$, indicating that the partial pressure profile of $SiO_{(g)}$ is linear because it is directly proportional to the $CO_{(g)}$ partial pressure profile. Similarly, Equation 363 shows that $n^2_{CO_{(g)}} \propto n_{B_2O_{2(g)}}$, indicating the partial pressure profile of $B_2O_{2(g)}$ is quadratic compared to the $CO_{(g)}$ partial pressure profile. Finally, Equation 364 shows that $n^3_{CO_{(g)}} \propto n_{B_2O_{3(g)}}$, indicating that the partial pressure profile of $B_2O_{3(g)}$ is cubic compared to the $CO_{(g)}$ partial pressure profile.

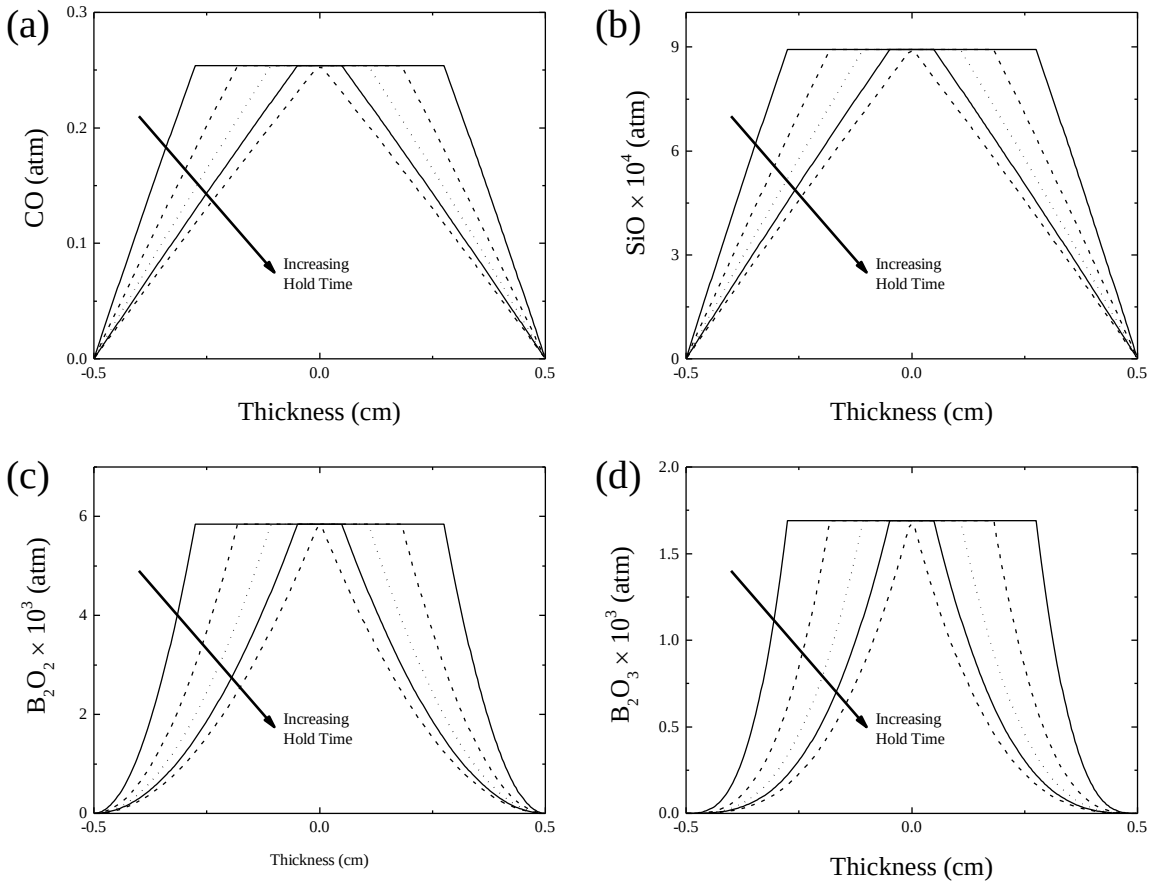

Figure 7-8: Partial pressure profile of (a) $CO_{(g)}$, (b) $SiO_{(g)}$, (c) $B_2O_{2(g)}$, and (d) $B_2O_{3(g)}$ across the porous medium as simulation time increases up to t_c=0.9950 h. Times shown are in increments of t_c, where t ~ 1/5, 2/5, 3/5, 4/5, and 1 t_c. Simulation conditions are SSC3.

Characteristics of the condensed and gas species behavior for the standard reference simulation of chemical set 3 were shown in this section. A major difference between chemical set 3 and chemical set 1 and 2 was that a solid species (*i.e.* B_4C) is both consumed and deposited across the sample thickness. The qualitative behavior associated with the movement of the reaction front and a transition from chemical regime 1 to regime 3 is representative of simulations where C is present in excess to allow for complete reduction of SiO_2. The remaining simulations involving chemical set 3 were all designed to satisfy this condition. Consequently, the curvature of partial pressure profile for each gas in the oxygen deficient region are all the same as this standard reference simulation. The rest of the simulations investigate changing the

sample length, starting SiO_2 content, and the holding temperature to quantify their effect on the residual B_4C composition.

7.2.2 Effect of Initial SiO_2 Content

The effect of the initial SiO_2 content on the residual B_4C and C profile was studied by varying the starting amount of SiO_2. The SSC3 in Table 7-3 were used for all parameters, excluding the initial composition of each species. The SiO_2 content was varied across the range including 0.5, 1.0, and 1.5 mol %. The starting molar ratio of C/SiO_2 was kept constant at 4.4, to ensure the complete reduction of all the starting oxide. This C/SiO_2 ratio is greater than the ratio of 3 needed to ensure carbon was in excess in chemical set 1. The amount of B_4C was kept constant at 0.25 mol %, with the remaining mole percentage of material (to equal 100 %) corresponding to SiC.

The relative percentage change of C (ΔC) and B_4C (ΔB_4C), for the range of initial SiO_2 concentrations, are shown in Figure 7-9(a) and (b), respectively. The ΔC profile is the same for all initial SiO_2 concentrations because the amount of C is in a fixed ratio of SiO_2. The spatial variation of the ΔC profiles are produced by the same reduction and deposition mechanisms presented in SRS3. The ΔB_4C profile for all of the initial SiO_2 concentrations have a characteristic minimum at the center and maximum at the edges. As the initial SiO_2 concentration increases, the minimum at the center decreases. This is due to the increased consumption of B_4C as SiO_2 is reduced in regime 1. At higher initial SiO_2 concentrations, greater amounts of $B_2O_{2(g)}$ and $B_2O_{3(g)}$ are produced and allow for more redistribution of boron. Accordingly, the more $B_2O_{2(g)}$ and $B_2O_{3(g)}$ that is transported into the oxygen deficient region leads to greater amounts of B_4C deposition at the edges of the sample.

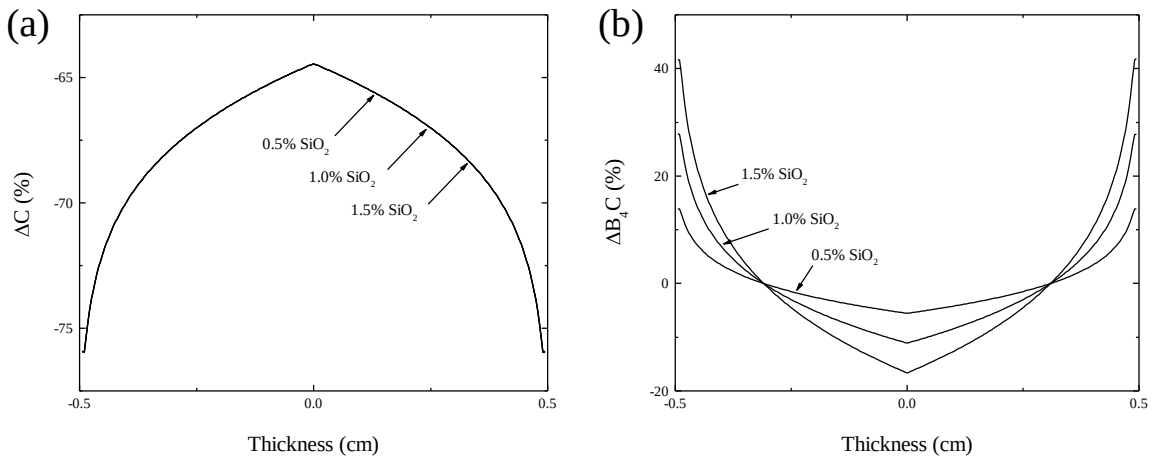

Figure 7-9: Relative percentage change of (a) C and (b) B_4C. Simulation conditions are SSC3 with initial SiO_2 concentrations set to 0.5, 1.0, and 1.5 mol % SiO_2.

The change in C (C/SiO_2) and B_4C (B_4C/SiO_2), normalized by the starting SiO_2 content, are shown in Figure 7-10(a) and (b), respectively. Similar to SRS3, there is a clear variation in the actual C/SiO_2 ratio from the predicted C/SiO_2 ratio of 3, assuming only $CO_{(g)}$ is essential to the SiO_2 removal process. The normalized C/SiO_2 and B_4C/SiO_2 ratios for all initial SiO_2 concentrations coincide, respectively. Since the normalized B_4C/SiO_2 ratio profile is constant for a given initial concentration of B_4C, it can be used to predict the ΔB_4C profile for arbitrary initial SiO_2 concentrations. Ultimately, the non-uniformity of the residual B_4C profile increases with increasing initial SiO_2 concentration.

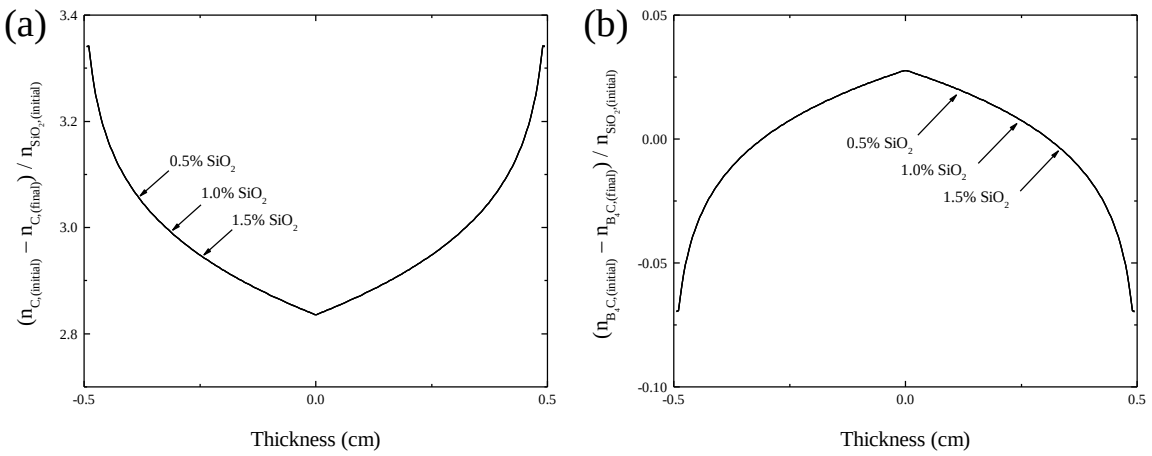

Figure 7-10: Normalized ratio of (a) C/SiO_2 and (b) B_4C/SiO_2. Simulation conditions are SSC3 with initial SiO_2 concentrations set to 0.5, 1.0, and 1.5 mol % SiO_2.

7.2.3 Effect of Temperature

The effect of the holding temperature on the residual B_4C and C profile was studied by varying the temperature while using the SSC3 in Table 7-3. The holding temperature was varied across the range of temperatures including 1623.15, 1673.15, 1723.15, 1773.15, 1823.15, 1873.15 and 1973.15 K.

The relative percentage change of C (ΔC) and B_4C (ΔB_4C), for the range of holding temperatures, are shown in Figure 7-11(a) and (b), respectively. Both the ΔC and ΔB_4C profile become increasingly non-uniform as the holding temperature is increased. Figure 7-12 shows the equilibrium gas pressure ratios as a function of temperature. The reduction in the gas pressure ratios, with increasing temperature, indicates the gas pressures are becoming more commensurate in magnitude. Secondary reactions due to the increased quantity of the minor gas species become more important and there is more non-uniformity in the residual solids compositions. This effect was also seen in chemical set 2.

At higher temperatures, more SiO_2 is reduced with both B_4C and C to produce $B_2O_{2(g)}$ and $B_2O_{3(g)}$. As B_4C becomes a more effective reducing agent, the amount of C depleted from the

center of the sample decreases and the amount of B_4C depleted increases. At higher temperatures, more $B_2O_{2(g)}$ and $B_2O_{3(g)}$ are transported into the oxygen deficient region, leading to greater amounts of B_4C deposition and C consumption at the edges of the sample.

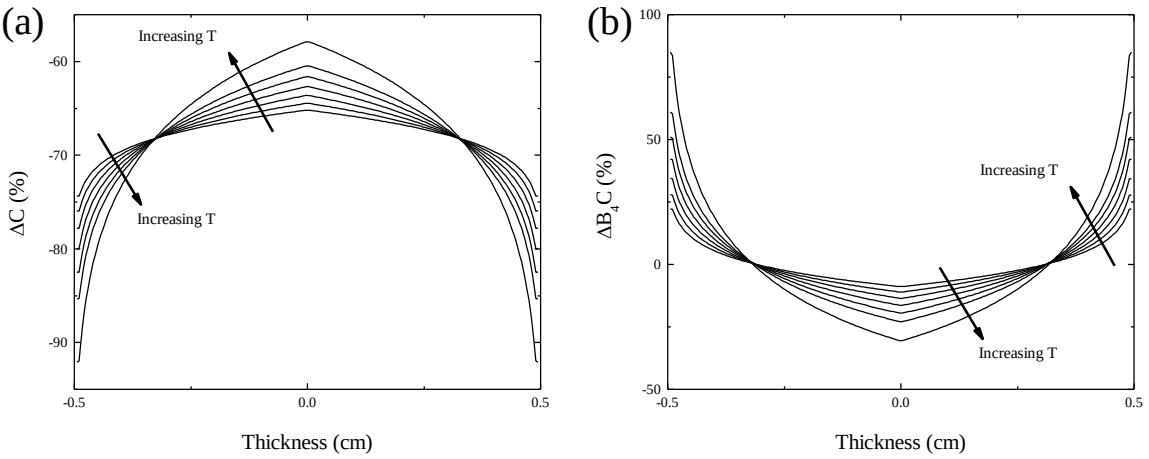

Figure 7-11: Relative percentage change of (a) C and (b) B_4C. Simulation conditions are SSC3 with the holding temperature set to 1973.15, 1873.15, 1823.15, 1773.15, 1723.15, 1673.15, and 1623.15 K.

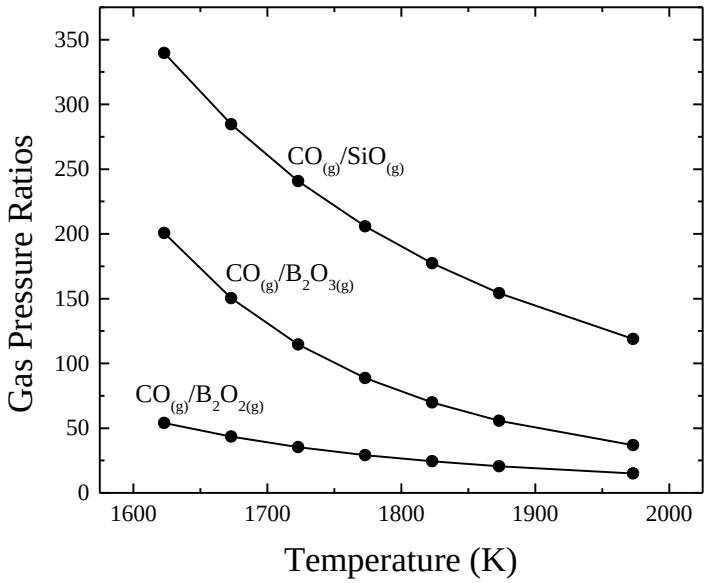

Figure 7-12: Equilibrium gas pressure ratios as a function of temperature in regime 1. CO/B_2O_2 (Bottom), CO/B_2O_3 (Middle), and CO/SiO (Top).

There is a large variation in the final B_4C profile from the initially uniform concentration. Figure 7-13 shows the range and the standard deviation about the mean of the ΔB_4C profile as a

function of the holding temperature. At 1973.15 K, the amount of B_4C is increased by ~84.96 % and decreased by ~30.55 % at the edges and center, respectively. The relative change of B_4C is large because of the small starting percentage of B_4C (at 0.25 mol %) compared to the other condensed species.

The change in C (C/SiO_2) and B_4C (B_4C/SiO_2) profiles, normalized by the starting SiO_2 content, are shown in Figure 7-14(a) and (b), respectively. Consistent with previous discussions, the C/SiO_2 ratio varies considerably from the predicted ratio of 3, indicating more carbon is needed at the edges compared to the center. Normalizing the change in B_4C by the starting amount of SiO_2 allows Figure 7-14(b) to be used as a way to estimate the ΔB_4C profile for various initial B_4C and SiO_2 concentrations, at different temperatures. For chemical set 1, using a higher temperature during oxide removal reduced t_c. For chemical set 3, using a higher temperature also reduces t_c, but it also results in non-uniform composition of B_4C; which can be detrimental to densification once the sintering temperature is reached.

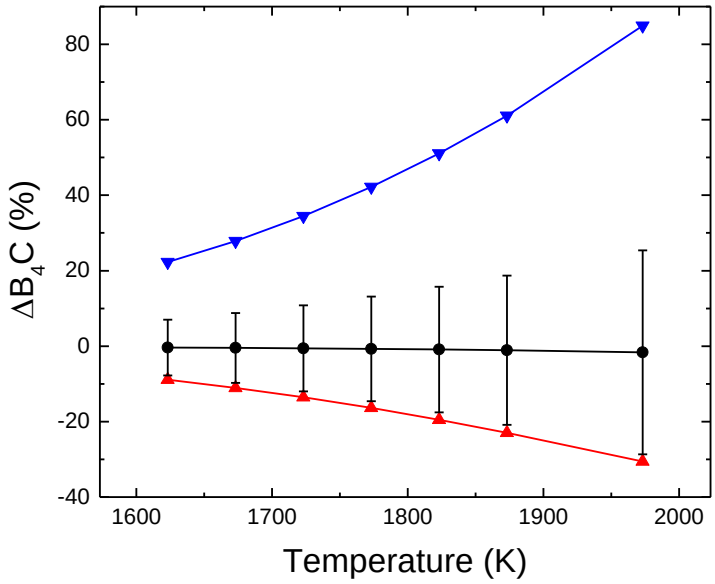

Figure 7-13: Variation of the ΔB_4C profile as a function of holding temperature. Maximum [Blue], Mean [Black], Minimum [Red], Standard deviation [Range] of the ΔB_4C profile across each sample.

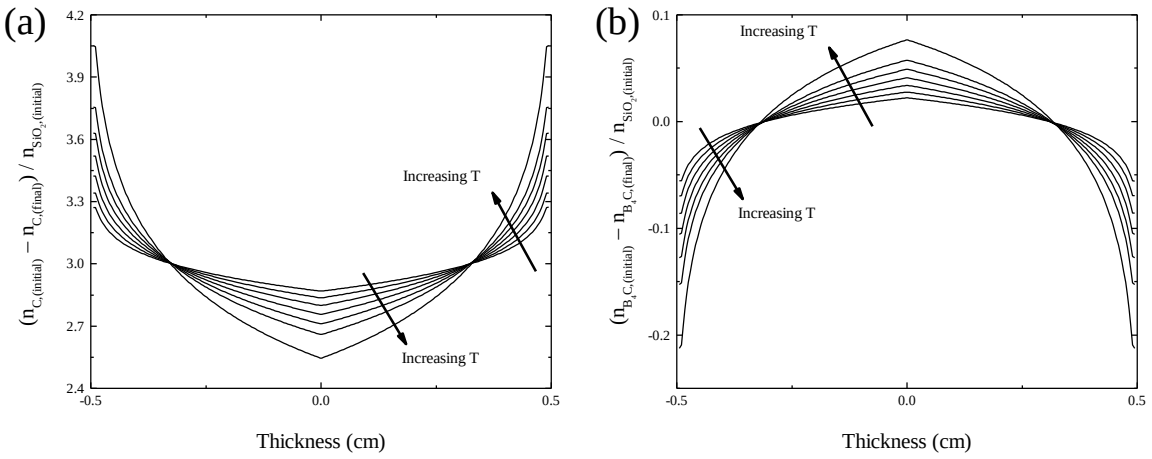

Figure 7-14: Normalized ratio of (a) C/SiO_2 and (b) B_4C/SiO_2. Simulation conditions are SSC3 with the holding temperature set to 1973.15, 1873.15, 1823.15, 1773.15, 1723.15, 1673.15, and 1623.15 K.

7.2.4 Effect of Thickness

The effect of sample thickness on the residual B_4C and C profile was studied by varying the sample thickness while using the SSC3 in Table 7-3. The thickness was varied across the range including 0.5, 1.0, and 2.0 cm.

The relative percentage change of C (ΔC) and B_4C (ΔB_4C), for the range of sample thickness, are shown in Figure 7-15(a) and (b), respectively. As the sample thickness becomes larger, the variation in the ΔC profile is spread over a larger distance. Additionally, there is an increase in the amount of C depleted from the edges of the larger samples. The ΔC decrease at the edges is 74.3, 75.9, and 77.6 % for sample thickness of 0.5, 1.0, and 2.0 cm, respectively. The variation in the ΔB_4C profile is also spread over a large distance as the sample thickness increases. However, there is an increase in the amount of B_4C deposited at the edges of the larger samples. The ΔB_4C increase at the edges is 22.1, 47.9, and 34.1 % for sample thickness of 0.5, 1.0, and 2.0 cm, respectively. The coupled increase in consumption of C and deposition B_4C at the edges has been explained previously and is a common feature chemical set 3. For each condensed species, the relative percentage change at the center each sample is the same regardless of the sample thickness. At the center of the sample, there is a 64.5 and 11.0 % decrease in the amount of C and B_4C, respectively.

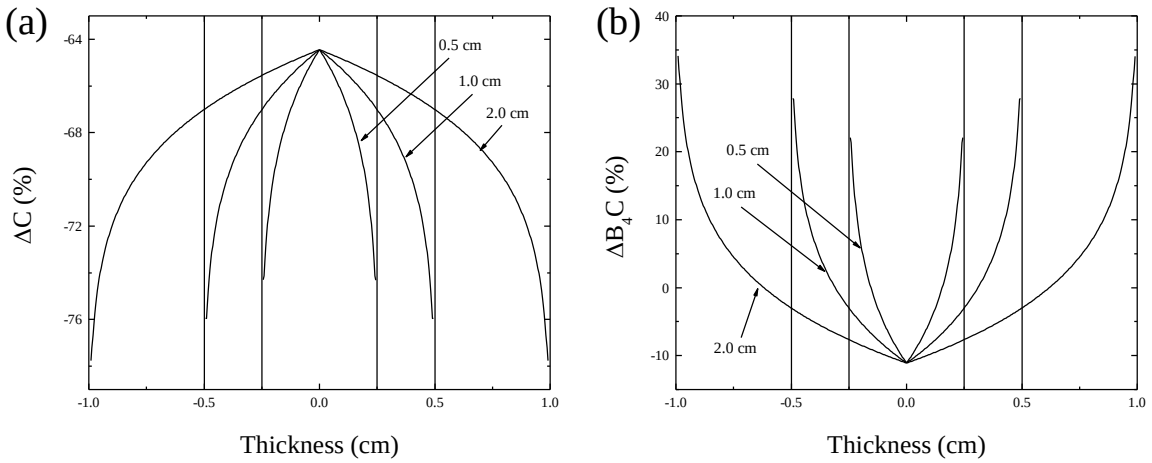

Figure 7-15: Relative percentage change of (a) C and (b) B_4C. Simulations conditions are SSC for samples thicknesses of 0.5, 1.0, and 2.0 cm.

The C/SiO_2 and B_4C/SiO_2 ratio profiles, for the range of samples thicknesses, are shown in Figure 7-16(a) and (b), respectively. These graphs are essentially a rescaling of data presented in Figure 7-15. The C/SiO_2 ratio at the edges is 3.27, 3.34, and 3.42 for sample thickness of 0.5,

1.0, and 2.0 cm, respectively. Consistent with previous simulations, there is a large variation from the predicted C/SiO_2 of 3. The B_4C/SiO_2 ratio at the edges is -5.53×10^{-2}, -6.97×10^{-2}, and -8.52×10^{-2} for sample thickness of 0.5, 1.0, and 2.0 cm, respectively. While the C/SiO_2 and B_4C/SiO_2 ratio at the center of each sample is 2.84 and 2.75×10^{-2}, respectively. These ratios can be used to predict the relative percentage change of C and B_4C when starting with various initial SiO_2 concentrations.

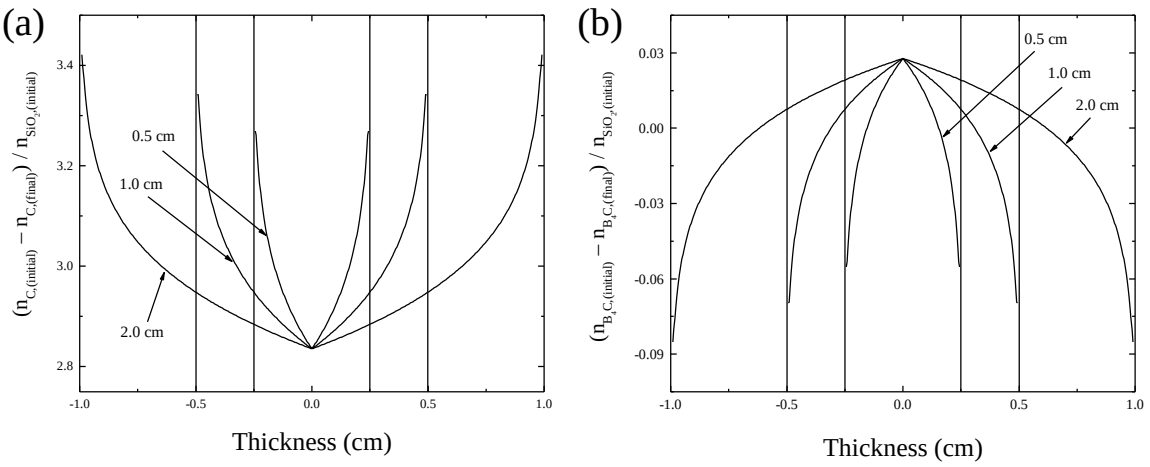

Figure 7-16: Normalized ratio of (a) C/SiO_2 and (b) B_4C/SiO_2. Simulation conditions are SSC3 for samples thicknesses of 0.5, 1.0, and 2.0 cm.

The variation in the C/SiO_2 and B_4C/SiO_2 ratio is closely connected to the partial pressure profiles of the gas species across the sample thickness. The gradients of the pressure profiles control the transport of the gas species from the center of the samples to the edges. As the reaction front proceeds, the shape of the partial pressure profile (for each gas species) is essentially the same if scaled by the distance between the edge and the reaction front. For each simulation, the C/SiO_2 and B_4C/SiO_2 ratio profiles are normalized by the sample thickness in Figure 7-17 and Figure 7-18, respectively. The normalized C/SiO_2 ratio profiles appear to almost coincide. However, the inset graph in Figure 7-17 shows that, at the sample edges, the deviation between the C/SiO_2 ratios increases modestly. Similarly, the normalized B_4C/SiO_2 ratio profiles are almost coincident. However, the inset graph in Figure 7-18 shows that, at the sample edges, the

deviation between the B_4C/SiO_2 ratios increases. Ultimately, increasing the thickness results in more redistribution at the edges, but the redistribution is spread over a broader length. Furthermore, if the scaled by the sample thickness the solids profile is almost independent of thickness.

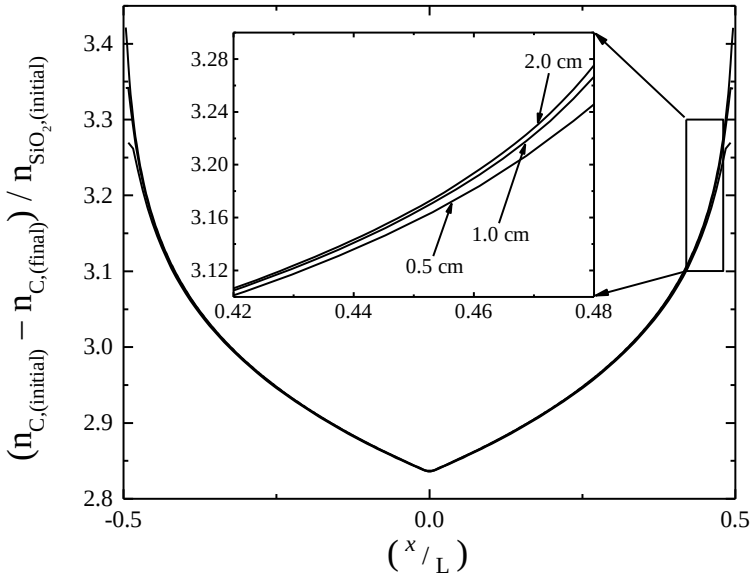

Figure 7-17: Normalized ratio of C/SiO_2 as a function of position normalized by the sample thickness. Inset: Magnified portion of the edge corresponding to the boxed region. Simulation conditions are SSC3 for sample thicknesses of 0.5, 1.0, and 2.0 cm.

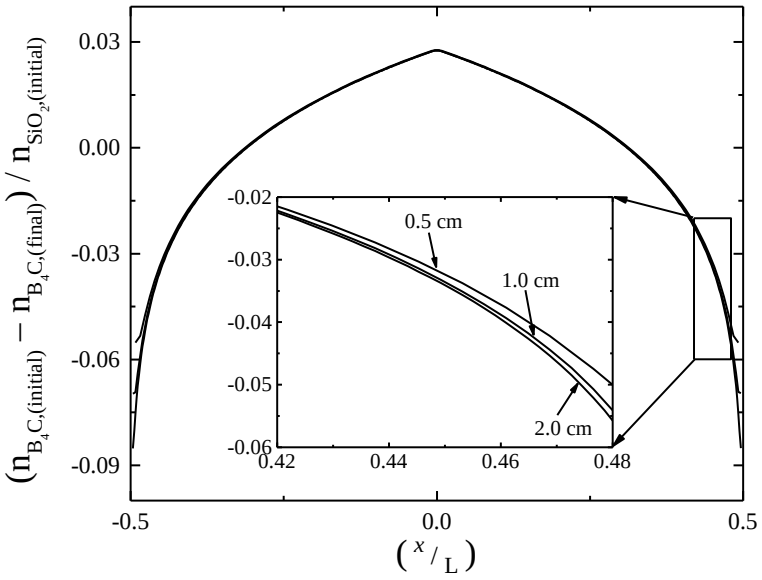

Figure 7-18: Normalized ratio of B_4C/SiO_2 as a function of position normalized by the sample thickness. Inset: Magnified portion of the edge corresponding to the boxed region. Simulation conditions are SSC3 for sample thicknesses of 0.5, 1.0, and 2.0 cm.

7.2.5 Combined Effect of Initial SiO_2 Content, Temperature, and Thickness

The combined effect on the residual B_4C profile by simultaneously varying the initial SiO_2 content, holding temperature, and sample thickness was studied in this section. The values for the non-varied parameters coincide with the SSC3 in Table 7-3. Additionally, the same set of parameter ranges for the previous studies for the initial SiO_2 content, holding temperature, and sample thickness were used. Thus, the SiO_2 content ranged between 0.5, 1.0, and 1.5 mol %, the holding temperature ranged between 1623.15, 1673.15, 1723.15, 1773.15, 1823.15, 1873.15 and 1973.15 K, and the sample thickness ranged between 0.5, 1.0, and 2.0 cm. Simulations not included were those which were simultaneously set to 1.5 mol % SiO_2 and 2.0 cm.

The ΔB_4C profile from each simulation was analyzed to get statistics on the minimum, maximum, mean, and standard deviation about the mean. These statistics are presented in Figure 7-19, using the same scale for each graph. Each graph in Figure 7-19 shows there is an increase in the non-uniformity of the ΔB_4C profile as the holding temperature is increased. Each row of Figure 7-19 displays the ΔB_4C profile variation for a constant sample thickness. While,

each column of Figure 7-19 displays the ΔB_4C profile variation for a constant initial SiO_2 content. For each column, the values representing the minimum ΔB_4C curve in each graph are the same; a general consequence of a constant initial SiO_2 content.

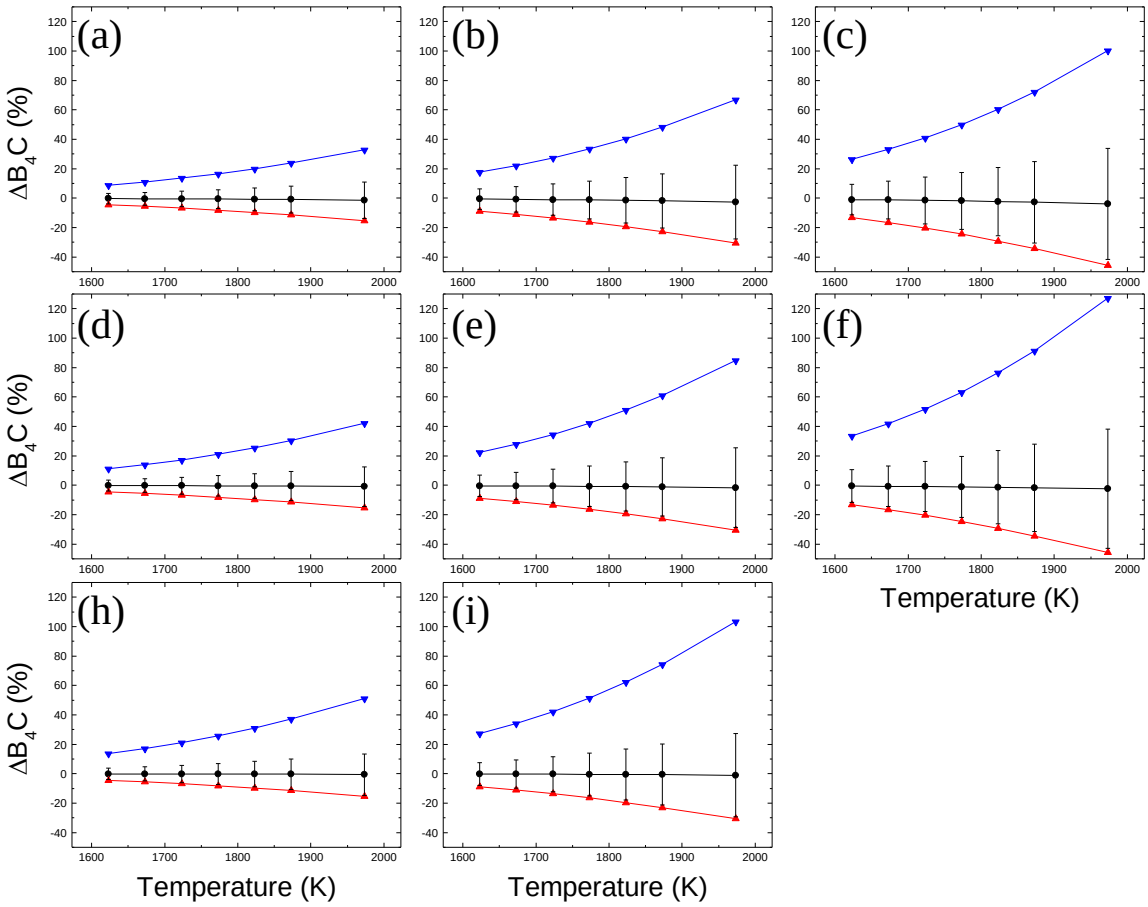

Figure 7-19: Variation of the ΔB_4C profile as a function of holding temperature. Maximum [Blue], Mean [Black], Minimum [Red], Standard deviation [Range] of the ΔB_4C profile across each sample. (Top) 0.5 cm (a) 0.5 mol % SiO_2, (b) 1.0 mol % SiO_2, (c) 1.5 mol % SiO_2; (Middle) 1.0 cm (d) 0.5 mol % SiO_2, (e) 1.0 mol % SiO_2, (f) 1.5 mol % SiO_2; (Bottom) 2.0 cm (h) 0.5 mol % SiO_2, (i) 1.0 mol % SiO_2.

It is clear that the variation across each row is greater than the variation down each column. This indicates that more non-uniformity is introduced by increasing the initial SiO_2 content than increasing the sample thickness. Comparing Figure 7-19(a) to (b) and (h), shows that doubling the SiO_2 content from 0.5 to 1.0 mol % has a greater influence on the non-uniformity than quadrupling the sample thickness from 0.5 to 2.0 cm. A higher initial SiO_2

content has the effect of causing any increase in the sample thickness to produce a greater variation in the ΔB_4C profile. This is seen by observing that the increase in ΔB_4C when doubling the thickness at 1.5 mol % SiO_2 (Figure 7-19 (c) and (f)) is greater than the increase in ΔB_4C when quadrupling the thickness at 0.5 mol % SiO_2 (Figure 7-19 (a) and (h)). Figure 7-19 can be used to identify trends regarding which parameters will most strongly influence the ΔB_4C profile. Ultimately, understanding these factors will allow for better control over the processing of porous media containing C, SiC, SiO_2, and B_4C.

7.3 Summary of Chemical Set 3

Chemical set 3 consists of simulations designed to analyze the variation of the residual B_4C additive profile during the removal of SiO_2 from a porous medium comprised of C, SiC, SiO_2, and B_4C. The reaction primarily responsible for the removal of SiO_2 is the reaction between SiO_2 and C, producing mainly $CO_{(g)}$ and SiC. The removal of SiO_2 is primarily limited by the ability to remove $CO_{(g)}$ from the porous medium, subsequently removing more SiO_2 to replenish the $CO_{(g)}$ that was removed. This is the same dominant oxide removal mechanism seen for chemical set 1. Therefore, the variation in t_c with simulation parameters for chemical set 3 will be analogous to the trends described in Chapter 5 for chemical set 1. However, SiO_2 will react with B_4C to produce $B_2O_{3(g)}$ and $B_2O_{2(g)}$, which results in a change in the B_4C compositional profile. The variation of the residual B_4C profile was studied for constant temperature simulations.

The constant temperature simulations were simulated using an isothermal hold temperature and varying the model parameters for thickness, holding temperature, and initial oxide content. It was found for all simulations that B_4C is depleted from the center and re-deposited at the edges of the samples. As the sample thickness is increased, the amount of B_4C

depleted from the center remains constant, but the amount re-deposited at the edges is slightly increased.

Increasing the holding temperature causes the equilibrium gas pressures of the boron containing gases to increase. Thus, at higher temperatures the secondary reactions occur to a greater extent causing the amount of B_4C depleted from the center and re-deposited at the edges to increase. Additionally, as the initial oxide content is increased, the amount depleted from the center and re-deposited at the edges are both increased. This results from the increased quantity of boron containing gases produced due to more reaction between SiO_2 and B_4C. This is similar to chemical set 2 where an increase in the amount of boron oxide gases resulted in a highly non-uniform residual C profile.

Simultaneously varying all of the parameters showed that increasing the temperature and/or initial oxide content resulted in the greatest amount of B_4C non-uniformity. Increasing the sample thickness did increase the non-uniformity, but this occurred over a broader length of the sample. Additionally, the changing the sample thickness did not change the amount of B_4C depleted from the center of the sample. In summary, understanding how the initial B_4C profile changes due to the removal of SiO_2 provides a practitioner useful insight into determining whether the residual B_4C profile will be adequate to help lower grain boundary energies to achieve the desired densification and microstructure upon reaching the sintering temperature.

8 Additional Simulations: Expanded Model Capabilities

In order to further demonstrate the flexibility of the modeling framework a few additional simulations are presented. Firstly, the removal of ZrO_2 from a ZrC porous medium with excess C was simulated. The ZrC simulation is used to demonstrate that the model can seamlessly handle switching between chemical sets. Secondly, a study of the effect of temperature gradients on the amount of C consumed while removing B_2O_3 from B_4C porous media (*i.e.* chemical set 2) was conducted. There are a number of additional capabilities of the modeling framework that allow all of the simulation parameters to be varied across the thickness of the sample, in addition to the temperature ramping capabilities shown in Chapter 5.3. The temperature gradient simulations are one set of examples demonstrating the use of these additionally capabilities to generate interesting behavior.

8.1 Chemical Set 4 Simulation: {C, ZrC, ZrO_2, $CO_{(g)}$, $CO_{2(g)}$, $ZrO_{(g)}$}

The results of a constant temperature simulation studying the transport and reaction in a porous medium comprised of condensed C, ZrC, and ZrO_2 is presented in this section. The chemical species modeled in the simulation are restricted to the chemical set {C, ZrC, ZrO_2, $CO_{(g)}$, $CO_{2(g)}$, $ZrO_{(g)}$}. This set accounts for initial condensed species and the three gases species with the largest equilibrium gas pressures, as indicated by Figure 8-1. Similar to the procedure for SiC in Chapter 5, the compositional profiles of the condensed species are represented by their percentage change. The compositional profile for ZrO_2 is denoted by ΔZrO_2 (%) and the *time for complete oxide removal*, t_c, is when ΔZrO_2 (%) = -100 across the whole porous medium.

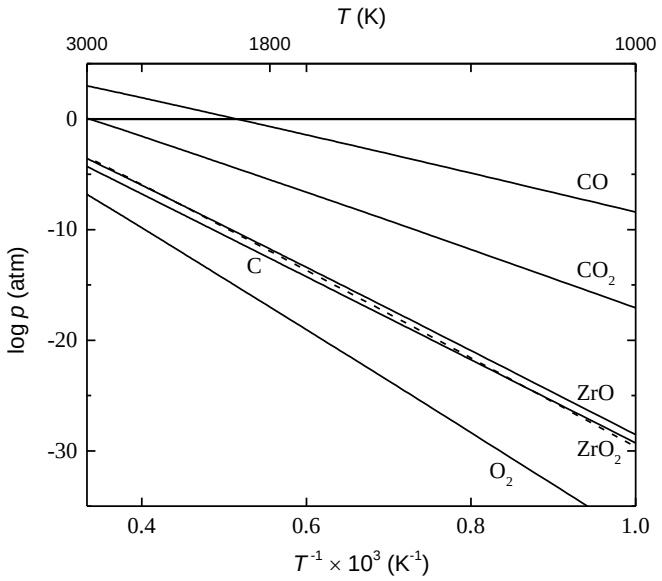

Figure 8-1: Gas pressures as a function of temperature for several species in equilibrium with solid C, ZrC, and ZrO_2.

8.1.1 Physical Constants, Expressions, and Simulation Conditions

The same collection of physical constants and simulation parameters as chemical set 1 (Chapter 5.1) are need for the current chemical set. The relevant parameters for C, ZrC, and ZrO_2 are provide in Table 6-1 and those for $CO_{(g)}$, $CO_{2(g)}$, and $ZrO_{(g)}$ are provide in Table 6-2. The Gibbs free energy function for each species is not explicitly listed, but the required data to construct them is provided in Appendix IV.iii. The parameters for the *standard simulation conditions* for chemical set 4 (SSC4) are listed in Table 6-3.

Table 8-1: Material properties for the condensed chemical species from chemical set 4.

Condensed Species	MM ($g \cdot mol^{-1}$)	ρ ($g \cdot cm^{-3}$)
C	12.0107	2.10
ZrC	103.2347	6.73
ZrO_2	123.2228	5.68

Table 8-2: Material properties for the gas chemical species from chemical set 4.

Gas Species	MM ($g \cdot mol^{-1}$)	σ (Å)	ϵ/k_B (K)
CO	28.0101	3.8	88
CO_2	44.0095	4.5	213
SiO	107.2234	4.8	100

Table 8-3: Standard simulation conditions (SSC4) reference parameter values for chemical set 4.

Parameter	Reference Value
C (X_{C})	3.3 mol %
ZrC (X_{ZrC})	95.7 mol %
ZrO_2 ($X_{\mathrm{ZrO_2}}$)	1.0 mol %
Porosity (ε)	0.4
Tortuosity (q)	5
Pore radius (r)	16 nm
Thickness (l)	1 cm
Temperature (T)	1823.15 K

8.1.2 Constant Temperature Simulation

This simulation was calculated at a constant temperature of 1823.15 K, otherwise using the same assumptions as SRS1 (Chapter 5.2.1) for the initial state of the system. Table 8-4 shows the equilibrium partial pressures of $CO_{(g)}$, $CO_{2(g)}$, and $ZrO_{(g)}$ at 1823.15 K for chemical set 4. The ratio of $CO_{(g)}/CO_{2(g)}$ and $CO_{(g)}/ZrO_{(g)}$ are approximately 5.6×10^{4} and 8.4×10^{10}, respectively. It is clear that $CO_{(g)}$ is the dominant gas and controls the transport behavior. Additionally, a neglible amount of secondary reactions are expected for this chemical set because the minor gas species concentrations are so low. The time for complete ZrO_2 removal was 0.8588 h.

Table 8-4: Equilibrium partial pressures for chemical set 4 at 1823.15 K

Gas Species	P_{eq} (atm)
CO	0.27237
CO_2	4.8392×10^{-6}
ZrO	3.2403×10^{-12}

The time evolution of compositional profiles for C, ZrC, and ZrO_2 are shown concisely in Figure 8-2, with an arrow indicating the progression of time. Similarly, the time evolution of the partial pressures for $CO_{(g)}$, $CO_{2(g)}$, and $ZrO_{(g)}$ are shown in Figure 8-3. The time evolution of the condensed and gas species are very similar to that of chemical set 1 shown in Figure 5-6 and Figure 5-8.

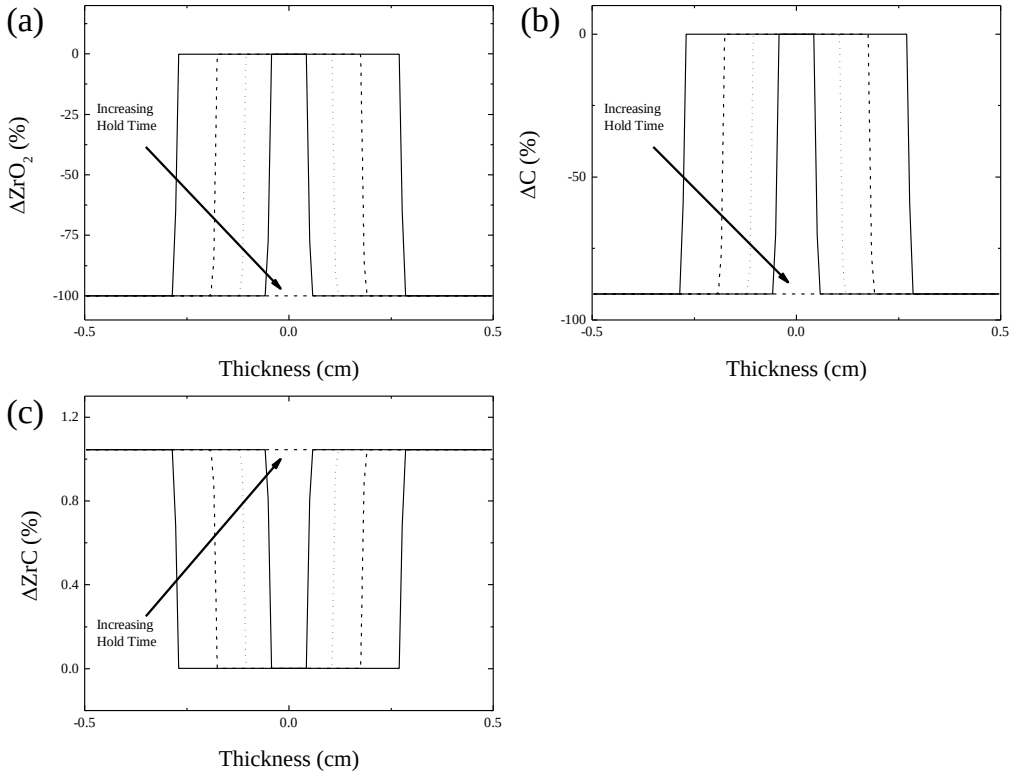

Figure 8-2: Compositional profile of (a) ZrO_2, (b) C, and (c) ZrC across the porous medium as simulation time increases up to t_c=0.8588 h. Times shown are in increments of t_c, where t ~ 1/5, 2/5, 3/5, 4/5, and 1 t_c. Simulation conditions are SSC4.

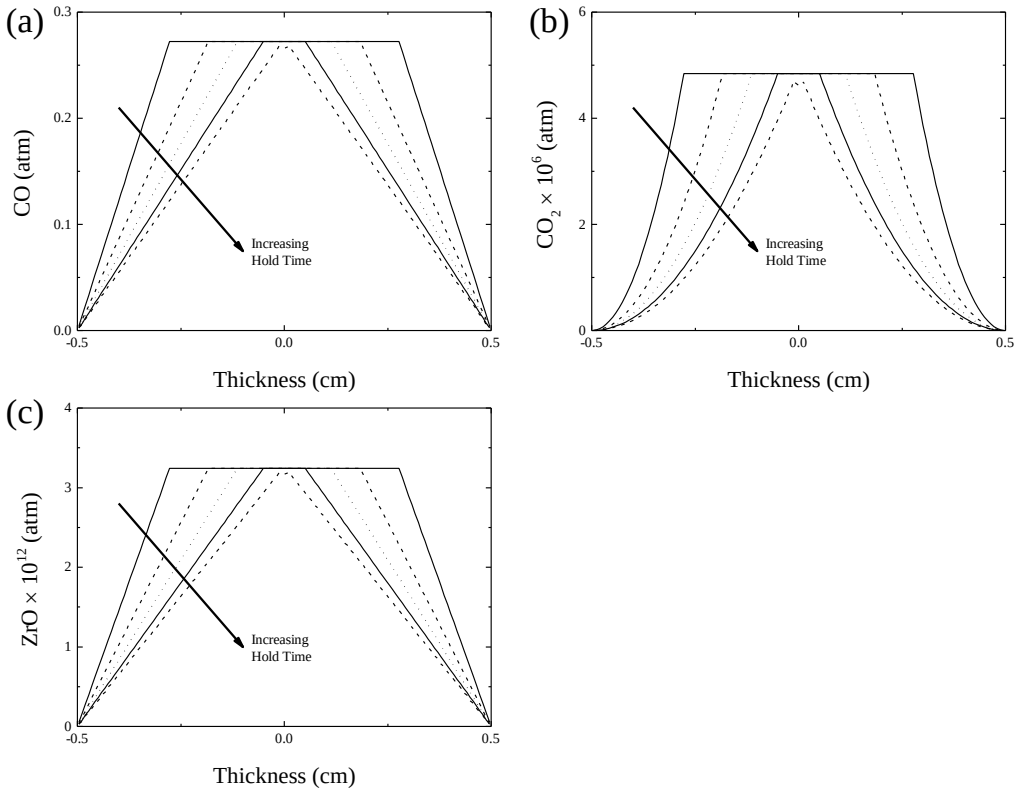

Figure 8-3: Partial pressure profile of (a) $CO_{(g)}$, (b) $CO_{2(g)}$, and (c) $ZrO_{(g)}$ across the porous medium as simulation time increases up to t_c=0.8588 h. Times shown are in increments of t_c, where t ~ 1/5, 2/5, 3/5, 4/5, and 1 t_c. Simulation conditions are SSC4.

The similarity in behavior is a result of both the elemental composition of the chemical species and that $CO_{(g)}$ greatly dominates over the minor gas species in each of the chemical sets. The similarity in the elemental composition is evident if one simply substitutes the element 'Zr' in for the element 'Si' in all of the species in chemical set 1. A consequence of this correspondence is that the stoichiometric coefficients, for the respective species, will be identical. Because the stoichiometric coefficients are identical, the behavior of the pressure profiles for $CO_{(g)}$, $CO_{2(g)}$, and $ZrO_{(g)}$ in chemical set 4 are exactly analogous to that of $CO_{(g)}$, $CO_{2(g)}$, and $SiO_{(g)}$ in chemical set 1, with the corresponding explanations given in Chapter 5.2.1.

An important result is that chemical set 4 has a uniform residual compositions for all the condensed species. Due to the dominance of $CO_{(g)}$ over the minor gas species there is a

negligible amount of secondary reactions in both chemical sets 1 and 4. This results in the extremely uniform residual condensed species concentration profiles that are seen in both Figure 5-6 and Figure 8-2. This can be contrasted to chemical set 2 where the $CO_{(g)}$ and $B_2O_{2(g)}$ pressures are more commensurate ($CO_{(g)}/B_2O_{2(g)}$ ratio of 59), allowing for secondary reactions to occur, resulting in a large degree of non-uniformity for the residual B_4C and C compositional profiles shown in Figure 6-6. Based upon the arguments in Chapter 5 and 6, it is expected that the time for complete oxide removal for chemical set 4 would have the same functional dependence as chemical sets 1 and 2 for varying any of the simulation parameters. This correspondence can be used as a rough estimate to predict the oxide removal behavior from ZrC without having to conduct additional simulations or experiments.

8.2 Temperature Gradient Simulations (Chemical Set 2)

Additional capabilities of the modeling framework allow for the variation of the simulation parameters across the thickness of the porous medium. This has been used to study the effect of imposing a temperature gradient across a porous medium comprised of the chemical species in chemical set 2. A temperature gradient will cause a pressure gradient in the porous medium, even before evacuating any gas, allowing for redistribution of matter within the porous medium. Chemical set 2 was chosen as the example system to study these temperature gradient effects because they were shown by Rossi *et al.* and in Chapter 6 to allow for a significant amount of secondary reactions to occur due to the transport of $B_2O_{2(g)}$ and $B_2O_{3(g)}$.[91]

Two comparison studies were conducted. The first simulations analyze a temperature difference of increasing magnitude across the sample thickness. The next simulations increase the sample thickness for a fixed temperature difference. These simulations use the same physical parameters and simulation conditions used for SRS2 in Chapter 6, excluding the

simulation temperature and the sample thickness. All of the temperature gradients were linear and such that the central temperature and the thickness averaged simulation temperature was 1713.15 K, which was the uniform temperature used in SRS2.

8.2.1 Varying Magnitude Temperature Gradient Simulations

The varying temperature gradient simulations were conducted to study how the resulting internal pressure gradient affects the residual solids profile. These simulations were all conducted on a sample with a thickness of 1 cm. The magnitude of the temperature differentials, the associated left and right boundary temperatures, and t_c are shown in Table 8-5. The associated temperature profiles are shown in Figure 8-4.

Table 8-5: Magnitude of the temperature differentials across a 1 cm sample for chemical set 2, with the time for complete B_2O_3 removal.

ΔT (K)	$T_{\text{left boundary}}$ (K)	$T_{\text{right boundary}}$ (K)	t_c (h)
0	1713.15	1713.15	0.995
20	1703.15	1723.15	0.998
40	1693.15	1733.15	1.008
60	1683.15	1743.15	1.024
80	1673.15	1753.15	1.047

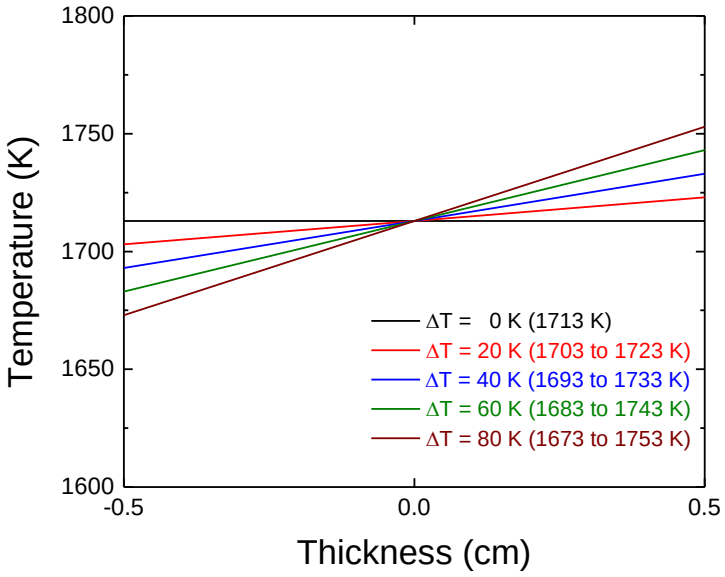

Figure 8-4: Temperature profiles for temperature gradients of various magnitudes.

The time for complete oxide removal is not drastically affected by the presence of a temperature gradient, the largest increase in simulation time is ~5% for a Δ*T* of 80 K. The increase in time is attributed to two different factors. The first factor is a reduction in the pressure at the lower temperature left boundary, which reduces the rate of oxide removal. Even though there is a corresponding increase in the pressure at the higher temperature right boundary, it is not effective at balancing out the loss of driving force at the left boundary and even partially exacerbates the problem.

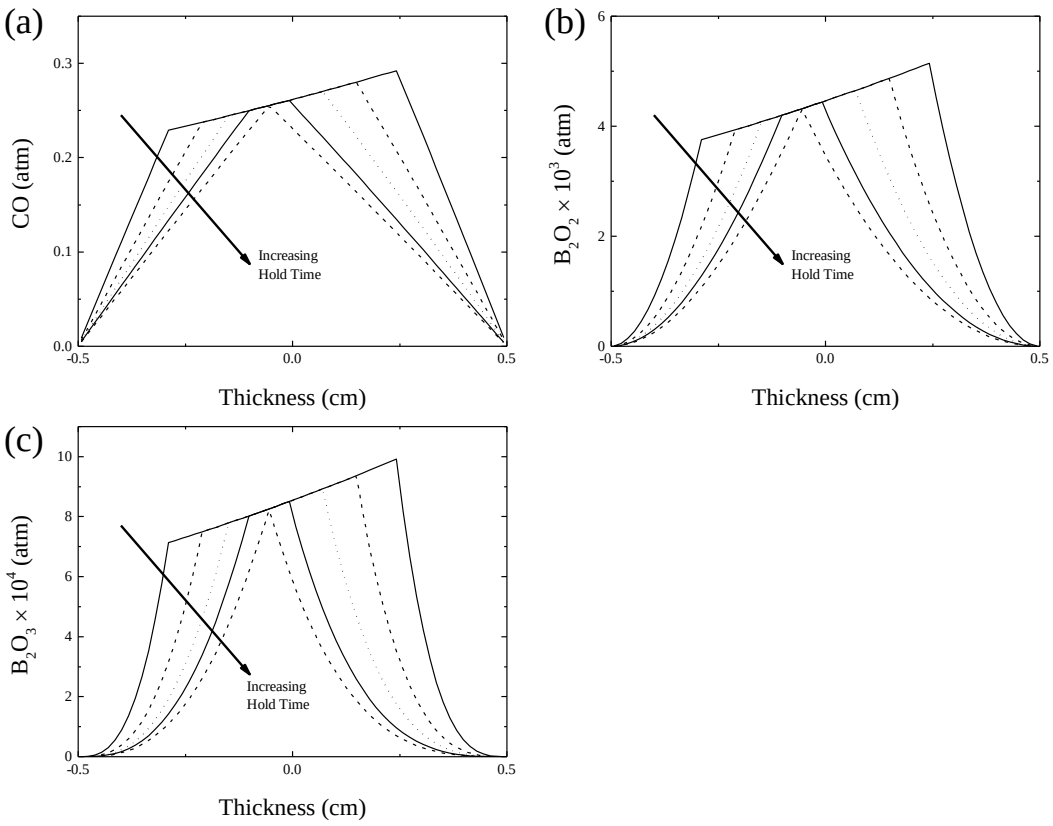

Figure 8-5: Partial pressure profile of (a) $CO_{(g)}$, (b) $B_2O_{2(g)}$, and (c) $B_2O_{3(g)}$ across the porous medium as simulation time increases up to t_c=1.008 h. Times shown are in increments of t_c, where t ~ 1/5, 2/5, 3/5, 4/5, and 1 t_c. Simulation conditions are SSC2 and ΔT of 40 K.

The second factor to increase t_c becomes clearer by looking at the time evolution of the partial pressure profiles for a ΔT of 40 K shown in Figure 8-5. The temperature gradient causes a pressure gradient, even in the oxide rich region. This results in a flow of gas from the right boundary towards the left boundary, increasing the diffusion path of the gas. This is in contrast to the flat pressure profile for the uniform temperature simulations shown in Figure 6-8, where there is no driving force for gas transport in the oxide rich region unless at the reaction front. The presence of a temperature gradient results in an asymmetry in the oxide removal rate from the left and right boundaries as seen in Figure 8-6 for a sample with a ΔT of 40 K.

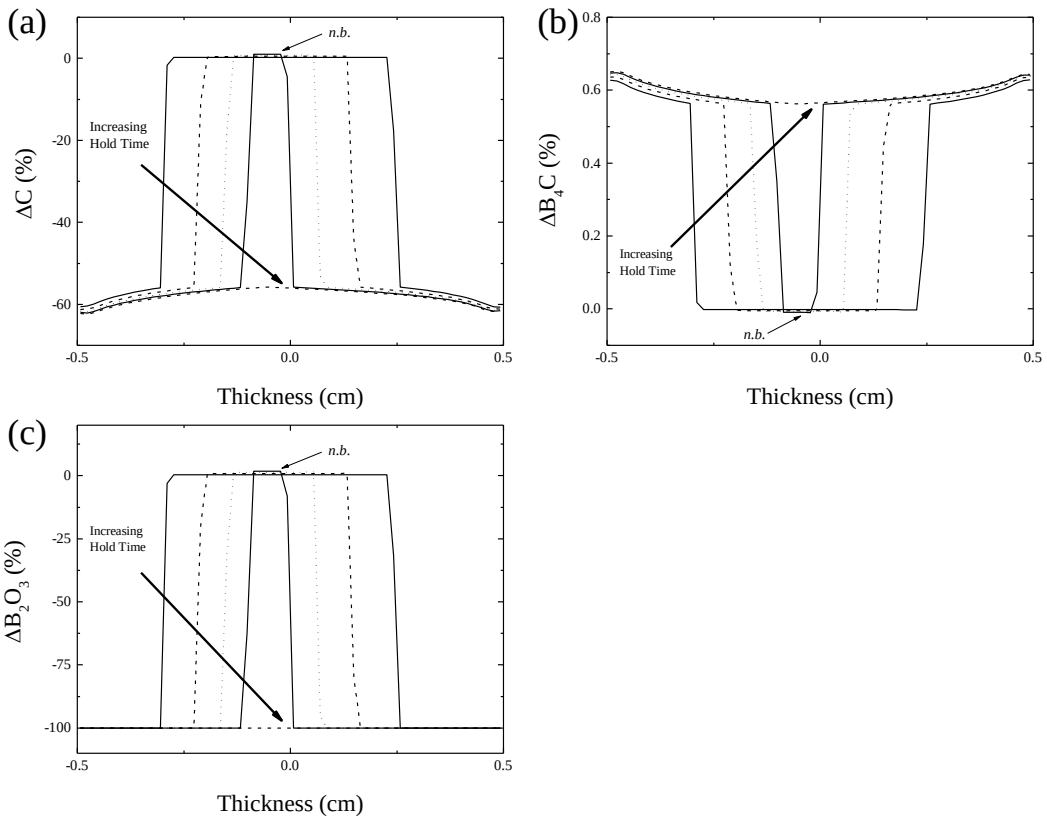

Figure 8-6: Compositional profile of (a) C, (b) B2O3, and (c) B4C across the porous medium as simulation time increases up to t_c=1.008 h. Times shown are in increments of t_c, where t ~ 1/5, 2/5, 3/5, 4/5, and 1 t_c. Simulation conditions are SSC2 and ΔT of 40 K. (*n.b.* explained in the text*)*

The time evolution of the condensed species shown in Figure 8-6 exhibit some additional behavior not seen in any of the other simulations. There is clearly an asymmetry that causes the two reaction fronts to meet on the colder (left) half of the sample when all of the oxide is removed. However, there is also a temporary increase in the amount of B_2O_3 and C with a corresponding temporary reduction in amount of B_4C in this region. This is attributed to the transport of gas into the oxygen rich region (regime 1), which would drive the reactions given by Equations 224-226 to produce a net increase in the deposition of C and B_2O_3 and reduction in B_4C. Ultimately, as the reaction front proceeds towards the center of the sample it consumes C to reduce all of the B_2O_3 and forms B_4C. However, the temporary redistribution of material does have a lasting effect on the residual condensed species compositional profiles.

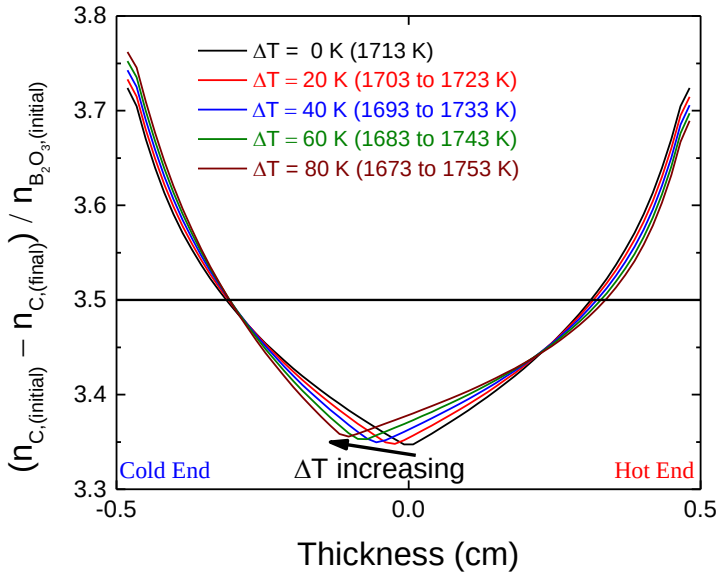

Figure 8-7: Normalized ratio of C/B_2O_3 for various temperature gradients. The C/B_2O_3 ratio of 3.5 is indicated (Naïve isothermal prediction). Simulation conditions are SSC2 with varied ΔT.

Figure 8-7 shows the amount of C consumed across the sample thickness, normalized by the initial amount of B_2O_3, giving the C/B_2O_3 ratio. In Chapter 6, it was explained that the C/B_2O_3 ratio should be 3.5, but due to the reaction of minor species it deviates from this prediction. As ΔT increases, there is slight increase and a noticeable shift in the minimum C/B_2O_3 ratio toward the colder end, increasing the asymmetry of the C/B_2O_3 compared to the isothermal temperature simulation. The shift and the increase in the minimum are attributed to greater amounts of B_2O_3 temporarily being deposited toward the colder end of the sample. Once the reaction front reaches this region, a greater amount of C is needed to reduce the larger amount of B_2O_3. There is also an asymmetry in the amount of C consumed at the edges. The increased transport of gas towards the cold end increases the amount of C consumed at that end and decreases the amount consumed from the hot end. Ultimately, even though a temperature gradient only causes a small increase in t_c, it also results in an asymmetric residual C profile that increases where the degree of the asymmetry increases with the magnitude of the temperature gradient.

8.2.2 Varying Sample Thickness Temperature Gradient Simulations

The varying sample thickness temperature gradient simulations were all conducted on a sample with a fixed temperature difference of ΔT = 40 K. The sample thickness was varied between 1, 2, and 4 cm with a corresponding t_c of 1.008 h, 4.031 h, and 11.751 h. The C/B_2O_3 profile ratios indicating the consumption of C necessary to reduce the initial B_2O_3 is shown in Figure 8-8.

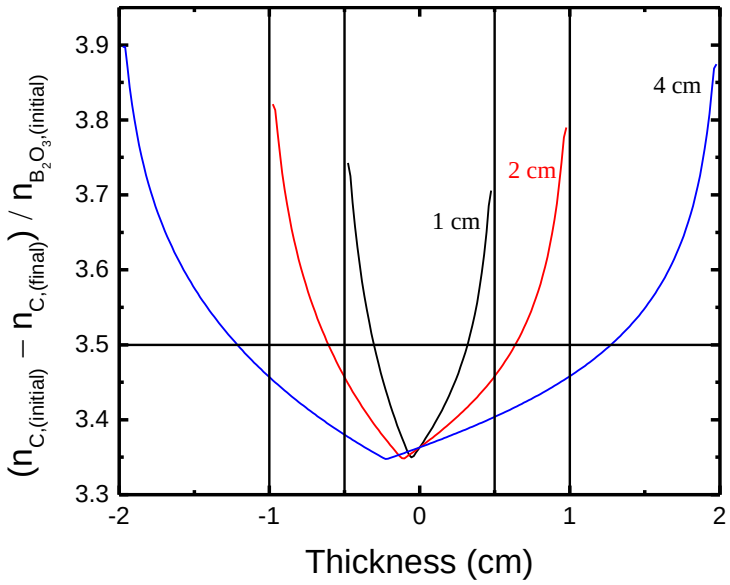

Figure 8-8: Normalized ratio of C/B_2O_3 for sample thickness of 1, 2, and 4 cm. The C/B_2O_3 ratio of 3.5 is indicated (Naïve isothermal prediction). Simulation conditions are SSC2 with a ΔT of 40 K.

For a fixed ΔT, as the sample thickness increases, the temperature gradient and resulting pressure gradient decrease. Despite the reduction in the pressure gradient across the sample, there is a larger shift in the C/B_2O_3 ratio. The pressure gradient across the sample persists for a longer duration in the thicker samples due to the rate of the reaction front progression slowing quadratically as the oxide depleted region grows. The persistent pressure gradient in thicker samples allows more gas to transport to the colder end and causes the shift in the C/B_2O_3 (due to reasons explained in the previous section). There is also an increase in the

C/B_2O_3 ratio for thicker samples at both edges because more gas transports over the edges allowing for continued reaction consistent with previous discussions.

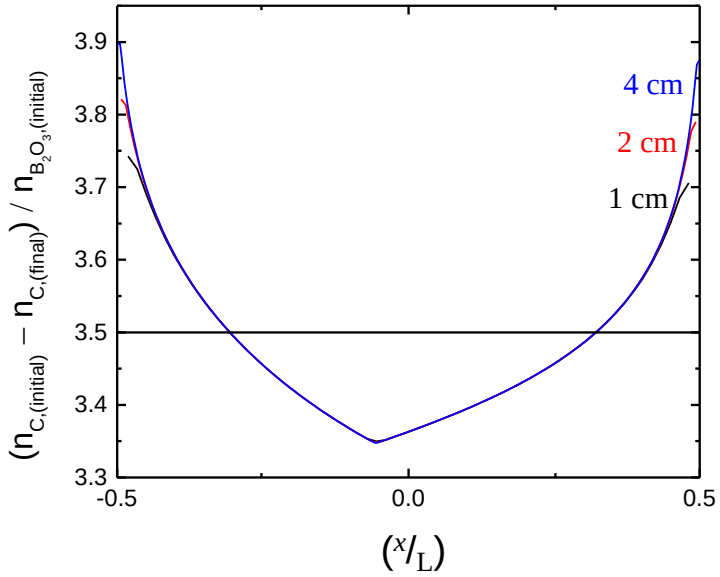

Figure 8-9: Normalized ratio of C/B_2O_3 as a function of position normalized by the sample thickness. Simulation conditions are SSC2 for sample thickness of 1, 2, and 4 cm with a ΔT of 40 K.

The C consumption behavior for samples of varying thickness is made commensurate by scaling the compositional profile by the sample thickness and is shown in Figure 8-9. This scaling behavior is consistent with the explanation and results from Chapter 7.2.4 and similar to the findings of Rossi *et al.*[91] The thickness scaled C/B_2O_3 profile can then be used to give estimates of the residual C composition due to changing the sample thickness when subject a temperature gradient.

8.3 Summary of Additional Simulations

This chapter demonstrates the use of the modeling framework to accomplish a few very different tasks in order to show its versatility. The first task demonstrated the versatility by simulating the behavior of a completely new chemical system. This was done to analyze the removal of ZrO_2 from ZrC porous media (*i.e.* chemical set 4). The ZrC system had not been previously studied and the modeling framework was able to successfully simulate the oxide

removal behavior for this system. A simple investigation showed that it has many similar characteristics to the SiC system (chemical set 1), such as $CO_{(g)}$ dominating all of the oxide removal behavior and there being insignificant amounts of secondary reactions. This result is important because it indicates that for chemical sets where the minor gas species are negligible, there will be a very uniform residual composition for all the condensed species. Additionally, due to the similarities of chemical set 1 and 4, many of the insights in Chapter 5 can be applied to directly to understanding oxide removal from ZrC when subject to different processing conditions.

The second task was to demonstrate the ability to vary the simulation parameters across the thickness of sample. This was done by imposing a temperature gradient across the thickness of the sample when removing B_2O_3 from B_4C (*i.e.* chemical set 2). As was shown in Chapter 6, the minor gas species can causes non-uniformity in the residual condensed species profile. These simulations showed that a temperature gradient will result in an asymmetry in the amount of C consumed when removing B_2O_3, shifting the minimum C/B_2O_3 ratio toward the cold end of the sample. Next, a constant temperature difference across samples of increasing thickness showed the C/B_2O_3 minimum would be shifted further toward the cold end of thicker samples. Additionally, normalizing this relationship by the sample thickness allows it to be used to predict the amount of C consumption due to increasing the sample thickness when subject to the same temperature difference.

The results of the simulations in this chapter are important and give insight into new systems and different processing conditions. However, the main goal was to demonstrate that this modeling framework can be used to investigate many different systems and more complicated processing conditions. In summary, the chemical sets and simulation conditions

investigated represent just a few of the many studies that could be accomplished using this modeling framework.

9 Conclusions

The modeling work performed in this thesis was conducted to study the different aspects of oxide removal from non-oxide porous media. To achieve this task, a general modeling framework was developed which can simulate gas transport and chemical equilibrium reaction in a porous medium. This general framework allows one to quickly transition between different chemical systems and processing parameters that may be encountered when manufacturing non-oxide ceramics. This model was validated against work done by Kaza *et al.* and Rossi *et al.* which studied oxide removal from SiC and B_4C systems, respectively.[90, 91] The study of oxide removal from SiC was expanded to include various heating cycles and their effect on the effusion rate of $CO_{(g)}$. The combined system of SiC with B_4C analyzed the effect oxide removal has on the residual B_4C concentration. Lastly, this versatility of the model was demonstrated by analyzing oxide removal from the ZrC system and the effect of temperature gradients in the B_4C system.

The development of the general modeling framework consists mainly of two parts which are coupled by a general transport and reaction equation. In Chapter 2, it was demonstrated how the combined transport and reaction equation could be separated into individual transport and chemical reaction problems, which could be solved by successive iteration. The two sub-problems were discretized using the finite control volume method (FCVM) and forward Euler time stepping. The transport problem was modeled using the Dusty Gas Model (DGM). In Chapter 3, an explanation of the DGM was given and it was shown that, using the FCVM discretization, it can be recast into a matrix problem. It was also demonstrated that, using symbolic programming techniques, a function can be created to calculate the gas flux predicted due to the current chemical composition profile.

A novel technique for calculating the chemical equilibrium composition of a closed system was presented in Chapter 4. The concept of a chemical set was introduced, with associated chemical regimes. This concept allowed the use of a model reduction approach to calculating equilibrium allowing for the elimination of any number of condensed chemical species due to reaction. Using the SiC system as an example, it was shown how stoichiometric equations for each regime can be created automatically in a form that could either be used to explicitly approximate the equilibrium gas partial pressures or combined with the mass balance constraints to generate a set of equations to be solved for calculating chemical equilibrium. It was shown that using symbolic programming techniques, this procedure can be used to automatically create the functions needed to calculate chemical equilibrium for a general system.

This modeling framework was validated against the work of Kaza *et al*. and Rossi *et al.,* which systematically studied the time for complete oxide removal (t_c) and its sensitivity to varying the processing parameters used when modeling the SiC and B_4C systems, respectively. [90, 91] A similar parameter variation procedure was conducted for SiC and B_4C in Chapter 5.2 and 6, respectively. Consistent with their results, the time for complete oxide removal (t_c) varied linearly as a function of tortuosity and initial oxide content, quadratically as a function of sample thickness, and inversely as a function of pore radius. It was found that t_c varied proportionally to $\exp\left(b_T \frac{1}{T}\right)$, in contrast to the other work which found t_c varied proportionally to $\exp(b_T T)$, where b_T is a temperature sensitivity parameter. However, this difference only amounts to a small deviation between the two studies. The only major deviation between the current work and the previous investigations is that current study found that t_c was proportional to $(1-\varepsilon)^{3/2}$, where ε is the porosity, and the previous work found that t_c was proportional to $(1-\varepsilon)/\varepsilon$. It is proposed that this difference is due to the fact that the current model adjusts

the porosity due to the depletion of material during reaction, while the previous investigators assume the porosity stays constant. Despite the minor differences, the current model compares very favorably to the previous work, validating the general modeling framework and providing confidence that it can be applied to other chemical systems and parameter investigations.

The systematic parameter variation of the SiC and B_4C systems exposed a number of similarities between these two systems and can be used to gain insight into other systems. The main similarity between the two systems is that t_c is controlled by the transport and removal of a single dominate gas species, namely $CO_{(g)}$. It was found that for both chemical systems the sensitivity to changing the tortuosity, pore radius, and thickness were exactly the same, because they do not depend on the chemical system being studied. Additionally, the sensitivity to changing porosity, initial oxide content, and temperature were similar between the two chemical systems, because they are both controlled by $CO_{(g)}$. The weak dependence on chemical system is a result of the interconnection with the density and amount of the oxide to the amount of porosity, along with the temperature dependence of $CO_{(g)}$ due to the thermodynamic constraints specific to each chemical system. These relationships can be used to predict the oxide removal behavior due to changes in the powder compact. Using a different powder to make a compact will alter the representative simulation parameters and the functional relationships can be used to predict how t_c will vary due to these changes. These trends in behavior could be applied to understanding any other system with similar controlling mechanisms.

The SiC and B_4C systems had key difference in the abundance of the minor gas species. The SiC system had a high ratio of $CO_{(g)}/SiO_{(g)}$ and $CO_{(g)}/CO_{2(g)}$, which limited the amount of secondary reactions. This resulted in a relatively uniform residual condensed species composition, with a C/SiO_2 ratio close to expected ratio of 3. The B_4C system had a low ratio of

$CO_{(g)}/B_2O_{2(g)}$, which allowed a considerable amount of secondary reactions to occur as the $B_2O_{2(g)}$ was removed. These secondary reactions resulted in a non-uniform residual condensed species composition. There was more than expected C consumption at the edges and less in the center, causing a significant deviation from the expected C/B_2O_3 ratio of 3.5. These simulations showed that the presence of minor gas species can have a major effect on the residual condensed species composition without significant effect on the time for oxide removal.

The SiC system was further studied in Chapter 5.3 to address the rate of $CO_{(g)}$ removal from a porous medium subject to various heating cycles. The study investigated different sample thicknesses, initial oxide contents, holding temperatures, and heating rates. It was found that ramping up to a hold temperature and dwelling is inefficient and leads to excessively long holding times for thicker samples; this should only be used if one does not want to exceed a maximum internal pressure. It was also demonstrated that if a once acceptable heating cycle does not account for increasing the sample thickness or oxide content, then the $CO_{(g)}$ effusion rate can reach an unacceptable level (based upon furnace and vacuum limitations). Lastly, it was shown how successively lowering the heating rate can be used to keep the $CO_{(g)}$ effusion rate close to a constant threshold level deemed acceptable for processing. Thus, it is recommended to successively lower the heating rate to substantially reduce the amount of time and energy need for oxide removal, while limiting the effusion rate and maximum internal pressure.

The modeling framework was applied to a combined system of SiC with B_4C, where small amounts of B_4C were added and the residual B_4C profile due to oxide removal was simulated. Since B_4C can be used as a sintering additive for SiC and its concentration effects the densification and grain growth of SiC during sintering, it is useful to know the effect of SiO_2 on the B_4C distribution upon reaching the sintering temperature. The study shown in Chapter 7, investigated changing the initial oxide content, sample thickness, and holding temperature.

Similar to chemical set 2, chemical set 3 also had a significant quantity of minor gas species, specifically $B_2O_{2(g)}$. Since the $CO_{(g)}/B_2O_{2(g)}$ ratio was low, it was expected and observed that there was a significant amount of secondary reactions occurred during oxide removal.

For chemical set 3,it was found that a uniform starting amount of B_4C resulted in a non-uniform residual composition, where the level of B_4C was lower in the center and higher at the edges of the sample. This also causes a shift from the C/SiO_2 ratio of 3 predicted to reduce all of the SiO_2. It was found that (depending on the temperature) a ratio above 4 was needed to ensure carbon was not depleted. At the reaction front, B_4C and C act to reduce SiO_2, but as gas (including $B_2O_{2(g)}$ and $B_2O_{3(g)}$) flows across the oxide depleted regions further reaction causes B_4C to re-deposited at the edges of the sample. The non-uniformity of the residual B_4C composition was found to increase slightly due to increasing sample thickness and more drastically due to the initial SiO_2 content and the holding temperature. The non-uniformity of B_4C upon reaching the sintering temperature can have an impact on SiC densification and this study provides insight into conditions that increase the non-uniformity so they can then be avoided.

A number of additional simulations were conducted to show the flexibility of the modeling framework to analyze a new chemical system and more complicated processing conditions. Firstly, the previously unstudied ZrC system was simulated to remove ZrO_2. The ZrC system was shown to be very similar to the SiC system, indicating that many of the explanations regarding the SiO_2 removal from SiC can be applied directly to ZrO_2 removal from ZrC. Also, a comparison of ZrC and SiC systems confirmed that secondary reactions will only be important when there is a significant abundance of the minor gas species. Secondly, B_2O_3 removal from B_4C was studied assuming a temperature gradient existed across the sample thickness. It was shown that the minimum in the C/B_2O_3 ratio shifted toward the colder end of the sample due to an internal pressure gradient and the temporary deposition of C and B_2O_3 (not exhibited by

isothermal holding temperatures). This shift was found to increase with the temperature difference and the sample thickness. These simulations, in addition to the thorough investigations of SiC, B_4C, and SiC with B_4C, were all simulated within one modeling framework which automatically constructs and solves the necessary equations to describe gas transport and equilibrium thermodynamic reaction for a chosen chemical system subject to a set of processing parameters.

10 SUGGESTIONS FOR FUTURE WORK

The work in this thesis was in part guided at eliminating the repetitive procedures used to construct the models built by Kaza *et al*. and Rossi *et al*.[90, 91] It was seen that every time that a new chemical system was to be studied, the same sequence of steps would have to be carried out by hand. There would be the same process of identifying the different possible chemical regimes, formulating stoichiometric equations to describe the chemical reactions for each regime, assembling the thermodynamic functions to calculate the equilibrium compositions, and assembling the Dusty Gas Model with the appropriate physical constants. All of these steps have been automated in the current modeling framework, allowing a user to simply investigate a new chemical system by specifying the new system and processing parameters without the need for any hand-coding. The suggestions for future can be divided into additional systems to study, validating the model through experimentation, and model enhancements.

This flexibility can be used in future work to examine oxide removal from many other systems. The ZrC system was shown as an example, but it can easily be extended to oxide removal from other systems such as TiB_2, TiC, HfB_2, ZrB2, etc. As was shown for the SiC with B_4C system, one can simply chose to include a number of condensed species and analyze the residual composition after oxide removal. The choice of B_4C was chosen as a sintering additive because the combined system resembles a combination of the SiC and B_4C system. Future work can study the combination of SiC with B as a sintering additive and compare the results to the SiC with B_4C study. Additionally, by simulating different possible sintering additives, some of which produce low quantities of minor species, it is possible to find additives that limit the amount of non-uniformity and redistribution of the residual condensed species.

It would be beneficial to experimentally validate the predictions made by the current model for the SiC and SiC with B_4C system. This includes confirming the sharp gradients in oxide content during removal, the CO effusion rate behavior due to the heating cycle, and the amount of additive redistribution due to varying the simulation parameters. The validation study can be facilitated by purposely using high oxide content powder compacts and only partially removing the oxide during heating. The properties of the green bodies can be varied and the predicted $CO_{(g)}$ effusion rate can be compared to the amount of $CO_{(g)}$ measured by a mass spectrometer. If an incomplete oxide removal cycle was used, sectioning the sample across the thickness should reveal distinct regions with higher oxide content. Similarly, there should be a large amount of B_4C additive redistribution, due to the high oxide content, which could also be measured from the section samples. Comparing the compositional gradients in the sectioned samples with the predictions from the model could be used to confirm if the assumption of local thermodynamic equilibrium is valid. There is also the possibility to study a number of other processing conditions. Some parameters may have a position dependence because powder segregation, non-ideal mixing, or density gradients in a green body due to pressing or forming. Each of the model parameters including initial composition, porosity, tortuosity, and pore radius can be varied as a function of position across the sample thickness. Additionally, the temperature can be varied across the sample thickness, but it can also be heated non-uniformly to replicate non-uniform heating due to a batch furnace or temperature gradients resulting from a sample traveling through a continuous furnace.

In addition to simply studying more systems, additional physical phenomenon can be add to the modeling framework. In work done by Kaza on the SiC system, models for vapor, surface, and lattice transport mechanisms were included and used information about the gas species behavior to predict neck growth during the oxide removal process.[88] These additions

provide useful information for investigators trying to understand the densification of powder compacts. These models can be added to the modeling framework, so they can be used for a general chemical system.

The current model assumes a superimposed temperature distribution, neglecting energy transfer and enthalpy changes due to reaction. It would be relatively straightforward to include enthalpy changes due to reaction, because the current model is already linked to a thermodynamic database. For each species, the specific heat, standard state entropy, and standard state enthalpy as a function of temperature are already present in the model. However, these are only currently used to construct the Gibbs free energy function.

Improvement to the numerical models used for calculating the gas transport and reaction behavior can also be improved. Specific improvements would be to formulate problem in a dimensionless form. This would act to highlight the important factors in a given simulation and improves the stability and accuracy when calculating the simulation. An implicit time stepping algorithm can be implemented to replace the forward Euler time stepping method to allow for large time steps to be used while reducing any potential oscillations in behavior. The code can also be parallelized. For example, parallelization of the chemical equilibrium calculation is straightforward. Each finite control volume does not depend on the others, allowing the calculation of equilibrium for each finite control volume to be distributed over a number of different processor and solved simultaneously. The ability to take larger time steps and reducing the amount of time needed to calculate each time step is essential for 3-d modeling, where the number of elements increases cubically. Thus, even to simulate a very small problem of 10 x 10 x 10 nodes (1000 nodes total), increases the amount of nodes to roughly the same amount of nodes used in the most detailed 1-D study currently performed.

Appendix I. Chemical Set 1: {C,SiC,SiO_2,$CO_{(g)}$,$CO_{2(g)}$,$SiO_{(g)}$}

This section shows results of the chemical equilibrium model reduction algorithm for the chemical set {C, SiC, SiO_2, $CO_{(g)}$, $CO_{2(g)}$, $SiO_{(g)}$}. An in-depth description of the algorithms for generating the necessary equations and expressions with their associated functions is shown in Chapter 4 on the Chemical Equilibrium Model; where this chemical set is used as the prototypical example. The model reduction algorithm applied to this chemical set yields the following 8 chemical regimes.

1. {C, SiC, SiO_2, $CO_{(g)}$, $CO_{2(g)}$, $SiO_{(g)}$}
2. {C, SiC, $CO_{(g)}$, $CO_{2(g)}$, $SiO_{(g)}$}
3. {C, SiO_2, $CO_{(g)}$, $CO_{2(g)}$, $SiO_{(g)}$}
4. {C, $CO_{(g)}$, $CO_{2(g)}$, $SiO_{(g)}$}
5. {SiC, SiO_2, $CO_{(g)}$, $CO_{2(g)}$, $SiO_{(g)}$}
6. {SiC, $CO_{(g)}$, $CO_{2(g)}$, $SiO_{(g)}$}
7. {SiO_2, $CO_{(g)}$, $CO_{2(g)}$, $SiO_{(g)}$}
8. {$CO_{(g)}$, $CO_{2(g)}$, $SiO_{(g)}$}

I.i Activity Checks

Chemical set 1 was used as an example in Chapter 4.2.4to show how the activity check equations can be systematically generated. The reader is referred back to that section for specific details on algorithm used to generate the activity check equations. For completeness, the final form of the activity check equations are reiterated as

$$\frac{K_{eq,C}\, n_{CO_{(g)}}^2}{n_{CO_{2(g)}}}\left(\frac{RT}{V_{pore}}\right) = a_C \tag{111}$$

$$\frac{K_{eq,SiC} n_{CO_{(g)}}^3 n_{SiO_{(g)}}}{n_{CO_2(g)}^2} \left(\frac{RT}{V_{pore}}\right)^2 = a_{SiC} \tag{112}$$

$$\frac{K_{eq,SiO_2} n_{CO_2(g)} n_{SiO_{(g)}}}{n_{CO_{(g)}}} \left(\frac{RT}{V_{pore}}\right) = a_{SiO_2} \tag{113}$$

assuming the gases obey the ideal gas law and the pore volume is

$$V_{pore} = V_{total} - \frac{(n_C M_C)}{\rho_C} - \frac{(n_{SiC} M_{SiC})}{\rho_{SiC}} - \frac{\left(n_{SiO_2} M_{SiO_2}\right)}{\rho_{SiO_2}} \tag{110}$$

I.ii Regime 1: {C, SiC, SiO_2, $CO_{(g)}$, $CO_{2(g)}$, $SiO_{(g)}$}

Chemical set 1 was used as an example in Chapter 4.4.4 to show how the gas substitution equations can be systematically generated and used to directly approximate the equilibrium gas composition. The reader is referred back to that section for specific details on algorithm used to generate the gas substitution equations. For completeness, the final form of the gas substitution equations for this regime are reiterated as

$$n_{SiO_{(g)}} = \frac{K_{eq,SiO_{(g)}} V_{pore}}{RT} \tag{158}$$

$$n_{CO_2(g)} = \frac{K_{eq,SiO_{(g)}} V_{pore}}{RT} \tag{159}$$

$$n_{CO_{(g)}} = \frac{K_{eq,CO_{(g)}} V_{pore}}{RT} \tag{160}$$

assuming the gases obey the ideal gas law and the pore volume is

$$V_{pore} = V_{total} - \frac{(n_C M_C)}{\rho_C} - \frac{(n_{SiC} M_{SiC})}{\rho_{SiC}} - \frac{\left(n_{SiO_2} M_{SiO_2}\right)}{\rho_{SiO_2}} \tag{110}$$

I.ii.a Chemical Regime Equilibrium Equations (Method 1)

Chemical set 1 was used as an example in Chapter 4.4to show a method (i.e. Method 2) for generating and iteratively solving the chemical regime equilibrium equations. The reader is referred back to that section for specific details on algorithm used to generate and solve the chemical regime equilibrium equations for this regime.

I.iii Regime 2: {C, SiC, $CO_{(g)}$, $CO_{2(g)}$, $SiO_{(g)}$}

Chemical set 1 was used as an example in Chapter 4.3.4 to show how the gas substitution equations can be systematically generated and used to formulate equations to solve for the equilibrium species composition. The reader is referred back to that section for details on algorithm used to generate the gas substitution equations. For completeness, the final form of the gas substitution equations for this regime are reiterated as

$$K_{eq,SiO_{(g)}} n_{CO_{(g)}} = n_{SiO_{(g)}} \tag{131}$$

$$\frac{K_{eq,CO_{2(g)}} n_{CO_{(g)}}^2 RT}{V_{pore}} = n_{CO_{2(g)}} \tag{132}$$

assuming the gases obey the ideal gas law and the pore volume is

$$V_{pore} = V_{total} - \frac{(n_C M_C)}{\rho_C} - \frac{(n_{SiC} M_{SiC})}{\rho_{SiC}} \tag{136}$$

I.iii.a Chemical Regime Equilibrium Equations (Method 1)

Chemical set 1 was used as an example in Chapter 4.3 to show a method (i.e. Method 1) for generating the chemical regime equilibrium constraints that can be solved to calculate the equilibrium species composition. The reader is referred back to that section for details on

algorithm used to generate and solve the chemical regime equilibrium equations for this regime. For completeness, the final form of the chemical regime equilibrium equations (Method 2) are reiterated as

$$b_C = \frac{K_{eq,CO_{2(g)}} n_{CO_{(g)},1}^2 RT}{V_{pore,0}} + n_{CO_{(g)},1} + n_{C,1} + n_{SiC,1} \tag{140}$$

$$b_O = 2\frac{K_{eq,CO_{2(g)}} n_{CO_{(g)},1}^2 RT}{V_{pore,0}} + n_{CO_{(g)},1} + K_{eq,SiO_g} n_{CO_{(g)},1} \tag{141}$$

$$b_{Si} = n_{SiC,1} + K_{eq,SiO_{(g)}} n_{CO_{(g)},1} \tag{142}$$

And the analytic Jacobian matrix for the chemical equilibrium constraints is

$$\boldsymbol{J_f}\left(n_C, n_{SiC}, n_{CO_{(g)}}\right) = \begin{pmatrix} -1 & -1 & \frac{-2K_{eq,CO_{2(g)}} n_{CO_{(g)}} RT}{V_{pore,0}} - 1 \\ 0 & 0 & \frac{-4K_{eq,CO_{2(g)}} n_{CO_{(g)}} RT}{V_{pore,0}} - K_{eq,SiO_g} - 1 \\ 0 & -1 & -K_{eq,SiO_g} \end{pmatrix} \tag{145}$$

The compositions of C, SiC, and $CO_{(g)}$ are calculated by using a numerical algorithm to find the solution to chemical equilibrium constraint equations, using the analytic Jacobian matrix to expedite the solution process. The updated pore volume is calculated by using Equation 136 with the updated condensed species compositions. The composition of the remaining unknown species, $CO_{2(g)}$ and $SiO_{(g)}$, are calculated by using the gas substitution equations 131 and 132, the updated pore volume, and the calculated species compositions of C, SiC, and $CO_{(g)}$.

I.iv Regime 3: {C, SiO_2, $CO_{(g)}$, $CO_{2(g)}$, $SiO_{(g)}$}

The element abundance matrix using a gas elimination ordering of the species is

	$SiO_{(g)}$	$CO2_{(g)}$	$CO_{(g)}$	C	SiO2
C	0	1	1	1	0
O	1	2	1	0	2
Si	1	0	0	0	1

(185)

The canonical stoichiometric matrix associated with Equation 185 is

	$SiO_{(g)}$	$CO2_{(g)}$	$CO_{(g)}$	C	SiO2
Rx 1	1	0	1	−1	−1
Rx 2	0	1	−2	1	0

(186)

The stoichiometric equations are given by Equations 187 and 188 for the canonical stoichiometric matrix in Equation 186.

$$C + SiO_2 = SiO_{(g)} + CO_{(g)} \tag{187}$$

$$2CO_{(g)} = CO_{2(g)} + C \tag{188}$$

I.v Regime 4: {C, $CO_{(g)}$, $CO_{2(g)}$, $SiO_{(g)}$}

The element abundance matrix using a gas elimination ordering of the species is

	$SiO_{(g)}$	$CO2_{(g)}$	$CO_{(g)}$	C
C	0	1	1	1
O	1	2	1	0
Si	1	0	0	0

(189)

The canonical stoichiometric matrix associated with Equation 189 is

	$SiO_{(g)}$	$CO2_{(g)}$	$CO_{(g)}$	C
Rx 1	0	1	−2	1

(190)

The stoichiometric equation is given by Equation 191 for the canonical stoichiometric matrix in Equation 190.

$$2CO_{(g)} = CO_{2(g)} + C \tag{191}$$

I.vi Regime 5: {SiC, SiO_2, $CO_{(g)}$, $CO_{2(g)}$, $SiO_{(g)}$}

The element abundance matrix using a gas elimination ordering of the species is

	$SiO_{(g)}$	$CO2_{(g)}$	$CO_{(g)}$	SiC	SiO2
C	0	1	1	1	0
O	1	2	1	0	2
Si	1	0	0	1	1

(192)

The canonical stoichiometric matrix associated with Equation 192 is

	$SiO_{(g)}$	$CO2_{(g)}$	$CO_{(g)}$	SiC	SiO2
Rx 1	1	0	$\frac{1}{3}$	$-\frac{1}{3}$	$-\frac{2}{3}$
Rx 2	0	1	$-\frac{4}{3}$	$\frac{1}{3}$	$-\frac{1}{3}$

(193)

The stoichiometric equations are given by Equations 194 and 195 for the canonical stoichiometric matrix in Equation 193.

$$\frac{1}{3}SiC + \frac{2}{3}SiO_2 = SiO_{(g)} + \frac{1}{3}CO_{(g)} \tag{194}$$

$$\frac{4}{3}CO_g + \frac{1}{3}SiO_2 = CO_{2(g)} + \frac{1}{3}SiC \tag{195}$$

I.vii Regime 6: {SiC, $CO_{(g)}$, $CO_{2(g)}$, $SiO_{(g)}$}

The element abundance matrix using a gas elimination ordering of the species is

	$SiO_{(g)}$	$CO2_{(g)}$	$CO_{(g)}$	SiC
C	0	1	1	1
O	1	2	1	0
Si	1	0	0	1

(196)

The canonical stoichiometric matrix associated with Equation 196 is

	$SiO_{(g)}$	$CO2_{(g)}$	$CO_{(g)}$	SiC
Rx 1	1	-2	3	-1

(197)

The stoichiometric equation is given by Equation 198 for the canonical stoichiometric matrix in Equation 197.

$$2CO_{2(g)} + SiC = SiO_{(g)} + 3CO_{(g)} \tag{198}$$

I.viii Regime 7: {SiO_2, $CO_{(g)}$, $CO_{2(g)}$, $SiO_{(g)}$}

The element abundance matrix using a gas elimination ordering of the species is

	$SiO_{(g)}$	$CO2_{(g)}$	$CO_{(g)}$	SiO2
C	0	1	1	0
O	1	2	1	2
Si	1	0	0	1

(199)

The canonical stoichiometric matrix associated with Equation 199 is

	$SiO_{(g)}$	$CO2_{(g)}$	$CO_{(g)}$	SiO2
Rx 1	1	1	−1	−1

(200)

The stoichiometric equation is given by Equation 201 for the canonical stoichiometric matrix in Equation 200.

$$CO_{(g)} + SiO_{2(g)} = SiO_{(g)} + CO_{2(g)} \tag{201}$$

I.ix Regime 8: {$CO_{(g)}$, $CO_{2(g)}$, $SiO_{(g)}$}

The element abundance matrix using a gas elimination ordering of the species is

	$SiO_{(g)}$	$CO2_{(g)}$	$CO_{(g)}$
C	0	1	1
O	1	2	1

(202)

Si	1	0	0

There is no canonical stoichiometric matrix associated with element abundance matrix because the columns of Equation 203 are linearly independent.

	$SiO_{(g)}$	$CO2_{(g)}$	$CO_{(g)}$
Rx 1	No feasible reactions		

(203)

Since there are no feasible reactions among the species assumed present in this chemical regime, any species composition is considered to be at equilibrium.

Appendix II. Chemical Set 2: {B_4C, B_2O_3, C, $CO_{(g)}$, $B_2O_{3(g)}$, $B_2O_{2(g)}$}

This section shows the result of applying the chemical equilibrium model reduction algorithm to the chemical set {B_4C, B_2O_3, C, $CO_{(g)}$, $B_2O_{3(g)}$, $B_2O_{2(g)}$}. An in-depth description of the algorithms for generating the necessary equations and expressions with their associated functions is shown in Chapter 4 on the Chemical Equilibrium Model. The model reduction applied to this chemical set yields the following 8 chemical regimes.

1. {B_4C, B_2O_3, C, $CO_{(g)}$, $B_2O_{3(g)}$, $B_2O_{2(g)}$}
2. {B_4C, B_2O_3, $CO_{(g)}$, $B_2O_{3(g)}$, $B_2O_{2(g)}$}
3. {B_4C, C, $CO_{(g)}$, $B_2O_{3(g)}$, $B_2O_{2(g)}$}
4. {B_4C, $CO_{(g)}$, $B_2O_{3(g)}$, $B_2O_{2(g)}$}
5. {B_2O_3, C, $CO_{(g)}$, $B_2O_{3(g)}$, $B_2O_{2(g)}$}
6. {B_2O_3, $CO_{(g)}$, $B_2O_{3(g)}$, $B_2O_{2(g)}$}
7. {C, $CO_{(g)}$, $B_2O_{3(g)}$, $B_2O_{2(g)}$}
8. {$CO_{(g)}$, $B_2O_{3(g)}$, $B_2O_{2(g)}$}

II.i Activity Checks

The element abundance matrix for an activity ordering of the species is

	B_4C	B_2O_3	C	$CO_{(g)}$	$B_2O_{3(g)}$	$B_2O_{2(g)}$
B	4	2	0	0	2	2
C	1	0	1	1	0	0
O	0	3	0	1	3	2

(204)

The element abundance equations are given by Equations 205, 206, and 207 for the associated element abundance matrix in Equation 204.

$$4n_{B_4C} + 2n_{B_2O_3} + 2n_{B_2O_{3(g)}} + 2n_{B_2O_{2(g)}} = b_B \tag{205}$$

$$n_{B_4C} + n_C + n_{CO_{(g)}} = b_C \tag{206}$$

$$3n_{B_2O_3} + n_{CO_{(g)}} + 3n_{B_2O_{3(g)}} + 2n_{B_2O_{2(g)}} = b_O \tag{207}$$

The canonical stoichiometric matrix associated with Equation 204 is

	B_4C	B_2O_3	C	$CO_{(g)}$	$B_2O_{3(g)}$	$B_2O_{2(g)}$
Rx 1	1	0	0	−1	5	−7
Rx 2	0	1	0	0	−1	0
Rx 3	0	0	1	−1	1	−1

(208)

The stoichiometric equations are given by Equations 209, 210, and 211 for the canonical stoichiometric matrix in Equation 208.

$$CO_{(g)} + 7B_2O_{2(g)} = B_4C + 5B_2O_{3(g)} \tag{209}$$

$$B_2O_{3(g)} = B_2O_3 \tag{210}$$

$$CO_{(g)} + B_2O_{2(g)} = C + B_2O_{3(g)} \tag{211}$$

The Gibbs free energies of reaction for the stoichiometric equations 209, 210, and 211 are

$$\Delta G_{rx,B_4C} = G_{B_4C} + 5G_{B_2O_{3(g)}} - G_{CO_{(g)}} - 7G_{B_2O_{2(g)}} \tag{212}$$

$$\Delta G_{rx,B_2O_3} = G_{B_2O_3} - G_{B_2O_{3(g)}} \tag{213}$$

$$\Delta G_{rx,C} = G_C + G_{B_2O_{3(g)}} - G_{CO_{(g)}} - G_{B_2O_{2(g)}} \tag{214}$$

The functional form of these equations can be generated using the methods described in Appendix IV. The equilibrium constant constraints associated with the stoichiometric equations 209, 210, and 211 are

$$K_{eq,B_4C} = \frac{a_{B_4C} p_{B_2O_3}^5}{p_{CO} p_{B_2O_2}^7} \tag{215}$$

$$K_{eq,B_2O_3} = a_{B_2O_3} p_{B_2O_3} \tag{216}$$

$$K_{eq,C} = \frac{a_C p_{B_2O_3}}{p_{CO} p_{B_2O_2}} \tag{217}$$

The equilibrium constant equations given by Equations 209, 210, and 211 are transformed into the activity check equations

$$\frac{K_{eq,B_4C} n_{CO_{(g)}} n_{B_2O_{2(g)}}^7}{n_{B_2O_{3(g)}}^5} \left(\frac{RT}{V_{pore}}\right)^3 = a_{B_4C} \tag{218}$$

$$\frac{K_{eq,B_2O_{3(g)}}}{n_{B_2O_{3(g)}}} \left(\frac{RT}{V_{pore}}\right)^{-1} = a_{B_2O_3} \tag{219}$$

$$\frac{K_{eq,C} n_{CO_{(g)}} n_{B_2O_{3(g)}}}{n_{B_2O_{2(g)}}} \left(\frac{RT}{V_{pore}}\right) = a_C \tag{220}$$

assuming the gases obey the ideal gas law and the pore volume is

$$V_{pore} = V_{total} - \frac{\left(n_{B_4C} M_{B_4C}\right)}{\rho_{B_4C}} - \frac{\left(n_{B_2O_3} M_{B_2O_3}\right)}{\rho_{B_2O_3}} - \frac{\left(n_C M_C\right)}{\rho_C} \tag{221}$$

II.ii Regime 1: {B_4C, B_2O_3, C, $CO_{(g)}$, $B_2O_{3(g)}$, $B_2O_{2(g)}$}

The element abundance matrix using a gas elimination ordering of the species is

	$B_2O_{2(g)}$	$B_2O_{3(g)}$	$CO_{(g)}$	B_4C	B_2O_3	C
B	2	2	0	4	2	0
C	0	0	1	1	0	1
O	2	3	1	0	3	0

(222)

The canonical stoichiometric matrix associated with Equation 222 is

	$B_2O_{2(g)}$	$B_2O_{3(g)}$	$CO_{(g)}$	B_4C	B_2O_3	C
Rx 1	1	0	0	$-\frac{1}{6}$	$-\frac{2}{3}$	$\frac{1}{6}$
Rx 2	0	1	0	0	-1	0
Rx 3	0	0	1	$\frac{1}{6}$	$-\frac{1}{3}$	$-\frac{7}{6}$

(223)

The stoichiometric equations are given by Equations 224, 225, and 226 for the canonical stoichiometric matrix in Equation 223.

$$\frac{1}{6}B_4C + \frac{2}{3}B_2O_3 = B_2O_{2(g)} + \frac{1}{6}C \tag{224}$$

$$B_2O_3 = B_2O_{3(g)} \tag{225}$$

$$\frac{1}{3}B_2O_3 + \frac{7}{6}C = CO_{(g)} + \frac{1}{6}B_4C \tag{226}$$

The Gibbs free energy of reaction for the stoichiometric equations 224, 225, and 226 are

$$\Delta G_{rx,B_2O_{2(g)}} = G_{B_2O_{2(g)}} + \frac{1}{6}G_C - \frac{1}{6}G_{B_4C} - \frac{2}{3}G_{B_2O_3} \tag{227}$$

$$\Delta G_{rx,B_2O_{3(g)}} = G_{B_2O_{3(g)}} - G_{B_2O_3} \tag{228}$$

$$\Delta G_{rx,CO_{(g)}} = G_{CO_{(g)}} + \frac{1}{6}G_{B_4C} - \frac{1}{3}G_{B_2O_3} - \frac{7}{6}G_C \tag{229}$$

The equilibrium constant constraints associated with the stoichiometric equations 224, 225, and 226 are

$$K_{eq,B_2O_{2(g)}} = \frac{p_{B_2O_2}a_C^{\frac{1}{6}}}{a_{B_4C}^{\frac{1}{6}}a_{B_2O_3}^{\frac{2}{3}}} \tag{230}$$

$$K_{eq,B_2O_{3(g)}} = p_{B_2O_3} a_{B_2O_3} \tag{231}$$

$$K_{eq,CO_{(g)}} = \frac{p_{CO} a_{B_4C}^{\frac{1}{6}}}{a_{B_2O_3}^{\frac{1}{3}} a_C^{\frac{7}{6}}} \tag{232}$$

The equilibrium constant equations given by Equations 230, 231, and 232 are transformed into the gas substitution equations

$$n_{B_2O_{2(g)}} = \frac{K_{eq,B_2O_{2(g)}} V_{pore}}{RT} \tag{233}$$

$$n_{B_2O_{3(g)}} = \frac{K_{eq,B_2O_{3(g)}} V_{pore}}{RT} \tag{234}$$

$$n_{CO_{(g)}} = \frac{K_{eq,CO_{(g)}} V_{pore}}{RT} \tag{235}$$

assuming the gases obey the ideal gas law and the pore volume is

$$V_{pore} = V_{total} - \frac{\left(n_{B_4C} M_{B_4C}\right)}{\rho_{B_4C}} - \frac{\left(n_{B_2O_3} M_{B_2O_3}\right)}{\rho_{B_2O_3}} - \frac{\left(n_C M_C\right)}{\rho_C} \tag{236}$$

II.ii.a Chemical Regime Equilibrium Equations (Method 2)

Following the algorithm presented in Chapter 4.4.5, a set of equations can be generated to iteratively calculate approximations to the equilibrium species composition. The gas substitution equations are used to generate the first approximation of the gas species compositions. The change in molar quantity of the gas species between the first approximation and the initial gas composition are

$$\Delta n_{B_2O_{2(g)},1} = n_{B_2O_{2(g)},1} - n_{B_2O_{2(g)},0} \tag{237}$$

$$\Delta n_{B_2O_{3(g)},1} = n_{B_2O_{3(g)},1} - n_{B_2O_{3(g)},0} \tag{238}$$

$$\Delta n_{B_2O_{3(g)},1} = n_{B_2O_{3(g)},1} - n_{B_2O_{3(g)},0} \tag{239}$$

The change in the molar quantity of the condensed species to account for the elemental change must satisfy

$$\Delta b_{B,1} = 2\Delta n_{B_2O_{2(g)},1} + 2\Delta n_{B_2O_{3(g)},1} \tag{240}$$

$$\Delta b_{C,1} = \Delta n_{CO_{(g)},1} \tag{241}$$

$$\Delta b_{O,1} = 2\Delta n_{B_2O_{2(g)},1} + 3\Delta n_{B_2O_{3(g)},1} + \Delta n_{CO_{(g)},1} \tag{242}$$

The change in the condensed species composition needed to compensate for the change in the elemental composition of the gas species is

$$\Delta n_{B_4C,1} = \frac{1}{4}\Delta b_{B,1} - \frac{1}{6}\Delta b_{O,1} \tag{243}$$

$$\Delta n_{B_2O_3,1} = \frac{1}{3}\Delta b_{O,1} \tag{244}$$

$$\Delta n_{C,1} = \Delta b_{C,1} - \frac{1}{4}\Delta b_{B,1} + \frac{1}{6}\Delta b_{O,1} \tag{245}$$

The first approximation of the condensed species compositions to account for the change in the gas species composition are

$$n_{B_4C,1} = n_{B_4C,0} - \frac{1}{6}\Delta n_{B_2O_{2(g)},1} + \frac{1}{6}\Delta n_{CO_{(g)},1} \tag{246}$$

$$n_{B_2O_3,1} = n_{B_2O_3,0} - \frac{2}{3}\Delta n_{B_2O_{2(g)},1} - \frac{1}{3}\Delta n_{CO_{(g)},1} - \Delta n_{B_2O_3(g),1} \tag{247}$$

$$n_{C,1} = n_{C,0} - \frac{7}{6}\Delta n_{CO_{(g)},1} + \frac{1}{6}\Delta n_{B_2O_{2(g)},1} \tag{248}$$

Equations 233-235 and 246-248 are used to iteratively approach the true equilibrium solution, after updating the pore volume using Equation 236 with the updated condensed species composition after each successive approximation.

II.iii Regime 2: {B_4C, B_2O_3, $CO_{(g)}$, $B_2O_{3(g)}$, $B_2O_{2(g)}$}

The element abundance matrix using a gas elimination ordering of the species is

	$B_2O_{2(g)}$	$B_2O_{3(g)}$	$CO_{(g)}$	B_4C	B_2O_3
B	2	2	0	4	2
C	0	0	1	1	0
O	2	3	1	0	3

(249)

The canonical stoichiometric matrix associated with Equation 249 is

	$B_2O_{2(g)}$	$B_2O_{3(g)}$	$CO_{(g)}$	B_4C	B_2O_3
Rx 1	1	0	$\frac{1}{7}$	$-\frac{1}{7}$	$-\frac{5}{7}$
Rx 2	0	1	0	0	-1

(250)

The stoichiometric equations are given by Equations 251 and 252 for the canonical stoichiometric matrix in Equation 250.

$$\frac{1}{7}B_4C + \frac{5}{7}B_2O_3 = B_2O_{2(g)} + \frac{1}{7}CO_{(g)} \tag{251}$$

$$B_2O_3 = B_2O_{3(g)} \tag{252}$$

II.iv Regime 3: {B_4C, C, $CO_{(g)}$, $B_2O_{3(g)}$, $B_2O_{2(g)}$}

The element abundance matrix using a gas elimination ordering of the species is

	$B_2O_{2(g)}$	$B_2O_{3(g)}$	$CO_{(g)}$	B_4C	C
B	2	2	0	4	0
C	0	0	1	1	1
O	2	3	1	0	0

(253)

The element abundance equations for the element abundance matrix in Equation 253 are

$$2n_{B_2O_{2(g)}} + 2n_{B_2O_{3(g)}} + 4n_{B_4C} = b_B \tag{254}$$

$$n_{CO_{(g)}} + n_{B_4C} + n_C = b_C \tag{255}$$

$$2n_{B_2O_{2(g)}} + 3n_{B_2O_{3(g)}} + n_{CO_{(g)}} = b_O \tag{256}$$

The canonical stoichiometric matrix associated with Equation 253 is

	$B_2O_{2(g)}$	$B_2O_{3(g)}$	$CO_{(g)}$	B_4C	C
Rx 1	1	0	-2	$-\frac{1}{2}$	$\frac{5}{2}$
Rx 2	0	1	-3	$-\frac{1}{2}$	$\frac{7}{2}$

(257)

The stoichiometric equations are given by Equations 258 and 259 for the canonical stoichiometric matrix in Equation 257.

$$2CO_{(g)} + \frac{1}{2}B_4C = B_2O_{2(g)} + \frac{5}{2}C \tag{258}$$

$$3CO_{(g)} + \frac{1}{2}B_4C = B_2O_{3(g)} + \frac{7}{2}C \tag{259}$$

The Gibbs free energy of reaction for the stoichiometric equations 258 and 259 are

$$\Delta G_{rx,B_2O_{2(g)}} = G_{B_2O_{2(g)}} + \frac{5}{2}G_C - \frac{1}{2}G_{B_4C} - 2G_{CO_{(g)}} \tag{260}$$

$$\Delta G_{rx,B_2O_{3(g)}} = G_{B_2O_{3(g)}} + \frac{7}{2}G_C - \frac{1}{2}G_{B_4C} - 3G_{CO_{(g)}} \tag{261}$$

The equilibrium constant constraints associated with the stoichiometric equations 258 and 259 are

$$K_{eq,B_2O_{2(g)}} = \frac{p_{B_2O_2}a_C^{\frac{5}{2}}}{a_{B_4C}^{\frac{1}{2}}p_{CO}^2} \tag{262}$$

$$K_{eq,B_2O_{3(g)}} = \frac{p_{B_2O_3}a_C^{\frac{7}{2}}}{a_{B_4C}^{\frac{1}{2}}p_{CO}^3} \tag{263}$$

The equilibrium constant equations given by Equations 262 and 263 are transformed into the gas substitution equations

$$\frac{K_{eq,B_2O_{2(g)}}n_{CO_{(g)}}^2RT}{V_{pore}} = n_{B_2O_{2(g)}} \tag{264}$$

$$\frac{K_{eq,B_2O_{3(g)}}n_{CO_{(g)}}^3R^2T^2}{V_{pore}^2} = n_{B_2O_{3(g)}} \tag{265}$$

assuming the gases obey the ideal gas law and the pore volume is

$$V_{pore} = V_{total} - \frac{\left(n_{B_4C}M_{B_4C}\right)}{\rho_{B_4C}} - \frac{(n_CM_C)}{\rho_C} \tag{266}$$

II.iv.a Chemical Regime Equilibrium Equations (Method 2)

A set of chemical equilibrium constraint equations are generated for this chemical regime using the algorithm presented in Chapter 4.3. A detailed example is given in Chapter 4.3 and highlights specific aspects regarding the construction of the constraint equations and their solution. The unknown gas species composition for $B_2O_{2(g)}$ and $B_2O_{3(g)}B_2O_{2(g)}$ and $B_2O_{3(g)}$are

explicitly eliminated from the element abundance equations. Substitution of the gas substitution equations 264 and 265 into the element abundance equations 254- 256 generates the chemical equilibrium constraint equations

$$b_B = 4n_{B_4C} + 2\frac{K_{eq,B_2O_{2(g)}} n_{CO_{(g)}}^2 RT}{V_{pore,0}} + 2\frac{K_{eq,B_2O_{3(g)}} n_{CO_{(g)}}^3 R^2T^2}{V_{pore,0}^2} \quad (267)$$

$$b_C = n_{B_4C} + n_C + n_{CO_{(g)}} \quad (268)$$

$$b_O = 2\frac{K_{eq,B_2O_{2(g)}} n_{CO_{(g)}}^2 RT}{V_{pore,0}} + 3\frac{K_{eq,B_2O_{3(g)}} n_{CO_{(g)}}^3 R^2T^2}{V_{pore,0}^2} + n_{CO_{(g)}} \quad (269)$$

The analytic Jacobian matrix for the chemical equilibrium constraints is

$$J_f\left(n_{B_4C}, n_C, n_{CO_{(g)}}\right) = \begin{pmatrix} -4 & 0 & -4\frac{K_{eq,B_2O_{2(g)}} n_{CO_{(g)}} RT}{V_{pore,0}} - 6\frac{K_{eq,B_2O_{3(g)}} n_{CO_{(g)}}^2 R^2T^2}{V_{pore,0}^2} \\ -1 & -1 & -1 \\ 0 & 0 & -4\frac{K_{eq,B_2O_{2(g)}} n_{CO_{(g)}} RT}{V_{pore,0}} - 9\frac{K_{eq,B_2O_{3(g)}} n_{CO_{(g)}}^2 R^2T^2}{V_{pore,0}^2} \end{pmatrix} \quad (270)$$

The compositions of B_4C, C, and $CO_{(g)}$ are calculated by using a numerical algorithm to find the solution to chemical equilibrium constraint equations, using the analytic Jacobian matrix to expedite solution process. The updated pore volume is calculated by using Equation 266 with the updated condensed species compositions. The compositions of the remaining unknown species, $B_2O_{2(g)}$ and $B_2O_{3(g)}$, are calculated by using the gas substitution equations 264 and 265, the updated pore volume, and the calculated species compositions ofB_4C, C, and $CO_{(g)}$.

II.v Regime 4: {B_4C, $CO_{(g)}$, $B_2O_{3(g)}$, $B_2O_{2(g)}$}

The element abundance matrix using a gas elimination ordering of the species is

	$B_2O_{2(g)}$	$B_2O_{3(g)}$	$CO_{(g)}$	B_4C
B	2	2	0	4
C	0	0	1	1

(271)

O	2	3	1	0

The canonical stoichiometric matrix associated with Equation 271 is

	$B_2O_{2(g)}$	$B_2O_{3(g)}$	$CO_{(g)}$	B_4C
Rx 1	1	$-\frac{5}{7}$	$\frac{1}{7}$	$-\frac{1}{7}$

(272)

The stoichiometric equation is given by Equation 273 for the canonical stoichiometric matrix in Equation 272.

$$\frac{1}{7}B_4C + \frac{5}{7}B_2O_{3(g)} = B_2O_{2(g)} + \frac{1}{7}CO_{(g)} \tag{273}$$

II.vi Regime 5: {B_2O_3, C, $CO_{(g)}$, $B_2O_{3(g)}$, $B_2O_{2(g)}$}

The element abundance matrix using a gas elimination ordering of the species is

	$B_2O_{2(g)}$	$B_2O_{3(g)}$	$CO_{(g)}$	B_2O_3	C
B	2	2	0	2	0
C	0	0	1	0	1
O	2	3	1	3	0

(274)

The canonical stoichiometric matrix associated with Equation 274 is

	$B_2O_{2(g)}$	$B_2O_{3(g)}$	$CO_{(g)}$	B_2O_3	C
Rx 1	1	0	1	-1	-1
Rx 2	0	1	0	-1	0

(275)

The stoichiometric equations are given by Equations 276 and 277 for the canonical stoichiometric matrix in Equation 275.

$$C + B_2O_3 = B_2O_{2(g)} + CO_{(g)} \tag{276}$$

$$B_2O_3 = B_2O_{3(g)} \tag{277}$$

II.vii Regime 6: {B_2O_3, $CO_{(g)}$, $B_2O_{3(g)}$, $B_2O_{2(g)}$}

The element abundance matrix using a gas elimination ordering of the species is

	$B_2O_{2(g)}$	$B_2O_{3(g)}$	$CO_{(g)}$	B_2O_3
B	2	2	0	2
C	0	0	1	0
O	2	3	1	3

(278)

The canonical stoichiometric matrix associated with Equation 278 is

	$B_2O_{2(g)}$	$B_2O_{3(g)}$	$CO_{(g)}$	B_2O_3
Rx 1	0	1	0	-1

(279)

The stoichiometric equation is given by Equation 280 for the canonical stoichiometric matrix in Equation 279.

$$B_2O_3 = B_2O_{3(g)} \tag{280}$$

II.viii Regime 7: {C, $CO_{(g)}$, $B_2O_{3(g)}$, $B_2O_{2(g)}$}

The element abundance matrix using a gas elimination ordering of the species is

	$B_2O_{2(g)}$	$B_2O_{3(g)}$	$CO_{(g)}$	C
B	2	2	0	0
C	0	0	1	1
O	2	3	1	0

(281)

The canonical stoichiometric matrix associated with Equation 281 is

	$B_2O_{2(g)}$	$B_2O_{3(g)}$	$CO_{(g)}$	C
Rx 1	1	-1	1	-1

(282)

The stoichiometric equation is given by Equation 283 for the canonical stoichiometric matrix in Equation 282.

$$B_2O_{3(g)} + C = B_2O_{2(g)} + CO_{(g)} \tag{283}$$

II.ix Regime 8: {$CO_{(g)}$, $B_2O_{3(g)}$, $B_2O_{2(g)}$}

The element abundance matrix using a gas elimination ordering of the species is

	$B_2O_{2(g)}$	$B_2O_{3(g)}$	$CO_{(g)}$
B	2	2	0
C	0	0	1
O	2	3	1

(284)

The canonical stoichiometric matrix, in Equation 285, is empty because the columns of the associated element abundance matrix, in Equation 284, are linearly independent.

	$B_2O_{2(g)}$	$B_2O_{3(g)}$	$CO_{(g)}$
Rx 1	No feasible reactions		

(285)

Since there are no feasible reactions among the species assumed present in this chemical regime, any species composition is considered to be at equilibrium.

Appendix III. Chemical Set 3: {C, SiC, SiO_2, B_4C, $CO_{(g)}$, $SiO_{(g)}$, $B_2O_{3(g)}$, $B_2O_{2(g)}$}

This section shows the result of applying the chemical equilibrium model reduction algorithm to the chemical set {C, SiC, SiO_2, B_4C, $CO_{(g)}$, $SiO_{(g)}$, $B_2O_{3(g)}$, $B_2O_{2(g)}$}. An in-depth description of the algorithms for generating the necessary equations and expressions with their associated functions is shown in Chapter 1 on the Chemical Equilibrium Model. The model reduction applied to this chemical set yields the following 16 chemical regimes.

1. {C, SiC, SiO_2, B_4C, $CO_{(g)}$, $SiO_{(g)}$, $B_2O_{3(g)}$, $B_2O_{2(g)}$}
2. {C, SiC, SiO_2, $CO_{(g)}$, $SiO_{(g)}$, $B_2O_{3(g)}$, $B_2O_{2(g)}$}
3. {C, SiC, B_4C, $CO_{(g)}$, $SiO_{(g)}$, $B_2O_{3(g)}$, $B_2O_{2(g)}$}
4. {C, SiC, $CO_{(g)}$, $SiO_{(g)}$, $B_2O_{3(g)}$, $B_2O_{2(g)}$}
5. {C, SiO_2, B_4C, $CO_{(g)}$, $SiO_{(g)}$, $B_2O_{3(g)}$, $B_2O_{2(g)}$}
6. {C, SiO_2, $CO_{(g)}$, $SiO_{(g)}$, $B_2O_{3(g)}$, $B_2O_{2(g)}$}
7. {C, B_4C, $CO_{(g)}$, $SiO_{(g)}$, $B_2O_{3(g)}$, $B_2O_{2(g)}$}
8. {C, $CO_{(g)}$, $SiO_{(g)}$, $B_2O_{3(g)}$, $B_2O_{2(g)}$}
9. {SiC, SiO_2, B_4C, $CO_{(g)}$, $SiO_{(g)}$, $B_2O_{3(g)}$, $B_2O_{2(g)}$}
10. {SiC, SiO_2, $CO_{(g)}$, $SiO_{(g)}$, $B_2O_{3(g)}$, $B_2O_{2(g)}$}
11. {SiC, B_4C, $CO_{(g)}$, $SiO_{(g)}$, $B_2O_{3(g)}$, $B_2O_{2(g)}$}
12. {SiC, $CO_{(g)}$, $SiO_{(g)}$, $B_2O_{3(g)}$, $B_2O_{2(g)}$}
13. {SiO_2, B_4C, $CO_{(g)}$, $SiO_{(g)}$, $B_2O_{3(g)}$, $B_2O_{2(g)}$}
14. {SiO_2, $CO_{(g)}$, $SiO_{(g)}$, $B_2O_{3(g)}$, $B_2O_{2(g)}$}
15. {B_4C, $CO_{(g)}$, $SiO_{(g)}$, $B_2O_{3(g)}$, $B_2O_{2(g)}$}
16. {$CO_{(g)}$, $SiO_{(g)}$, $B_2O_{3(g)}$, $B_2O_{2(g)}$}

III.i Activity Checks

The element abundance matrix for an activity ordering of the species is

	C	SiC	SiO_2	B_4C	$CO_{(g)}$	$SiO_{(g)}$	$B_2O_{3(g)}$	$B_2O_{2(g)}$
B	0	0	0	4	0	0	2	2
C	1	1	0	1	1	1	0	0
O	0	0	2	0	1	0	3	2
Si	0	1	1	0	0	1	0	0

(286)

The element abundance equations are given by Equations 287-290 for the associated element abundance matrix in Equation 286.

$$4n_{B_4C} + 2n_{B_2O_{3(g)}} + 2n_{B_2O_{2(g)}} = b_B \tag{287}$$

$$n_C + n_{SiC} + n_{B_4C} + n_{CO_{(g)}} = b_C \tag{288}$$

$$2n_{SiO_2} + n_{CO_{(g)}} + n_{SiO_{(g)}} + 3n_{B_2O_{3(g)}} + 2n_{B_2O_{2(g)}} = b_O \tag{289}$$

$$n_{SiC} + n_{SiO_2} + n_{SiO_{(g)}} = b_{Si} \tag{290}$$

The canonical stoichiometric matrix associated with Equation 286 is

	C	SiC	SiO_2	B_4C	$CO_{(g)}$	$SiO_{(g)}$	$B_2O_{3(g)}$	$B_2O_{2(g)}$
Rx 1	1	0	0	0	−1	0	1	−1
Rx 2	0	1	0	0	−1	−1	2	−2
Rx 3	0	0	1	0	0	−1	−1	1
Rx 4	0	0	0	1	−1	0	5	−7

(291)

The stoichiometric equations are given by Equations 292-295 for the canonical stoichiometric matrix in Equation 291.

$$CO_{(g)} + B_2O_{2(g)} = C + B_2O_{3(g)} \tag{292}$$

$$CO_{(g)} + SiO_{(g)} + 2B_2O_{2(g)} = SiC + 2B_2O_{3(g)} \quad (293)$$

$$B_2O_{3(g)} + SiO_{(g)} = SiO_2 + B_2O_{2(g)} \quad (294)$$

$$CO_{(g)} + 7B_2O_{2(g)} = B_4C + 5B_2O_{3(g)} \quad (295)$$

The Gibbs free energies of reaction for the stoichiometric equations 292-295 are

$$\Delta G_{rx,C} = G_C + G_{B_2O_{3(g)}} - G_{CO_{(g)}} - G_{CO_{(g)}} \quad (296)$$

$$\Delta G_{rx,SiC} = G_{SiC} + 2G_{B_2O_{3(g)}} - G_{CO_{(g)}} - G_{SiO_{(g)}} - 2G_{B_2O_{2(g)}} \quad (297)$$

$$\Delta G_{rx,SiO_2} = G_{SiO_2} + G_{B_2O_{2(g)}} - G_{B_2O_{3(g)}} - G_{SiO_{(g)}} \quad (298)$$

$$\Delta G_{rx,B_4C} = G_{B_4C} + 5G_{B_2O_{3(g)}} - 7G_{B_2O_{2(g)}} - G_{CO_{(g)}} \quad (299)$$

The functional form of these equations can be generated using the methods described in Appendix IV. The equilibrium constant equations associated with the stoichiometric equations 292-295 are

$$K_{eq,C} = \frac{a_C p_{B_2O_3}}{p_{CO} p_{B_2O_2}} \quad (300)$$

$$K_{eq,SiC} = \frac{a_{SiC} p_{B_2O_3}^2}{p_{B_2O_2}^2 p_{SiO} p_{CO}} \quad (301)$$

$$K_{eq,SiO_2} = \frac{a_{SiO_2} p_{B_2O_2}}{p_{B_2O_3} p_{SiO}} \quad (302)$$

$$K_{eq,B_4C} = \frac{a_{B_4C} p_{B_2O_3}^2}{p_{CO} p_{B_2O_2}^7} \quad (303)$$

The equilibrium constant equations given by Equations 300-303 are transformed into the activity check equations

$$\frac{K_{eq,C} n_{CO_{(g)}} n_{B_2O_{2(g)}}}{n_{B_2O_{3(g)}}} \left(\frac{RT}{V_{pore}}\right) = a_C \tag{304}$$

$$\frac{K_{eq,SiC} n^2_{B_2O_{2(g)}} n_{SiO_{(g)}} n_{CO_{(g)}}}{n^2_{B_2O_{3(g)}}} \left(\frac{RT}{V_{pore}}\right)^2 = a_{SiC} \tag{305}$$

$$\frac{K_{eq,SiO_2} n_{B_2O_{3(g)}} n_{SiO_{(g)}}}{n_{B_2O_{2(g)}}} \left(\frac{RT}{V_{pore}}\right) = a_{SiO_2} \tag{306}$$

$$\frac{K_{eq,B_4C} n_{CO_{(g)}} n^7_{B_2O_{2(g)}}}{n^2_{B_2O_{3(g)}}} \left(\frac{RT}{V_{pore}}\right)^6 = a_{B_4C} \tag{307}$$

assuming the gases obey the ideal gas law and the pore volume is

$$V_{pore} = V_{total} - \frac{(n_C M_C)}{\rho_C} - \frac{(n_{SiC} M_{SiC})}{\rho_{SiC}} - \frac{\left(n_{SiO_2} M_{SiO_2}\right)}{\rho_{SiO_2}} - \frac{\left(n_{B_4C} M_{B_4C}\right)}{\rho_{B_4C}} \tag{308}$$

III.ii Regime 1: {C, SiC, SiO_2, B_4C, $CO_{(g)}$, $SiO_{(g)}$, $B_2O_{3(g)}$, $B_2O_{2(g)}$}

The element abundance matrix using a gas elimination ordering of the species is

	$B_2O_{2(g)}$	$B_2O_{3(g)}$	$SiO_{(g)}$	$CO_{(g)}$	C	SiC	SiO_2	B_4C
B	2	2	0	0	0	0	0	4
C	0	0	1	1	1	1	0	1
O	2	3	0	1	0	0	2	0
Si	0	0	1	0	0	1	1	0

(309)

The canonical stoichiometric matrix associated with Equation 309 is

	$B_2O_{2(g)}$	$B_2O_{3(g)}$	$SiO_{(g)}$	$CO_{(g)}$	C	SiC	SiO_2	B_4C
Rx 1	1	0	0	0	$-\frac{1}{2}$	1	−1	$-\frac{1}{2}$
Rx 2	0	1	0	0	−1	$\frac{3}{2}$	$-\frac{3}{2}$	$-\frac{1}{2}$
Rx 3	0	0	1	0	$\frac{1}{2}$	$-\frac{1}{2}$	$-\frac{1}{2}$	0
Rx 4	0	0	0	1	$-\frac{3}{2}$	$\frac{1}{2}$	$-\frac{1}{2}$	0

(310)

The stoichiometric equations are given by Equations 311-314 for the canonical stoichiometric matrix in Equation 310.

$$\frac{1}{2}C + SiO_2 + \frac{1}{2}B_4C = B_2O_{2(g)} + SiC \tag{311}$$

$$C + \frac{3}{2}SiO_2 + \frac{1}{2}B_4C = B_2O_{3(g)} + \frac{3}{2}SiC \tag{312}$$

$$\frac{1}{2}SiC + \frac{1}{2}SiO_2 = SiO_{(g)} + \frac{1}{2}C \tag{313}$$

$$\frac{3}{2}C + \frac{1}{2}SiO_2 = CO_{(g)} + \frac{1}{2}SiC \tag{314}$$

The Gibbs free energy of reaction for the stoichiometric equations 311-314 are

$$\Delta G_{rx,B_2O_{2(g)}} = G_{B_2O_{2(g)}} + G_{SiC} - \frac{1}{2}G_C - G_{SiO_2} + \frac{1}{2}G_{B_4C} \tag{315}$$

$$\Delta G_{rx,B_2O_{3(g)}} = G_{B_2O_{3(g)}} + \frac{3}{2}G_{SiC} - G_C - \frac{3}{2}G_{SiO_2} - \frac{1}{2}G_{B_4C} \tag{316}$$

$$\Delta G_{rx,SiO_{(g)}} = G_{SiO_{(g)}} + \frac{1}{2}G_C - \frac{1}{2}G_{SiO_2} - \frac{1}{2}G_{SiC} \tag{317}$$

$$\Delta G_{rx,CO_{(g)}} = G_{CO_{(g)}} + \frac{1}{2}G_{SiC} - \frac{1}{2}G_{SiO_2} - \frac{3}{2}G_{SiO_{(g)}} \tag{318}$$

The equilibrium constant constraints associated with the stoichiometric equations 311-314 are

$$K_{eq,B_2O_{2(g)}} = \frac{p_{B_2O_2}a_{SiC}}{a_C^{\frac{1}{2}}a_{SiO_2}a_{B_4C}^{\frac{1}{2}}} \tag{319}$$

$$K_{eq,B_2O_{3(g)}} = \frac{p_{B_2O_3} a_{SiC}^{\frac{3}{2}}}{a_C^{\frac{3}{2}} a_{SiO_2}^{\frac{1}{2}} a_{B_4C}^{\frac{1}{2}}} \tag{320}$$

$$K_{eq,SiO_{(g)}} = \frac{p_{SiO} a_C^{\frac{1}{2}}}{a_{SiC}^{\frac{1}{2}} a_{SiO_2}^{\frac{1}{2}}} \tag{321}$$

$$K_{eq,CO_{(g)}} = \frac{p_{CO} a_{SiC}^{\frac{1}{2}}}{a_C^{\frac{3}{2}} a_{SiO_2}^{\frac{1}{2}}} \tag{322}$$

The equilibrium constant equations given by Equations 319-322 are transformed into the gas substitution equations

$$n_{B_2O_{2(g)}} = \frac{K_{eq,B_2O_{2(g)}} V_{pore}}{RT} \tag{323}$$

$$n_{B_2O_{3(g)}} = \frac{K_{eq,B_2O_{3(g)}} V_{pore}}{RT} \tag{324}$$

$$n_{SiO_{(g)}} = \frac{K_{eq,SiO_{(g)}} V_{pore}}{RT} \tag{325}$$

$$n_{CO_{(g)}} = \frac{K_{eq,CO_{(g)}} V_{pore}}{RT} \tag{326}$$

assuming the gases obey the ideal gas law and the pore volume is

$$V_{pore} = V_{total} - \frac{(n_C M_C)}{\rho_C} - \frac{(n_{SiC} M_{SiC})}{\rho_{SiC}} - \frac{(n_{SiO_2} M_{SiO_2})}{\rho_{SiO_2}} - \frac{(n_{B_4C} M_{B_4C})}{\rho_{B_4C}} \tag{327}$$

III.ii.a Chemical Regime Equilibrium Equations (Method 2)

Following the algorithm presented in Chapter 4.4.5, a set of equations can be generated to iteratively calculate approximations to the equilibrium species composition. The gas

substitution equations are used to generate the first approximation of the gas species compositions. The change in molar quantity of the gas species between the first approximation and the initial gas composition are

$$\Delta n_{B_2O_{2(g)},1} = n_{B_2O_{2(g)},1} - n_{B_2O_{2(g)},0} \tag{328}$$

$$\Delta n_{B_2O_{3(g)},1} = n_{B_2O_{3(g)},1} - n_{B_2O_{3(g)},0} \tag{329}$$

$$\Delta n_{SiO_{(g)},1} = n_{SiO_{(g)},1} - n_{SiO_{(g)},0} \tag{330}$$

$$\Delta n_{CO_{(g)},1} = n_{CO_{(g)},1} - n_{CO_{(g)},0} \tag{331}$$

The change in the molar quantity of the condensed species to account for the elemental change must satisfy

$$\Delta b_{B,1} = 2\Delta n_{B_2O_{2(g)},1} + 2\Delta n_{B_2O_{3(g)},1} \tag{332}$$

$$\Delta b_{C,1} = \Delta n_{CO_{(g)},1} \tag{333}$$

$$\Delta b_{O,1} = \Delta n_{SiO_{(g)},1} + \Delta n_{CO_{(g)},1} + 2\Delta n_{B_2O_{2(g)},1} + 3\Delta n_{B_2O_{3(g)},1} \tag{334}$$

$$\Delta b_{Si,1} = \Delta n_{SiO_{(g)},1} \tag{335}$$

The change in the condensed species composition needed compensate for the change in the elemental composition of the gas species is

$$\Delta n_{B_4C,1} = \frac{1}{4}\Delta b_{B,1} \tag{336}$$

$$\Delta n_{C,1} = \Delta b_{C,1} + \frac{1}{2}\Delta b_{O,1} - \Delta b_{Si,1} - \frac{1}{4}\Delta b_B, 1 \tag{337}$$

$$\Delta n_{SiO_2,1} = \frac{1}{2}\Delta b_{O,1} \tag{338}$$

$$\Delta n_{SiO_2,1} = \frac{1}{2}\Delta b_{O,1} \tag{339}$$

The first approximation of the condensed species compositions to account for the change in the gas species composition are

$$n_{C,1} = n_{C,0} + \frac{1}{2}\Delta n_{SiO_{(g)},1} - \Delta n_{B_2O_{3(g)},1} - \frac{1}{2}\Delta n_{B_2O_{2(g)},1} - \frac{3}{2}\Delta n_{CO_{(g)},1} \tag{340}$$

$$n_{SiC,1} = n_{SiC,0} + \Delta n_{B_2O_{2(g)},1} + \frac{1}{2}\Delta n_{CO_{(g)},1} + \frac{3}{2}\Delta n_{B_2O_{3(g)},1} - \frac{1}{2}\Delta n_{SiO_{(g)},1} \tag{341}$$

$$n_{SiO_2,1} = n_{SiO_2,0} - \frac{1}{2}\Delta n_{CO_{(g)},1} - \frac{3}{2}\Delta n_{B_2O_{3(g)},1} - \Delta n_{B_2O_{2(g)},1} - \frac{1}{2}\Delta n_{SiO_{(g)},1} \tag{342}$$

$$n_{B_4C,1} = n_{B_4C,0} - \frac{1}{2}\Delta n_{B_2O_{3(g)},1} - \frac{1}{2}\Delta n_{B_2O_{2(g)},1} \tag{343}$$

Equations 323-326 and 340-343 are used to iteratively approach the true equilibrium solution, after updating the pore volume using Equation 327 with the updated condensed species composition after each successive approximation.

III.iii Regime 2: {C, SiC, SiO_2, $CO_{(g)}$, $SiO_{(g)}$, $B_2O_{3(g)}$, $B_2O_{2(g)}$}

The element abundance matrix using a gas elimination ordering of the species is

	$B_2O_{2(g)}$	$B_2O_{3(g)}$	$SiO_{(g)}$	$CO_{(g)}$	C	SiC	SiO_2
B	2	2	0	0	0	0	0
C	0	0	1	1	1	1	0
O	2	3	0	1	0	0	2
Si	0	0	1	0	0	1	1

(344)

The canonical stoichiometric matrix associated with Equation 344 is

	$B_2O_{2(g)}$	$B_2O_{3(g)}$	$SiO_{(g)}$	$CO_{(g)}$	C	SiC	SiO_2
Rx 1	1	-1	0	0	$\frac{1}{2}$	$-\frac{1}{2}$	$\frac{1}{2}$
Rx 2	0	0	1	0	$\frac{1}{2}$	$-\frac{1}{2}$	$-\frac{1}{2}$
Rx 3	0	0	0	1	$-\frac{3}{2}$	$\frac{1}{2}$	$-\frac{1}{2}$

(345)

The stoichiometric equations are given by Equations 346, 347, and 348 for the canonical stoichiometric matrix in Equation 345.

$$B_2O_{3(g)} + \frac{1}{2}SiC = B_2O_{2(g)} + C + SiO_2 \tag{346}$$

$$\frac{1}{2}SiC + \frac{1}{2}SiO_2 = SiO_{(g)} + \frac{1}{2}C \tag{347}$$

$$\frac{3}{2}C + \frac{1}{2}SiO_2 = CO_{(g)} + \frac{1}{2}SiC \tag{348}$$

III.iv Regime 3: {C, SiC, B_4C, $CO_{(g)}$, $SiO_{(g)}$, $B_2O_{3(g)}$, $B_2O_{2(g)}$}

The element abundance matrix using a gas elimination ordering of the species is

	$B_2O_{2(g)}$	$B_2O_{3(g)}$	$SiO_{(g)}$	$CO_{(g)}$	C	SiC	B_4C
B	2	2	0	0	0	0	4
C	0	0	1	1	1	1	1
O	2	3	0	1	0	0	0
Si	0	0	1	0	0	1	0

(349)

The element abundance equations for the element abundance matrix in Equation 349 are

$$2n_{B_2O_{2(g)}} + 2n_{B_2O_{3(g)}} + 4n_{B_4C} = b_B \tag{350}$$

$$n_{CO_{(g)}} + n_C + n_{SiC} + n_{B_4C} = b_C \tag{351}$$

$$2n_{B_2O_{2(g)}} + 3n_{B_2O_{3(g)}} + n_{SiO_{(g)}} + n_{CO_{(g)}} = b_O \tag{352}$$

The canonical stoichiometric matrix associated with Equation 349 is

	$B_2O_{2(g)}$	$B_2O_{3(g)}$	$SiO_{(g)}$	$CO_{(g)}$	C	SiC	B_4C
Rx 1	1	0	0	−2	$\frac{5}{2}$	0	$-\frac{1}{2}$
Rx 2	0	1	0	−3	$\frac{7}{2}$	0	$-\frac{1}{2}$
Rx 3	0	0	1	−1	2	−1	0

(353)

The stoichiometric equations are given by Equations 354, 355, and 356 for the canonical stoichiometric matrix in Equation 353.

$$2CO_{(g)} + \frac{1}{2}B_4C = B_2O_{2(g)} + \frac{5}{2}C \tag{354}$$

$$3CO_{(g)} + \frac{1}{2}B_4C = B_2O_{3(g)} + \frac{7}{2}C \tag{355}$$

$$CO_{(g)} + SiC = SiO_{(g)} + 2C \tag{356}$$

The Gibbs free energies of reaction for the stoichiometric equations 354, 355, and 356 are

$$\Delta G_{rx,B_2O_{2(g)}} = G_{B_2O_{2(g)}} + \frac{5}{2}G_C - \frac{1}{2}G_{B_4C} - 2G_{CO_{(g)}} \tag{357}$$

$$\Delta G_{rx,B_2O_{3(g)}} = G_{B_2O_{3(g)}} + \frac{7}{2}G_C - \frac{1}{2}G_{B_4C} - 3G_{CO_{(g)}} \tag{358}$$

$$\Delta G_{rx,SiO_{(g)}} = G_{SiO_{(g)}} + 2G_C - G_{SiC} - G_{CO_{(g)}} \tag{359}$$

The equilibrium constant constraints associated with the stoichiometric equations 354, 355, and 356 are

$$K_{eq,B_2O_{2(g)}} = \frac{p_{B_2O_2} a_C^{\frac{5}{2}}}{a_{B_4C}^{\frac{1}{2}} p_{CO}^2} \tag{360}$$

$$K_{eq,B_2O_{3(g)}} = \frac{p_{B_2O_3} a_C^{\frac{7}{2}}}{a_{B_4C}^{\frac{1}{2}} p_{CO}^3} \tag{361}$$

$$K_{eq,SiO_{(g)}} = \frac{p_{SiO_{(g)}} a_C^2}{a_{SiC} p_{CO}} \tag{362}$$

The equilibrium constant equations given by Equations 360, 361, and 362 are transformed into the gas substitution equations

$$\frac{K_{eq,B_2O_{2(g)}} n_{CO_{(g)}}^2 RT}{V_{pore}} = n_{B_2O_{2(g)}} \tag{363}$$

$$\frac{K_{eq,B_2O_{3(g)}} n_{CO_{(g)}}^3 R^2T^2}{V_{pore}^2} = n_{B_2O_{3(g)}} \tag{364}$$

$$K_{eq,SiO_{(g)}} n_{CO_{(g)}} = n_{SiO_{(g)}} \tag{365}$$

assuming the gases obey the ideal gas law and the pore volume is

$$V_{pore} = V_{total} - \frac{(n_{SiC} M_{SiC})}{\rho_{SiC}} - \frac{(n_C M_C)}{\rho_C} - \frac{\left(n_{B_4C} M_{B_4C}\right)}{\rho_{B_4C}} \tag{366}$$

III.iv.a Chemical Regime Equilibrium Equations (Method 2)

A set of chemical equilibrium constraint equations are generated for this chemical regime using the algorithm presented in Chapter 4.3. A detailed example is given in Chapter 4.3 and highlights specific aspects regarding the construction of the constraint equations and their solution. The unknown gas species compositions for $B_2O_{2(g)}$, $B_2O_{3(g)}$, and $SiO_{(g)}$ are explicitly

eliminated from the element abundance equations. Substituting the gas substitution equations 363-365 into the element abundance equations 350- 352 generates the chemical equilibrium constraint equations

$$b_B = 4n_{B_4C} + 2\frac{K_{eq,B_2O_{2(g)}} n_{CO_{(g)}}^2 RT}{V_{pore,0}} + 2\frac{K_{eq,B_2O_{3(g)}} n_{CO_{(g)}}^3 R^2T^2}{V_{pore,0}^2} \tag{367}$$

$$b_C = n_C + n_{CO_{(g)}} + n_{SiC} + n_{B_4C} \tag{368}$$

$$b_O = n_{CO_{(g)}} + K_{eq,SiO_{(g)}} n_{CO_{(g)}} + 2\frac{K_{eq,B_2O_{2(g)}} n_{CO_{(g)}}^2 RT}{V_{pore,0}} + 3\frac{K_{eq,B_2O_{3(g)}} n_{CO_{(g)}}^3 R^2T^2}{V_{pore,0}^2} \tag{369}$$

$$b_{Si} = n_{SiC} + K_{eq,SiO_{(g)}} n_{CO_{(g)}} \tag{370}$$

The analytic Jacobian matrix for the chemical equilibrium constraints is

$$J_f\left(n_C, n_{SiC}, n_{B_4C}, n_{CO_{(g)}}\right) = \begin{pmatrix} 0 & 0 & -4 & -4\frac{K_{eq,B_2O_{2(g)}} n_{CO_{(g)}} RT}{V_{pore,0}} - 6\frac{K_{eq,B_2O_{3(g)}} n_{CO_{(g)}}^2 R^2T^2}{V_{pore,0}^2} \\ -1 & -1 & -1 & -1 \\ 0 & 0 & 0 & -1 - K_{eq,SiO_{(g)}} - 4\frac{K_{eq,B_2O_{2(g)}} n_{CO_{(g)}} RT}{V_{pore,0}} - 9\frac{K_{eq,B_2O_{3(g)}} n_{CO_{(g)}}^2 R^2T^2}{V_{pore,0}^2} \\ 0 & -1 & 0 & -K_{eq,SiO_{(g)}} \end{pmatrix} \tag{371}$$

The compositions of C, SiC, B_4C, and $CO_{(g)}$ are calculated by using a numerical algorithm to find the solution to chemical equilibrium constraint equations, using the analytic Jacobian matrix to expedite the solution process. The updated pore volume is calculated by using Equation 366 with the updated condensed species compositions. The compositions of the remaining unknown species, $B_2O_{2(g)}$, $B_2O_{3(g)}$, and $SiO_{(g)}$, are calculated by using the gas substitution equations 363-365, the updated pore volume, and the calculated species compositions of C, SiC, B_4C, and $CO_{(g)}$.

III.v Regime 4: {C, SiC, $CO_{(g)}$, $SiO_{(g)}$, $B_2O_{3(g)}$, $B_2O_{2(g)}$}

The element abundance matrix using a gas elimination ordering of the species is

	$B_2O_{2(g)}$	$B_2O_{3(g)}$	$SiO_{(g)}$	$CO_{(g)}$	C	SiC
B	2	2	0	0	0	0
C	0	0	1	1	1	1
O	2	3	0	1	0	0
Si	0	0	1	0	0	1

(372)

The canonical stoichiometric matrix associated with Equation 372 is

	$B_2O_{2(g)}$	$B_2O_{3(g)}$	$SiO_{(g)}$	$CO_{(g)}$	C	SiC
Rx 1	1	−1	0	1	−1	0
Rx 2	0	0	1	−1	2	−1

(373)

The stoichiometric equations are given by Equations 374 and 375 for the canonical stoichiometric matrix in Equation 373.

$$B_2O_{3(g)} + C = B_2O_{2(g)} + CO_{(g)} \tag{374}$$

$$SiC + CO_{(g)} = SiO_{(g)} + 2C \tag{375}$$

III.vi Regime 5: {C, SiO_2, B_4C, $CO_{(g)}$, $SiO_{(g)}$, $B_2O_{3(g)}$, $B_2O_{2(g)}$}

The element abundance matrix using a gas elimination ordering of the species is

	$B_2O_{2(g)}$	$B_2O_{3(g)}$	$SiO_{(g)}$	$CO_{(g)}$	C	SiO_2	B_4C
B	2	2	0	0	0	0	4
C	0	0	1	1	1	0	1
O	2	3	0	1	0	2	0
Si	0	0	1	0	0	1	0

(376)

The canonical stoichiometric matrix associated with Equation 376 is

	$B_2O_{2(g)}$	$B_2O_{3(g)}$	$SiO_{(g)}$	$CO_{(g)}$	C	SiO_2	B_4C
Rx 1	1	0	0	−2	$\frac{5}{2}$	0	$-\frac{1}{2}$

(377)

Rx 2	0	1	0	-3	$\frac{7}{2}$	0	$-\frac{1}{2}$
Rx 3	0	0	1	1	-1	-1	0

The stoichiometric equations are given by Equations 378, 379, and 380 for the canonical stoichiometric matrix in Equation 377.

$$2CO_{(g)} + \frac{1}{2}B_4C = B_2O_{2(g)} + \frac{5}{2}C \tag{378}$$

$$3CO_{(g)} + \frac{1}{2}B_4C = B_2O_{3(g)} + \frac{7}{2}C \tag{379}$$

$$C + SiO_2 = SiO_{(g)} + \frac{1}{2}CO_{(g)} \tag{380}$$

III.vii Regime 6: {C, SiO_2, $CO_{(g)}$, $SiO_{(g)}$, $B_2O_{3(g)}$, $B_2O_{2(g)}$}

The element abundance matrix using a gas elimination ordering of the species is

	$B_2O_{2(g)}$	$B_2O_{3(g)}$	$SiO_{(g)}$	$CO_{(g)}$	C	SiO_2
B	2	2	0	0	0	0
C	0	0	1	1	1	0
O	2	3	0	1	0	2
Si	0	0	1	0	0	1

(381)

The canonical stoichiometric matrix associated with Equation 381 is

	$B_2O_{2(g)}$	$B_2O_{3(g)}$	$SiO_{(g)}$	$CO_{(g)}$	C	SiO_2
Rx 1	1	-1	0	1	-1	0
Rx 2	0	0	1	1	-1	-1

(382)

The stoichiometric equations are given by Equations 383 and 384 for the canonical stoichiometric matrix in Equation 382.

$$B_2O_{3(g)} + C = B_2O_{2(g)} + CO_{(g)} \tag{383}$$

$$C + SiO_2 = SiO_{(g)} + CO_{(g)} \tag{384}$$

III.viii Regime 7: {C, B_4C, $CO_{(g)}$, $SiO_{(g)}$, $B_2O_{3(g)}$, $B_2O_{2(g)}$}

The element abundance matrix using a gas elimination ordering of the species is

	$B_2O_{2(g)}$	$B_2O_{3(g)}$	$SiO_{(g)}$	$CO_{(g)}$	C	B_4C
B	2	2	0	0	0	4
C	0	0	1	1	1	1
O	2	3	0	1	0	0
Si	0	0	1	0	0	0

(385)

The canonical stoichiometric matrix associated with Equation 385 is

	$B_2O_{2(g)}$	$B_2O_{3(g)}$	$SiO_{(g)}$	$CO_{(g)}$	C	B_4C
Rx 1	1	0	0	-2	$\frac{5}{2}$	$-\frac{1}{2}$
Rx 2	0	1	0	-3	$\frac{7}{2}$	$-\frac{1}{2}$

(386)

The stoichiometric equations are given by Equations 387 and 388 for the canonical stoichiometric matrix in Equation 386.

$$2CO_{(g)} + \frac{1}{2}B_4C = B_2O_{2(g)} + \frac{5}{2}C \tag{387}$$

$$3CO_{(g)} + \frac{1}{2}B_4C = B_2O_{3(g)} + \frac{7}{2}C \tag{388}$$

III.ix Regime 8: {C, $CO_{(g)}$, $SiO_{(g)}$, $B_2O_{3(g)}$, $B_2O_{2(g)}$}

The element abundance matrix using a gas elimination ordering of the species is

	$B_2O_{2(g)}$	$B_2O_{3(g)}$	$SiO_{(g)}$	$CO_{(g)}$	C
B	2	2	0	0	0
C	0	0	1	1	1

(389)

O	2	3	0	1	0
Si	0	0	1	0	0

The canonical stoichiometric matrix associated with Equation 389 is

	$B_2O_{2(g)}$	$B_2O_{3(g)}$	$SiO_{(g)}$	$CO_{(g)}$	C
Rx 1	1	−1	0	1	−1

(390)

The stoichiometric equation is given by Equation 391 for the canonical stoichiometric matrix in Equation 390.

$$B_2O_{3(g)} + C = B_2O_{2(g)} + CO_{(g)} \tag{391}$$

III.x Regime 9: {SiC, SiO_2, B_4C, $CO_{(g)}$, $SiO_{(g)}$, $B_2O_{3(g)}$, $B_2O_{2(g)}$}

The element abundance matrix using a gas elimination ordering of the species is

	$B_2O_{2(g)}$	$B_2O_{3(g)}$	$SiO_{(g)}$	$CO_{(g)}$	SiC	SiO_2	B_4C
B	2	2	0	0	0	0	4
C	0	0	1	1	1	0	1
O	2	3	0	1	0	2	0
Si	0	0	1	0	1	1	0

(392)

The canonical stoichiometric matrix associated with Equation 392 is

	$B_2O_{2(g)}$	$B_2O_{3(g)}$	$SiO_{(g)}$	$CO_{(g)}$	SiC	SiO_2	B_4C
Rx 1	1	0	0	$-\frac{1}{3}$	$\frac{5}{6}$	$-\frac{5}{6}$	$-\frac{1}{2}$
Rx 2	0	1	0	$-\frac{2}{3}$	$\frac{7}{6}$	$-\frac{7}{6}$	$-\frac{1}{2}$
Rx 3	0	0	1	$\frac{1}{3}$	$-\frac{1}{3}$	$-\frac{2}{3}$	0

(393)

The stoichiometric equations are given by Equations 394, 395, and 396 for the canonical stoichiometric matrix in Equation 393.

$$\frac{1}{3}CO_{(g)} + \frac{5}{6}SiO_2 + \frac{1}{2}B_4C = B_2O_{2(g)} + \frac{5}{6}SiC \tag{394}$$

$$\frac{2}{3}CO_{(g)} + \frac{7}{6}SiO_2 + \frac{1}{2}B_4C = B_2O_{3(g)} + \frac{7}{6}SiC \tag{395}$$

$$\frac{1}{3}SiC + \frac{2}{3}SiO_2 = SiO_{(g)} + \frac{1}{3}CO_{(g)} \tag{396}$$

III.xi Regime 10: {SiC, SiO_2, $CO_{(g)}$, $SiO_{(g)}$, $B_2O_{3(g)}$, $B_2O_{2(g)}$}

The element abundance matrix using a gas elimination ordering of the species is

	$B_2O_{2(g)}$	$B_2O_{3(g)}$	$SiO_{(g)}$	$CO_{(g)}$	SiC	SiO_2
B	2	2	0	0	0	0
C	0	0	1	1	1	0
O	2	3	0	1	0	2
Si	0	0	1	0	1	1

(397)

The canonical stoichiometric matrix associated with Equation 397 is

	$B_2O_{2(g)}$	$B_2O_{3(g)}$	$SiO_{(g)}$	$CO_{(g)}$	SiC	SiO_2
Rx 1	1	-1	0	$\frac{1}{3}$	$-\frac{1}{3}$	$\frac{1}{3}$
Rx 2	0	0	1	$\frac{1}{3}$	$-\frac{1}{3}$	$-\frac{2}{3}$

(398)

The stoichiometric equations are given by Equations 399 and 400 for the canonical stoichiometric matrix in Equation 398.

$$B_2O_{3(g)} + \frac{1}{3}SiC = B_2O_{2(g)} + \frac{1}{3}CO_{(g)} + \frac{1}{3}SiO_2 \tag{399}$$

$$\frac{1}{3}SiC + \frac{2}{3}SiO_2 = SiO_{(g)} + CO_{(g)} \tag{400}$$

III.xii Regime 11: {SiC, B_4C, $CO_{(g)}$, $SiO_{(g)}$, $B_2O_{3(g)}$, $B_2O_{2(g)}$}

The element abundance matrix using a gas elimination ordering of the species is

	$B_2O_{2(g)}$	$B_2O_{3(g)}$	$SiO_{(g)}$	$CO_{(g)}$	SiC	B_4C
B	2	2	0	0	0	4
C	0	0	1	1	1	1
O	2	3	0	1	0	0
Si	0	0	1	0	1	0

(401)

The canonical stoichiometric matrix associated with Equation 401 is

	$B_2O_{2(g)}$	$B_2O_{3(g)}$	$SiO_{(g)}$	$CO_{(g)}$	SiC	B_4C
Rx 1	1	0	$-\frac{5}{4}$	$-\frac{3}{4}$	$\frac{5}{4}$	$-\frac{1}{2}$
Rx 2	0	1	$-\frac{7}{4}$	$-\frac{5}{4}$	$\frac{7}{4}$	$-\frac{1}{2}$

(402)

The stoichiometric equations are given by Equations 403 and 404 for the canonical stoichiometric matrix in Equation 402.

$$\frac{5}{4}SiO_{(g)} + \frac{3}{4}CO_{(g)} + \frac{1}{2}B_4C = B_2O_{2(g)} + \frac{5}{4}SiC \tag{403}$$

$$\frac{7}{4}SiO_{(g)} + \frac{5}{4}CO_{(g)} + \frac{1}{2}B_4C = B_2O_{3(g)} + \frac{7}{4}SiC \tag{404}$$

III.xiii Regime 12: {SiC, $CO_{(g)}$, $SiO_{(g)}$, $B_2O_{3(g)}$, $B_2O_{2(g)}$}

The element abundance matrix using a gas elimination ordering of the species is

	$B_2O_{2(g)}$	$B_2O_{3(g)}$	$SiO_{(g)}$	$CO_{(g)}$	SiC
B	2	2	0	0	0
C	0	0	1	1	1
O	2	3	0	1	0
Si	0	0	1	0	1

(405)

The canonical stoichiometric matrix associated with Equation 405 is

	$B_2O_{2(g)}$	$B_2O_{3(g)}$	$SiO_{(g)}$	$CO_{(g)}$	SiC
Rx 1	1	-1	$\frac{1}{2}$	$\frac{1}{2}$	$-\frac{1}{2}$

(406)

The stoichiometric equation is given by Equation 407 for the canonical stoichiometric matrix in Equation 406.

$$B_2O_{3(g)} + \frac{1}{2}SiC = B_2O_{2(g)} + \frac{1}{2}SiO_2 + \frac{1}{2}CO_{(g)} \tag{407}$$

III.xiv Regime 13: {SiO_2, B_4C, $CO_{(g)}$, $SiO_{(g)}$, $B_2O_{3(g)}$, $B_2O_{2(g)}$}

The element abundance matrix using a gas elimination ordering of the species is

	$B_2O_{2(g)}$	$B_2O_{3(g)}$	$SiO_{(g)}$	$CO_{(g)}$	SiO_2	B_4C
B	2	2	0	0	0	4
C	0	0	1	1	0	1
O	2	3	0	1	2	0
Si	0	0	1	0	1	0

(408)

The canonical stoichiometric matrix associated with Equation 408 is

	$B_2O_{2(g)}$	$B_2O_{3(g)}$	$SiO_{(g)}$	$CO_{(g)}$	SiO_2	B_4C
Rx 1	1	0	$\frac{5}{2}$	$\frac{1}{2}$	$-\frac{5}{2}$	$-\frac{1}{2}$
Rx 2	0	1	$\frac{7}{2}$	$\frac{1}{2}$	$-\frac{7}{2}$	$-\frac{1}{2}$

(409)

The stoichiometric equations are given by Equations 410 and 411 for the canonical stoichiometric matrix in Equation 409.

$$\frac{5}{2}SiO_2 + \frac{1}{2}B_4C = B_2O_{2(g)} + \frac{5}{2}SiO_{(g)} + \frac{1}{2}CO_{(g)} \tag{410}$$

$$\frac{7}{2}SiO_2 + \frac{1}{2}B_4C = B_2O_{3(g)} + \frac{7}{2}SiO_{(g)} + \frac{1}{2}CO_{(g)} \tag{411}$$

III.xv Regime 14: {SiO_2, $CO_{(g)}$, $SiO_{(g)}$, $B_2O_{3(g)}$, $B_2O_{2(g)}$}

The element abundance matrix using a gas elimination ordering of the species is

	$B_2O_{2(g)}$	$B_2O_{3(g)}$	$SiO_{(g)}$	$CO_{(g)}$	SiO_2
B	2	2	0	0	0
C	0	0	1	1	0
O	2	3	0	1	2
Si	0	0	1	0	1

(412)

The canonical stoichiometric matrix associated with Equation 412 is

	$B_2O_{2(g)}$	$B_2O_{3(g)}$	$SiO_{(g)}$	$CO_{(g)}$	SiO_2
Rx 1	1	−1	−1	0	−1

(413)

The stoichiometric equation is given by Equation 414 for the canonical stoichiometric matrix in Equation 413.

$$B_2O_{3(g)} + SiO_{(g)} = B_2O_{2(g)} + SiO_2 \tag{414}$$

III.xvi Regime 15: {B_4C, $CO_{(g)}$, $SiO_{(g)}$, $B_2O_{3(g)}$, $B_2O_{2(g)}$}

The element abundance matrix using a gas elimination ordering of the species is

	$B_2O_{2(g)}$	$B_2O_{3(g)}$	$SiO_{(g)}$	$CO_{(g)}$	B_4C
B	2	2	0	0	4
C	0	0	1	1	1
O	2	3	0	1	0
Si	0	0	1	0	0

(415)

The canonical stoichiometric matrix associated with Equation 415 is

	$B_2O_{2(g)}$	$B_2O_{3(g)}$	$SiO_{(g)}$	$CO_{(g)}$	B_4C
Rx 1	1	$-\frac{5}{7}$	0	$\frac{1}{7}$	$-\frac{1}{7}$

(416)

The stoichiometric equation is given by Equation 417 for the canonical stoichiometric matrix in Equation 416.

$$\frac{5}{7}B_2O_{3(g)} + \frac{1}{7}B_4C = B_2O_{2(g)} + \frac{1}{7}CO_{(g)} \tag{417}$$

III.xvii Regime 16: {$CO_{(g)}$, $SiO_{(g)}$, $B_2O_{3(g)}$, $B_2O_{2(g)}$}

The element abundance matrix using a gas elimination ordering of the species is

	$B_2O_{2(g)}$	$B_2O_{3(g)}$	$SiO_{(g)}$	$CO_{(g)}$
B	2	2	0	0
C	0	0	1	1
O	2	3	0	1
Si	0	0	1	0

(418)

The canonical stoichiometric matrix, in Equation 419, is empty because the columns of the associated element abundance matrix, in Equation 418, are linearly independent.

	$B_2O_{2(g)}$	$B_2O_{3(g)}$	$SiO_{(g)}$	$CO_{(g)}$
Rx 1	No Feasible Reactions			

(419)

Since there are no feasible reactions among the species assumed present in this chemical regime, any species composition is considered to be at equilibrium.

Appendix IV. Thermodynamic Data

In order to calculate the thermodynamic chemical equilibrium composition of a closed system it is necessary to have the thermodynamic and material properties associated with the species being modeled in the system. The sections in this appendix describe how a thermodynamic database can be imported into a useful data structure , demonstrate its use to build functions need for calculating chemical equilibrium, and provide a subset of the database for species considered in this thesis. This data structure and associated methods were used throughout this thesis whenever the value of an equilibrium constant for an associated stoichiometric equation is needed.

IV.i Database Import and Data Structure

Thermodynamic data used for equilibrium calculations was obtained from the NASA STI Program at http://www.sti.nasa.gov. The import format for the database is provided by Zehe *et al*. (2002).[74] To obtain the raw database file, a direct request must be made to the NASA STI Program. A flow chart outlining the creation of the thermodynamic and material property data structure is shown in Figure 10-1.

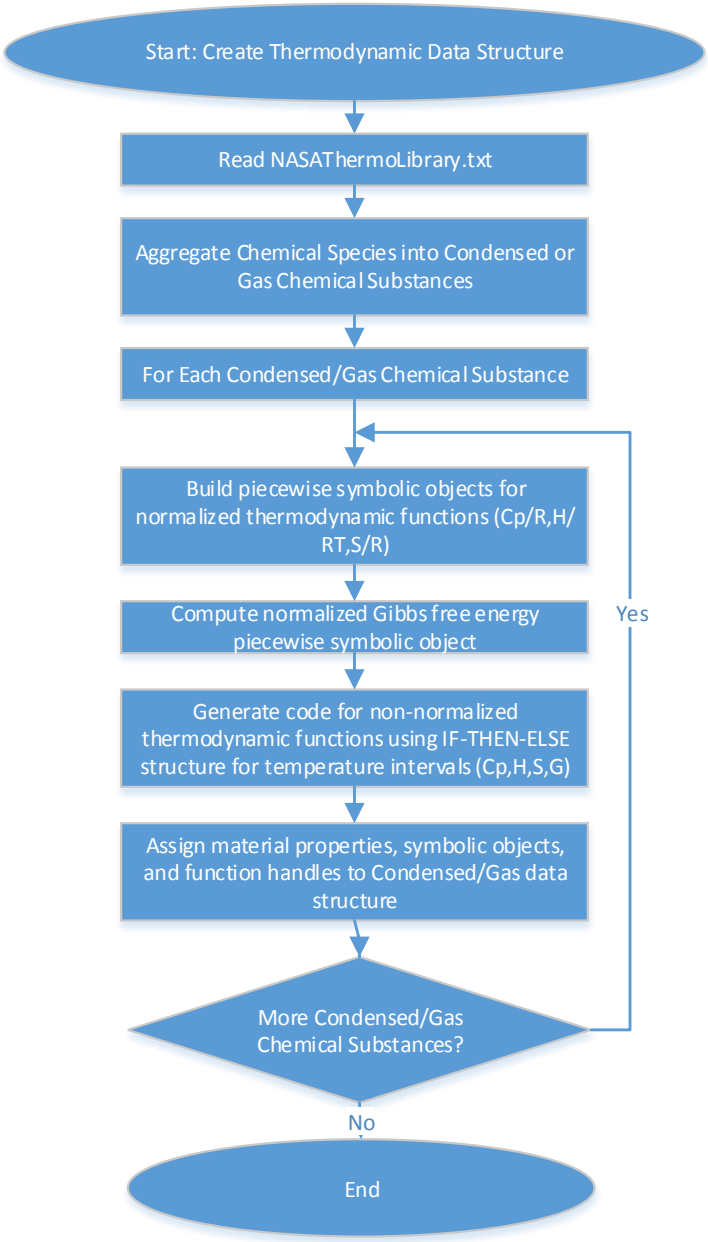

Figure 10-1: Thermodynamic data structure flowchart.

The database file separates the gas and condensed forms of all the chemical substances into separate groups. A sample excerpt from the database file for all condensed forms of the chemical substance SiO_2 is shown in Figure 10-2.

```
SiO2(a-qz)        Alpha-quartz,hexagonal. Gurvich,1991 pt1 p250 pt2 p228.
 1 tpis91 SI  1.000   2.00     0.00     0.00     0.00 1   60.0843000    -910700.000
    200.000    848.0007 -2.0 -1.0  0.0  1.0  2.0  3.0  4.0  0.0          6916.000
-5.776895500D+05 7.214661110D+03-3.145730294D+01 7.412177150D-02-8.670077820D-06
-1.080461312D-07 8.316324910D-11                -1.462398375D+05 1.842424399D+02
SiO2(b-qz)        Beta-quartz,hexagonal. Gurvich,1991 pt1 p250 pt2 p228.
 1 tpis91 SI  1.000   2.00     0.00     0.00     0.00 2   60.0843000    -910700.000
    848.000   1200.0007 -2.0 -1.0  0.0  1.0  2.0  3.0  4.0  0.0          6916.000
 2.317635074D+04 0.000000000D+00 7.026511484D+00 1.241925261D-03 0.000000000D+00
 0.000000000D+00 0.000000000D+00                -1.117012474D+05-3.580751356D+01
SiO2(b-crt)       Beta-cristobalite,cubic. Gurvich,1991 pt1 p250 pt2 p228.
 1 tpis91 SI  1.000   2.00     0.00     0.00     0.00 3   60.0843000    -910700.000
   1200.000   1996.0007 -2.0 -1.0  0.0  1.0  2.0  3.0  4.0  0.0          6916.000
-5.356419079D+05 0.000000000D+00 9.331036946D+00-7.306503931D-04 3.339944266D-07
 0.000000000D+00 0.000000000D+00                -1.134326721D+05-4.998768383D+01
SiO2(L)           Liquid. Gurvich,1991 pt1 p250 pt2 p228.
 1 tpis91 SI  1.000   2.00     0.00     0.00     0.00 4   60.0843000    -910700.000
   1996.000   6000.0007 -2.0 -1.0  0.0  1.0  2.0  3.0  4.0  0.0          6916.000
 0.000000000D+00 0.000000000D+00 1.004268442D+01 0.000000000D+00 0.000000000D+00
 0.000000000D+00 0.000000000D+00                -1.140002976D+05-5.554279592D+01
```

Figure 10-2: All data for condensed forms of SiO_2 from the NASA thermodynamic database.

The import format for the thermodynamic database file is shown in Figure 10-3.

Record	Contents	Fortran format	Columns
1	Species name or formula Comments and data source	A16 A62	1 to 16 19 to 80
2	Number of T intervals Optional identification code Chemical formula—symbols and numbers (all capitals) Zero for gas, nonzero for condensed Molecular weight Heat of formation at 298.15 K, J/mol	I2 A6 5(A2, F6.2) I2 F13.7 F15.5	1 to 2 4 to 9 11 to 50 51 to 52 53 to 65 66 to 80
3	Temperature range Number of coefficients for $C_p^o(T)/R$ T exponents in empirical equation for $C_p^o(T)/R$ $[H^o(298.15) - H^o(0)]$, J/mol	2F11.3 I1 8F5.1 F15.3	1 to 22 23 24 to 63 66 to 80
4	First five coefficients for $C_p^o(T)/R$	5D16.9	1 to 80
5	Last two coefficients for $C_p^o(T)/R$ Integration constants b_1 and b_2	2D16.9 2D16.9	1 to 32 49 to 80
– –	Repeat 3, 4, and 5 for each interval	– – – –	– – – – –

Figure 10-3: NASA thermodynamic database file import format.

The functional form of the thermodynamic properties, supplied by the NASA database, for the normalized specific heat, enthalpy and entropy are

$$\frac{C_p^\circ(T)}{R} = a_1T^{-2} + a_2T^{-1} + a_3 + a_4T + a_5T^2 + a_6T^3 + a_7T^4 \tag{420}$$

$$\frac{H^{\circ}(T)}{RT} = -a_1 T^{-2} + \frac{a_2 \ln(T)}{T} + a_3 + \frac{a_4 T}{2} + \frac{a_5 T^2}{3} + \frac{a_6 T^3}{4} + \frac{a_7 T^4}{5} + \frac{b_1}{T} \tag{421}$$

$$\frac{S^{\circ}(T)}{R} = -\frac{a_1 T^{-2}}{2} - a_2 T^{-1} + a_3 \ln T + a_4 T + \frac{a_5 T^2}{2} + \frac{a_6 T^3}{3} + \frac{a_7 T^4}{4} + b_2 \tag{422}$$

, respectively. Each equation is a function of temperature, *T*, in Kelvin and normalized by the gas constant, *R*, or *RT* to yield a unit independent value.

The normalized Gibbs free energy is generated by

$$\frac{G^{\circ}(T)}{RT} = \frac{H^{\circ}(T)}{RT} - \frac{S^{\circ}(T)}{R} \tag{423}$$

The specific heat for the alpha quartz phase of SiO_2 valid between 200 K and 848 K is

$$\begin{aligned} \frac{C_p^{\circ}(T)}{R} = {} & -5.77689500 \times 10^5 \times T^{-2} - 7.214661110 \times 10^3 \times T^{-1} \\ & - 3.145730294 \times 10 + 7.412177150 \times 10^{-2} \times T \\ & - 8.670077820 \times 10^{-6} \times T^2 \\ & - 1.080461312 \times 10^{-7} \times T^3 + 8.316324910 \\ & \times 10^{-11} \times T^4 \end{aligned} \tag{424}$$

The thermodynamic properties of the condensed phases of SiO_2 vary continuously from 200 K to 6000 K. Only one condensed phase of SiO_2 is stable at a given temperature. This is reflected by the piecewise structure of functions in the database. The continuous transition between the most stable phases of a condensed chemical substance allows, for each property, a single piecewise thermodynamic function labeled by the condensed chemical substance to represent all the phases.

A symbolic programming language or computer algebra system can be used to define piecewise expressions over different domains of an independent variable. The MuPad symbolic

programming engine provided by the MATLAB symbolic toolbox is used to generate piecewise symbolic expressions. The raw NASA data file is imported and converted to a form that can be evaluated by the symbolic engine. The form of the MATLAB input and output generated for the piecewise expression for the normalized specific heat of the condensed species SiO_2 is shown in Figure 10-4 and Figure 10-5, respectively.

```
SiO2.Cp_R = evalin(symengine,'piecewise([x<=200,3.92],[6000<x,10.0426844],[200<x<=
        848,0.0741217715*x + 7214.66111/x - 577689.55/x^2 - 0.00000867007782*x^2 -
        0.000000108046131*x^3 + 0.0000000000831632491*x^4 - 31.4573029],[848< x<=
        1200,0.00124192526*x + 23176.3507/x^2 + 7.02651148],[1200<x<=
        1996,0.000000333994427*x^2 - 535641.908/x^2 - 0.000730650393*x + 9.33103695],
        [1996<x<=6000,10.0426844]')
```

Figure 10-4: MATLAB input to create a piecewise symbolic expression for normalized specific heat for condensed SiO2.

```
SiO2.Cp_R = piecewise([x <= 200,3.92],[6000 < x,10.0426844],[x in Dom::Interval(200,
        [848]),0.0741217715*x + 7214.66111/x - 577689.55/x^2 - 0.00000867007782*x^2 -
        0.000000108046131*x^3 + 0.0000000000831632491*x^4 - 31.4573029],[x in
        Dom::Interval(848,[1200]),0.00124192526*x + 23176.3507/x^2 + 7.02651148],[x in
        Dom::Interval(1200,[1996]),0.000000333994427*x^2 - 535641.908/x^2 -
        0.000730650393*x + 9.33103695],[x in Dom::Interval(1996,[6000]),10.0426844])
```

Figure 10-5: MATLAB output for the piecewise symbolic expression for normalized specific heat for condensed SiO2.

The output into MATLAB is a structure variable, *'SiO2'*, where the value of the MuPad expression is assigned to the field *'Cp_R'*. The independent variable for temperature is represented by the symbolic variable 'x*'.* The value of the function at the minimum or maximum defined temperature is used if the function is evaluated outside the range defined by the database. This is done to avoid errors that may arise from extrapolating outside of the fitting domain. The enthalpy and entropy for SiO_2 can be defined in a similar manner as *'Cp_R'* and are assigned to the fields '*H_RT*' and '*S_R*', respectively.

Using Equation 423, the normalized Gibbs free energy can be calculated using the normalized enthalpy and entropy and assigned to the field *'G_RT'*. The MATLAB input and output is shown in Figure 10-6 and Figure 10-7, respectively.

```
SiO2.G_RT = SiO2.H_RT - SiO2.S_R
```

Figure 10-6: MATLAB input to calculate the normalized Gibbs free energy.

```
SiO2.G_RT = piecewise([x <= 200,-553.0949],[6000 < x,-40.7811],[x in Dom::Interval(200,[848]),
    31.4573029*log(x) - 0.0370608857*x + (7214.66111*log(x))/x - 139025.17589/x +
    288844.775/x^2 + 0.00000144501297*x^2 + 0.0000000090038443*x^3 -
    0.0000000000041581625*x^4 - 215.6997429],[x in Dom::Interval(848,
    [1200]),42.83402508 - 7.02651148*log(x) - 111701.247/x - 11588.1753/x^2 -
    0.000620962629*x],[x in Dom::Interval(1200,[1996]),0.000365325196*x - 9.33103695
    *log(x) - 113432.672/x + 267820.954/x^2 - 0.000000055665737*x^2 + 59.31872075],
    [x in Dom::Interval(1996,[6000]),65.5854803 - 114000.298/x - 10.0426844*log(x)])
```

Figure 10-7: MATLAB output for the calculated normalized Gibbs free energy.

Once the base expressions are created, very complicated expressions can easily be created by applying simple operations to these base expressions. It is important to note that the 'log' function in MuPad objects and MATLAB refers to the natural logarithm function, usually denoted by 'ln'.

Code generation functions were written to interpret piecewise symbolic expressions and generate numeric functions that can be compiled and executed by MATLAB without requiring recourse to the MuPad symbolic expression. The code generation functions recast the symbolic expression as an IF-THEN-ELSE structure to evaluate the thermodynamic expression for the correct temperature interval. An example of the generated code corresponding to the non-normalized Gibbs free energy for condensed SiO_2 is shown in Figure 10-8.

```
function T = SiO2(x)
len = length(x);
T = zeros(len,1);
for i=1:len;
  if (x(i) <= 2.0E2)
    T(i)=x(i)*-4.598690953203E3;
  else
    if (6.0E3 < x(i))
        T(i)=x(i)*-3.39073232517E2;
      else
        if ((2.0E2 < x(i)) && (x(i) <= 8.48E2))
          T(i)=x(i)*(x(i)*-3.70608857E-2+log(x(i))*3.14573029E1+(log(x(i))*7.21466111E3)...
                  /x(i)-1.3902517589E5/x(i)+1.0/(x(i)*x(i))*2.88844775E5+(x(i)*x(i))...
                  *1.44501297E-6+(x(i)*x(i)*x(i))*9.0038443E-9-(x(i)*x(i)*x(i)*x(i))...
                  *4.1581625E-12-2.156997429E2)*8.31447;
        else
          if ((8.48E2 < x(i)) && (x(i) <= 1.2E3))
            T(i)=x(i)*(x(i)*6.20962629E-4+log(x(i))*7.02651148+1.11701247E5/x(i)+1.0/...
                  (x(i)*x(i))*1.15881753E4-4.283402508E1)*(-8.31447);
          else
            if ((1.2E3 < x(i)) && (x(i) <= 1.996E3))
                T(i)=x(i)*(x(i)*3.65325196E-4-log(x(i))*9.33103695-1.13432672E5/x(i)+...
                  1.0/(x(i)*x(i))*2.67820954E5-(x(i)*x(i))*5.5665737E-8+5.931872075E1)*8.31447;
            else
              if ((1.996E3 < x(i)) && (x(i) <= 6.0E3))
                T(i)=x(i)*(log(x(i))*1.00426844E1+1.14000298E5/x(i)-6.55854803E1)*(-8.31447);
              else
                T(i)=NaN;
end;end;end;end;end;end;end;
```

Figure 10-8: Gibbs free energy function for condensed SiO_2. Code generated from the piecewise symbolic MuPad object for the non-normalized Gibbs free energy. Input: x (K). Output: T ($J \cdot mol^{-1} \cdot K^{-1}$).

Each condensed and gas chemical substance from the database is stored as a MATLAB structure with fields to store the information provided by the database, symbolic and numeric functions built from the database information, and additional fields to store material properties needed for the gas transport simulation. An example of the MATLAB structure built for the condensed phases of SiO_2 is shown in Figure 10-9.

```
SiO2 =

        Name: 'SiO2'
       Tints: 4
          MM: 60.0843
       Phase: 'Condensed'
      TRange: [200 848 1200 1996 6000]
        Cp_R: [1x1 sym]
        H_RT: [1x1 sym]
         S_R: [1x1 sym]
        G_RT: [1x1 sym]
     Density: 2200
    Diameter: []
     RedTemp: []
           G: @SiO2
           H: @SiO2
           S: @SiO2
          Cp: @SiO2
```

Figure 10-9: MATLAB structure built for the condensed phases of SiO_2.

The fields *'Name'*, *'Tints'*, *'MM'*, *'Phase'*, and *'TRange'* represent the species name, the number of temperature intervals, the molar mass ($g \cdot mol^{-1}$), an indicator whether the substance is in the *'Condensed'* or *'Gas'* state, and an array of temperatures (K) for the boundary of each interval, respectively. The fields *'Cp_R'*, *'H_RT'*, *'S_R'*, and *'G_RT'* are the piecewise symbolic objects representing the normalized thermodynamic functions built from the database. The fields *'G'*, *'H'*, *'S'*, and *'Cp'* are function handles used to numerically evaluate the non-normalized thermodynamic functions at a specific temperature, where the gas constant used is $R = 8.31447\ \mathrm{J/(mol \cdot K)}$; the field *'SiO2.*G' is a function handle to the function in Figure 10-8. Lastly, the fields '*Density'*, *'Diameter'*, '*RedTemp'* are used to store the density of substance ($kg \cdot m^{-3}$), the hard sphere diameter of a gas molecule (m), and the reduced temperature of the interaction potential energy (K), respectively; if applicable to the phase. The last set of fields are properties not provided by the database and the user is prompted to provide them before executing a gas flow simulation.

IV.ii Data Structure Usage

Once the import procedure is repeated for all gas and condensed species in the database, these objects can be grouped into arrays and/or matrices. This allows them to be operated on by mathematical functions or by using linear algebra techniques, while maintaining their piecewise structure. A useful extension is to generate ΔG_{rx} for an equilibrium stoichiometric reaction. Using the relationship $\Delta G_{rx} = -RT\ln(K_{eq})$, it is then possible to compute the expression for the equilibrium constant, K_{eq}, of the reaction.

A simple example is for the formation of $CO_{(g)}$ and SiC from C and SiO_2. A stoichiometric equation for this reaction is

$$\frac{3}{2}C + \frac{1}{2}SiO_2 = CO_{(g)} + \frac{1}{2}SiC \tag{425}$$

and the associated Gibbs free energy of reaction is

$$\Delta G_{rx} = G_{CO} + \frac{1}{2}G_{SiC} - \frac{3}{2}G_C - \frac{1}{2}G_{SiO_2} \tag{426}$$

The equilibrium constant for this reaction is

$$K_{eq} = \frac{p_{CO}a_{SiC}^{\frac{1}{2}}}{a_C^{\frac{3}{2}}a_{SiO_2}^{\frac{1}{2}}} \tag{427}$$

Assuming that all of the condensed species are present and ideal (*i.e.* $a_i \equiv 1$), then the equilibrium constant expression yields the equilibrium partial pressure of $CO_{(g)}$:

$$\frac{K_{eq}a_C^{\frac{3}{2}}a_{SiO_2}^{\frac{1}{2}}}{a_{SiC}^{\frac{1}{2}}} = p_{CO} \rightarrow K_{eq} = p_{CO} \tag{428}$$

The normalized Gibbs free energy for a collection of species can be grouped into a column array. Assuming data structures for *'C.G_RT'*, *'COg.G_RT'*, and *'SiC.G_RT'* exist in addition to *'SiO2.G_RT'*, a sequence of MATLAB instructions can be used to form $K_{eq}$for the reaction. Figure 10-10 shows the MATLAB input needed to construct the equilibrium constant.

```
G_RT = [C.G_RT; SiO2.G_RT; COg.G_RT; SiC.G_RT]
Coefficients = [-3/2 -1/2 1 1/2]
deltaG_RT = Coefficients * G_RT
Keq = exp(-deltaG_RT)
```

Figure 10-10: MATLAB input to create the piecewise symbolic expression for the equilibrium constant, Keq. The column array of piecewise symbolic Gibbs free energies, row array of stoichiometric coefficients, and Gibbs free energy of reaction are given by G_RT, Coefficients, and deltaG_RT, respectively.

The MATLAB computations for constructing K_{eq} respect the piecewise nature of the variables, creating new temperature intervals for the overall reaction when the intervals defined for the individual species do not coincide. The MATLAB output for the Keq consists of 13 temperature intervals that continuously represent K_{eq} from 100 K to 20,000 K and is shown in Figure 10-11.

```
Keq = piecewise([x <= 100,4.5074237767257405956221383436594e-62],[20000 <
      x,44911300.38500550908807647251600 9],[x in Dom::Interval(200,[298.15]), exp
      (0.01533103062*x + 0.704960739*log(x) + (928.926629*log(x))/x - 41147.295981/x +
      66331.983075/x^2 - 0.000022382646415*x^2 + 0.0000000171316316*x^3 -
      0.000000000005281878378*x^4 + 9.372669686)],[x in Dom::Interval(100,[200]), exp
      (0.00317886769*x - 0.267455031*log(x) + 4596.58745/x - 571.374095/x^2 -
      186.249479294)],[x in Dom::Interval(298.15,[600]), exp(0.013022599075*x +
      2.85105925*log(x) + (928.926629*log(x))/x - 40510.544631/x + 35175.69062/x^2 -
      0.0000225177014775*x^2 + 0.000000171425111748*x^3 -
      0.000000000005281878378*x^4 - 3.9401422)],[x in Dom::Interval(600,[848]), exp
      (12.908559235*log(x) - 0.019134497165*x + (4.766594*log(x))/x - 33874.307406/x -
      131560.38238/x^2 + 0.0000025545757605*x^2 + 0.000000003669536 5488*x^3 -
      0.000000000001931997137 25*x^4 - 56.277267685)],[x in Dom::Interval(848,[1000]),
      exp(0.0000018320692755*x^2 - 6.333347955*log(x) - (3602.563961*log(x))/x -
      20212.342961/x - 281776.85753/x^2 - 0.0009145356295*x -
      0.000000008323856012*x^3 + 0.000000000000014708411275*x^4 +
      72.989616305)],[x in Dom::Interval(1000,[1200]), exp(0.0028903677485*x -
      6.141160945*log(x) - (1950.087695*log(x))/x - 29124.924415/x - 58262.2212/x^2 -
      0.0000005727895988*x^2 + 0.000000000 7257991516*x^3 -
      0.000000000000004264874572*x^4 + 66.782539545)],[x in Dom::Interval(1200,
      [1996]), exp(0.003383511661*x - 7.29342368*log(x) - (1950.087695*log(x))/x -
      29990.636915/x + 81442.34345/x^2 - 0.0000006006224673*x^2 +
      0.000000000 7257991516*x^3 - 0.000000000000004264874572*x^4 +
      75.02488738)],[x in Dom::Interval(1996,[2000]), exp(0.003200849063*x -
      7.649247405*log(x) - (1950.087695*log(x))/x - 30274.449915/x - 52468.13355/x^2 -
      0.0000005727895988*x^2 + 0.000000000 7257991516*x^3 -
      0.000000000000004264874572*x^4 + 78.158267155)],[x in Dom::Interval(2000,
      [3105]), exp(0.0007247575829*x - 2.77640379*log(x) + (237.350995*log(x))/x -
      40290.99585/x + 47499.31245/x^2 - 0.0000012760069505*x^2 +
      0.000000000 1027341484*x^3 + 0.000000000000000002308890815*x^4 +
      41.39155714)],[x in Dom::Interval(3105,[6000]), exp((237.350995*log(x))/x -
      0.866489675*log(x) - 0.0001456785621*x - 41630.60515/x + 79226.979/x^2 +
      0.0000000 745436745*x^2 - 0.000000000000060615996*x^3 +
      0.000000000000000002308890815*x^4 + 28.189654925)],[x in Dom::Interval(6000,
      [20000]), exp(249.547498*log(x) - 0.0197817555*x + (750037.784*log(x))/x -
      4951383.346/x + 443433148/x^2 + 0.00000054962868*x^2 -
      0.000000000 0109867495*x^3 + 0.000000000000000000 99946897*x^4 -
      2331.023088)])
```

Figure 10-11: MATLAB output for the piecewise symbolic expression representing the equilibrium constant, Keq, for stoichiometric reaction given by Equation 425.

The symbolic expression assigned to '*Keq*' is converted to the MATLAB function named Keq with an IF-THEN-ELSE structure for numeric evaluation of the piecewise defined equilibrium constant, shown in Figure 10-12.

```
function T = Keq(x)%#codegen
len=length(x);
T=zeros(len,1);
for i=1:len;
  if (x(i) <= 1.0E2)
    T(i)=4.507423776725741E-62;
  else
    if (2.0E4 < x(i))
      T(i)=4.491130038500551E7;
    else
      if ((x(i) <= 2.9815E2) && (2.0E2 < x(i)))
        T(i)=exp(x(i)^1.533103062E-2+log(x(i))^7.04960739E-1+(log(x(i))^9.28926629E2)...
            /x(i)-4.1147295981E4/x(i)+1.0/(x(i)*x(i))*6.6331983075E4-(x(i)*x(i))*...
            2.2382646415E-5+(x(i)*x(i)*x(i))^1.71316316E-8-(x(i)*x(i)*x(i)*x(i))...
            ^5.281878378E-12+9.372669686);
      else
        if ((1.0E2 < x(i)) && (x(i) <= 2.0E2))
          T(i)=exp(x(i)^3.17886769E-3-log(x(i))^2.67455031E-1+4.59658745E3/x(i)...
              -1.0/(x(i)*x(i))^5.71374095E2-1.86249479294E2);
        else
          if ((2.9815E2 < x(i)) && (x(i) <= 6.0E2))
            T(i)=exp(x(i)^1.3022599075E-2+log(x(i))^2.85105925+(log(x(i))^9.28926629E2)/...
                x(i)-4.0510544631E4/x(i)+1.0/(x(i)*x(i))^3.517569062E4-(x(i)*x(i))*...
                2.25177014775E-5+(x(i)*x(i)*x(i))^1.7142511174E-8-(x(i)*x(i)*x(i)*x(i))*...
                5.281878378E-12-3.9401422);
          else
            if ((6.0E2 < x(i)) && (x(i) <= 8.48E2))
              T(i)=exp(x(i)^-1.9134497165E-2+log(x(i))^1.2908559235E1+(log(x(i))^4.766594)/x(i)...
                  -3.3874307406E4/x(i)-1.0/(x(i)*x(i))^1.3156038238E5+(x(i)*x(i))*...
                  2.5545757605E-6+(x(i)*x(i)*x(i))^3.6695365488E-9-(x(i)*x(i)*x(i)*x(i))*...
                  1.93199713725E-12-5.6277267685E1);
            else
              if ((8.48E2 < x(i)) && (x(i) <= 1.0E3))
                T(i)=exp(x(i)^-9.145356295E-4-log(x(i))^6.333347955-(log(x(i))^3.602563961E3)/...
                    x(i)-2.0212342961E4/x(i)-1.0/(x(i)*x(i))^2.8177685753E5+(x(i)*x(i))*...
                    1.8320692755E-6-(x(i)*x(i)*x(i))^8.323856012E-10+(x(i)*x(i)*x(i)*x(i))...
                    ^1.4708411275E-13+7.2989616305E1);
              else
                if ((1.0E3 < x(i)) && (x(i) <= 1.2E3))
                  T(i)=exp(x(i)^2.8903677485E-3-log(x(i))^6.141160945-(log(x(i))^1.950087695E3)...
                      /x(i)-2.9124924415E4/x(i)-1.0/(x(i)*x(i))^5.82622212E4-(x(i)*x(i))^5.727895988E-7...
                      +(x(i)*x(i)*x(i))^7.257991516E-11-(x(i)*x(i)*x(i)*x(i))^4.264874572E-15+6.6782539545E1);
                else
                  if ((1.2E3 < x(i)) && (x(i) <= 1.996E3))
                    T(i)=exp(x(i)^3.383511661E-3-log(x(i))^7.29342368-(log(x(i))^1.950087695E3)/x(i)...
                        -2.9990636915E4/x(i)+1.0/(x(i)*x(i))^8.144234345E4-(x(i)*x(i))^6.006224673E-7...
                        +(x(i)*x(i)*x(i))^7.257991516E-11-(x(i)*x(i)*x(i)*x(i))^4.264874572E-15+7.50248738E1);
                  else
                    if ((1.996E3 < x(i)) && (x(i) <= 2.0E3))
                      T(i)=exp(x(i)^3.200849063E-3-log(x(i))^7.649247405-(log(x(i))^1.950087695E3)/x(i)...
                          -3.0274449915E4/x(i)-1.0/(x(i)*x(i))^5.246813355E4-(x(i)*x(i))^5.727895988E-7...
                          +(x(i)*x(i)*x(i))^7.257991516E-11-(x(i)*x(i)*x(i)*x(i))^4.264874572E-15+7.8158267155E1);
                    else
                      if ((2.0E3 < x(i)) && (x(i) <= 3.105E3))
                        T(i)=exp(x(i)^7.247575829E-4-log(x(i))^2.77640379+(log(x(i))^2.37350995E2)/x(i)...
                            -4.029099585E4/x(i)+1.0/(x(i)*x(i))^4.749931245E4-(x(i)*x(i))^1.2760069505E-7...
                            +(x(i)*x(i)*x(i))^1.027341484E-11+(x(i)*x(i)*x(i)*x(i))^2.308890815E-17+4.139155714E1);
                      else
                        if ((3.105E3 < x(i)) && (x(i) <= 6.0E3))
                          T(i)=exp(x(i)^-1.456785621E-4-log(x(i))^8.66489675E-1+(log(x(i))^2.37350995E2)...
                              /x(i)-4.163060515E4/x(i)+1.0/(x(i)*x(i))^7.9226979E4+(x(i)*x(i))^7.45436745E-9...
                              -(x(i)*x(i)*x(i))^6.0615996E-13+(x(i)*x(i)*x(i)*x(i))^2.308890815E-17+2.8189654925E1);
                        else
                          if ((6.0E3 < x(i)) && (x(i) <= 2.0E4))
                            T(i)=exp(x(i)^-1.97817555E-2+log(x(i))^2.49547498E2+(log(x(i))^7.50037784E5)/x(i)...
                                -4.951383346E6/x(i)+1.0/(x(i)*x(i))^4.4343314BE8+(x(i)*x(i))^5.4962868E-7-...
                                (x(i)*x(i)*x(i))^1.09867495E-11+(x(i)*x(i)*x(i)*x(i))^9.9946897E-17-2.331023088E3);
                          else
                            T(i) = NaN;
end;end;end;end;end;end;end;end;end;end;end;end;end;
```

Figure 10-12: Equilibrium constant function for Keq. Code generated from the piecewise symbolic MuPad expression. Input: x (K). Output: T (unitless). The output value for this particular function is also equivalent to the partial pressure of CO (atm).

The input, *x*, of Keq is the absolute temperature (K) and is used to identify the correct temperature interval and evaluate only the functional form for the corresponding interval. The output of the function Keq is the equilibrium constant for the stoichiometric reaction given by Equation 425, but also represents the partial pressure of CO in atmospheres according to Equation 428, assuming the solids are ideal.

In summary, the previous two sections have shown how to import thermodynamic data and expressions, for chemical species using a NASA thermodynamic database, into a useful data structure. The thermodynamic properties are valid over a large temperature range, but defined over different continuous temperature intervals. This complexity is effectively handled using piecewise symbolic expressions for each temperature interval. The piecewise symbolic expressions are then used as building blocks to produce more complicated thermodynamic expressions, automatically introducing subdivisions of the temperature intervals and expressions to accommodate non-overlapping intervals. Piecewise symbolic thermodynamic expressions representing the Gibbs free energy of reaction and/or reaction equilibrium constants are then used to construct MATLAB functions to numerically calculate the property value at a given temperature. This process greatly simplifies the procedure for generating the functions needed for calculating the equilibrium composition of an arbitrary chemical system without having to manually write the mathematical expressions and functions.

IV.iii Thermodynamic Database for Select Chemical Species

There are three chemical systems modeled in this thesis. Included in these chemical systems are the gas chemical species, {$B_2O_{2(g)}$, $B_2O_{3(g)}$, $CO_{(g)}$, $CO_{2(g)}$, $SiO_{(g)}$}, and the condensed chemical species, {B_2O_3, B_4C, C, SiC, SiO_2}. The methods of APPENDIX IV.i are applied to the NASA thermodynamic database to create a data structure for the select chemical species. The data structure facilitates the use of the physical and thermodynamic properties when generating the chemical equilibrium model for each system. An excerpt from the NASA thermodynamic database used for generating the data structure for the select chemical species is shown below.

```
B2O2              Gurvich,1996a pt1 p19 pt2 p15.
 2 tpis96 B   2.00O   2.00    0.00    0.00    0.00 0   53.6208000    -457711.486
    200.000   1000.0007 -2.0 -1.0  0.0  1.0  2.0  3.0  4.0  0.0         13396.618
 8.174391690D+04-1.732702797D+03 1.605560926D+01-2.160057288D-02 3.566854570D-05
-2.660198794D-08 7.531833240D-12               -4.899632900D+04-6.172702390D+01
   1000.000   6000.0007 -2.0 -1.0  0.0  1.0  2.0  3.0  4.0  0.0         13396.618
 4.605789660D+05-2.990079203D+03 1.256764079D+01-7.850974950D-04 1.672537624D-07
-1.867694780D-11 8.486190670D-16               -4.015748150D+04-4.874413710D+01
B2O3              Gurvich,1996a pt1 p25 pt2 p18.
 2 tpis96 B   2.00O   3.00    0.00    0.00    0.00 0   69.6202000    -835382.271
    200.000   1000.0007 -2.0 -1.0  0.0  1.0  2.0  3.0  4.0  0.0         14418.729
 7.379611910D+04-1.263620592D+03 1.072681512D+01 3.841383720D-04 5.976058380D-06
-6.552891350D-09 2.123951064D-12               -9.628183140D+04-3.088078011D+01
   1000.000   6000.0007 -2.0 -1.0  0.0  1.0  2.0  3.0  4.0  0.0         14418.729
 3.905035300D+05-3.691348210D+03 1.555502598D+01-9.707645510D-04 2.068887872D-07
-2.310858356D-11 1.050136734D-15               -8.263054410D+04-6.390863440D+01
CO                Gurvich,1979 pt1 p25 pt2 p29.
 3 tpis79 C   1.00O   1.00    0.00    0.00    0.00 0   28.0101000    -110535.196
    200.000   1000.0007 -2.0 -1.0  0.0  1.0  2.0  3.0  4.0  0.0          8671.104
 1.489045326D+04-2.922285939D+02 5.724527170D+00-8.176235030D-03 1.456903469D-05
-1.087746302D-08 3.027941827D-12               -1.303131878D+04-7.859241350D+00
   1000.000   6000.0007 -2.0 -1.0  0.0  1.0  2.0  3.0  4.0  0.0          8671.104
 4.619197250D+05-1.944704863D+03 5.916714180D+00-5.664282830D-04 1.398814540D-07
-1.787680361D-11 9.620935570D-16               -2.466261084D+03-1.387413108D+01
   6000.000  20000.0007 -2.0 -1.0  0.0  1.0  2.0  3.0  4.0  0.0          8671.104
 8.868662960D+08-7.500377840D+05 2.495474979D+02-3.956351100D-02 3.297772080D-06
-1.318409933D-10 1.998937948D-15                5.701421130D+06-2.060704786D+03
CO2               Gurvich,1991 pt1 p27 pt2 p24.
 3 g 9/99 C   1.00O   2.00    0.00    0.00    0.00 0   44.0095000    -393510.000
    200.000   1000.0007 -2.0 -1.0  0.0  1.0  2.0  3.0  4.0  0.0          9365.469
 4.943650540D+04-6.264116010D+02 5.301725240D+00 2.503813816D-03-2.127308728D-07
-7.689988780D-10 2.849677801D-13               -4.528198460D+04-7.048279440D+00
   1000.000   6000.0007 -2.0 -1.0  0.0  1.0  2.0  3.0  4.0  0.0          9365.469
 1.176962419D+05-1.788791477D+03 8.291523190D+00-9.223156780D-05 4.863676880D-09
-1.891053312D-12 6.330036590D-16               -3.908350590D+04-2.652669281D+01
   6000.000  20000.0007 -2.0 -1.0  0.0  1.0  2.0  3.0  4.0  0.0          9365.469
-1.544423287D+09 1.016847056D+06-2.561405230D+02 3.369401080D-02-2.181184337D-06
 6.991420840D-11-8.842351500D-16               -8.043214510D+06 2.254177493D+03
SiO               Gurvich,1991 pt1 p247 pt2 p227
 2 tpis91 SI  1.00O   1.00    0.00    0.00    0.00 0   44.0849000     -98842.418
    200.000   1000.0007 -2.0 -1.0  0.0  1.0  2.0  3.0  4.0  0.0          8715.105
-4.722771050D+04 8.063137640D+02-1.636976133D+00 1.454275546D-02-1.723202046D-05
 1.042397340D-08-2.559365273D-12               -1.666585903D+04 3.355795700D+01
```

```
   1000.000   6000.0007 -2.0 -1.0  0.0  1.0  2.0  3.0  4.0  0.0         8715.105
-1.765134162D+05-3.199177090D+01 4.477441930D+00 4.591764710D-06 3.558143150D-08
-1.327012559D-11 1.613253297D-15               -1.350842360D+04-8.386957330D-01
ZrO               Gurvich,1982 pt1 p118 pt2 p118.
 3 tpis82 ZR  1.00O   1.00    0.00    0.00    0.00 0  107.2234000      83922.708
    200.000   1000.0007 -2.0 -1.0  0.0  1.0  2.0  3.0  4.0  0.0         8970.108
-5.091761400D+05 8.652770090D+03-5.294740150D+01 1.728961761D-01-2.457230895D-04
 1.672135156D-07-4.423012380D-11               -3.095129818D+04 3.132576719D+02
   1000.000   6000.0007 -2.0 -1.0  0.0  1.0  2.0  3.0  4.0  0.0         8970.108
 4.648098310D+05 3.442314470D+02 4.815779180D+00-4.660633140D-04 2.140489079D-07
-2.054364483D-11 4.084667760D-16                7.317340700D+03 1.502933548D+00
   6000.000  20000.0007 -2.0 -1.0  0.0  1.0  2.0  3.0  4.0  0.0         8970.108
 1.343456923D+08-7.851088360D+04 1.981614195D+01-8.027211020D-04 2.522081797D-09
 7.959625600D-13-1.684162816D-17                6.406670590D+05-1.358472283D+02
B2O3(cr)          Hexagonal. Gurvich,1996a pt1 p21 pt2 p16.
 1 tpis96 B   2.00O   3.00    0.00    0.00    0.00 1   69.6202000   -1273500.000
    100.000    723.0007 -2.0 -1.0  0.0  1.0  2.0  3.0  4.0  0.0         9301.499
-5.595297380D+04 1.311214190D+03-1.178535942D+01 7.702795250D-02-9.740126500D-05
 4.692119720D-08 1.804813810D-12               -1.599672923D+05 5.866759160D+01
B2O3(L)           Liquid. Gurvich,1996a pt1 p21 pt2 p16.
 1 tpis96 B   2.00O   3.00    0.00    0.00    0.00 2   69.6202000   -1273500.000
    723.000   6000.0007 -2.0 -1.0  0.0  1.0  2.0  3.0  4.0  0.0         9301.499
 3.774124994D+05 0.000000000D+00 1.528015481D+01 0.000000000D+00 0.000000000D+00
 0.000000000D+00 0.000000000D+00               -1.562115789D+05-8.056094941D+01
B4C(cr)           Hexagonal. Gurvich,1996a pt1 p111 pt2 p89
 2 tpis96 B   4.00C   1.00    0.00    0.00    0.00 1   55.2547000     -62000.000
    200.000    500.0007 -2.0 -1.0  0.0  1.0  2.0  3.0  4.0  0.0         5611.469
-3.582115390D+07 6.748884130D+05-5.160630080D+03 2.049973510D+01-4.453648770D-02
 5.049831300D-05-2.340979136D-08               -3.040618105D+06 2.693617477D+04
    500.000   2743.0007 -2.0 -1.0  0.0  1.0  2.0  3.0  4.0  0.0         5611.469
-5.772904970D+05 0.000000000D+00 1.274373364D+01 5.718209610D-05 1.287030822D-06
 0.000000000D+00 0.000000000D+00               -1.320621763D+04-7.266962500D+01
B4C(L)            Liquid. Chase,1998 pp556-8.
 1 j 6/83 B   4.00C   1.00    0.00    0.00    0.00 2   55.2547000     -62000.000
   2743.000   6000.0007 -2.0 -1.0  0.0  1.0  2.0  3.0  4.0  0.0         5611.469
 0.000000000D+00 0.000000000D+00 1.635454164D+01 0.000000000D+00 0.000000000D+00
 0.000000000D+00 0.000000000D+00               -1.250553215D+03-9.163227046D+01
C(gr)             Graphite. Ref-Elm. TRC(4/83) vc,uc,tc1000-1002.
 3 n 4/83 C   1.00    0.00    0.00    0.00    0.00 1   12.0107000          0.000
    200.000    600.0007 -2.0 -1.0  0.0  1.0  2.0  3.0  4.0  0.0         1053.500
 1.132856760D+05-1.980421677D+03 1.365384188D+01-4.636096440D-02 1.021333011D-04
-1.082893179D-07 4.472258860D-11                8.943859760D+03-7.295824740D+01
    600.000   2000.0007 -2.0 -1.0  0.0  1.0  2.0  3.0  4.0  0.0         1053.500
 3.356004410D+05-2.596528368D+03 6.948841910D+00-3.484836090D-03 1.844192445D-06
-5.055205960D-10 5.750639010D-14                1.398412456D+04-4.477183040D+01
   2000.000   6000.0007 -2.0 -1.0  0.0  1.0  2.0  3.0  4.0  0.0         1053.500
 2.023105106D+05-1.138235908D+03 3.700279500D+00-1.833807727D-04 6.343683250D-08
-7.068589480D-12 3.335435980D-16                5.848134850D+03-2.350925275D+01
SiC(b)            Beta,cubic. Gurvich,1991 pt1 p298 pt2 p264.
 2 tpis91 SI  1.00C   1.00    0.00    0.00    0.00 1   40.0962000     -73000.000
    100.000    298.1507 -2.0 -1.0  0.0  1.0  2.0  3.0  4.0  0.0         3272.000
-2.285496383D+03 0.000000000D+00-5.349100620D-01 1.271547084D-02 0.000000000D+00
 0.000000000D+00 0.000000000D+00               -9.193174900D+03 1.241441354D+00
    298.150   3105.0007 -2.0 -1.0  0.0  1.0  2.0  3.0  4.0  0.0         3272.000
-1.269106658D+05 0.000000000D+00 3.757286960D+00 3.481744565D-03-1.620660748D-06
 2.611097948D-10 0.000000000D+00               -1.046667760D+04-2.109198538D+01
SiC(L)            Liquid. Gurvich,1991 pt1 p298 pt2 p264.
 1 tpis91 SI  1.00C   1.00    0.00    0.00    0.00 2   40.0962000     -73000.000
   3103.000   6000.0007 -2.0 -1.0  0.0  1.0  2.0  3.0  4.0  0.0         3272.000
 0.000000000D+00 0.000000000D+00 7.577115188D+00 0.000000000D+00 0.000000000D+00
 0.000000000D+00 0.000000000D+00               -7.787459000D+03-4.367596159D+01
SiO2(a-qz)        Alpha-quartz,hexagonal. Gurvich,1991 pt1 p250 pt2 p228.
 1 tpis91 SI  1.00O   2.00    0.00    0.00    0.00 1   60.0843000    -910700.000
    200.000    848.0007 -2.0 -1.0  0.0  1.0  2.0  3.0  4.0  0.0         6916.000
-5.776895500D+05 7.214661110D+03-3.145730294D+01 7.412177150D-02-8.670077820D-06
-1.080461312D-07 8.316324910D-11               -1.462398375D+05 1.842424399D+02
SiO2(b-qz)        Beta-quartz,hexagonal. Gurvich,1991 pt1 p250 pt2 p228.
 1 tpis91 SI  1.00O   2.00    0.00    0.00    0.00 2   60.0843000    -910700.000
    848.000   1200.0007 -2.0 -1.0  0.0  1.0  2.0  3.0  4.0  0.0         6916.000
 2.317635074D+04 0.000000000D+00 7.026511484D+00 1.241925261D-03 0.000000000D+00
 0.000000000D+00 0.000000000D+00               -1.117012474D+05-3.580751356D+01
```

```
SiO2(b-crt)       Beta-cristobalite,cubic. Gurvich,1991 pt1 p250 pt2 p228.
 1 tpis91 SI  1.00O   2.00    0.00    0.00    0.00 3   60.0843000    -910700.000
   1200.000   1996.0007 -2.0 -1.0  0.0  1.0  2.0  3.0  4.0  0.0         6916.000
-5.356419079D+05 0.000000000D+00 9.331036946D+00-7.306503931D-04 3.339944266D-07
 0.000000000D+00 0.000000000D+00               -1.134326721D+05-4.998768383D+01
SiO2(L)           Liquid. Gurvich,1991 pt1 p250 pt2 p228.
 1 tpis91 SI  1.00O   2.00    0.00    0.00    0.00 4   60.0843000    -910700.000
   1996.000   6000.0007 -2.0 -1.0  0.0  1.0  2.0  3.0  4.0  0.0         6916.000
 0.000000000D+00 0.000000000D+00 1.004268442D+01 0.000000000D+00 0.000000000D+00
 0.000000000D+00 0.000000000D+00               -1.140002976D+05-5.554279592D+01
ZrC(cr)           Crystal. Chase,1998 pp658-60.
 2 j12/64 ZR  1.00C   1.00    0.00    0.00    0.00 1  103.2347000    -196648.000
    200.000    800.0007 -2.0 -1.0  0.0  1.0  2.0  3.0  4.0  0.0         5862.000
-1.329596558D+05 1.766908163D+03-9.907099000D+00 5.427909170D-02-8.887722520D-05
 7.332246190D-08-2.420411623D-11               -3.297124410D+04 5.279964170D+01
    800.000   3805.0007 -2.0 -1.0  0.0  1.0  2.0  3.0  4.0  0.0         5862.000
 8.297591180D+05-4.224196050D+03 1.308509211D+01-5.018095870D-03 2.155019459D-06
-4.233046770D-10 3.266859200D-14               -7.112782350D+02-7.921945570D+01
ZrO2(III)         Monoclinic. Gurvich,1982 pt1 p123 pt2 p122.
 2 tpis82 ZR  1.00O   2.00    0.00    0.00    0.00 1  123.2228000   -1100300.000
    200.000    500.0007 -2.0 -1.0  0.0  1.0  2.0  3.0  4.0  0.0         8751.000
-4.214621830D+06 7.918732350D+04-6.071267910D+02 2.463358622D+00-5.388665930D-03
 6.144154000D-06-2.860860736D-09               -4.893051030D+05 3.163542730D+03
    500.000   1445.0007 -2.0 -1.0  0.0  1.0  2.0  3.0  4.0  0.0         8751.000
-1.616911113D+05 0.000000000D+00 8.218464380D+00 1.091902502D-03 0.000000000D+00
 0.000000000D+00 0.000000000D+00               -1.353760676D+05-4.200007680D+01
ZrO2(II)          Tetragonal. Gurvich,1982 pt1 p123 pt2 p122.
 1 tpis82 ZR  1.00O   2.00    0.00    0.00    0.00 2  123.2228000   -1100300.000
   1445.000   2620.0007 -2.0 -1.0  0.0  1.0  2.0  3.0  4.0  0.0         8751.000
 0.000000000D+00 0.000000000D+00 9.393217399D+00 0.000000000D+00 0.000000000D+00
 0.000000000D+00 0.000000000D+00               -1.348114469D+05-4.823174581D+01
ZrO2(I)           Cubic. Gurvich,1982 pt1 p123 pt2 p122.
 1 tpis82 ZR  1.00O   2.00    0.00    0.00    0.00 3  123.2228000   -1100300.000
   2620.000   2983.0007 -2.0 -1.0  0.0  1.0  2.0  3.0  4.0  0.0         8751.000
 0.000000000D+00 0.000000000D+00 9.621733572D+00 0.000000000D+00 0.000000000D+00
 0.000000000D+00 0.000000000D+00               -1.338466275D+05-4.943361269D+01
ZrO2(L)           Liquid. Gurvich,1982 pt1 p123 pt2 p122.
 1 tpis82 ZR  1.00O   2.00    0.00    0.00    0.00 4  123.2228000   -1100300.000
   2983.000   6000.0007 -2.0 -1.0  0.0  1.0  2.0  3.0  4.0  0.0         8751.000
 0.000000000D+00 0.000000000D+00 1.202716696D+01 0.000000000D+00 0.000000000D+00
 0.000000000D+00 0.000000000D+00               -1.301975851D+05-6.505001424D+01
```

References

1. Somiya, S. and Y. Inomata, eds. *Silicon Carbide Ceramics - 1: Fundamental and Solid Reaction*. Sintering Behavior of Ultrafine SiC Powder, ed. J. Hojo. Vol. 7. 1991, Elsevier: New York, NY.
2. Weimer, A.W., *Carbide, nitride, and boride materials synthesis and processing*. 1st ed. 1997, London ; New York: Chapman & Hall. 671 p.
3. Thevenot, F., *Boron Carbide- A Comprehensive Review.* Journal of the European Ceramic Society, 1990. **6**(205-225).
4. Somiya, S. and Y. Inomata, eds. *Silicon Carbide Ceramics - 1: Fundamental and Solid Reaction*. 1991, Elsevier: New York, NY.
5. Sōmiya, S., *Handbook of advanced ceramics*. 2003, Amsterdam ; Boston: Elsevier Academic Press.

6. Rice, R.W., *Ceramic fabrication technology*. Materials engineering. 2003, New York: Marcel Dekker. xi, 357 p.
7. Grigor'ev, O.N., et al., *Sintered Ceramics Based on Boron Nitride and Carbide.* Powder Metall.Met.Ceram., 2007. **46**(1-2): p. 46-50.
8. Cawley, J.D. and C.E. Semler, eds. *Ceramic Transactions: Silicon Carbide '87*. Vol. 2. 1987, The American Ceramic Society: USA.
9. Carter, C.B. and M.G. Norton, *Ceramic Materials: Science and Engineering*. 2007, New York, NY: Springer.
10. Barsoum, M.W., *Fundamentals of Ceramics*. 2 ed. 2003, London: Institute of Physics.
11. Ring, T.A., *Fundamentals of Ceramic Powder Processing and Synthesis*. 1996, San Diego, California: Academic Press.
12. Rahaman, M.N., *Ceramic Processing and Sintering*. 1995, New York, NY: Marcel Dekker.
13. Somiya, S. and Y. Inomata, eds. *Silicon Carbide Ceramics - 1: Fundamental and Solid Reaction*. Sintering of Silicon Carbide, ed. H. Tanaka. Vol. 7. 1991, Elsevier: New York, NY.
14. Cawley, J.D. and C.E. Semler, eds. *Ceramic Transactions: Silicon Carbide '87*. Synthesis and Characterization of HSC Silicon Carbide, ed. W.M. Goldberger, A.K. Reed, and R. Morse. Vol. 2. 1987, The American Ceramic Society: USA.
15. Gerhardt, R., ed. *Properties and Applications of Silicon Carbide*. Silicon Carbide: Synthesis and Properties, ed. H. Abderrazak and E. Hmida. 2011.
16. Reed, J.S., *Principles of Ceramics Processing*. 2 ed. 1995, New York: Wiley.
17. Cawley, J.D. and C.E. Semler, eds. *Ceramic Transactions: Silicon Carbide '87*. Turbomilling Parameters Affecting the Ultrafine Grinding of Alpha-SiC, ed. J.L. Hoyer. Vol. 2. 1987, The American Ceramic Society.
18. Baik, S. and P.F. Becher, *Effect of oxygen contamination on densification of TiB2.* J. Am. Ceram. Soc., 1987. **70**(8): p. 527-30.
19. Gasch, M., et al., *Processing, properties and arc jet oxidation of hafnium diboride/silicon carbide ultra high temperature ceramics.* Journal of Materials Science, 2004. **39**: p. 5925-5937.
20. Raider, S.I., et al., *Surface Oxidation of Silicon Nitride Films.* J. Electrochem. Soc., 1976. **123**(4): p. 561-565.
21. Kim, K.H., et al., *Methanol Washing Effects on Spark Plasma Sintering Behavior and Mechanical Properties of B4C Ceramics.* Journal of Ceramic Processing Research, 2007. **8**(4): p. 238-42.
22. Sriamporn, T., et al., *Dental zirconia can be etched by hydrofluoric acid.* Dental Materials Journal, 2014. **33**(1): p. 79-85.
23. Xie, Y., *Solution-based Synthesis and Processing of Nanocrystalline ZrB2-Based Composites*, in *Materials Science and Engineering*2008, Georgia Institute of Technology.
24. Hackley, J.C., J.D. Demaree, and T. Gougousi, *Interface of atomic layer deposited HfO[sub 2] films on GaAs (100) surfaces.* Applied Physics Letters, 2008. **92**(16): p. 162902.
25. Warren, A., A. Nylund, and I. Olefjord, *Oxidation of Tungsten and Tungsten Carbide in Dry and Humid Atmospheres.* Int. J. of Refractory Metals & Hard Materials, 1996. **14**: p. 345-353.
26. Webb, W.W., J.T. Norton, and C. Wagner, *Oxidation Studies in Metal-Carbon Systems.* J. Electrochem. Soc., 1956. **103**(2): p. 112-117.

27. Takayuki Narushima, T.G., Makoto Maruyama, Haruo Arashi, Yasutaka Iguchi, *Oxidation of Boron Carbide–Silicon Carbide Composite at 1073 to 1773 K.* Materials Transactions, 2003. **44**(3): p. 401-6.
28. Steinbrück, M., *Oxidation of boron carbide at high temperatures.* Journal of Nuclear Materials, 2005. **336**(2-3): p. 185-193.
29. Semond, F., et al., *Direct SiO2/β-SiC(100)3×2 interface formation from 25 °C to 500 °C.* Applied Physics Letters, 1996. **68**(15): p. 2144.
30. Shanefield, D.J., *Organic Additives and Ceramic Processing, Second Edition: With Applications in Powder Metallurgy, Ink, and Paint*, 1996, Kluwer Academic Publishers: Norwell, Massachusetts.
31. Rijswijk, W.v. and D.J. Shanefield, *Effects of Carbon as a Sintering Aid in Silicon Carbide.* J. Am. Ceram. Soc., 1990. **73**(1): p. 148-49.
32. Roy, T.K., C. Subramanian, and A.K. Suri, *Pressureless sintering of boron carbide.* Ceramics International, 2006. **32**(3): p. 227-233.
33. Stobierski, L. and A. Gubernat, *Sintering of silicon carbideI. Effect of carbon.* Ceramics International, 2003. **29**(3): p. 287-292.
34. Prochazka, S. and R.M. Scanlan, *Effect of Boron and Carbon on Sintering of SiC.* J. Am. Ceram. Soc., 1975. **58**(1-2): p. 72.
35. Prochazka, S., *Sintered Dense Silicon Carbide*, 1977: N.Y.
36. Ness, E.A. and W. Rafaniello, *Orgin of Density Gradients in Sintered β-Silicon Carbide Parts.* J.Am.Ceram.Soc, 1994. **77**(11): p. 2879-2884.
37. Wiik, K. and K. Motzfeldt. *Kinetics of Reactions Between Silica and Carbon and the Formation of Silicon Carbide*. in *Materials Research Society Symposia Proceedings* 1995. MRS.
38. Clegg, W.J., *Role of Carbon in the Sintering of Boron-Doped Silicon Carbide.* J.Am.Ceram.Soc., 2000. **83**(5): p. 1039-1043.
39. Raczka, M., et al., *Effect of carbon content on the microstructure and properties of silicon carbide based sinters.* Materials Characterization, 2001. **46**: p. 245-249.
40. Suzuki, H., *Review: Preparation of beta-silicon carbide sintered ceramics.* Materials Chemistry and Physics, 1995. **42**: p. 1-5.
41. Hamminger, R., *Carbon Inclusions in Sintered Silicon Carbide.* J. Am. Ceram. Soc., 1989. **72**(9): p. 1741-44.
42. Ermer, E., P. Wieslaw, and L. Stobierski, *Influence of sintering activators on structure of silicon carbide.* solid state ionics, 2001. **141-142**: p. 523-8.
43. Ermer, E. and W.S. Ptak, *FTIR studies of structural effects due to boron addition in sintered silicon carbide.* Vibrational Spectroscopy, 2002. **29**: p. 211-215.
44. Datta, M.S., A.K. Bandyopadhyay, and B. Chaudhuri, *Sintering of nano crystalline a silicon carbide by doping with B4C.* Bull. Mater. Sci., 2002. **25**(3): p. 181-9.
45. Stobierski, L. and A. Gubernat, *Sintering of silicon carbide II. Effect of boron.* Ceramics International, 2003. **29**(4): p. 355-361.
46. Obata, S., et al., *Fabrication of dense silicon carbide through aqueous slurries containing well-dispersed C.* Journal of Materials Science, 2005. **40**: p. 757-760.
47. Zhang, Z. and N. Kong, *Nonequilibrium Thermal Dynamic Modeling of Porous Medium Vacuum Drying Process.* Mathematical Problems in Engineering, 2012. **2012**: p. 1-22.
48. Yun, J.W. and S.J. Lombardo, *Determination of rapid heating cycles for binder removal from open pore green ceramic components.* Advances in Applied Ceramics, 2009. **108**(2): p. 92-101.

49. Weber, A.Z. and J. Newman, *Modeling gas-phase flow in porous media.* International Communications in Heat and Mass Transfer, 2005. **32**(7): p. 855-860.
50. Strang, G., *Computational Science and Engineering*. 2007, Wellesley, MA: Wellesley-Cambridge Press.
51. Saaf, F., *A Study of Reactive Transport Phenomena in Porous Media*, 1996, Rice. p. 204.
52. Patankar, S.V., *Numerical Heat Transfer and Fluid Flow*. 1980, New York: Hemisphere.
53. Mason, E.A. and A.P. Malinauskas, *Gas Transport in Porous Media: The Dusty Gas Model*, 1983, Elsevier: N.Y.
54. Lombardo, S.J. and Z.C. Feng, *Pressure distribution during binder burnout in three-dimensional porous ceramic bodies with anisotropic permeability.* Journal of Materials Research, 2002. **17**(6): p. 1434-1440.
55. Lichtner, P.C., *Multi-Phase Reactive Transport Theory*, C.f.N.W.R. Analyses, Editor 1995: Southwest Research Institute.
56. Kräutle, S. and P. Knabner, *A new numerical reduction scheme for fully coupled multicomponent transport-reaction problems in porous media.* Water Resources Research, 2005. **41**(9).
57. Dullien, F.A.L., *Porous media : fluid transport and pore structure*. 2nd ed. 1992, San Diego: Academic Press. xx, 574 p.
58. Civan, F., *Porous media transport phenomena*. 2011, Hoboken, N.J.: Wiley. xx, 463 p.
59. Chunge, T.J., *Computational Fluid Dynamics*. 2002, United Kingdom: Cambridge University Press.
60. Rappaz, M., et al., *Numerical modeling in materials science and engineering*. Springer series in computational mathematics,. 2010, Berlin: Springer. xi, 540 p.
61. Boek, E., *Pore Scale Simulation of Flow in Porous Media Using Lattice-Boltzmann Computer Simulations*, in *SPE Annual Technical Conference*2010: Florence, Italy.
62. Martys, N.S., J.G. Haagedorn, and J.E. Devaney, *Lattice Boltzmann Simulations of Single and Mulit-Component Flow in Porous Media*, N.I.o.S.a. Technology, Editor.
63. Chen, S. and G.D. Doolen, *Lattice Boltzmann Method for Fluid Flows.* Annu. Rev. Fluid Mech., 1998. **30**: p. 329-64.
64. Bastian, P., *Numerical Computation of Multiphase Flows in Porous Media*, in *Computer Science*1999, Christian - Albrechts University of Kiel.
65. Webb, S.W., *Gas-Phase Diffusion in Porous Media - Evaluation of an Advection-Dispersive Formulation and the Dusty-Gas Model Including Comparison to Data for Binary Mixtures*, U.D.o. Energy, Editor 1996, Sandia National Laboratories.
66. Pruess, K., C. Oldenburg, and G. Moridis, *TOUGH2 Users Guide - Version 2*, L.B.N.L. Earth Sciences Division, Editor 2012.
67. Ghassemi, A. and A. Pak, *Pore scale study of permeability and tortuosity for flow through particulate media using Lattice Boltzmann method.* International Journal for Numerical and Analytical Methods in Geomechanics, 2011. **35**(8): p. 886-901.
68. Smith, W.R. and R.W. Missen, *Chemical Reaction Equilibrium Analysis: Theory and Algorithms.* 1982, USA: Wiley.
69. Pyun, C.W., *Steady-State and Equilibrium Approximations in Chemical Kinetics.* Journal of Chemical Education, 1971. **48**(3): p. 194-196.
70. Hill, C.G., *An introduction to chemical engineering kinetics & reactor design*. 1977, New York: Wiley. xi, 594 p.
71. Gaskell, D.R., *Introduction to the thermodynamics of materials*. 5th ed. 2008, New York: Taylor & Francis. xv, 618 p.

72. Denbigh, K.G., *The principles of chemical equilibrium : with applications in chemistry and chemical engineering*. 4th ed. 1981, Cambridge Eng. ; New York: Cambridge University Press. xxi, 494 p.
73. Chase, M.W., et al., *JANAF Thermochemical Tables*. Vol. Third. 1986, New York: American Institute of Physics.
74. Zehe, M.J., S. Gordon, and B.J. McBride, *CAP- A Computer Code for Generating Tabular Thermodynamic Functions from NASA Lewis Coefficients*, N.J.H.G.R.C.a.L. Field, Editor 2002: NASA Center for AeroSpace Information.
75. McBride, B.J. and S. Gordon, *Computer Program for Calculation of Complex Chemical Equilibrium Compositions and Applications: II. Users Manual and Program Description*, 1996.
76. Gordon, S. and B.J. McBride, *Computer Program for Calculation of Complex Chemical Equilibrium Compositions and Applications: I. Analysis*, NASA, Editor 1994.
77. Paz-García, J.M., et al., *Computing multi-species chemical equilibrium with an algorithm based on the reaction extents.* Computers & Chemical Engineering, 2013. **58**: p. 135-143.
78. Yeh, G.T. and V.S. Tripathi, *Critical Evaluation of Recent Developments in Hydrogeochemical Tranport Models of Reactive Multichemical Components.* Water Resources Research, 1989. **25**(1): p. 93-108.
79. Buchholzer, H., et al., *The semismooth Newton method for the solution of reactive transport problems including mineral precipitation-dissolution reactions.* Computational Optimization and Applications, 2010. **50**(2): p. 193-221.
80. Hairer, E. and G. Wanner, *Solving ordinary differential equations II: Stiff and Differential-Algebraic Problems*. Springer series in computational mathematics. Vol. 2. 1980, Berlin ; New York: Springer-Verlag.
81. Runchal, A., *ACRi Software Tools - ANSWER, PORFLOW, TIDAL*, I. Analytic & Computational Research, Editor 2010.
82. Chapman, S. and T.G. Cowling, *The mathematical theory of non-uniform gases : an account of the kinetic theory of viscosity, thermal conduction, and diffusion in gases*. 3rd ed. Cambridge mathematical library. 1990, Cambridge ; New York: Cambridge University Press. xxiv, 422 p.
83. Hirschfelder, J.O., C.F. Curtiss, and B.R. Bird, *Molecular Theory of Gases and Liquids*. 1954, New York: Wiley.
84. Poling, B.E., J.M. Prausnitz, and J.P. O'Connell, *The properties of gases and liquids*. 5th ed. 2001, New York: McGraw-Hill.
85. McGee, B.C., M.L. Hobbs, and M.R. Baer, *Exponential 6 Parameterization for the JCZ3-EOS*, S.N. Laboratories, Editor 1998.
86. Cloutman, L.D., *A Selected Library of Transport Coefficients for Combustion and Plasma Physics Applications*, L.L.N. Laboratory, Editor 2000.
87. Neufeld, P.D., *Empirical Equations to Calculate 16 of the Transport Collision Integrals Ω(l, s).* The Journal of Chemical Physics, 1972. **57**(3): p. 1100.
88. Kaza, A., *Effect of gas phase composition in pores, during initial stages of sintering*, in *Materials Science and Engineering*2006, Rutgers University. p. 202.
89. Strang, G., *Introduction to Linear Algebra*. 2009, Wellesley, MA: Wellesley-Cambridge Press.
90. Kaza, A., et al., *A Model of Gas-Phase Transport During the Initial Stages of Sintering of Silicon Carbide.* Journal of the American Ceramic Society, 2009. **92**(11): p. 2517-2527.

91. Rossi, M.A., et al., *Modeling of Gas-Phase Transport and Composition Evolution during the Initial-Stage Sintering of Boron Carbide with Carbon Additions.* Journal of the American Ceramic Society, 2010. **93**(11): p. 3691-3699.